The effect of different magnetospheric structures on predictions of gamma-ray pulsar light curves

M Breed

20574266

Dissertation submitted in partial fulfilment of the requirements for the degree *Magister Scientiae* in Space Physics at the Potchefstroom Campus of the North-West University

Supervisor: Prof C Venter

Co-supervisor: Dr AK Harding

October 2015

I dedicate this work to my loving Father for his grace, guidance, and love. Special thanks to Him for providing me with the love and support from family, friends, and work colleagues at the Physics Department. Thanks to my husband for his love and unwavering faith in me, and encouraging me to follow my dreams. It gives me great pleasure in acknowledging the support of my supervisor (Prof. Venter) and co-supervisor (Dr. Harding) for their guidance, patience, invaluable advice, and constantly challenging me. Your perseverance and ideas are truly inspirational. Lastly, this work is supported by the South African National Research Foundation (NRF). AKH acknowledges the support from the NASA Astrophysics Theory Program. CV, TJJ, and AKH acknowledge support from the *Fermi* Guest Investigator Program.

"Lift up your eyes on high,
And see who has created these things,
Who brings out their host by number;
He calls them all by name,
By the greatness of His might
And the strength of His power;
Not one is missing."
(Isaiah 40:26, NKJV)

The effect of different magnetospheric structures on predictions of gamma-ray pulsar light curves

Abstract: The field of γ-ray pulsars has been revolutionised by the launch of the *Fermi* Large Area Telescope, increasing the population from 7 to 161 detected pulsars. The light curves of these γ-ray pulsars exhibit a variety of profile shapes, and also different relative phase lags with respect to their radio pulses. We investigated the impact of different magnetospheric structures on the predicted γ-ray pulsar light curve characteristics. We performed geometric light curve modelling utilising the static dipole, retarded vacuum dipole, and a symmetric offset dipole field (characterised by a parameter ϵ), in conjunction with standard emission geometries, i.e., the two-pole caustic (with the slot gap its physical representation), and outer gap models (assuming uniform emissivity). This offset dipole field is a heuristic model that mimics deviations from the static dipole (corresponding to $\epsilon = 0$). We also considered a slot gap electric field for this case, which modulates the γ-ray emissivity. We solved the particle transport equation and found that the particle energy only became large enough to yield significant curvature radiation at large altitudes above the stellar surface, given the relatively low electric field (in the case of the Vela pulsar). Therefore, the particles did not always attain the radiation-reaction limit (where the acceleration rate balances the radiation loss rate). The B-field structure and emission geometry determined the pulsar's visibility and its pulse shape. For the symmetric offset dipole field we observed a small but noticeable effect in the phase plots and light curves for larger ϵ (for both the constant and variable emissivity cases). We noted that the inclusion of the slot gap electric field led to qualitatively different light curves compared to those produced by the geometric models. We fitted our model light curves to the superior-quality γ-ray light curve of the Vela pulsar (for energies > 100 MeV) for each B-field and geometric model combination using a χ^2 fitting method. We found an overall optimal fit for the retarded vacuum dipole field and outer gap model combination. For the retarded vacuum dipole field, the two-pole caustic model was statistically disfavoured compared to all other model combinations, since the Vela light curve possesses low off-peak emission. For the static dipole field, neither geometric model was significantly preferred. We lastly found that the offset dipole field favour smaller values of ϵ for constant emissivity and larger ϵ values for variable emissivity, but not significantly so.
Key words: *Fermi* Large Area Telescope – Gamma Rays – Pulsars – Vela pulsar (PSR J0835−4510) – Magnetic fields.

Die effek van verskillende magnetosferiese strukture op voorspelde gamma-straal pulsarligkrommes

Opsomming: *Fermi* Large Area Telescope het 'n omwenteling meegebring in die veld van γ-straal pulsare deur die populasie van waargenome pulsare van 7 tot 161 te verhoog. Die ligkrommes van hierdie γ-straal pulsare vertoon 'n verskeidenheid profielmorfologieë asook verskeie relatiewe fasevertragings m.b.t. hulle radioprofiele. Ons het die impak van verskillende magnetosferiese strukture op die eienskappe van die voorspelde γ-straal pulsarligkrommes ondersoek. Ons het geometriese ligkromme-modellering uitgevoer en gebruik gemaak van die statiese dipool, vertraagde vakuum-dipool, en 'n simmetriese verskuifde-dipoolmagneetveld (gekarakteriseer deur 'n parameter ϵ), tesame met standaard stralingsgeometrieë onder aanname van uniforme emissiwiteit, naamlik die "two-pole caustic" en die "outer gap" modelle. Die verskuifde dipoolveld is 'n heuristiese model wat afwykings vanaf die statiese dipool (wat ooreenstem met $\epsilon = 0$) naboots. Ons het ook 'n "slot gap" elektriese veld, wat die γ-straal emissiwiteit moduleer, beskou. Ons het die deeltjie-transportvergelyking opgelos en gevind dat die deeltjie-energie slegs groot genoeg word om beduidende krommingstraling te lewer hoog bo die steroppervlak, gegee die relatiewe swak elektriese veld (in die geval van die Vela-pulsar). Die deeltjies het dus nie altyd die stralingsreaksie-limiet (waar die versnellingstempo gelyk is aan die stralingsverliestempo) bereik nie. Die B-veldstruktuur en stralingsgeometrie bepaal die pulsarsigbaarheid en pulsvorm. Vir die simmetriese verskuifde-dipoolveld het ons 'n klein maar waarneembare effek in die twee-dimensionele stralingsgrafieke en ligkrommes opgemerk vir groter ϵ-waardes (vir beide konstante en veranderlike emissiwiteit). Ons het opgemerk dat die insluiting van die "slot gap" elektriese veld gelei het tot kwalitatiewe verskille in die ligkrommes in vergelyking met dié van die geometriese modelle. Ons het ons modelligkrommes op die hoë-kwaliteit γ-straal ligkrommes van die Vela-pulsar gepas (vir energieë > 100 MeV) vir elke kombinasie van B-velde en geometriese modelle deur gebruik te maak van 'n χ^2-passingsmetode. Ons algehele optimale oplossing was vir die kombinasie van die vertraagde vakuum-dipoolveld en "outer gap" model. Vir die vertraagde vakuum-dipoolveld word die "two-pole caustic" model statisties verwerp in vergelyking met alle ander modelkombinasies, omdat die Vela-ligkromme 'n lae vlak van straling vir fases buite die hoofpieke het. Ons het laastens vir die geval van die verskuifde-dipoolveld gevind dat kleiner waardes van ϵ verkies word vir konstante emissiwiteit, terwyl groter waardes van ϵ verkies word vir veranderlike emissiwiteit, maar dit was nie statisties beduidend nie.

Sleutelwoorde: *Fermi* Large Area Telescope – Gamma-strale – Pulsare – Vela-pulsar (PSR J0835−4510) – Magneetvelde.

Nomenclature

AGILE	Astro-rivelatore Gamma a Immagini LEggero
ASCA	Advanced Satellite for Cosmology and Astrophysics
AXP	Anomalous X-ray pulsar
B-field	Magnetic field
COS-B	Cosmic Ray Satellite-B
CR	Curvature radiation
CRR	Curvature radiation reaction
EGRET	Energetic Gamma-Ray Experiment Telescope
E-field	Electric field
EUVE	Extreme Ultraviolet Explorer
Fermi LAT	*Fermi* Large Area Telescope
FF	Force-free
GBM	Gamma-ray Burst Monitor
HE	High-energy
HEAO 1	High Energy Astrophysical Observatory 1
HEAO 2	High Energy Astrophysical Observatory 2
HEAO 3	High Energy Astrophysical Observatory 3
H.E.S.S.	High Energy Stereoscopic System
H.E.S.S.-II	High Energy Stereoscopic System Phase 2
ICS	Inverse Compton scattering
MAGIC	Major Atmospheric Gamma-Ray Imaging Cherenkov
MSP	Millisecond pulsar
NS	Neutron star
OG	Outer gap
PC	Polar cap
PFF	Pair formation front
PSPC	Pair-starved polar cap
PSR	Pulsar
PWN	Pulsar wind nebula
ROSAT	Röntgensatellit
RPP	Rotation-powered pulsar
RR	Radiation reaction

RRATS	Rotating radio transients
RVD	Retarded vacuum dipole
RVM	Rotating vector model
RXTE	Rossi X-ray Timing Explorer
SAS-1	Small Astronomy Satellite 1 (*Uhuru*)
SAS-2	Small Astronomy Satellite 2
SCLF	Space charge limited flow
SGR	Soft gamma-ray repeater
SG	Slot gap
SR	Synchrotron radiation
SSC	Synchrotron self-Compton
TPC	Two-pole caustic
VERITAS	Very Energetic Radiation Imaging Telescope Array System
VHE	Very-high-energy
XMM-Newton	X-ray Multi-Mirror Mission
2D	Two-dimensional
3D	Three-dimensional

Frequently used symbols

γ	Associated with gamma-ray radiation
γ_e	Particle energy (Lorentz factor)
P	Pulsar period
$\dot{P}$	Time derivative of the pulsar period
α	Inclination angle
ζ	Observer angle
B	Magnetic field / Magnetic field strength
c	Speed of light
$\phi_{\rm L}$	Pulse phase
E	Electric field / Electric field strength
ϵ_ν	Emissivity
χ^2	Chi-square
$M_\odot$	Solar mass
M	Stellar mass
τ	Characteristic pulsar age
R	Stellar radius
Ω	Angular velocity
I	Moment of inertia
μ	Magnetic moment
B_0	Surface magnetic field strength
e^+	Positron
e^-	Electron
$\boldsymbol{\mu}$	Magnetic dipole vector (magnetic axis)
$\boldsymbol{\Omega}$	Spin axis
$\theta_{\rm PC}$	Polar cap angle
$\rho_{\rm GJ}$	Goldreich-Julian charge density
$\mathbf{r}$	Position vector
$E_{\parallel}$	Accelerating electric field parallel to the local magnetic field
$\rho_{\rm curv}$	Curvature radius
$\Delta\xi_{\rm SG}$	Colatitudinal gap width of the slot gap model
$R_{\rm LC}$	Light cylinder radius
r	Radial distance from the stellar centre

a	Characterizes the effective offset of the polar cap
ϵ	Offset parameter related to the magnitude of the shift of the polar cap from the magnetic axis
ϕ'_0	Magnetic azimuthal angle defining the plane in which the offset occurs
$r_{\rm PC}$	Polar cap radius
$R_{\rm min}$	Minimum emission radius
$R_{\rm max}$	Maximum emission radius
$R_{\rm NCS}$	Null charge surface radius
θ	Magnetic polar angle
ϕ'	Magnetic azimuthal angle
$r_{\rm ovc}^{\rm min}$	Innermost ring
$r_{\rm ovc}^{\rm max}$	Polar cap rim
w	Gap width of the geometric models
$E_{\|,\rm SG}$	Slot gap electric field parallel to the local magnetic field
$E_{\|,\rm low}$	Low-altitude slot gap electric field
$E_{\|,\rm high}$	High-altitude slot gap electric field
x	Normalised radial distance in units of light cylinder radius
η	Normalised radial distance in units of light cylinder radius
$\eta_{\rm cut}$	Intersection radius (scaled by R) of $E_{\|,\rm low}$ and $E_{\|,\rm high}$
$\eta_{\rm c}$	Critical scaled radius where the low and high-altitude electric field solutions are matched
$\phi_{\rm PC}$	Magnetic azimuthal angle defined for usage with the E-field (π out of phase with ϕ')
$\xi = \theta/\theta_{\rm PC}$	Dimensionless colatitude of the gap field lines
$\mathcal{L}$	Likelihood
$Y_{{\rm d},i}$	Number of counts of the observed light curve
$Y_{{\rm m},i}$	Number of counts of the modelled light curve
$\sigma_{{\rm d},i}$	Standard deviation of the observed light curve
$\sigma_{{\rm m},i}$	Standard deviation of the modelled light curve
$N_{\rm bins}$	Number of bins
$\Delta\phi_{\rm L}$	Pulsar phase shift
A	Amplitude
$\chi^2_{\rm opt}$	Chi-square value associated with the optimal best-fit solution
$Y_{{\rm opt},i}$	Number of counts of the optimal modelled light curve
ξ^2	Scaled chi-square
ξ^2_ν	Reduced scaled chi-square
$\xi^2_{\rm opt}$	Scaled chi-square associated with the optimal best-fit solution
$\xi^2_{{\rm opt},\nu}$	Reduced scaled chi-square associated with the optimal best-fit solution
$N_{\rm dof}$	Number of degrees of freedom
$1\sigma, 2\sigma, 3\sigma$	Significance contours with 68%, 95.4%, and 99.73% confidence intervals respectively
$\Delta\xi^2$	Difference between the optimal and alternative models
X	Maximum factor allowed for the ratio of model to data flux in each light curve bin
$\beta = \zeta - \alpha$	Impact angle between the inclination and observer angle

Contents

List of Figures

List of Tables

Chapter 1

Introduction

1.1 Context and motivation

Pulsars have been identified as compact neutron stars (NSs), formed in supernova explosions. These stars rotate at tremendous rates and contain strong electric, magnetic, and gravitational fields. The fact that pulsars are characterised by such extreme conditions make them valuable laboratories for studying a wide range of topics, including nuclear physics, plasma physics, electrodynamics, magnetohydrodynamics, and general relativistic physics. Pulsars are capable of emitting pulsed emission across the entire electromagnetic spectrum, including radio, optical, X-rays, and γ-rays, in addition to injecting high-energy (HE) particles into the ambient environment (e.g., Manchester & Taylor, 1977; Lyne & Graham-Smith, 1990; Lorimer & Kramer, 2004).

There are mainly two pulsar populations – the canonical pulsars and the millisecond pulsars (MSPs). These distinct populations are evident on a $P\dot{P}$-diagram (the time derivative of the period $\dot{P}$ versus the rotational period P, see Figure 2.3), which indicates the properties and evolution of each population. The canonical radio pulsar population (situated in the centre of the $P\dot{P}$-diagram) is identified with the younger pulsars with high magnetic fields (B-fields), whereas the MSP population (situated in the bottom left corner) is associated with older pulsars with low B-fields (for more details, see Section 2.3 and 2.4).

The field of γ-ray pulsars has been revolutionised by the launch of the *Fermi* Large Area Telescope (LAT). The *Fermi* LAT is a γ-ray satellite which is much more sensitive than its predecessor, *EGRET (Energetic Gamma-Ray Experiment Telescope)*, measuring the cosmic γ-ray flux in the energy range between 20 MeV and 300 GeV (Atwood et al., 2009; see Section 2.8). Over the past seven years *Fermi* has detected over 160 γ-ray pulsars, of which the Crab, Vela, and Geminga pulsars are the brightest sources. It has furthermore measured their light curves and spectral characteristics in spectacular detail. A light curve or profile is the flux as a function of time (or phase), averaged over many pulsar rotations. *Fermi* has recently released its Second Pulsar Catalogue (2PC; Abdo et al., 2013) describing the properties of some 117 of these pulsars in the energy range 100 MeV to 100 GeV. This catalogue includes the Vela pulsar (Abdo et al., 2009), the brightest persistent source in the GeV sky. This pulsar also serves as a calibration source for *Fermi* and has been detected at a very high significance. A notable conclusion from the 2PC was that the spectra and light curves of both the MSP and young pulsar populations show remarkable similarities, pointing to common radiation mechanisms (discussed in Section 2.6) and emission regions (see Section 2.7 and 3.2) in their respective magnetospheres (see Section 3.1). Recently, *VERITAS* and *MAGIC* detected pulsed emission from the Crab pulsar in the very-high-

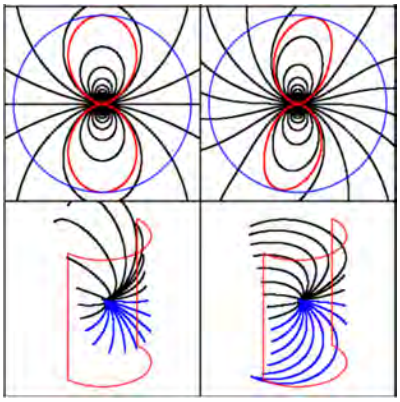

Figure 1.1: Different B-field structures. On the left is the static vacuum dipole and on the right is the RVD. The top panels show the field lines in the equatorial plane (for $\alpha = 90°$). The red B-field lines indicate the boundary between the open and closed field lines and are called the last open / closed field lines; they are tangent to the light cylinder (where the corotation speed equals the speed of light c) shown in blue. The bottom panels show the B-fields for $\alpha = 80°$. The red curve indicates the light cylinder. The sweepback of field lines is evident for the RVD case. From Romani & Watters (2010).

energy (VHE; >100 GeV) regime (and now possibly up to 1 TeV, Aleksić et al., 2011; Aliu et al., 2011; Aleksić et al., 2012). Furthermore, *H.E.S.S. (High Energy Stereoscopic System)* has now detected pulsed emission from the Vela pulsar in the 20−120 GeV range (Abramowski *et al.*, in prep.).

After nearly 50 years since the discovery of the first pulsar (Hewish et al., 1968), many questions still remain regarding the electrodynamical character of the magnetosphere, including particle acceleration, current closure, and radiation of a complex multi-wavelength spectrum. Geometric light curve modelling presents a crucial avenue for probing the pulsar magnetosphere, as such models may be used to constrain the pulsar geometry (inclination angle α and the observer's viewing angle ζ), as well as the γ-ray emission region's location and extent. This will provide vital insight to the boundary conditions and geometry to be assumed in the development of next-generation full radiation models.

Geometric light curve modelling has been performed by e.g., Dyks et al. (2004a); Venter et al. (2009); Watters et al. (2009); Johnson et al. (2014); Pierbattista et al. (2014), using standard pulsar emission geometries (cf. Section 2.7 for a discussion on the standard physical pulsar models), including a two-pole caustic (TPC of which the slot gap (SG) is its physical representation; Dyks & Rudak, 2003), outer gap (OG; Romani, 1996), and pair-starved polar cap (PSPC; Harding et al., 2005) geometry (see Section 2.7 and 3.2). The assumed B-field structure is, however, essential for predicting the light curves seen by the observer, since photons are expected to be emitted tangentially to the local B-field lines in the corotating pulsar frame (Daugherty & Harding, 1982). Even a small difference in the magnetospheric structure will therefore have an impact on the light curve predictions. For all of the above geometric models, the most commonly employed B-field is the retarded vacuum dipole (RVD) solution first obtained by Deutsch (1955). However, other solutions also exist. One example is the static dipole (non-rotating) field, a special case of the RVD (rotating) field (Dyks & Harding, 2004). In Figure 1.1 the static dipole field and the RVD field are contrasted. Bai & Spitkovsky (2010) furthermore modelled HE light curves in the context of OG and TPC models using a force-free (FF) B-field geometry (assuming a plasma-filled magnetosphere), proposing a separatrix layer model close to the last open field line (tangent to the light cylinder), up to and beyond the light cylinder. In addition, the annular gap model of Du et al. (2010), using the static dipole field, has been successful in reproducing the main characteristics of the γ-ray light curves of three MSPs. This model does, however, not attempt to replicate the nonzero phase offsets between the γ-ray and radio profiles. The recent detection of pulsed VHE emission led to the development of new physical models. These include a pulsar wind model by Aharonian et al. (2012) who invokes synchrotron-self-Compton (SSC) emission, as well as a striped wind model (Mochol & Pétri, 2015), using a split monopole B-field beyond the light cylinder, in which GeV emission originates via synchrotron radiation (SR) from relativistic particles that are accelerated by magnetic reconnection.

In this study, we investigate the impact of different magnetospheric structures on the predicted pulsar light curves. We assume standard emission geometries, the TPC and OG models. We have access to a geometric modelling code (see Section 3.3) which already includes the static-dipole and RVD solutions, and we will incorporate an additional B-field, i.e., the offset dipole field. Sky maps (radiated intensity per solid angle as a function of ζ and pulse phase $\phi_{\rm L}$, for a constant α) and light curves (intensity vs. $\phi_{\rm L}$; e.g., Figure 1.2) for the various B-field and radiation model combinations, as well as for several different pulsar parameters are constructed. These sky maps and light curves are compared to study their effect on the predicted pulsar light curves. As an application, our model light curves are compared with *Fermi* LAT data for the Vela pulsar, allowing us to infer the most probable configuration in this case, thereby constraining Vela's high-altitude magnetic structure and system geometry. We recently published some of this work in the following refereed proceedings of the South African Institute of Physics:

- Breed, M., Venter, C., Harding, A. K. and Johnson, T. J. 2012, *The Effect of Different Magnetospheric Structures on Predictions of Gamma-ray Pulsar Light Curves*, Conf. Proc. of the 57^{th} Ann. Conf. of the SA Institute of Physics hosted by the University of Pretoria, ed. J. Janse van Rensburg, 316–21 (astro-ph/1501.05117)

- Breed, M., Venter, C., Harding, A. K. and Johnson, T. J. 2013, *Implementation of an offset dipole magnetic field in a pulsar modelling code*, Conf. Proc. of the 58^{th} Ann. Conf. of the SA Institute of Physics hosted by the University of Zululand, ed. R. Botha and T. Jili, 350–5 (astro-ph/1411.1835)

- Breed, M., Venter, C., Harding, A. K. and Johnson, T. J. 2014, *The effect of an offset dipole magnetic field on the Vela pulsar's γ-ray light curves*, Conf. Proc. of the 59^{th} Ann. Conf. of the SA Institute of Physics hosted by the University of Johannesburg, ed. C. Engelbrecht and S. Karataglidis 311–6 (astro-ph/1504.06816)

1.2 Research aims and objectives

The aim of this project is to implement a new offset dipole B-field solution in an existing geometric light curve modelling code (Harding & Muslimov, 2011a,b), and to study its effect on the predicted γ-ray pulsar light curves. This solution affords a heuristic model that mimics deviations from the static dipole analytically such as occur in complex solutions, e.g., dissipative (e.g., Kalapotharakos et al., 2012; Li et al., 2012; Li, 2014; Tchekhovskoy et al., 2013) and force-free (Contopoulos et al., 1999) fields. These complex B-fields have only numerical solutions, and are limited by the resolution of the spatial grid. The implementation of this offset

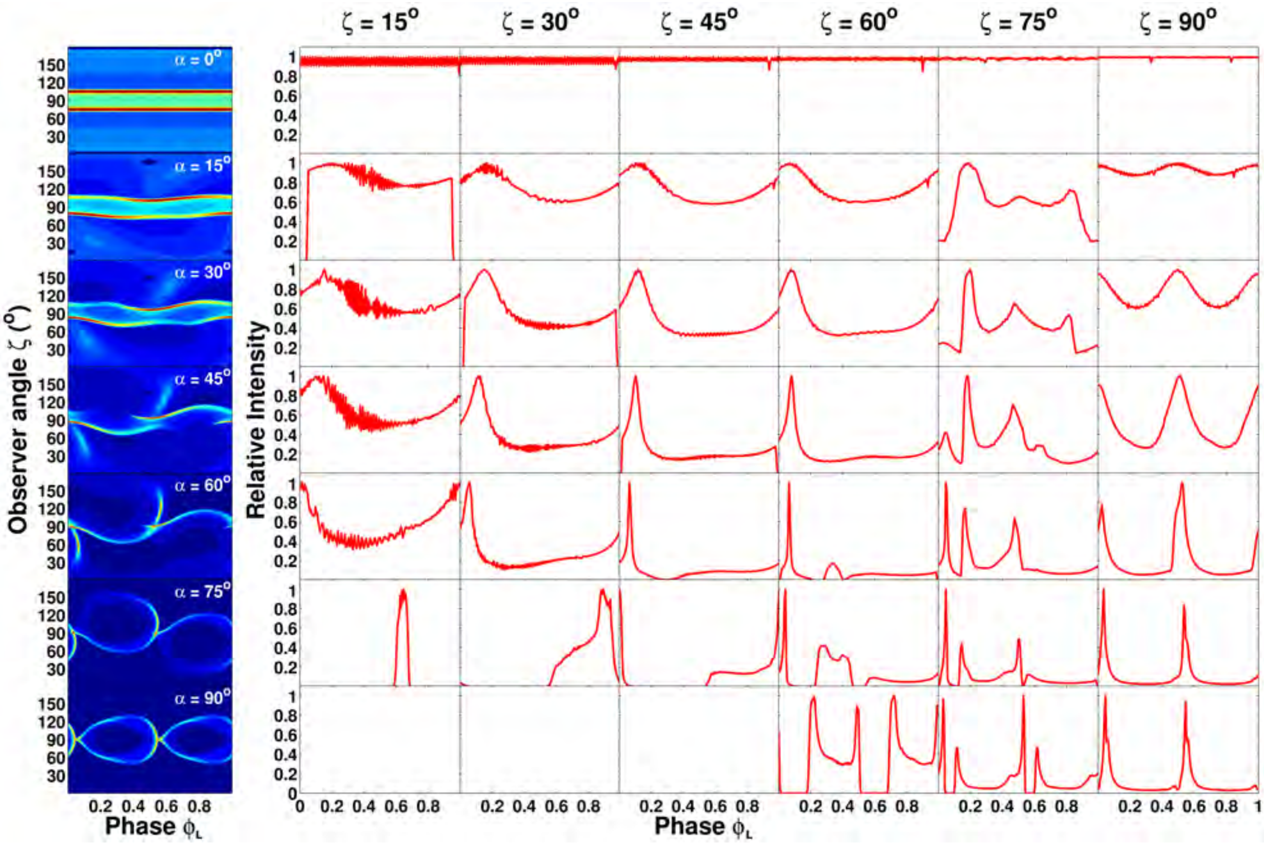

Figure 1.2: Example sky maps (left) and light curves (right) as predicted by the TPC model using the static dipole B-field, for different values of α and ζ (in degrees).

dipole field involves a transformation of the B-field components from the magnetic to the rotational frame, as well as Cartesian to spherical co-ordinates (discussed in Appendix A). In addition to the offset dipole field we will also study the static-dipole and RVD solutions, in conjunction with the TPC and OG geometric models.

We have also incorporated an SG electric field (E-field) associated with the offset dipole field. This allows us to calculate the emissivity ϵ_ν in the acceleration region (see Section 4.3). We have only considered the TPC (assuming uniform ϵ_ν) and SG (assuming variable ϵ_ν as modulated by the E-field) models for the offset dipole field, since we do not have E-field expressions available for the OG model. There are low-altitude and high-altitude analytical expressions available for the SG E-field. To obtain a general expression for the E-field, we need to match these low-altitude and high-altitude solutions by determining the matching parameter, η_c (see Section 4.3 and 4.4). The fact that we have an E-field enables us to solve the particle transport equation on each B-field line, yielding the particle energy (Lorentz factor γ_e) as a function of position. We can then use this factor to test whether the particle reaches the CRR limit, i.e., where acceleration balances curvature radiation losses.

Several sky maps were constructed (see first column of Figure 1.2) to study the emission properties of the HE beam. Light curves are obtained by making constant-ζ cuts through the sky maps (see second column and onwards of Figure 1.2). This has been done for each of the different geometric model and B-field combinations. As an example, we have compared our results to the superior-quality light curve of the Vela pulsar, measured by *Fermi* in the GeV energy range.

We have developed a chi-squared (χ^2) method to search the multivariate solution space for optimal model parameters. This facilitates the statistical selection of the best-fit solution for the Vela pulsar light curve for each of the different models. In this way, we are able to determine which *B*-field and geometric model yield the best light curve solution, how the different light curve predictions compare with each other, and which pulsar geometry (α,ζ) is optimal. In summary, we want to constrain the high-altitude *B*-field and the geometry of the emission gap using geometric light curve modelling.

1.3 Thesis outline

In Chapter 2, I give an overview of various topics such as: the history of pulsars, their formation, different pulsar classes, standard models of pulsar electrodynamics, pulsar emission models, and important radiation mechanisms. This serves as a basis for the next chapters. Chapter 3 describes the geometric pulsar models and the different *B*-field structures. Chapter 4 explains the implementation of a new *B*-field, the offset dipole. Chapter 5 describes the statistical procedure we used for searching for the best-fit solution to the Vela light curve, for each different geometric model and *B*-field combination. In Chapter 6, I present my results which include the generation of sky maps, light curve atlases, and best-fit contours and their associated light curves for the Vela pulsar. Chapter 7 summarises the conclusions drawn from our results. The two appendices cover additional information, involving the transformation of the *B*-field and light curve atlases.

Chapter 2

Pulsar astrophysics

In this chapter, I give an overview of several relevant pulsar topics in order to provide context for the present study. I briefly describe the historical development of the pulsar field (Section 2.1), the mechanism of pulsar formation (Section 2.2), different classes of pulsars (Section 2.3), the standard model that explains the conversion of rotational energy of pulsars into radiation and particle acceleration (Section 2.4), the traditional Goldreich-Julian model (Section 2.5), some relevant radiation mechanisms and pair production (Section 2.6), and pulsar emission models (Section 2.7). Given the fact that this project mainly deals with γ-ray light curves of the Vela pulsar as measured by the *Fermi* Large Area telescope (LAT), I lastly describe this telescope in some detail (Section 2.8).

2.1 A survey of pulsar history

The neutron was discovered by James Chadwick in 1932 (Chadwick, 1932). The concept of a neutron star (NS) originated more or less at the same time. Chandrasekhar studied stellar evolution and discovered that a collapsing stellar core consisting of a mass larger than 1.4 $M_{\odot}$ (the well-known Chandrasekhar limit, applicable to white dwarf stars) should continue collapsing, since it can not balance its own gravity after all its nuclear fuel has been exhausted (Chandrasekhar, 1931). Landau (1932) also studied white dwarf stars and speculated on the existence of a star which could be more dense than white dwarf stars, composed entirely of neutrons and supported by neutron degeneracy pressure. Walter Baade and Fritz Zwicky analysed observations of supernova explosions and discovered that supernovae appeared to be less frequent than common novae, and to emit enormous amounts of energy during each explosion (Baade & Zwicky, 1934b). They also observed that supernovae explode faster than novae. Their calculations implied that a supernova remnant can not have a larger radius than a nova. Baade and Zwickey proposed that NSs could form in supernova explosions, since a supernova represents a transition from an ordinary star into a very dense object with a small radius and mass (Baade & Zwicky, 1934a). In 1939, Oppenheimer and Volkoff constructed the first models which could describe the structure of an NS, also incorporating general relativity. They stated that NSs are so dense that spacetime is curved around and within them, motivating the importance of general relativistic effects (Haensel et al., 2007). They calculated that stars reaching a mass larger than 3 $M_{\odot}$ (known as the Oppenheimer-Volkoff limit) would undergo gravitational collapse to form a black hole (Oppenheimer & Volkoff, 1939). The concept of NSs was not taken too seriously until the late 1960s when new discoveries were made in high-energy (HE) and radio astronomy (Becker & Pavlov, 2002).

Results from HE cosmic-ray experiments implied that there could be astrophysical objects, e.g. supernova remnants, which could produce high-energy cosmic rays as well as X-rays and γ-rays (Morrison et al., 1954; Morrison, 1958). In 1962, Rossi and Giaconni confirmed these notions when they detected X-rays from Sco X-1 (a source located in the constellation Scorpio), the brightest X-ray source in the sky (Giacconi et al., 1962). These X-rays were believed to be the result of SR by cosmic electrons carrying energies of the order of tens of keV. Bowyer et al. (1964) detected a second X-ray source Tau X-1, situated in the constellation Taurus. This source coincided with the Crab supernova remnant. Among all the different theories and processes proposed for the origin of these X-rays, Chiu & Salpeter (1964) proposed that this was due to thermal radiation emitted from the surface of a hot NS. Since NSs are expected to appear as point sources and the X-radiation from the Crab supernova remnant had a finite angular size of $\sim 1'$, the existence of an actual NS still remained uncertain. Hoyle et al. (1964) made the visionary prediction that there could be an NS with a strong B-field of $\sim 10^{10}$ G at the centre of the Crab nebula.

In 1967, Anthony Hewish directed the construction of a radio telescope at the Mullard Radio Astronomy Observatory, which was designed to detect interplanetary scintillation from cosmic sources (Hewish et al., 1968). The first discovery made with this new radio telescope was by Jocelyn Bell, a graduate student from Cambridge University supervised by Hewish. She detected a weak, variable radio source displaying a series of stable periodic pulses (Hewish et al., 1968; Hewish, 1975). These radio pulses arrived at a precise period of 1.3373012 s. They jestingly called this source “Little Green Man 1”. After three more similar pulsating radio sources were detected (PSR B1133+16, PSR B0834+06, PSR B0950+08), it became clear that a new kind of natural phenomenon was discovered. Another faster pulsar – the Vela pulsar – was discovered in 1968 by the Molonglo group, possessing a pulse period of 0.089 s and situated near the centre of the Vela X supernova remnant (Large et al., 1968). Staelin and Reifenstein discovered two more pulsars in 1968, one of which (the Crab pulsar) was located within $5'$ from the centre of the famous Crab nebula, having a period of 33 ms (Staelin & Reifenstein, 1968). In the same year that the first known pulsar (PSR B1919+21) was discovered, over 100 theoretical papers were published proposing interpretations or models for pulsars (Will, 1994). During this time, Wheeler (1966) and Pacini (1967) proposed that the energy source in the Crab nebula could possibly be a rapidly rotating, and highly magnetised NS. Gold (1968; 1969) suggested that since supernova remnants are associated with fast rotating NSs, a pulsar is none other than a rotating NS. Therefore, it is believed that NSs are born in core-collapsed supernovae of highly evolved massive stars. Cocke et al. (1969) next discovered strong optical pulses from the Crab pulsar. This important discovery that the “remnant star” which survived the Crab supernova explosion (Minkowski, 1942) was in fact a pulsar, a rapidly rotating NS, therefore solidified the link between supernovae, NSs, and pulsars. Soon after, Bradt et al. (1969) and Fritz et al. (1969) detected X-ray pulsations from the Crab pulsar in the $1.5 - 10$ keV range, and Hillier et al. (1970) detected γ-ray pulsations at energies > 0.6 MeV with a significance of $\sim 3.5\sigma$.

During the mid-seventies γ-ray astronomy expanded with the launch of two satellites: *Small Astronomy Satellite 2 (SAS-2)* in 1972 (Fichtel et al., 1975), which confirmed the existence of γ-ray emission from the Crab pulsar (Kniffen et al., 1974) and the Vela pulsar (Thompson et al., 1975), and *Cosmic Ray Satellite-B (COS-B)* in 1975, which provided a complete detailed map of the γ-ray sky (Schönfelder, 2001). The number of detected radio pulsars also increased rapidly in this era. The idea that pulsars have high B-fields ($\sim 10^{12}$ G)

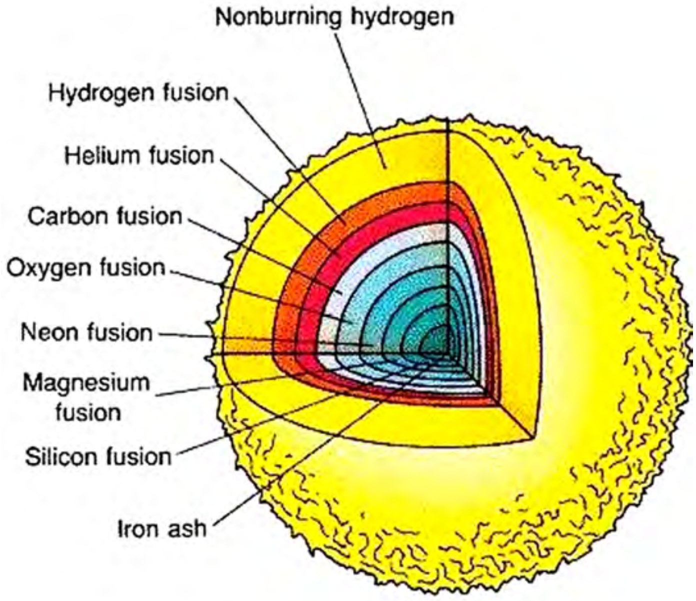

Figure 2.1: Illustration of the chemical composition of a highly evolved massive star, with each layer representing a different element, and an iron core at the centre. From Chaisson & McMillan (2002).

was confirmed by the *Uhuru* (i.e., *Small Astronomy Satellite 1 (SAS-1)*) observation of an accreting X-ray binary pulsar Her X-1 in the constellation Hercules (Tananbaum et al., 1972). A spectral feature at 58 keV was interpreted as resonant electron cyclotron emission or absorption in the hot polar plasma of the NS, implying a B-field of $\sim 6 \times 10^{12}$ G (Truemper et al., 1978).

The launch of other satellite missions that made important contributions to HE astrophysics, especially isolated NSs, include *High Energy Astrophysical Observatories* (*HEAO 1*, *HEAO 2*, and *HEAO 3*), *Chandra X-ray Observatory*, and *X-ray Multi-Mirror Mission* (XMM-Newton; Rudak et al., 2002). The field of γ-ray pulsars has been revolutionised by the launch of *Astro-rivelatore Gamma a Immagini LEggero (AGILE)* and the *Fermi* LAT, which is much more sensitive than its predecessor, *EGRET* (Atwood et al., 2009). Very recently, the ground-based imaging atmospheric Cherenkov telescopes, *Major Atmospheric Gamma-Ray Imaging Cherenkov* (*MAGIC*; Aleksić et al., 2011, 2012, 2014; Aliu et al., 2008) and *Very Energetic Radiation Imaging Telescope Array System* (*VERITAS*; Aliu et al., 2011) detected γ-ray pulsations from the Crab pulsar up to several hundred GeV. Furthermore, *High Energy Stereoscopic System Phase II (H.E.S.S.-II)* has now detected the Vela pulsar around 30 GeV (Djannati-Ataï, private communication).

2.2 Pulsar formation

The formation of pulsars is initiated by death of high-mass ($M > 8M_{\odot}$) stars (Chaisson & McMillan, 2002). A high-mass star is made up of various layers of elements, starting with the hydrogen surface, then helium, carbon, oxygen, and other heavier elements at the core, as illustrated in Figure 2.1. There are two mechanisms operating during the burning and evolutionary stages of such stars, namely fusion and fission. Fusion takes place during the burning process. Each element (from the outer layers down to the inner layers) burns its

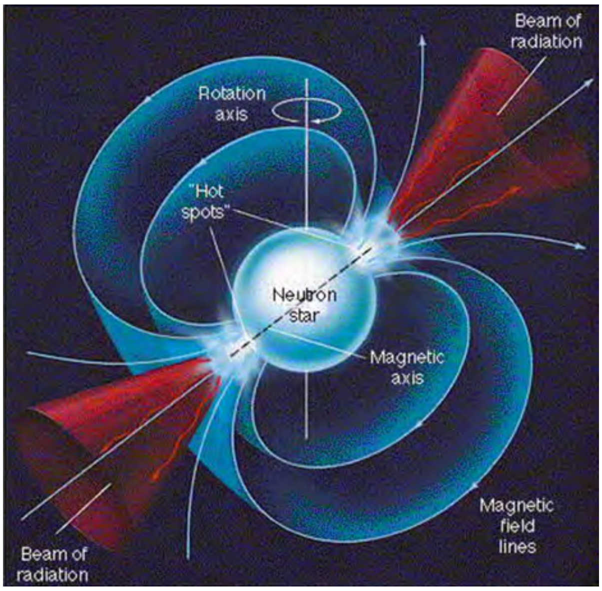

Figure 2.2: A pulsar may be compared to a lighthouse. The charged particles are accelerated along the B-field lines of the rotating NS, producing radiation in the form of beams. Figure from Chaisson & McMillan (2002).

nuclei, causing an increase in temperature with depth. The released nuclear energy produces gas and radiation pressure which counteracts the star's gravity. Once a particular element is exhausted, the burning of a heavier one is initiated by gravitational contraction (Chaisson & McMillan, 2002).

The burning process continues until an iron core is established. Since iron is the most stable element, it serves as the division between operation of the fusion and fission processes. The iron core becomes unstable when the star attempts to contract again and the nuclear reactions (which have been supplying energy) cease, so that all equilibrium is destroyed (Tayler, 1994). The gravity exceeds the gas pressure and the core collapses in on itself, causing the central regions to reach high densities and extremely high temperatures. After the collapse, fission takes place and the thermal energy from the core is absorbed to enable the photons to break the iron up into lighter nuclei, which in turn dissociate into protons and neutrons (a process known as photo-disintegration, Chaisson & McMillan, 2002). As the temperature and pressure of the core (now consisting of elementary particles) decrease, the gravitational force becomes stronger and the density increases even more, enabling the collapse to continue. The compression inside the core causes the protons and electrons to combine, producing neutrons and neutrinos (the process is known as neutronisation, Tayler, 1994). These neutrons and neutrinos escape from the star, carrying energy with them. The pressure decreases again, so that the core collapses to a point were the neutrons make contact with each other, reaching stellar core densities of $\sim 10^{15}$ kg m^{-3}. Neutron degeneracy pressure now opposes further gravitational collapse, slowing it down. The core contracts, exceeding the equilibrium point, and is accompanied by the release of gravitational binding energy and emission of neutrinos and gravitational waves (Bowers & Deeming, 1984). A "hydrodynamic bounce" may occur as the core rebounds and a shock wave will sweep through the star at high speed, outward into the mantle, and may lead to a spectacular supernova explosion (Bowers & Deeming, 1984; Tayler, 1994).

Two types of supernovae exist. Type I supernovae occur in binary systems (Palen, 2002) involving white dwarfs, and Type II supernovae involve isolated, highly evolved massive stars. When a massive star explodes as a Type II supernova, the remains of the star are carried outward into space by the shock wave. These remains may form a nebula, sometimes observed as being surrounded by a supernova remnant shell. Nebulae are regions of glowing, ionised gas with the brightness of these clouds depending on the brightness of the central degenerate NS (Chaisson & McMillan, 2002).

The maximum predicted mass of an NS is between $1.5M_\odot$ and $2.7M_\odot$ (Palen, 2002). The highest mass observed so far is $2.01 \pm 0.04M_\odot$, for PSR J0348+0431 (Antoniadis et al., 2013). For higher stellar masses, it is believed that a black hole will be formed after gravitational collapse (Kanbach, 2001). NSs are small, very dense objects. According to the law of conservation of angular momentum, a rotating object will spin faster as it shrinks, implying that the NS rotates very rapidly, with subsecond periods, and having strong B-fields. Such a rapidly, highly magnetised NS is known as a (rotation-powered) pulsar which radiates energy into space. The simplest analogy of a pulsar is a lighthouse, as shown in Figure 2.2.

The magnetic poles of the pulsar are known as polar caps (PCs), from where charged particles are accelerated more or less steadily along the B-field lines to very high energies. The radio radiation is emitted in a searchlight pattern, and as the radio beam sweeps past Earth, a pulse is observed. All pulsars are NSs but not all NSs are (observable as) pulsars, for two reasons. Firstly, an NS only pulses because of a strong B-field and rapid rotation, which diminish with time, causing the radio pulses to weaken and occur less frequently. Secondly, young pulsars are not always visible from Earth because the radio beam is very narrow, and may miss Earth (Chaisson & McMillan, 2002).

2.3 Pulsar classes

Pulsars are generally divided into two categories according to the B-field and age. Canonical pulsars are young ($\tau \sim 10^3 - 10^6$ yr) and have high B-fields ($B \sim 10^{12} - 10^{13}$ G), while MSPs are old ($\tau \sim 10^8 - 10^9$ yr) and are characterised by low B-fields ($B \sim 10^8 - 10^9$ G). Since the launch of several satellite observatories, for instance *Röntgensatellit (ROSAT)*, *Extreme Ultraviolet Explorer (EUVE)*, *Advanced Satellite for Cosmology and Astrophysics (ASCA)*, *Rossi X-ray Timing Explorer (RXTE)*, *Chandra*, *XXM-Newton*, and the *Fermi* LAT, the number of detections of rotation-powered pulsars (RPPs, pulsars driven by the rotational energy of the NS) have increased dramatically (Becker & Pavlov, 2002). These RPPs have been detected in various energy bands including radio, X-ray, γ-ray, and optical, enabling the study of multi-wavelength pulsar emission.

The Crab pulsar is a famous canonical pulsar. Its light curves have been detected in radio, optical, X-ray, and γ-ray bands, all being phase-aligned (Abdo et al., 2010a). Several other pulsars have similar emission properties as those of the Crab pulsar, including B0540−69, J0537−6909, and B1509−58 (Becker & Pavlov, 2002). Another well-known example is the Vela pulsar (PSR B0833−45), the brightest persistent GeV source in the sky (Abdo et al., 2009). It has a period $P = 0.089$ s, period derivative $\dot{P} = 1.24 \times 10^{-13}$ s s^{-1}, a characteristic age $\tau = P/2\dot{P} = 1.2 \times 10^4$ yr, and it is also one of the pulsars closest to Earth, lying at a distance of $d = 287^{+19}_{-17}$ pc (Dodson et al., 2003). Vela was first detected emitting HE pulses by *SAS-2* (Thompson et al., 1975), followed by phase-resolved studies with *COS-B* (Grenier et al., 1988) and *EGRET* (Kanbach et al., 1994; Fierro et al., 1998). Vela was the first source investigated by *AGILE* (Pellizzoni et al., 2009), and the *Fermi* LAT used the Vela pulsar as a calibration source. Vela-like pulsars (e.g., PSR B0833−45, PSR B1706−44, PSR B1046−58, and PSR B1951+32) possess spin-down ages in the range $\sim 10^{4-5}$ years and are detected in various wavebands. Another source detected by *SAS-2* and *COS-B* was Geminga, which was identified as a radio-quiet pulsar when the *ROSAT* satellite detected pulsed X-ray emission from it (Halpern & Holt, 1992). *SAS-2* and *COS-B* confirmed, using a timing solution from *ROSAT* data, that Geminga is also a bright γ-ray pulsar (Mattox et al., 1992).

A new class of radio pulsars was discovered in 1981 by Backer and his colleagues, following the detection of PSR B1937+21, which has a period of 1.56 ms (Backer et al., 1982). MSPs originate from ordinary pulsars which are in binary systems. These normal pulsars "switch off" due to continued rotational energy loss, but following angular momentum and mass transfer via accretion from their companion star, they "switch on" again and become visible as MSPs (Alpar et al., 1982). MSPs have relatively short spin periods ($P \lesssim 10$ ms), small period derivatives ($\dot{P} \sim 10^{-21} - 10^{-19}$, i.e., they are very stable rotators), large spin-down ages, and low B-field strength compared to those of normal pulsars and magnetars (Alpar et al., 1982).

An interesting new class of pulsars has recently been discovered. These so-called rotating radio transients (RRATs) are associated with single, dispersed bursts of emission having durations in the range of $2 - 30$ ms, with the average time interval between bursts ranging from a few minutes to hours. It is suggested that these sources originate from rotating NSs, since radio emission from these objects is usually detectable for < 1 s per day, with their periodicities ranging between $0.4 - 7.0$ s (McLaughlin et al., 2006). RRATs may be examples of pulsars whose magnetospheres switch between stable configurations (Keane et al., 2011).

Magnetars, including anomalous X-ray pulsars (AXPs) and soft γ-ray repeaters (SGRs), are NSs that have extremely strong surface B-fields of $B \sim 10^{14-15}$ G, increasing in strength from the surface down to the core (Duncan & Thompson, 1992). These sources are also characterised by burst-like emission. They exhibit very strong X-ray emission, which is too high and variable to be explained by conversion of rotational energy alone, but possibly involve the decay and instability of their enormous B-fields (Rea & Esposito, 2011). They have long rotation periods that range from $2 - 12$ s (exceeding those of radio pulsars), as well as large period derivatives ($\dot{P} \sim 10^{-13} - 10^{-9}$ s s^{-1}; Mereghetti, 2008).

2.4 The standard braking model for rotation-powered pulsars

Let us consider the NS to be a rapidly rotating object possessing a dipolar B-field. This NS has an angular momentum $J \approx M_i R_i^2 \Omega_i$, which is assumed to be conserved during the collapse of the progenitor, with M_i, R_i, and $\Omega_i = 2\pi/P_i$ the initial mass, radius, angular velocity, and P_i the initial rotational period. The relation between the initial and final angular velocity is therefore (since $M_i \approx M_f$)

$$\Omega_f \sim \Omega_i \left(\frac{R_i}{R_f}\right)^2. \tag{2.1}$$

This relation states that for values $R_i > R_f$ the angular velocity increases so that the rotational period P_f becomes much shorter, ranging from milliseconds up to seconds. The interior of the NS is assumed to be fully conductive, implying conservation of the magnetic flux $\Phi = \oint \mathbf{B} \cdot d\mathbf{a} \sim B_i R_i^2$ during the collapse of the core. The magnitude of the final B-field is then given by

$$B_f \sim B_i \left(\frac{R_i}{R_f}\right)^2. \tag{2.2}$$

From this relation it follows that for $R_i > R_f$ the B-field will increase, yielding high values of $B_f \sim 10^{12}$ G. The collapse of a compact neutron core therefore leads to high magnetic strengths and short periods. The rotational energy of the pulsar will be converted into electromagnetic and particle energy, leading to a slower rotational rate. The basic outcome of this rotation-powered pulsar model is to predict the rate at which this slow-down occurs. The angular kinetic energy of the rotating NS is given by

$$E_{\rm rot} = \frac{1}{2} I\Omega^2, \tag{2.3}$$

with $I \sim MR^2$ the moment of inertia. In this model the polar B-field strength at the stellar surface can be estimated by equating the rotational energy loss rate to the magnetic dipole radiation loss rate $L_{\rm md}$ and the power associated with plasma flow, i.e., related to the Poynting flux $L_{\rm pf}$ (Ostriker & Gunn, 1969; Spitkovsky, 2006; Li et al., 2012)

$$\dot{E}_{\rm rot} = \frac{d}{dt}\Big(\frac{1}{2}I\Omega^2\Big) = I\Omega\dot{\Omega} = -\frac{4\pi^2 I}{P^3}\dot{P} \approx L_{\rm pf} + L_{\rm md} = -\frac{2}{3c^3}\mu^2\Omega^4\left(1+\sin^2\alpha\right), \tag{2.4}$$

with $\mu \equiv B_0R^3/2$ the magnetic moment of the dipole, $\dot{P}$ the time derivative of the period in s s^{-1}, B_0 the surface B-field strength (polar B-field strength in Gaussian units), R the stellar radius, α the inclination angle between the magnetic and spin axes of the NS, and c the speed of light. The magnitude of B_0 can now be estimated by inserting typical values of $I = 10^{45}$ g cm^2, $R = 10^6$ cm and $\alpha \sim 90°$, giving (Manchester & Taylor, 1977)

$$B_0 \approx 4.5 \times 10^{19}\sqrt{P\dot{P}}. \tag{2.5}$$

For Eq. (2.6), we neglected the term associated with radiation (L_γ), since this is thought to be much smaller than $L_{\rm pf}$ (particle acceleration) and $L_{\rm md}$. For the vacuum case one may set $\dot{E}_{\rm rot} = L_{\rm md}$ which yields the more familiar expression

$$B_0 \approx 6.4 \times 10^{19}\sqrt{P\dot{P}}. \tag{2.6}$$

We can estimate the pulsar rotational (characteristic) age as follows. Assume that the change in $\dot{\Omega} = -K\Omega^n$ is due to magnetic dipole radiation losses (Bowers & Deeming 1984), where K is a positive constant, and the parameter $n = \ddot{\Omega}\Omega/\dot{\Omega}^2$ is the braking index, which comes from differentiating the equation for $\dot{\Omega}$. This expression for $\dot{\Omega}$ is motivated by Eq. (2.4), assuming that $\mu_\perp \equiv \sin\alpha$ stays constant. Next, integrate this expression and substitute $\Omega^2 = -\dot{\Omega}/k_1\Omega$ where k_1 is a constant (see Eq. [2.4]). The characteristic age is then given by (Manchester & Taylor, 1977)

$$\tau = -\frac{\Omega}{(n-1)\dot{\Omega}}\left[1-\Big(\frac{\Omega}{\Omega_0}\Big)^{n-1}\right] \approx -\frac{\Omega}{(n-1)\dot{\Omega}} \equiv \frac{P}{(n-1)\dot{P}}, \tag{2.7}$$

with the assumptions $n \neq 1$ and $\Omega \ll \Omega_0$, with Ω_0 the angular velocity at time $t = 0$. This is approximately equal to

$$\tau \approx -\frac{\Omega}{2\dot{\Omega}} \equiv \frac{P}{2\dot{P}}, \tag{2.8}$$

when setting $n = 3$ for the case of magneto-dipole braking (Becker & Pavlov, 2002). This characteristic age serves as an upper limit for the true age of the pulsar, since the value for n is chosen to be a constant. However,

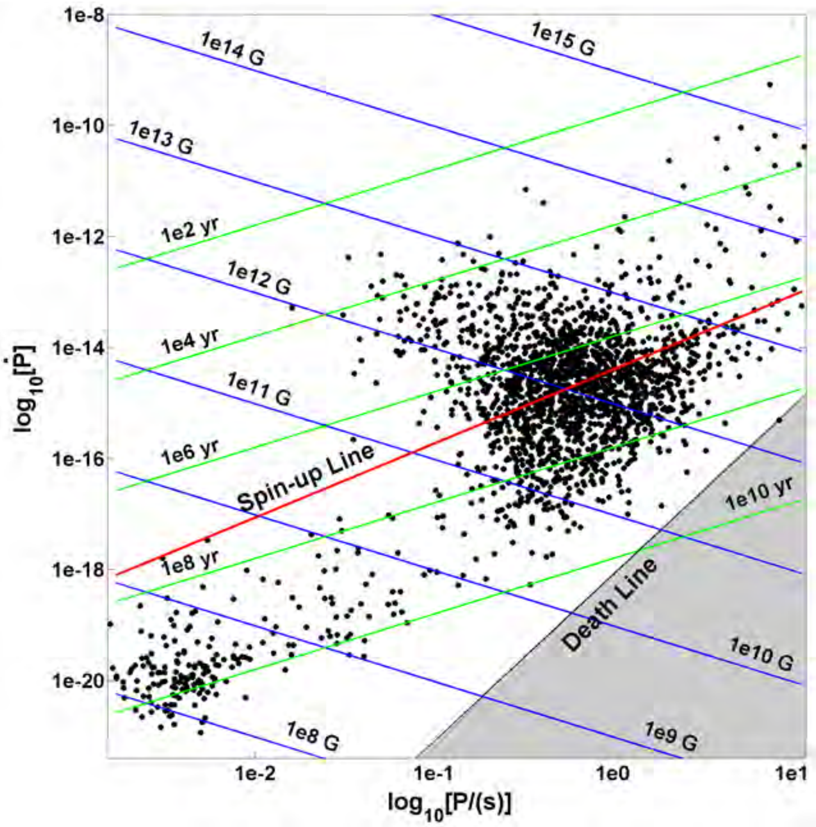

Figure 2.3: A $P\dot{P}$-diagram indicating the two pulsar populations including the canonical pulsars (in the centre) and the MSPs (in the lower left corner). The black dots are radio pulsars from the Parkes Observatory *ATNF* Pulsar Catalogue for $\dot{P} > 0$ (Manchester et al., 2005). The blue solid lines represent constant surface magnetic field B_0 contours, while the green solid lines represent characteristic pulsar ages τ. The grey area is the "graveyard" where the canonical pulsars turn off and are spun up again so that they eventually enter the MSP region. The spin-up line (red line) is the equilibrium period of spin-up by accretion which is the Keplerian orbital period at the Alfvén radius (Alpar et al., 1982).

when $\Omega \lesssim \Omega_0$, the true age of the pulsar will be smaller than τ.

The evolution and properties of different pulsar populations are best described by drawing a $P\dot{P}$-diagram (Figure 2.3, the time derivative of the period $\dot{P}$ versus P, using the pulsars from the Parkes Observatory *ATNF* Pulsar Catalogue for $\dot{P} > 0$; Manchester et al., 2005). Rotation-powered pulsars could also have $\dot{P} < 0$, e.g., when there is acceleration along the line of sight for such objects embedded in a globular cluster. As mentioned in Section 2.3, one can distinguish two pulsar populations: the canonical pulsars and MSPs. The canonical radio pulsar population is identified with the younger pulsars and is situated at the centre of the $P\dot{P}$-diagram. The canonical pulsars typically have high surface magnetic fields of $B_0 \sim 10^{12} - 10^{13}$ G and rotational ages of $\tau \sim 10^6 - 10^8$ yr (as indicated by the contours of constant B_0 and τ). During the evolution of pulsars as they age, three things happen. Firstly the magnetic dipole field drops (although the timescale for this process is uncertain), secondly the pulsar slows down due to energy losses (mostly by dipole radiation and particle loss), causing the pulse period to increase, and lastly the particles emitted by the pulsar form a pulsar wind. On the $P\dot{P}$-diagram there is a "death valley" where the canonical pulsars turn off (Chen & Ruderman, 1993).

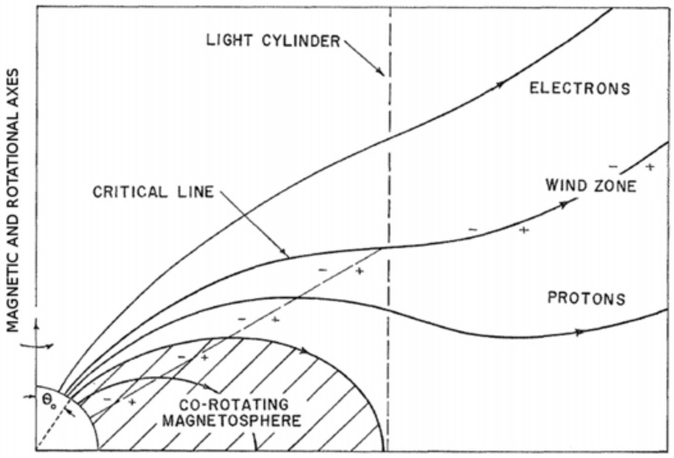

Figure 2.4: The pulsar magnetosphere as envisioned by Goldreich & Julian (1969). The corotating zone is represented by the shaded region within the light cylinder, where the particles corotate with the closed B-field lines. The B-field lines which go beyond the light cylinder are open and the particles escape along them. The electrons flow out near the PC along the higher-latitude lines, whereas the protons (or possibly iron nuclei) flow out near the PC angle ($\theta_{\rm PC}$) along the lower-latitude line. These two magnetospheric regions are separated by the critical field line (which is at the same potential as the interstellar medium). The dashed line represents the condition where the charge density $\rho_{\rm GJ} \propto -\mathbf{\Omega}\cdot\mathbf{B} = 0$. Above this dashed line $\mathbf{\Omega}\cdot\mathbf{B} > 0$ (negative $\rho_{\rm GJ}$), and below it $\mathbf{\Omega}\cdot\mathbf{B} < 0$ (positive $\rho_{\rm GJ}$).

This turn-off is due to the fact that the PC potential responsible for electron-positron ($e^{\pm}$) pair creation and subsequent radio emission becomes too low, inhibiting pair production (see Section 2.6.5), and leading to the "death" of canonical radio pulsars (i.e., they become invisible). Some pulsars inside the death valley are spun up again by the transfer of mass and angular momentum from a binary companion (Alpar et al., 1982), so that they enter the MSP region (lower left corner). These MSPs have relatively short periods ($P \lesssim 10$ ms) and lower surface B-fields ($B_0 \sim 10^8 - 10^9$ G) compared to the canonical pulsars. The spin-up line, representing the spin-up upper limit of MSPs, is also indicated.

2.5 The Goldreich-Julian model

In 1969, Peter Goldreich and William Julian studied a simple model describing the properties of the magnetosphere around a highly magnetised, rotating pulsar. In this model, they considered an NS to be a uniformly magnetised, perfectly conducting sphere, with an internal magnetic field $\mathbf{B}_{\rm in} = B_0\vec{e}_z \parallel \boldsymbol{\mu}$, and with an external dipole B-field (e.g., Padmanabhan, 2001). They considered an aligned rotator, i.e., the rotation axis being aligned with a magnetic dipole vector ($\mathbf{\Omega} \parallel \boldsymbol{\mu}$; see Figure 2.4). Another assumption is that there are initially no charges filling the surrounding magnetosphere (Mészáros, 1992).

As the pulsar rotates with a velocity $\mathbf{v} = \mathbf{\Omega} \times \mathbf{r}$, the charged particles at the stellar surface will experience a Lorentz force $(q/c)(\mathbf{v} \times \mathbf{B}_{\rm in})$, with q the particle charge. Since the NS is a perfect conductor ($\mathbf{E}_{\rm in} \cdot \mathbf{B}_{\rm in} = 0$, implying that the B-field lines are equipotentials) the charges will be redistributed in order for the electric force to counter balance the magnetic force, due to charge separation. This implies

$$\mathbf{E}_{\rm in} = -\frac{\mathbf{\Omega}\times\mathbf{r}\times\mathbf{B}_{\rm in}}{c} = -\frac{\Omega B_0 r\sin\theta}{c}(\sin\theta\vec{e_r} + \cos\theta\vec{e_\theta}). \tag{2.9}$$

Since $\nabla\times\mathbf{E}_{\rm in} = 0$, we can write

$$\mathbf{E}_{\rm in} = -\nabla\Phi_{\rm in}(r,\theta), \tag{2.10}$$

with $\Phi_{\rm in}(r,\theta)$ the electric potential. After integration, we find

$$\Phi_{\rm in}(r,\theta) = \frac{\Omega B_0 r^2}{2c}\sin^2\theta + \Phi_0, \tag{2.11}$$

with Φ_0 a constant. This implies a potential difference between the magnetic axis and PC angle (colatitude of the PC rim, $\theta_{\rm PC} \sim \sqrt{\Omega R/c}$) of

$$\Delta\Phi_{\rm in} = \frac{1}{2}\left(\frac{\Omega R}{c}\right)^2 B_0 R. \tag{2.12}$$

The external E-field now follows by solving the Laplace equation and requiring a continuous electric potential at the stellar surface:

$$E_{r,\rm out} = -\frac{9Q}{r^4}\left(\cos^2\theta - \frac{1}{3}\right), \tag{2.13}$$

$$E_{\theta,\rm out} = -\frac{6Q}{r^4}\cos\theta\sin\theta, \tag{2.14}$$

with $Q = B_0\Omega R^5/6c$. Using these expressions for $E_{\rm out}$ it follows that the electric force on surface charges vastly exceeds the gravitational force (by a factor of $\sim 5\times10^8/P$ for a proton and $\sim 8\times10^{11}/P$ for an electron; Goldreich & Julian, 1969). This constitutes an existence proof for a plasma-filled pulsar magnetosphere, since the accelerating E-field parallel to the local B-field ($E_{\|}$) will extract particles from the stellar surface to fill the magnetosphere.

An expression for the charge density in the corotating magnetosphere follows from Eq. (2.9)

$$\rho_{\rm GJ} = \frac{\nabla\cdot\mathbf{E}}{4\pi} \approx -\frac{\mathbf{\Omega}\cdot\mathbf{B}}{2\pi c}. \tag{2.15}$$

This implies a number density of

$$n_{\rm e} = 7\times10^{-2}\frac{B_0}{P}\,{\rm cm}^{-3}. \tag{2.16}$$

at the stellar surface. Despite its success, the model has a few problems, most notably the question of the return current (charge neutrality) and its inherent instability, as well as the charge supply (which cannot be only from the NS surface).

2.6 High-energy radiation mechanisms and pair production

2.6.1 Particle acceleration

Charged particles that are accelerated will emit electromagnetic radiation. If the speed v of the charged particle is much less than the speed of light c, i.e., $v \ll c$, the particle is non-relativistic. The power radiated by such charged particles in the non-relativistic regime is calculated by using the Larmor formula (Jackson, 1999)

$$P_{\text{total}} = \frac{2q^2a^2}{3c^3}, \tag{2.17}$$

with q the charge of the particle and a its acceleration.

However, when charged particles are accelerated to extremely high energies (GeV−TeV), they will emit HE γ-ray photons, e.g., those detected by *Fermi*. At these HEs the particle's speed becomes relativistic ($\beta \equiv v/c \approx 1$) with a Lorentz factor of $\gamma_e \equiv 1/\sqrt{1-\beta^2} \gg 1$. The relativistic Larmor formula (or Liénard formula, see Jackson, 1999) for these HE particles is as follows

$$P_{\text{total}} = \frac{2q^2}{3c^3}\gamma_e^4(a_\perp^2 + \gamma_e^2 a_\parallel^2), \tag{2.18}$$

with $a_\perp$ the perpendicular acceleration component and $a_\parallel$ the parallel acceleration component (with respect to the particle's velocity direction). In the following subsections radiation mechanisms including synchrotron radiation (SR), curvature radiation (CR), and inverse Compton scattering (ICS), that are relevant for HE pulsar emission models are discussed. The first two are due to relativistic particles which are accelerated along curved paths inside the magnetosphere, whereas the latter occurs due to the interaction between photons and the relativistic particles. In the last subsection we discuss pair production, where an HE photon converts into an electron and positron pair.

2.6.2 Synchrotron radiation

SR (magneto-bremsstrahlung) occurs when relativistic charged particles gyrate about a B-field line. For non-relativistic particles, this is known as cyclotron radiation. When the particle's perpendicular momentum becomes relativistic, it is known as SR (Rybicki & Lightman, 1979). Neglecting radiation losses, the equation of motion for a relativistic particle reveals that the particle travels at a constant speed parallel to the B-field with an acceleration perpendicular to the B-field. This implies that the particle will follow a helical path as it gyrates along a B-field. The gyration frequency (rotation around a field line) is given by (Rybicki & Lightman, 1979)

$$\omega_{\text{B}} = \frac{qB}{\gamma_e mc}, \tag{2.19}$$

with m the particle's mass, and B the magnitude of the B-field. If $\mathbf{v} \cdot \mathbf{B} = 0$ the gyroradius is

$$r_{\text{B}} = \frac{v}{\omega_{\text{B}}}. \tag{2.20}$$

Since the particle is accelerated it will emit radiation and the assumption of no radiation losses will no longer be valid. The total SR energy loss rate is given by

$$\dot{E}_{\rm SR} = \frac{2}{3c}(r_0\gamma_e B v_\perp)^2, \tag{2.21}$$

with $v_\perp$ the charged particle's speed perpendicular to the B-field (Blumenthal & Gould, 1970) and $r_0 \equiv e^2/m_e c^2$ the classical electron radius (with m_e the electron mass and $m_e c^2$ its rest-mass energy). For the gyrating component we assume $a_\perp = \omega_{\rm B} v_\perp$ and $a_\parallel = 0$, then Eq. (2.18) is the total emitted radiation

$$P_{\rm total} = \frac{2q^2}{3c^3}\gamma_e^4\left(\frac{qB}{\gamma_e mc}\right)^2 v_\perp^2. \tag{2.22}$$

When Eq. (2.22) is averaged over all angles, for an isotropic distribution of velocities, the SR power emitted is (Padmanabhan, 2000)

$$P_{\rm SR,total} = \frac{4}{3}\sigma_{\rm T}(c\beta^2\gamma_e^2)U_{\rm B} \propto E_\gamma^2 B^2, \tag{2.23}$$

with $\sigma_{\rm T} \equiv 8\pi r_0^2/3$ the Thomson cross-section, E_γ the particle energy, and $U_{\rm B} = B^2/8\pi$ the magnetic energy density.

The radiation emitted by these relativistic particles will be beamed into a cone shape with an angular width $\sim 1/\gamma_e$ around the velocity direction. Since the particle's acceleration and velocity are perpendicular for SR, the observed pulses are a factor of γ_e^3 smaller than the gyration period, leading to a broader spectrum with a maximum characterised by a critical frequency

$$\omega_{\rm c} = \frac{3}{2}\gamma_e^3\omega_{\rm B}\sin\alpha^{\rm P}, \tag{2.24}$$

with $\alpha^{\rm P} = \arctan(v_\perp/v_\parallel)$ the pitch angle (Rybicki & Lightman, 1979). The total SR per unit frequency emitted by a single electron is

$$P_{\rm SR}(\omega) = \frac{\sqrt{3}}{2\pi}\frac{q^3 B}{mec^2}\sin\alpha^{\rm P} F\left(\frac{\omega}{\omega_{\rm c}}\right), \tag{2.25}$$

with

$$F(x) \equiv x\int_x^\infty K_{5/3}(\xi)d\xi, \tag{2.26}$$

where $K_{5/3}$ is the modified Bessel function of order 5/3, and

$$F(x) \sim \begin{cases} \frac{4\pi}{\sqrt{3}\Gamma(\frac{1}{3})}\left(\frac{x}{2}\right)^{1/3} & x \ll 1 \\ (\frac{\pi}{2})^{1/2}e^{-x}x^{1/2} & x \gg 1, \end{cases} \tag{2.27}$$

with $x = \omega/\omega_c$. For $\omega \ll \omega_c$, $F \propto \omega^{1/3}$, while for $\omega \gg \omega_c$, $F \propto e^{-(\omega/\omega_c)}\omega^{1/2}$.

In many astrophysical sources the photon spectra reveal a power law distribution of energies. Assume that the number density $N(E_\gamma)$ of particles over some energy range $(E_\gamma, E_\gamma + dE_\gamma)$ can be described by a power law $N(E_\gamma)dE_\gamma = CE_\gamma^{-p}dE_\gamma$, with C a constant and p the power-law index of the emitting particles. Following the same procedure as Rybicki & Lightman (1979), the total SR power radiated per unit volume per unit frequency can be shown to be a power-law spectrum

$$P_{\rm SR}(\omega) \quad \propto \quad \omega^{-s}, \tag{2.28}$$

with $s = (p-1)/2$ the index of the energy spectrum. The latter relation implies that the injection and radiated spectral indices are related in this case.

SR is an important process for pulsars. For example, in PC and SG models primary photons are emitted via CR and undergo magnetic photon absorption (see Section 2.6.5) to create $e^{\pm}$ pairs. The perpendicular energy from these secondary pairs is converted to HE radiation via SR. It is possible that radio photons are absorbed by charged particles present in the B-field via the process of synchrotron self-absorption (Harding et al., 2008). The above discussion is only valid for B-field strengths $B < 4 \times 10^{12}$ G. For larger B-fields, a quantum SR approach is necessary (e.g., Sokolov & Ternov, 1968; Harding & Preece, 1987; Harding & Lai, 2006).

2.6.3 Curvature radiation

CR is the radiation process associated with relativistic particles that are constrained to move along a curved B-field line. This implies that its perpendicular velocity component $v_{\perp} = 0$, and $\alpha^{\rm P} = 0$ (see above Sections for definitions). CR is therefore linked to a change in longitudinal kinetic energy with respect to the B-field, as opposed to SR, where there is change in transverse energy (see Figure 2.5). In some pulsar models, primary particles are accelerated from the stellar surface along the open field lines. The kinetic energy longitudinal to the B-field will exceed the transverse energy (which will be radiated away very rapidly via SR), and therefore CR will be more important than SR regarding energy loss of primary particles (Sturrock, 1971). The curvature radius is the instantaneous radius of curvature of the field line, i.e., $\rho = \rho_{\rm curv}$. The critical frequency is then defined as (Daugherty & Harding, 1982; Story et al., 2007; Venter et al., 2009)

$$\omega_{\rm CR} = \frac{3c}{2\rho_{\rm curv}}\gamma_e^3, \tag{2.29}$$

and the critical energy

$$E_{\rm CR} = \hbar\omega_{\rm CR} = \frac{3\hbar c\gamma_e^3}{2\rho_{\rm curv}} = \frac{3\lambda\!\!\!^{-}_{\rm c}\gamma_e^3}{2\rho_{\rm curv}}m_ec^2, \tag{2.30}$$

where $h = 6.626 \times 10^{-27}$ erg s^{-1} is Planck's constant, $\lambda\!\!\!^{-}_{\rm c} \equiv \hbar/m_ec$ (with $\hbar = h/2\pi$ and $\lambda\!\!\!^{-}_{\rm c} = \lambda_{\rm c}/2\pi$), and $\lambda_{\rm c}$ the Compton wavelength. The instantaneous power spectrum (in units of erg s^{-1} erg^{-1}) is given by (e.g., Venter & De Jager, 2010)

$$\left(\frac{dP}{dE}\right)_{\rm CR} = \frac{\sqrt{3}\alpha_f\gamma_ec}{2\pi\rho_{\rm curv}}F\left(\frac{E_\gamma}{E_{\rm CR}}\right), \tag{2.31}$$

with α_f the fine structure constant, $K_{5/3}$ the modified Bessel function of order 5/3, $x = E_\gamma/E_{\rm CR}$, with E_γ the photon energy. Similar to SR, for $E_\gamma \ll E_{\rm CR}$, $F \propto E_\gamma^{1/3}$, while for $E_\gamma \gg E_{\rm CR}$, $F \propto e^{-(E_\gamma/E_{\rm CR})}E_\gamma^{1/2}$ (see Eq. [2.27], Erber, 1966). The total power radiated by the electron primary can be determined by integrating Eq. (2.31) over energy. The latter is equal to the total CR loss rate of electrons,

$$\dot{E}_{\rm CR} = \frac{2e^2c\gamma_e^4}{3\rho_{\rm curv}^2}, \tag{2.32}$$

with e the electron charge.

HE emission in standard pulsar models is believed to be from CR of primary electrons accelerated tangentially to the B-field in the radiation-reaction regime. The curvature radiation reaction (CRR) limit is reached when the energy gained via acceleration of relativistic electrons (by an E-field parallel to the B-field) is equal to the energy loss via radiation, and can be expressed as follows (e.g., Harding et al., 2005)

$$c|E_{\parallel}| \sim \frac{2ce\gamma_e^4}{3\rho_{\rm curv}^2}, \tag{2.33}$$

yielding $\gamma_e = (1.5E_{\parallel}/e)^{1/4}\rho_{\rm curv}^{1/2}$, the Lorentz factor corresponding to radiation reaction. For pulsars with surface magnetic field strengths $B_0 \sim 10^{12}$ G and electric potentials $\Phi \sim 10^{13}$ V, the E-field strength is $E_{\parallel} \sim 10^4$ statvolts/cm (for young pulsars $E_{\parallel} > 10^4$ statvolts/cm) and depends on B and P. In these strong fields, the CR spectral cutoffs are therefore around a few GeV for emitting particles with Lorentz factors of $\gamma_e \sim 10^7$ (Yadigaroglu, 1997). These high Lorentz factors are connected to beamed radiation in the form of a cone with an opening angle $\sim 1/\gamma_e \ll 1$, implying emission tangentially to the B-field lines. We used this approximation to simplify the geometric models described in Chapter 3 as well as in Chapter 6. Given the fact that we expect spectral cutoffs in the GeV range for typical pulsar parameters, as well as rather hard power-law low-energy tails, this process has become the standard explanation for HE pulsar spectra such as those observed by the *Fermi* LAT satellite (e.g., Abdo et al., 2013).

2.6.4 Inverse Compton scattering

Compton scattering involves the collision between HE photons and low-energy electrons, where the photons transfer some of their momenta $p = hf/c = h/\lambda$ (with h Planck's constant, f the frequency and λ the wavelength) and energy to the electrons. This transfer leads to an increase in photon wavelength, implying a lower photon energy. The inverse case of Compton scattering is ICS, where the HE electrons scatter the low-energy photons, resulting in photons with very high energies (i.e., "boosting" of photon energies).

When a relativistic electron with Lorentz factor γ_e upscatters a photon from a low energy to a high energy, the energy E_γ of the Compton-boosted photon, with an initial energy ϵ, may be approximated as (Ramana Murthy & Wolfendale, 1986)

$$E_\gamma \sim \epsilon\gamma_e^2, \quad \gamma_e\epsilon \ll m_ec^2 \quad \text{- Thomson limit} \tag{2.34}$$

$$E_\gamma \sim \gamma_e m_e c^2, \quad \gamma_e\epsilon \gg m_ec^2 \quad \text{- Extreme Klein-Nishina limit.} \tag{2.35}$$

The total power lost due to ICS by an electron in an isotropic radiation field of low-energy photons, in the Thomson limit, is given by

$$P_{\rm ICS,total} = \frac{4}{3}\sigma_{\rm T}(c\beta^2\gamma_e^2)U_{\rm rad}, \tag{2.36}$$

which has the same form as Eq. (2.23), but with $U_{\rm rad}$ the soft photon energy density, and $\sigma_{\rm T}$ the classical Thomson scattering cross section (see Section 2.6.2). In order to obtain the total radiated Compton spectrum we need to integrate the production rate $dN'(\epsilon, \gamma_e)/dE_\gamma$, valid for a single electron, over the soft-photon energy

ϵ and the electron energy γ_e (Blumenthal & Gould, 1970):

$$\left(\frac{dN}{dE_\gamma}\right)_{\rm total} = \int\int N_e(\gamma_e)\left(\frac{dN'(\epsilon,\gamma_e)}{dE_\gamma}\right)d\gamma_e d\epsilon, \tag{2.37}$$

with $dN_e = N_e(\gamma_e)d\gamma_e$ the differential number of electrons in the interval $(\gamma_e, \gamma_e + d\gamma_e)$. Similar to SR (see Eq. [2.28]), if we assume that the electron spectral energy distribution is a power law, $N_e \sim \gamma_e^{-p}$ with index p, and a blackbody soft-photon distribution, then it follows from Eq. (2.37) that the ICS spectrum is also power law:

$$\left(\frac{dN}{dE_\gamma}\right)_{\rm total} \propto \begin{cases} E_\gamma^{-(p+1)/2} & \text{– Thomson limit} \\ E_\gamma^{-(p+1)} & \text{– Extreme Klein-Nishina limit.} \end{cases} \tag{2.38}$$

All of the above equations follow a classical approach for photon energies $\gamma_e\epsilon \lesssim 100$ keV for which $\sigma_{\rm T}$ is valid. However, when we consider the soft photons of higher energies, quantum effects become important and $\sigma_{\rm T}$ should be replaced by the Klein-Nishina cross section $\sigma_{\rm KN}$ (Rybicki & Lightman, 1979). As the photon energy increases, the cross section reduces, leading to a steeper photon spectrum (reduced loss rate) in the extreme Klein-Nishina limit (with $\sigma_{\rm T} > \sigma_{\rm KN}$).

The ICS process is important for pulsars. One example is MSPs such as PSR J0437−4715 from which thermal and non-thermal (possibly SR) X-ray emission have been observed (see e.g., Zavlin et al., 2002). These energetic photons provide a background field which may be upscattered to TeV energies by relativistic particles in the magnetosphere. Another example is afforded by the pulsed very-high-energy (VHE) emission recently observed from the Crab pulsar. This has been explained using a revised OG model (Hirotani, 2008a,b) which produces IC radiation of up to ~400 GeV when secondary and tertiary pairs upscatter infrared to ultraviolet photons (Aleksić et al., 2012). Another suggestion to explain this VHE emission is proposed by Lyutikov et al. (2012), invoking the SSC radiation process where relativistic pairs upscatter the SR photons emitted previously by the same particle population. Other examples include pulsar wind nebulae (PWNe, see e.g., De Jager et al., 1996) and many other VHE sources which display typical spectral components corresponding to SR and IC radiation as part of their broadband emission spectrum.

2.6.5 Pair production

Pulsar magnetospheres consist of strong B and E-fields especially near the NS surface and the latter can accelerate particles to relativistic energies. Efficient radiation processes (see Sections 2.6.2 to 2.6.4) and a pair creation mechanism, necessary for particle-photon cascades to ensue, also operate in these extreme environments (Daugherty & Harding, 1982). There are two different pair creation processes that may occur, namely single photon (magnetic) and two-photon pair production.

Magnetic pair production can only occur in the presence of a strong B-field ($B_\perp > 10^9$ G, perpendicular to the particle's direction of motion) with which the photons, if they have a high enough energy, can interact to produce $e^\pm$-pairs. The probability that $e^\pm$-pairs will be produced via this process is expressed by the photon attenuation coefficient given by

$$\alpha'(\chi) = \frac{1}{2}\left(\frac{\alpha_f}{\lambda_{\rm c}}\right)\left(\frac{B_\perp}{B_{\rm cr}}\right)T(\chi), \tag{2.39}$$

which determines the number of pairs n_p created for each photon that travels a path length d through the B-field

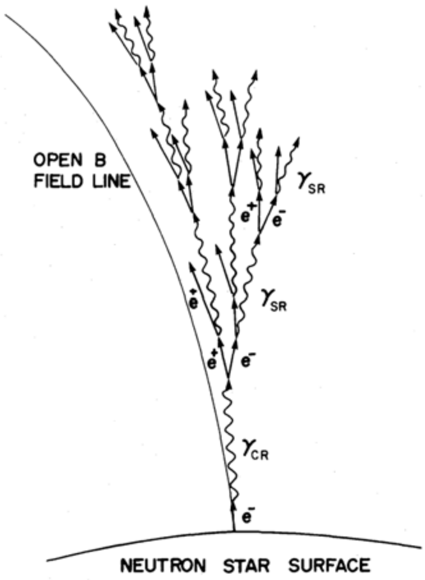

Figure 2.5: Schematic illustration by Daugherty & Harding (1982) of a photon pair cascade emerging from the acceleration of a primary electron above the PC along the curved B-field of an NS. Four generations of photons, including both CR photons $\gamma_{\rm CR}$ and SR photons $\gamma_{\rm SR}$ are shown.

(Erber, 1966):

$$n_p = n_\gamma\left(1 - \exp[-\alpha'(\chi)d]\right) \simeq n_\gamma\alpha'(\chi)d, \tag{2.40}$$

with $\alpha_f = e^2/\hbar c \approx 1/137$ the fine structure constant, $\chi \equiv 0.5(h\nu/m_ec^2)(B_\perp/B_{\rm cr})$ the Erber parameter, ν the photon frequency, $B_{\rm cr} = m_e^2c^3/eh = 4.414\times10^{13}$ G the critical B-field value in which the electron's gyroenergy (cyclotron) equals its rest mass (Daugherty & Harding, 1983), $T(\chi)$ a dimensionless function, and n_γ is the photon number density. Sturrock (1971) approximated the condition for magnetic pair production as

$$E_\gamma B\sin\theta_{\gamma B} = E_\gamma B_\perp \gtrsim 10^{11.9}, \tag{2.41}$$

with E_γ in units of m_ec^2, $\theta_{\gamma B}$ the photon propagation angle with respect to the B-field, and $B_\perp$ measured in Gauss. In the PC model (see Section 2.7.1) primary particles are accelerated from the PC surface along the curved field lines and CR occurs. When the emitted CR photon energy and the local B-field are high enough or $\theta_{\gamma B} \gg 1$, magnetic pair production will occur, leading to a cascade of secondary $e^\pm$ pairs which will screen the $E_\parallel$-field. An $E_\parallel$-field develops because there is a deficit of negative charges and due to the backflow of the first generation of pair e^+ to the NS surface, a space charge accumulates which counteracts any charge imbalances and screens out the accelerated $E_\parallel$-field, significantly so above the so-called pair-formation front (PFF). ICS photons may also be converted into $e^\pm$ pairs. The pair cascade is characterised by the so-called multiplicity, i.e., the number of pairs spawned by a single primary, as represented in Figure 2.5.

Two-photon pair creation is due to a collision between two photons with high enough energies, where the minimum photon energy required is $E_\gamma = 2m_ec^2 \sim 1$ MeV, creating an $e^\pm$ pair. The cross section for two-photon pair production (in a region devoid of a B-field) in terms of the photon energy in the centre-of-momentum frame,

$\epsilon_{\rm cm} = [\epsilon_1\epsilon_2(1-\cos\theta_{12})/2]^{1/2}$, is (Svensson, 1982)

$$\sigma_{2\gamma} \simeq \frac{3}{8}\sigma_T \begin{cases} (\epsilon_{\rm cm}^2 - 1)^{1/2} & (\epsilon_{\rm cm} - 1) \ll 1 \\ [2\ln(2\epsilon_{\rm cm}) - 1]/\epsilon_{\rm cm}^6 & \epsilon_{\rm cm} \gg 1, \end{cases} \tag{2.42}$$

where ϵ_1 and ϵ_2 refer to the energies of the photons, and θ_{12} is the angle between the photon propagation directions. Two-photon pair production can also take place in the presence of a strong B-field. In this case, the resulting $e^{\pm}$ pair will have non-zero velocity to ensure that the energy and parallel momentum are conserved. In a strong B-field the requirement for producing a pair in the ground state, using the conservation equations, is given by (Harding & Lai, 2006):

$$(\epsilon_1 \sin\theta_1 + \epsilon_2 \sin\theta_2)^2 + 2\epsilon_1\epsilon_2[1-\cos(\theta_{12})] > 4, \tag{2.43}$$

where θ_1 and θ_2 are the angles between the photon propagation directions and the B-field. The first term in the above equation is due to the non-conservation of perpendicular momentum, implying that pair production is possible when photons travel parallel to each other ($\theta_{12} = 0$, $\theta_1 = \theta_2 \neq 0$), an event not permitted in field-free space. In the high-altitude SG model electrons are accelerated away from the NS, such that the angle of each of the photons to the B-field is too small to tap the perpendicular momentum of the B-field and no pairs are produced.

However, in high-altitude OG model particles are also accelerated downward so that these particles (and therefore their emitted CR photons) have large angles with respect to soft photons originating at the hot stellar surface. The two-photon pair creation process is therefore expected to occur. The resulting pairs play an important role in gap closure (Hirotani, 2008a). Burns & Harding (1984) found that the one-photon pair creation process will generally dominate over the two-photon process in B-fields above $\approx 10^{12}$ G, since the first is a lower-order process than the second.

2.7 Overview of physical pulsar models

Several pulsar emission models have been developed over the last forty years including the PC, SG, and OG models. These geometries are illustrated in Figure 2.6. Each model differs in its assumption of the geometry and location of the acceleration region were HE radiation takes place. To simulate the HE emission from these physical models, the assumed electrodynamics and B-field structures are important.

2.7.1 Polar cap model

In PC models (Ruderman & Sutherland, 1975; Daugherty & Harding, 1982) HE particles ($e^{\pm}$) are assumed to originate at the NS surface layer. These are then accelerated by large, rotation-induced E-fields at the magnetic poles (known as the magnetic PCs) up to heights just above the PC ($h \lesssim R$ see Figure 2.6). There exist two types of polar cap accelerators: the vacuum gaps with $\mathbf{\Omega}\cdot\mathbf{B} < 0$ (Ruderman & Sutherland, 1975; Usov & Melrose, 1995) and space-charge-limited-flow (SCLF) gaps with $\mathbf{\Omega}\cdot\mathbf{B} > 0$ (Arons & Scharlemann, 1979; Harding & Muslimov, 1998; see Figure 2.7). The formation of these gaps depends primarily on the surface temperature T_s of the NS, and the thermionic emission temperatures for the charges (electrons and ions) $T_{e,i}$.

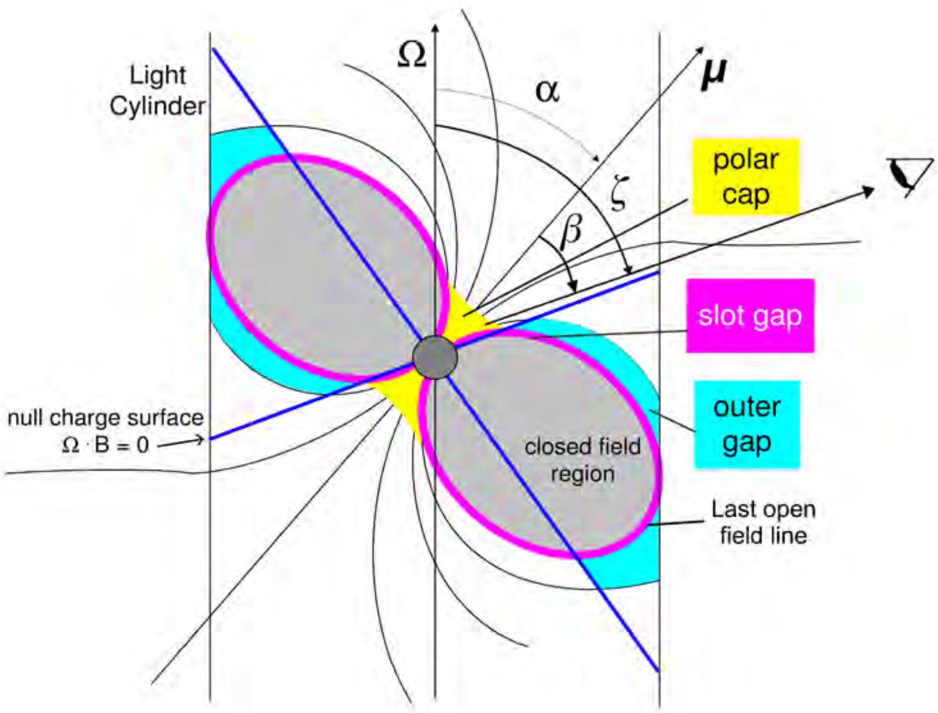

Figure 2.6: Schematic view of the different pulsar emission models, with $\boldsymbol{\mu}$ the magnetic axis inclined by an angle α with respect to the rotation axis $\boldsymbol{\Omega}$, and ζ the observer angle measured with respect to $\boldsymbol{\Omega}$. From Harding (2005b).

For the vacuum accelerator the surface temperature, $T_s < T_{e,i}$, causing the charges to be trapped inside the NS surface and a full vacuum E-field (or potential drop) develops above the surface (Usov & Melrose, 1995). However, at high surface temperatures, $T_s > T_{e,i}$ the binding energy of the charges due to lattice structures in strong B-fields is exceeded (Medin & Lai, 2007) and the charges are "boiled off" the surface layers and flow freely along the open field lines in the SCLF regime. These two acceleration gaps differ primarily in their surface boundary conditions (at the stellar surface $r = R$) which state that for the vacuum gap the space charge $\rho(r) = 0$ and $E_{\|}(R) \neq 0$, whereas for the SCLF accelerator the full Goldreich-Julian charge can be provided, $\rho(r) = \rho_{GJ}$ (which may be modified by curvature of B-field line as well as inertial frame dragging, Muslimov & Tsygan, 1992) and $E_{\|}(R) = 0$ (Harding, 2007a). Both accelerators will be self-limited by the development of pair cascades (initiated by the conversion of radiated photons into $e^{\pm}$ pairs; see Section 2.6.5), with the particles being accelerated to altitudes where they will reach high enough Lorentz factors to radiate γ-ray photons.

The pair production in the vacuum gap differs from that in the SCLF model. In the vacuum gap the potential breaks down when a random photon crosses the B-field and creates a pair. The resulting electron and positron are accelerated in opposite directions. This electron and positron can then initiate more pairs since they will radiate photons which may again be converted into pairs, causing a pair cascade and discharge of the vacuum gap. In contrast, in the SCLF model electrons and positrons are accelerated from the NS surface upwards until the radiated photons reach the pair creation threshold. A pair cascade ensues at the PFF. The $E_{\|}$ is screened

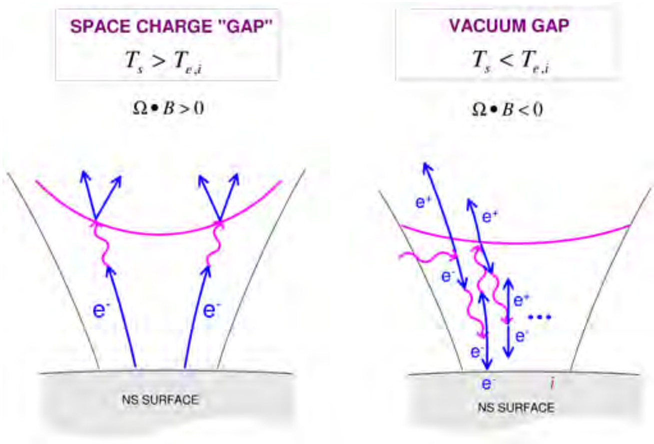

Figure 2.7: Illustration of the two types of PC accelerators, including the SCLF gap on the left (Daugherty & Harding, 1982), and the vacuum gap on the right (Ruderman & Sutherland, 1975). If the NS surface temperature T_s exceeds the ion or electron thermionic temperature $T_{i,e}$ then the SCLF gap will form, otherwise the vacuum gap will dominate. Figure from Harding (2007a).

due to the polarisation of pairs above this front, halting any further acceleration (with the relativistic charges 'coasting' outward, potentially emitting SR). Since these accelerators can maintain a steady current, there will be an upward current of electrons ($j_{\|}^{-} \simeq c\rho_{GJ}$) and also a downward current of positrons ($j_{\|}^{+} \ll c\rho_{GJ}$), which will heat the PC. The height of the PFF determines the eventual potential of these accelerators. Simulations of time-dependent vacuum (Timokhin, 2010) and SCLF (Timokhin & Arons, 2013) gaps show that the pair cascades are non-steady.

2.7.2 Slot gap model

In SG models (Arons, 1983; see Figure 2.6) it is assumed that HE particles originate from the NS surface layer and are accelerated from the PCs along the last open field lines and up to high altitudes, comparable to the light cylinder radius $R_{\rm LC} = c/\Omega$ (Harding & Grenier, 2011). This SG model is very similar to the SCLF accelerator of the PC model, except that the SG model extends up to high altitudes. The altitude of the PFF (Figure 2.8) strongly varies with magnetic colatitude across the PC due to the B-field geometry and the boundary conditions ($E_{\|} = 0$ on the surface and last open B-field lines) assumed for the SG accelerator (Harding & Muslimov, 1998). The PFF will occur at higher and higher altitudes closer to the closed field line region boundary. This is because the mean free path for magnetic (one-photon) pair production increases as $E_{\|}$ decreases toward this boundary. The radiating particle therefore needs to be accelerated over a longer distance before it can radiate photons of high enough energy so that pair formation can take place. The mean free path becomes infinite at and asymptotically tangent to the last open field line. The $E_{\|}$ is screened above the PFF, and a narrow gap surrounded by two conducting walls will form, as represented in Figure 2.8 (Harding & Muslimov, 2003). The electrons accelerated in the SG will radiate CR, ICR and SR, although their Lorentz factors are constrained by the CR. We note that new solutions for the $E_{\|}$ were determined by Muslimov & Harding (2003, 2004a), including the general relativistic effect of inertial frame-dragging near the NS surface, enhancing this field significantly.

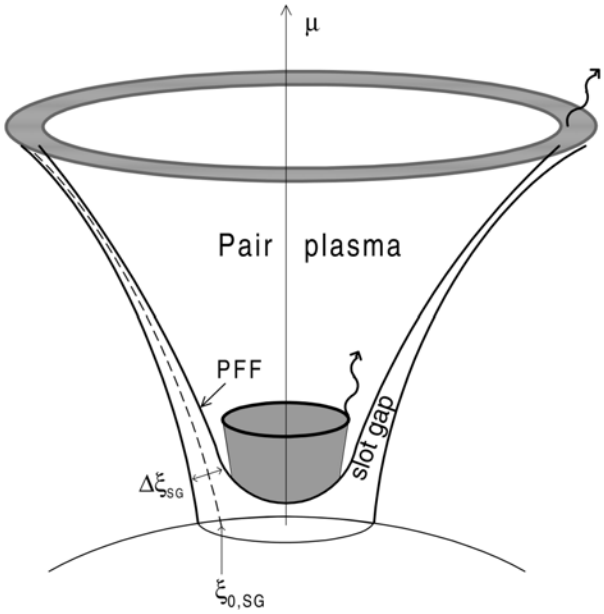

Figure 2.8: Schematic view of the SG, which is the region between the PFF and the outer boundary formed by the last open field lines (with $\boldsymbol{\mu}$ the magnetic axis and $\Delta\xi_{\rm SG}$ the gap width). The SG forms a hollow cone emitting HE radiation. From Muslimov & Harding (2003).

2.7.3 Outer gap model

The OG model (Figure 2.6) was introduced by Cheng et al. (1986a,b), initially assuming an inclined rotator with a charge density of ρ_{GJ}. They proposed that when the primary current passes through the neutral sheet (where $\mathbf{\Omega} \cdot \mathbf{B} = 0$ and $\rho_{GJ} = 0$) the negative charges above this sheet will escape beyond the light cylinder. A vacuum gap region is then formed (in which $E_{\|} \neq 0$). Charges will be accelerated in this gap region and will emit CR photons, the energy of which depends on the E-field strength. Therefore, as the vacuum region grows, $E_{\|}$ will increase, and hence the energy of the CR photons will increase until the photons have enough energy to produce electron and positron pairs when they collide with the background soft photons via photon-photon (or two-photon) pair production (see Section 2.6.5, Cheng, 2011).

The outer magnetosphere is divided into three regions (see Figure 2.9). In region I the primary electrons and positrons are accelerated in opposite directions due to the $E_{\|}$ present in the gap, with the acceleration limited by CR losses or ICS on infrared photons. Although some γ-rays undergo pair creation, most of them move over into region II, where the $E_{\|}$ is small and secondary $e^{\pm}$ pairs are produced, radiating secondary γ-rays and X-rays via SR. In region III, tertiary $e^{\pm}$ pairs are created and are responsible for the emission of softer radiation (Cheng et al., 1986b). This is also the region where γ-rays are produced by ICS involving the primary pairs. The radiation in this region may furthermore interact with primary CR γ-rays to create pairs in region II. Romani (1996) investigated an OG model based on CRR limited charges (see Section 2.6.3) in the outer magnetosphere, showing that photon-photon pair production may limit the gap width. He also demonstrated that radiation efficiency should increase with pulsar age, and discussed spectral variations in the optical and X-ray SR spectra. More modern approaches have solved the electrodynamical equations of the OG in a 2D and 3D geometry (e.g., Takata et al., 2004; Hirotani, 2006, 2008a).

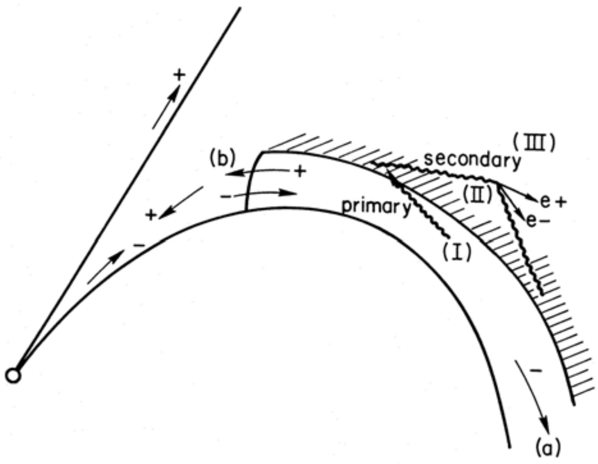

Figure 2.9: Schematic representation of the location of the three regions in an OG model which include the primary (I) (where primary particle acceleration and pair production occur), secondary (II) (where a small $E_{||}$ is present and secondary pair production as well as SR occur) and tertiary (III) regions (where tertiary pair production occurs, producing soft γ-rays). From Cheng et al. (1986b).

2.7.4 Pair-starved polar cap model

The PSPC model for MSPs was first introduced by Harding et al. (2005). They studied X-ray and γ-ray emission emitted by rotation-powered MSPs (see Section 2.3). These MSPs have very low surface B-field strengths and short periods (compared to younger pulsars). The electrodynamics is based on a (young-pulsar) model that considers the acceleration of particles and pair production (see Section 2.6.5) on the open field lines above the PCs (Muslimov & Harding, 2004b). Harding et al. (2005) assumed a PC geometry (see Section 2.7.1) and a dipole field (see Section 3.1.1). They found that most MSPs are below the CR pair death line (i.e., the $P\dot{P}$ death line for creating pairs via CR, see Section 2.4), due to the low surface B-fields (see Eq. [2.41]), implying that pairs are rather produced by ICS radiation.

Since the pair cascade multiplicity is very low in PSPC pulsars, the accelerating E-field is inefficiently screened by these pairs and no PFF is formed as in the case of young pulsars. This leads to a pair-starved PC. Therefore, the primary particles and possibly a few pairs continue to accelerate to high altitudes, up to the light cylinder, over the full open volume (in contrast to the traditional PC model where particles are only accelerated up to the PFF, and then coast along the field lines after which they escape from the magnetosphere). There exists a progression between models, depending on the pair multiplicity: the SG model has very narrow gaps for pulsars with high multiplicity, but these gaps increase in thickness and the model eventually tends toward a PSPC geometry as pair creation is more and more inhibited (Harding, 2007a).

2.8 *Fermi* Large Area Telescope

Since the launch of the *Fermi* γ-ray Space Telescope in June 2008, over 160 γ-ray pulsars have been detected, of which the Geminga and Vela pulsars are the brightest sources (see Section 2.3). *Fermi* consists of two parts including the Large Area Telescope (LAT) and the Gamma-ray Burst Monitor (GBM). *Fermi* measures the cosmic γ-ray flux in the energy range between 20 MeV and 300 GeV (Atwood et al., 2009), and is much more sensitive than its predecessor, *EGRET*, with supporting measurements for γ-ray bursts in the range 8 keV to 30 MeV (measured by the GBM). The very large field of view of 2.4 sr enables *Fermi* to observe 20% of the sky at any instant and scan the entire sky on a time scale of a few hours. *Fermi* opened up a new and important window on a wide variety of phenomena, including radio-quiet and radio-loud γ-ray pulsars and MSPs, active galactic nuclei, the optical-ultraviolet extragalactic background light, γ-ray bursts, the origin of cosmic rays, supernova remnants, and searches for dark matter (Atwood et al., 2009).

Over the past seven years, *Fermi* has released two pulsar catalogues both describing the light curve profiles and spectral characteristics of γ-ray pulsars (Abdo et al., 2010b, 2013). The rotation-powered pulsars discovered by the *Fermi* LAT are excellent laboratories for studying particle acceleration and fundamental physics involving strong gravity, strong B-fields, high plasma densities, and relativity (Harding, 2007b). The *Fermi* LAT is helping to answer some of the most fundamental questions in pulsar physics, while detailed geometric modelling of the radio and γ-ray light curves is providing constraints on the pulsar B-field structure and emission geometry.

Chapter 3

Geometric pulsar models and magnetospheres

In the physical models (see Section 2.7), the electrodynamics, which includes the formation of a putative gap region where the relativistic particles are accelerated, is important for understanding the HE emission. However, in these physical emission models there are a number of uncertainties in the pulsar electrodynamics. We therefore consider geometric models, in which we make the simplifying assumption of uniform emissivity ϵ_ν along the curved B-field within the gap region in the corotating frame (sidestepping the need to specify an E-field, charge density, or current). Since the γ-rays are expected to be emitted tangentially to the local B-field in this frame (Dyks et al., 2004a), the assumed magnetospheric structure is of importance.

In Section 3.1 we give an overview of the pulsar magnetospheres we have studied, including the static dipole (Section 3.1.1), the RVD (see Section 3.1.2), and the offset dipole (Section 3.1.3) fields. In Section 3.2 we describe the geometric models we have considered, including the TPC (geometric representation of the SG; see Section 2.7.2) and OG models. These geometric pulsar models and magnetospheres assist us in performing geometric light curve modelling in order to predict the shape of the γ-ray profiles detected by *Fermi* (see Appendix B). In Section 3.3 we describe the geometric modelling code in which the different B-field solutions and geometric gap models have been implemented. The geometric models are particularly concerned with the magnetospheric structure (sweepback) and special relativistic effects, i.e., aberration and time-of-flight delays. These geometry and special relativistic effects lead to piling up of photons at particular phases, giving rise to caustic structure in the pulsar emission beam and leading to peaks in the predicted light curves (Section 3.3.3).

3.1 Magnetospheric structures

The B-field is one of the basic assumptions of the geometric models (others include the gap region's location, and the ϵ_ν profile in the gap). Several B-field structures have been studied, including the static dipole (Griffiths, 1995), the RVD (a rotating vacuum magnetosphere which can in principle accelerate particles but do not contain any charges or currents; Deutsch, 1955), the force-free field (FF; filled with charges and currents, but unable to accelerate particles, since the accelerating E-field is screened everywhere; Contopoulos et al., 1999), and the offset dipole (to mimic deviations from the static dipole near the stellar surface analytically; Harding &

Muslimov, 2011a,b). A more realistic, pulsar magnetosphere, i.e., a dissipative solution (Kalapotharakos et al., 2012; Li et al., 2012; Tchekhovskoy et al., 2013; Li, 2014), would be one that is intermediate between the RVD and the FF fields. The dissipative B-field is characterised by the plasma conductivity $\sigma_{\rm c}$ (e.g., Lichnerowicz, 1967) which can be set in order to alternate between the vacuum ($\sigma_{\rm c} \rightarrow 0$) and FF ($\sigma_{\rm c} \rightarrow \infty$) cases (see Li et al., 2012). We studied the effect of different magnetospheric structures (static dipole, RVD, and offset dipole, further discussed below) and emission geometries (TPC and OG) on pulsar visibility and γ-ray pulse shape, particularly for the case of the Vela pulsar.

3.1.1 Static dipole magnetic field

The static dipole field is studied since the calculations are simpler for this B-field. We derive its form below. In order to obtain an approximate formula for a vector potential associated with a localized current distribution, valid at distant points, a multipole expansion can be used and the potential is written in the form of a power series in $1/r$, with r the radial distance to the point in question. If r is very large the whole power series is dominated by the lowest non-vanishing contribution and the higher-order terms can be ignored. The first term (which goes like $1/r$) in the multipole expansion is called a monopole term, the second term (which goes like $1/r^2$) the dipole term, and the third term (which goes like $1/r^3$) the quadrupole, etc. (Griffiths, 1995). The magnetic monopole term is zero (i.e., $\nabla \cdot \mathbf{B} = 0$). The next term is the magnetic dipole. The vector potential can be written as a function of position vector $\mathbf{r}$:

$$\mathbf{A}_{\rm dip}(\mathbf{r}) = \frac{I}{r^2}\oint r' \cos\theta' d\mathbf{l}' = \frac{I}{r^2}\oint (\hat{\mathbf{r}} \cdot r') d\mathbf{l}', \tag{3.1}$$

with $\hat{\mathbf{r}}$ the unit radial vector and I the current. By rewriting this integral, the vector potential becomes

$$\mathbf{A}_{\rm dip}(\mathbf{r}) = \frac{\boldsymbol{\mu} \times \hat{\mathbf{r}}}{r^2}, \tag{3.2}$$

where $\boldsymbol{\mu}$ is the magnetic dipole moment (aligned with the magnetic axis, therefore sometimes defined by the same symbol) defined as (in cgs units)

$$\boldsymbol{\mu} \equiv \frac{I}{c}\int d\mathbf{a} = \frac{I\mathbf{a}}{c}, \tag{3.3}$$

with $\mathbf{a}$ the enclosed area of the current loop, and c the speed of light. To calculate the B-field of a dipole, $\boldsymbol{\mu}$ may be set at the origin, pointing in the z-direction. The vector potential, Eq. (3.2) can then be written in spherical co-ordinates,

$$\mathbf{A}_{\rm dip}(\mathbf{r}) = \frac{\mu \sin\theta}{r^2}\hat{\boldsymbol{\phi}}, \tag{3.4}$$

hence the dipole B-field is given by (Griffiths, 1995):

$$\mathbf{B}_{\rm static}(\mathbf{r}) = \nabla \times \mathbf{A}_{\rm dip}(\mathbf{r}) = \frac{\mu}{r^3}(2\cos\theta\hat{\mathbf{r}} + \sin\theta\hat{\boldsymbol{\theta}}) \tag{3.5}$$

in the magnetic ($\boldsymbol{\mu}$) frame or where the inclination angle $\alpha = 0$ (the angle between the rotation $\boldsymbol{\Omega}$ and the $\boldsymbol{\mu}$ axes).

When the light curve shapes and features for the static dipole are compared to those for the other B-fields (see Chapter 6), the importance of the near-$R_{\rm LC}$ (with $R_{\rm LC}$ the light cylinder radius where the corotation speed equals the speed of light) distortions in the B-fields for predicted radiation characteristics can be gauged (Dyks et al., 2004a). The static (non-rotating) dipole is a special case of the retarded (rotating) dipole which we consider next.

3.1.2 Retarded vacuum dipole magnetic field

The solution for a B-field surrounding an NS was first derived by Deutsch (1955) and may be approximated by a dipole rotating in vacuum. Previous investigators (Yadigaroglu, 1997, Arendt & Eilek, 1998, Jackson, 1999, Cheng et al., 2000, Dyks et al., 2004a) implemented methods which considered distortions in the B-field structure due to sweepback of the field lines as the NS rotates with an angular frequency Ω about the $\hat{\mathbf{z}}$-axis. The general expression for this RVD field is given by

$$\mathbf{B}_{\rm ret} = -\left[\frac{\boldsymbol{\mu}(t)}{r^3} + \frac{\dot{\boldsymbol{\mu}}(t)}{cr^2} + \frac{\ddot{\boldsymbol{\mu}}(t)}{c^2 r}\right] + \hat{\mathbf{r}}\hat{\mathbf{r}}\cdot\left[3\frac{\boldsymbol{\mu}(t)}{r^3} + 3\frac{\dot{\boldsymbol{\mu}}(t)}{cr^2} + \frac{\ddot{\boldsymbol{\mu}}(t)}{c^2 r}\right], \tag{3.6}$$

with

$$\boldsymbol{\mu}(t) = \mu(\sin\alpha\cos\Omega t\hat{\mathbf{x}} + \sin\alpha\sin\Omega t\hat{\mathbf{y}} + \cos\alpha\hat{\mathbf{z}}). \tag{3.7}$$

the magnetic moment, with $\dot{\boldsymbol{\mu}}(t)$ and $\ddot{\boldsymbol{\mu}}(t)$ its first and second time-derivatives, and $\hat{\mathbf{r}} = r/\mathbf{r}$ the unit radial vector. The RVD solution can also be described by the following B-field equations in spherical co-ordinates in the laboratory frame (where $\hat{\mathbf{z}} \parallel \boldsymbol{\Omega}$; Dyks & Harding, 2004):

$$\begin{aligned}
B_{{\rm ret},r} &= \frac{2\mu}{r^3}\Big[\cos\alpha\cos\theta + \sin\alpha\sin\theta(r_{\rm n}\sin\lambda + \cos\lambda)\Big], && (3.8)\\
B_{{\rm ret},\theta} &= \frac{\mu}{r^3}\Big(\cos\alpha\sin\theta + \sin\alpha\cos\theta[-r_{\rm n}\sin\lambda + (r_{\rm n}^2 - 1)\cos\lambda]\Big), && (3.9)\\
B_{{\rm ret},\phi} &= -\frac{\mu}{r^3}\sin\alpha\Big[(r_{\rm n}^2 - 1)\sin\lambda + r_{\rm n}\cos\lambda\Big], && (3.10)
\end{aligned}$$

with $\lambda = r_{\rm n} + \phi_{\rm L} - \Omega t$, $r_{\rm n} = r/R_{\rm LC}$, Ω the angular velocity, and $\phi_{\rm L}$ the phase. These equations can be rewritten to give the B-field components in the Cartesian frame and co-ordinates (where $\hat{\mathbf{z}} \parallel \boldsymbol{\Omega}$; Dyks & Harding, 2004)

$$\begin{aligned}
B_{{\rm ret},x} &= \frac{\mu}{r^5}\Big(3xz\cos\alpha + \sin\alpha\Big\{[(3x^2 - r^2) + 3xyr_n + (r^2 - x^2)r_n^2]\cos(\Omega t - r_n)\\
&\quad +[3xy - (3x^2 - r^2)r_n - xyr_n^2]\sin(\Omega t - r_n)\Big\}\Big), && (3.11)\\
B_{{\rm ret},y} &= \frac{\mu}{r^5}\Big(3yz\cos\alpha + \sin\alpha\Big\{[3xy + (3y^2 - r^2)r_n - xyr_n^2]\cos(\Omega t - r_n)\\
&\quad +[(3y^2 - r^2)r_n - 3xyr_n + (r^2 - y^2)r_n^2]\sin(\Omega t - r_n)\Big\}\Big), && (3.12)\\
B_{{\rm ret},z} &= \frac{\mu}{r^5}\Big\{(3z^2 - r^2)\cos\alpha + \sin\alpha[(3xz + 3yzr_n - xzr_n^2)\cos(\Omega t - r_n)\\
&\quad +(3yz - 3xzr_n - yzr_n^2)\sin(\Omega t - r_n)]\Big\}. && (3.13)
\end{aligned}$$

The above expressions are obtained when assuming the limit of the Deutsch solution where $R/R_{\rm LC} \ll 1$, with R the stellar radius. By setting $r_{\rm n} = 0$, the retarded field simplifies to the non-aligned static dipole ($\alpha \neq 0$).

As was shown in Chapter 1, the difference between the static dipole and RVD is illustrated in Figure 3.1

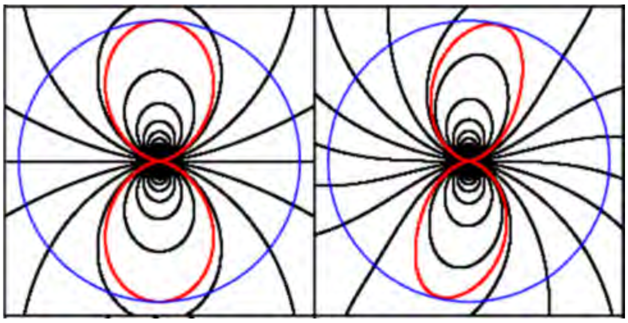

Figure 3.1: Illustration of the static dipole (left) and RVD (right) B-field structures in the equatorial plane, where $\alpha = 90°$. The red curve indicates the last closed field line which closes at the light cylinder, where the corotation speed is equal to c. The sweepback of field lines is evident for the RVD case. The blue circle indicates a slice through the light cylinder. From Romani & Watters (2010).

for $\alpha = 90°$, i.e. field lines in the equatorial plane. For the static dipole (left) the field lines are symmetric, whereas in the RVD case (right) the field lines are distorted due to sweepback of the field lines as the NS rotates. This has implications for the definition of the PC (see Figure 3.5). These distortions in the RVD B-field are illustrated in Figure 3.2 for an $\alpha = 65°$ as seen from different points of view.

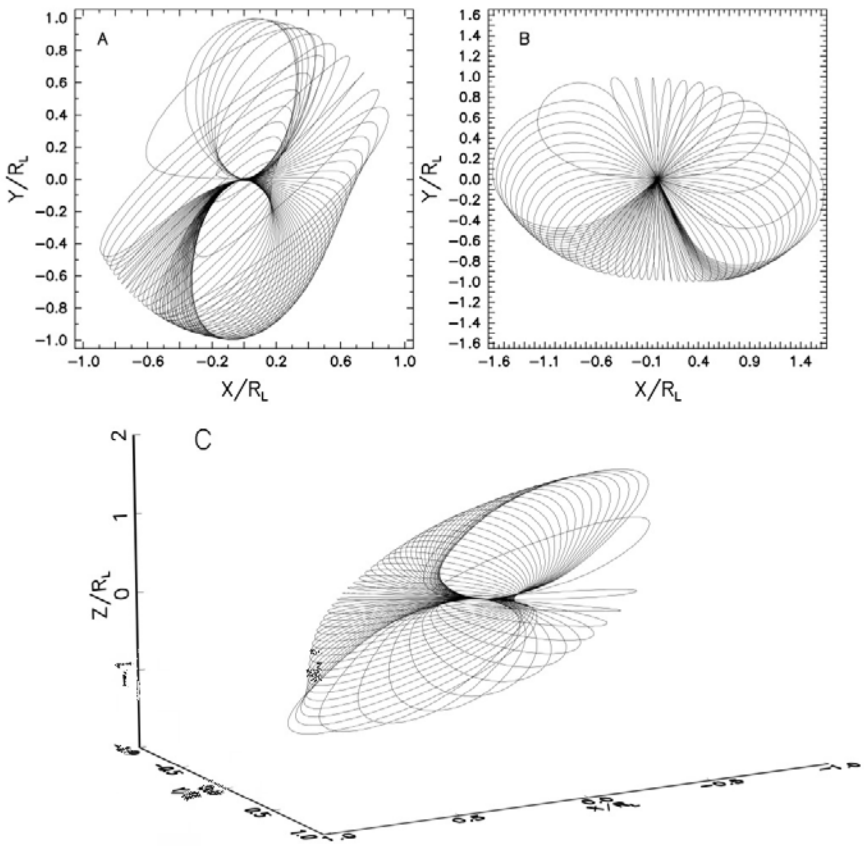

Figure 3.2: Illustration of an RVD B-field for the last closed field lines, inclined with respect to $\mathbf{\Omega}$ by an angle $\alpha = 65°$. Three projections are presented: (a) looking down $\mathbf{\Omega}$, (b) looking down $\boldsymbol{\mu}$, and (c) a 3D view. Strong distortions are visible as the inclination becomes larger (see Arendt & Eilek, 1998). From Cheng et al. (2000).

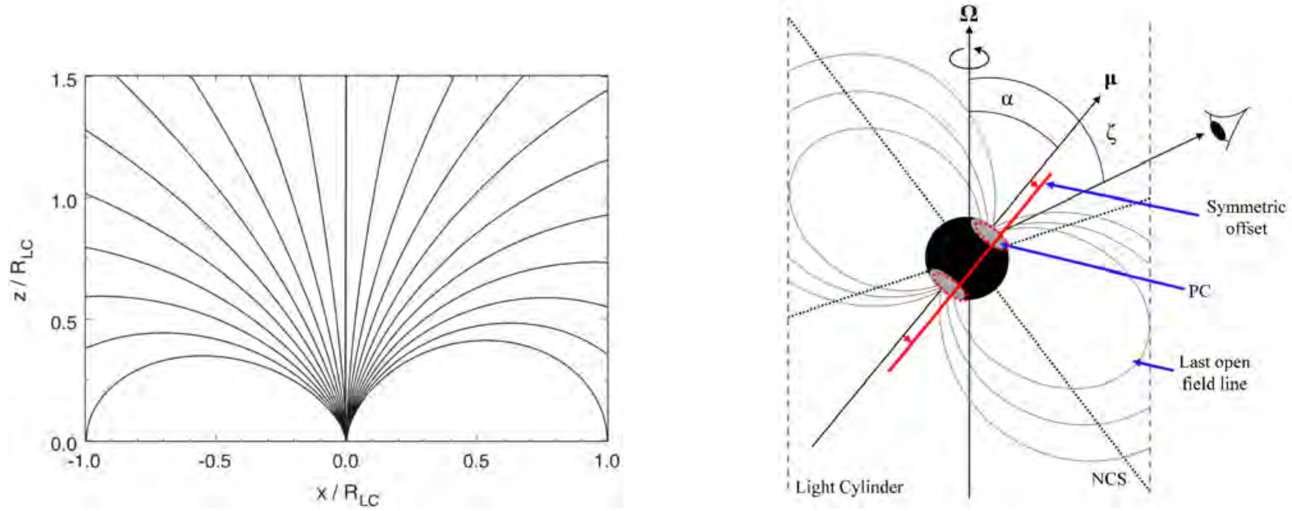

(a) (b)

Figure 3.3: In (a) we illustrate the distorted field lines of the offset dipole B-field having symmetrically offset PCs in the $x - z$ plane, for an offset $\epsilon = 0.2$ (Harding & Muslimov, 2011b). In (b) we represent the symmetric offset geometrically, where the PCs (grey ovals) are shifted from the magnetic axis in the same direction, resulting in symmetric PC offsets (red dashed circles). The curved arrow around $\boldsymbol{\Omega}$ indicates the direction of rotation.

3.1.3 Offset dipole magnetic field

The offset dipole is a heuristic model of a non-dipolar magnetic structure where the PCs are offset from the $\boldsymbol{\mu}$-axis. The B-field lines of an offset dipole field are azimuthally asymmetric compared to those of a pure dipole field. This leads to field lines having a smaller curvature radius $\rho_{\rm curv}$ over half of the PC compared to those of the other half. Such small distortions in the B-field structure are due to retardation and asymmetric currents, thereby shifting the PCs by small amounts in different directions.

There are two cases, i.e., symmetric and asymmetric. The symmetric case involves an offset of both PCs in the same direction and applies to NSs with some interior current distortions that produce multipolar components near the stellar surface (see Figure 3.3; Harding & Muslimov, 2011b). The asymmetric case is associated with asymmetric PC offsets in opposite directions and applies to PC offsets due to retardation and/or currents of the global magnetosphere (see Figure 3.4; Harding & Muslimov, 2011b). These non-dipolar B-field geometries are motivated by observations of thermal X-ray emission, e.g., pulse profiles from MSPs such as PSR J0437−4715 (Bogdanov et al., 2007) and PSR J0030+0451 (Bogdanov & Grindlay, 2009), with the B-fields of NSs in low mass X-ray binaries even more distorted (Lamb et al., 2009). Magnetic fields such as the FF solution (characterised by different PC currents than those assumed in SCLF models; Contopoulos et al., 1999; Timokhin, 2006) will undergo larger sweepback of field lines near the light cylinder, and consequently display a larger offset of the PC toward the trailing side (opposite to the rotation direction) than in the RVD field (which has offset PCs due to rotation alone; see Section 3.1.2). Both these cases were modelled by introducing an offset parameter ϵ. Thus, as seen in Figure 3.3a the global open field lines of a centred dipole are bent toward the dipole axis on one side and bent away from the dipole axis on the other side of the PC. Therefore, one side of the PC is larger and the PC is effectively shifted from the centre of symmetry (see Figure 3.3b).

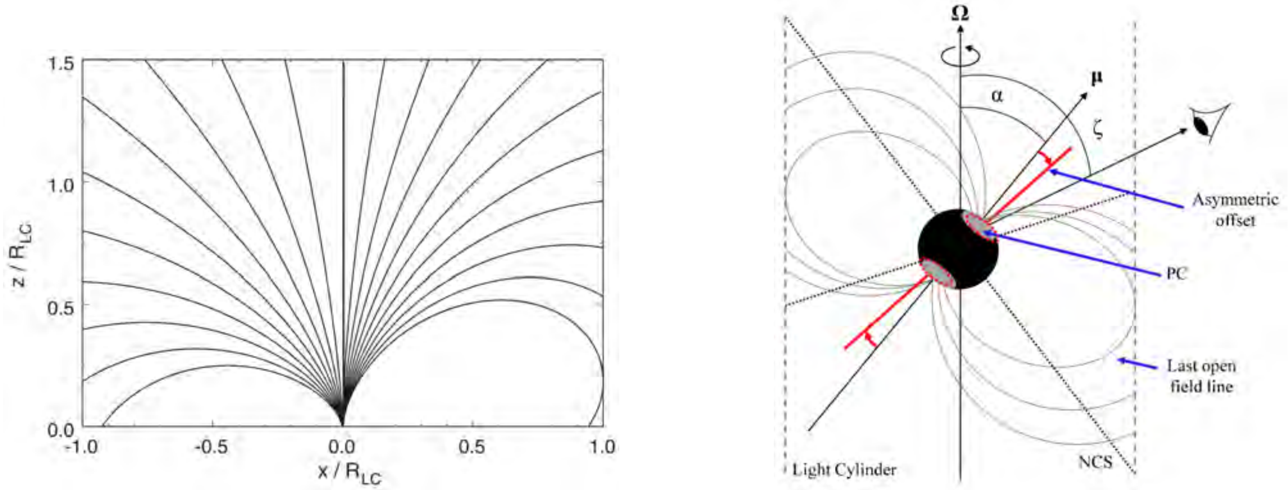

(a) (b)

Figure 3.4: In (a) we illustrate the distorted field lines of the offset dipole B-field having asymmetric offset PCs in the $x - z$ plane, for an offset $\epsilon = 0.2$ (Harding & Muslimov, 2011b). In (b) we represent the offset geometrically, with the PCs (grey ovals) shifted from the magnetic axis in opposite directions, resulting in asymmetric PC offsets (red dashed circles). The curved arrow around $\boldsymbol{\Omega}$ indicates the direction of rotation.

The general expression for a symmetric offset dipole B-field in terms of spherical co-ordinates (r', θ', ϕ') in the magnetic frame (indicated by the primed co-ordinates, where $\hat{\mathbf{z}}' \parallel \boldsymbol{\mu}$) is as follows (Harding & Muslimov, 2011b)

$$\mathbf{B}'_{\rm offset,s}(r', \theta', \phi') \approx \frac{\mu}{r'^3}[\cos\theta'\hat{\mathbf{r}}' + \frac{1}{2}(1+a)\sin\theta'\hat{\boldsymbol{\theta}}' - \epsilon\sin\theta'\cos\theta'\sin(\phi' - \phi'_0)\hat{\boldsymbol{\phi}}'], \tag{3.14}$$

where $\mu = B_0R^3$ is the magnetic moment, B_0 the surface B-field strength at the magnetic pole, ϕ'_0 the magnetic azimuthal angle defining the plane in which the offset occurs, and $a = \epsilon\cos(\phi' - \phi'_0)$ characterizes the distortion of the field lines in the $x - z$ plane. This distortion depends on parameters ϵ (related to the magnitude of the shift of the PC from the magnetic axis) and ϕ'_0. If we set $\epsilon = 0$ the symmetric case reduces to a symmetric static dipole, as given in Eq. (3.5).

The general expression for an asymmetric B-field is as follows (Harding & Muslimov, 2011b)

$$\mathbf{B}'_{\rm offset,a}(r', \theta', \phi') \approx \frac{\mu}{r'^3}[\cos[\theta'(1+a)]\hat{\mathbf{r}}' + \frac{1}{2}\sin[\theta'(1+a)]\hat{\boldsymbol{\theta}}' - \frac{1}{2}\epsilon(\theta' + \sin\theta'\cos\theta')\sin(\phi' - \phi'_0)\hat{\boldsymbol{\phi}}'], \tag{3.15}$$

with the distortion of the field lines occurring in the $x - z$ plane. If we set $\epsilon = 0$ the asymmetric case also reduces to a symmetric static dipole as given in Eq. (3.5).

The distance by which the PCs are shifted on the NS surface is given by

$$\Delta r_{\rm PC} \simeq R\theta_{\rm PC}\left[1 - \theta^{\epsilon}_{\rm PC}\right], \tag{3.16}$$

where $\theta_{\rm PC} = (\Omega R/c)^{1/2}$ is the standard half-angle of the PC, and Ω the angular speed. This effective shift of the PCs is a fraction of $\theta_{\rm PC}$, therefore it is a larger fraction of R for pulsars with shorter periods (Harding & Muslimov, 2011a). Harding & Muslimov (2011b) found that for the RVD solution, $\epsilon = 0.03 - 0.1$, where offsets as large as 0.1 are associated with MSPs with large $\theta_{\rm PC}$. However, $\epsilon = 0.09 - 0.2$ is expected for FF fields, with the larger offset values related to MSPs (Bai & Spitkovsky, 2010). One of the main focus points of our study was the implementation of an offset dipole *B*-field, for the symmetric case only.

3.2 Geometric pulsar models

There are a few distinct geometric models which differ as to the gap location and geometry (or extent). In these geometries the γ-rays are emitted tangentially to the curved *B*-field lines in the corotating frame. In our study we considered the TPC and OG geometric pulsar models. These geometric models assume that the peaks of the light curves are of caustic origin due to special relativistic effects on emission in the outer magnetosphere (Section 3.3.3). Both these geometries are narrow and differ in longitudinal and transverse extent. In these geometric models we assume ϵ_ν to be uniform. In the next chapter we consider a physical model, i.e., an SG model for which we calculated the parallel *E*-field, $E_\parallel$ in order to modulate ϵ_ν. Other studies modelled HE light curves in the context of TPC and OG models using a FF *B*-field, proposing a separatrix layer model close to the last open field line, up to and beyond the light cylinder (Bai & Spitkovsky, 2010). Furthermore, Du et al. (2010) investigated the annular gap model (with emission occurring in a gap formed between the critical *B*-field line which intersects the light cylinder perpendicularly and the last open field line), using the static dipole field, and has been successful in reproducing the main characteristics of the HE light curves of three MSPs.

3.2.1 Two-pole caustic model

The TPC (purely geometric) pulsar model was first introduced by Dyks & Rudak (2003). Muslimov & Harding (2003) revived the SG model of Arons (1983), with general relativistic corrections, and argued that the SG model may be considered a physical representation of the TPC model (see Figure 2.6 and Section 2.7.2).

The TPC geometry was proposed as an extension of the PC and OG models to explain some particular characteristics of the γ-ray light curves, since the PC and OG models had shortcomings regarding this. The PC geometry prefers nearly aligned rotators that provide long HE duty cycles and narrow opening angles for γ-ray emission (Daugherty & Harding, 1994), whereas the OG model prefers highly inclined rotators. The OG model is unable to produce light curves with some features such as outer wings in the double-peak profiles, as well as significant off-peak emission (see Appendix B).

Dyks et al. (2004b) investigated the influence of special relativistic effects, i.e., aberration and light-travel time delays (see Section 3.3.3) on the γ-ray light curves for the PC, OG, and TPC models. For the TPC model, some prominent features (i.e., mostly double-peak profiles, well-developed wings, bridge or interpeak emission, a level of non-vanishing off-pulse emission, and the radio pulse leading the γ-ray pulse) are visible in the light curves, consistent with the observed characteristics of HE pulsar emission.

The TPC model is a high-altitude model which has a large longitudinal extent from the NS surface, along the last closed field line (or enclosed by the surface formed by the last open *B*-field lines) up to the light cylinder. The original definition stated that the longitudinal extent of the TPC model is at maximum radial distances of $R_{\rm max}\simeq 0.8R_{\rm LC}$ (Muslimov & Harding, 2004a). Later these radial distances were extended to $R_{\rm max}\simeq 1.2R_{\rm LC}$ for improved fits (e.g., Venter et al., 2009, 2012). Typical transverse gap extents of $0-5\%$ of the PC angle have been used (Venter et al., 2009; Watters et al., 2009).

3.2.2 Outer gap geometric model

In the OG model (Cheng et al., 1986a,b; see Section 2.7.3) the γ-ray emission is emitted along curved field lines (near the last open field line), and has a longitudinal extent from beyond the null-charge surface (NCS, with a radius of $R_{\rm NCS}$, i.e., the geometric surface across which the charge density changes sign, i.e., where the Goldreich-Julian charge density $\rho_{\rm GJ} = 0$) up to the light cylinder. Thus, the OG model extends from a minimum emission radius $R_{\rm min} = R_{\rm NCS}$ up to a maximum emission radius $R_{\rm max} \lesssim R_{\rm LC}$. Venter et al. (2009) considered the OG model as a one-layer model in which they assumed emission altitudes of $(R_{\rm min}, R_{\rm max}) = (R_{\rm NCS}, 1.2R_{\rm LC})$ and a transverse extent along the inner edge of the gap (close to $r_{\rm ovc}^{\rm min}$; see Section 3.3.1 for the definition of $r_{\rm ovc}$).

In a geometric sense, the OG model may be also referred to as a "one-pole caustic model", since the assumed geometry of the gap region allows emission from a single magnetic pole only to arrive at the observer (Harding, 2005a). Since emission only starts above the NCS, the emission from the OG models is not visible at all angle combinations (different α and ζ; see Appendix B), while emission from the TPC model generally is.

3.3 Geometric pulsar code

3.3.1 Finding the PC rim

We performed geometric light curve modelling using the code first developed by Dyks et al. (2004a). We extended this code by implementing an offset dipole (symmetric case) B-field, as well as the SG $E_{\|}$-field corrected for general relativistic effects (see Chapter 4). We studied the static dipole, RVD, and offset dipole B-field solutions, in conjunction with the TPC and OG geometries. To simulate light curves, the geometric code starts by finding the PC rim. The code first selects a magnetic polar angle θ at a fixed magnetic azimuthal angle ϕ and then performs a fourth-order Runge-Kutta integration method which traces the field line to check whether it closes at the light cylinder. If the field line closes inside the light cylinder the code chooses a smaller θ value. If this new line closes outside of the light cylinder the code next chooses a larger θ. This is done iteratively. Once a field line is found that closes at (is tangent to) the light cylinder, the B-field line footpoint is saved and the next field line is obtained by taking a step in ϕ (using the previous optimal θ) and then repeating the entire procedure. This continues until the boundary for the PC rim has been determined (Figure 3.5a; see Dyks et al., 2004a).

Importantly, the shape of PC rim depends on the B-field structure at $R_{\rm LC}$. In Figure 3.5a we present the PC shape of the static dipole (dashed line) and RVD (thick solid line) fields for an inclination angle $\alpha = 45°$ (the dependence of the PC shape on α has been studied by, e.g., Cheng et al. (2000) and Arendt & Eilek (1998)). For the static dipole and $\alpha = 0$ (an aligned rotator), the PC is circular with a radius $r_{\rm PC} = (\Omega R^3 c^{-1})^{1/2}$. The RVD B-field presents an asymmetrically distorted PC, possessing a "notch" or "glitch" due to the sweepback of field lines as the NS rotates. This distorted PC rim is divided into two parts, R1 and R2, by the critical points C1 (the tip of the notch) and C2. The field lines emerging from R1 and R2 respectively are tangent to the light cylinder.

Once the PC rim is determined, the PC is divided into self-similar (interior) rings. These rings are calculated by using open-volume co-ordinates ($r_{\rm ovc}$ and $l_{\rm ovc}$; see Figure 3.5b and Figure 3.5c). The co-ordinate $r_{\rm ovc} \equiv$

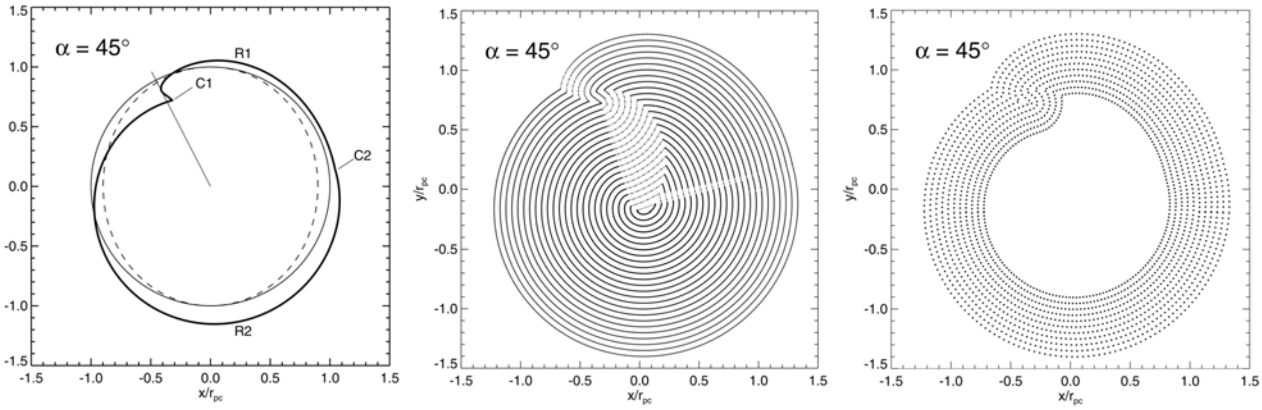

(a) (b) (c)

Figure 3.5: Illustrations of the PC rim and its self-similar (interior) rings for the Crab pulsar for an $\alpha = 45°$. In panel (a) the shape of the PC rim for the static dipole (dashed oval) and RVD (thick line with a notch) cases are shown and as a reference, a circular PC (with radius $r_{\rm PC} = (\Omega R^3 c^{-1})^{1/2}$) of a dipole aligned with the rotation axis is shown (thin solid line). For all three panels (from Dyks et al. (2004a)) the magnetic axis $\boldsymbol{\mu}$ (perpendicular to page) of both the static dipole and RVD are aligned. For a broad range in ϕ the reference PC (thin line) approximates the RVD case better than the static dipole. Panel (b) represents a grid of constant values for the open volume co-ordinate $r_{\rm ovc}$ (see text), in the range between 0.05 and 1.25, with a ring separation of 0.05. The sixth ring (counting inward) is the PC rim (the thick solid line in Panel (a)). Panel (c) shows a sample distribution of footpoints of B-field lines along which photon emission is modelled. In this case there are 180 footpoints uniformly distributed along each ring of constant $r_{\rm ovc}$, ranging between 0.75 and 1.25, with a ring separation of 0.05.

$1 \pm d_{\rm ovc}$ (with $d_{\rm ovc}$ the minimum distance of a point to the rim, normalised by the PC radius $r_{\rm PC}$) labels the rings inside (or outside) the PC rim, with $r_{\rm ovc} = 1$ corresponding to the locus of the last open field line footpoints (i.e., the rim). The co-ordinate $l_{\rm ovc}$ is the arclength of a particular ring (constant $r_{\rm ovc}$), and is analogous to azimuthal angle measured counter clockwise from the positive x-axis (see Harding et al., 2008). After the footpoints of the field lines have been determined, particles are followed along these lines (Figure 3.5c) and emission from them is collected in bins of pulse phase $\phi_{\rm L}$ and ζ, i.e., a sky map is formed (see Chapter 6).

3.3.2 Defining the gap

For the TPC (see Section 3.2.1) and OG (see Section 3.2.2) models we assume uniform emissivity in the corotating frame, i.e., no explicit electric field ($E_{||}$) or particle transport calculations are included along the field lines. The transverse gap region is restricted to lie between two B-field lines, with $r_{\rm ovc} \in [r_{\rm ovc}^{\rm min}, r_{\rm ovc}^{\rm max}]$, implying a gap width of $w \equiv r_{\rm ovc}^{\rm max} - r_{\rm ovc}^{\rm min}$. We assume that these standard gaps are confined to lie within a cylindrical radius of $\rho_{\rm max}$, i.e., the "cutoff" altitude at which the emission ceases (in units of $R_{\rm LC}$; Dyks et al., 2004a), since the B-field geometry is uncertain at the light cylinder. The distortions in the B-field structure are mainly determined by the magnitude of the current. For example, for the FF B-field the currents are stronger than for vacuum B-fields, so that FF field lines are more swept back than vacuum field lines. However, the distribution of the current (or conductivity) remains uncertain, leading to uncertainties in the B-field geometry at the light cylinder. These gap geometries can also be varied longitudinally by changing the minimum and maximum emission altitudes ($R_{\rm min}$ and $R_{\rm max}$).

As in Section 3.2.1 the standard TPC gap region assumes a $\rho_{\rm max}$ between $0.75R_{\rm LC}$ and $0.95R_{\rm LC}$. The gap extends from the stellar surface with a minimum radius $R_{\rm min} = R$, up to a maximum radius $R_{\rm max} \lesssim R_{\rm LC}$. However, the standard OG model the gap assumes a $\rho_{\rm max}$ between 0.8 and $1.0R_{\rm LC}$, and extends from a minimum radius of $R_{\rm NCS}$ up to a maximum radius $R_{\rm max} \lesssim R_{\rm LC}$ (Section 3.2.2). More recently these gap regions have been altered by making $R_{\rm min}$ and $R_{\rm max}$ free parameters. These models are called altitude limited models, e.g., Abdo et al. (2010b) and Venter et al. (2012).

Venter et al. (2009) investigated the gap regions in the context of the TPC and OG models, for MSPs, assuming a constant emissivity across the gap. For their models they assumed emission altitudes of $(R_{\rm min}, R_{\rm max}) = (R_{\rm NS}, 1.2R_{\rm LC})$ for the TPC model and $(R_{\rm min}, R_{\rm max}) = (R_{\rm NCS}, 1.2R_{\rm LC})$ for the OG models. They found that for different choices of $r_{\rm ovc}^{\rm min}$ and $r_{\rm ovc}^{\rm max}$, a large w ($\lesssim 0.1$) for the TPC model does not produce good light curve fits, whereas for the OG case they considered emission produced along the inner edge of the gap (close to $r_{\rm ovc}^{\rm min}$; Wang et al., 2010; Johnson et al., 2014). However, Watters et al. (2009) assumed that the emission occurs along the inner edge of the gaps (i.e., $w = 0$) along a single field line, not equal to the gap width as assumed by Venter et al. (2009). In this study we use $r_{\rm ovc}^{\rm min} = 0.95$, $r_{\rm ovc}^{\rm max} = 1.0$, $(R_{\rm min}, R_{\rm max}) = (R, 1.2R_{\rm LC})$ for the TPC model and $(R_{\rm min}, R_{\rm max}) = (R_{\rm NCS}, 1.2R_{\rm LC})$ for the OG model.

3.3.3 Caustic effects

There are three important effects to take into account when calculating HE emission from pulsars: the structure/geometry of the B-field (see Section 3.1), aberration of the photon emission direction, and time-of-flight delays. By understanding these effects we can identify the corresponding features displayed in light curves. These relativistic effects were first applied by Morini (1983) and are responsible for the formation of emission caustics, i.e., the bright peaks observed in the light curves.

Consider a rapidly rotating NS with a vacuum dipole B-field (see Section 3.1.2; Deutsch, 1955). We assume that the HE emission is emitted from the stellar surface, tangent to the curved B-field lines, up to the light cylinder in the corotating frame. As the star rotates the B-field lines will experience a sweepback in a direction opposite to that of rotation, leading to a change in the emission direction tangent to the field lines.

Second, since the photons are emitted at different radii they will arrive at different phases $\phi_{\rm L}$ at the observer. Therefore, a photon emitted along the last open field line at some altitude $r_{\rm em}$ (in units of $R_{\rm LC}$) will arrive at an earlier phase $\phi_{\rm L}$ at the observer than a photon emitted from the stellar surface (where $r_{\rm em} = 0$ and $\phi_{\rm L} = 0$) due to constant speed of light c. The phase shift due to time-of-flight delays (i.e., phase delays) in the arrival times of the emission radiated at different $r_{\rm em}$ is (Dyks et al., 2004b)

$$\Delta\phi_{\rm ret} \approx -\frac{r_{\rm em}}{R_{\rm LC}}. \tag{3.17}$$

Third, as seen by an observer in the inertial frame, the emission direction appears shifted in phase $\phi_{\rm L}$ (in the rotation direction). This effect is referred to as aberration, causing a relative phase shift at an emission radius $r_{\rm em}$ (to the first-order) as given by (Dyks et al., 2004b)

$$\Delta\phi_{\rm ab} \simeq -\frac{r_{\rm em}}{R_{\rm LC}}. \tag{3.18}$$

The time-of-flight and aberration delays are the same, to the first order in corotation velocity $\beta_{\rm cor} = \mathbf{\Omega} \times \mathbf{r} =$

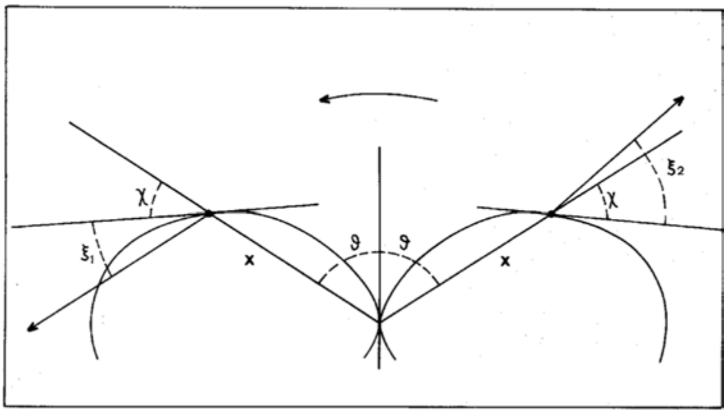

Figure 3.6: Emission field lines geometry with the curved arrow indicating the direction of rotation. The special relativistic effects as first noted by Morini (1983) are illustrated, with the leading edge on the left-hand side and the trailing edge on the right (see text for definition of symbols). From Morini (1983).

$(r_{\rm em}/R_{\rm LC})\sin\zeta$ at the emission point.

The phase shifts discussed above give rise to emission caustics. On the trailing edge (opposite to the direction of rotation) these relative phase shifts (together with the B-field geometry) nearly cancel and therefore the emission along these field lines bunch in $\phi_{\rm L}$. The trailing edge therefore represents the sharp peaks observed in the light curves (see Appendix B). On the leading edge (in direction of rotation) the relative phase shifts of all these effects add up causing the emission along these field lines to spread out in $\phi_{\rm L}$.

A simple example is provided in Figure 3.6 for an orthogonal rotator (i.e., $\alpha = 90°$) with a dipolar B-field. In Figure 3.6 the above mentioned effects are visible as first noted by Morini (1983). Consider a photon emitted along the last open field line at a radius $x = r/R_{\rm LC}$ and magnetic colatitude θ. The phase at which the observer sees an emitted photon is $\phi_{{\rm L},i}$, with χ the angle between the B-field line and radial direction, and ξ_i the aberration angle, with $i = 1$ for the trailing (right) and $i = 2$ for the leading (left) edges. This is given by

$$\begin{array}{rcl} 2\pi\phi_{\rm L,1} & = & -(\theta + \chi + \xi_1 + x\cos(\xi_1+\chi)), \quad \text{leading edge} \\ 2\pi\phi_{\rm L,2} & = & \theta + \chi - \xi_2 - x\cos(\xi_2+\chi). \quad \text{trailing edge} \end{array} \tag{3.19}$$

with the rotation direction counter clockwise as indicated by the curved arrow. In Eq. (3.19) on the right hand side for both edges, the first two terms are due to the structure of the B-field, whereas the term $x\cos(\xi_i + \chi)$ is due to the time-of-flight delays. As seen from Eq. (3.19), on the leading edge the relative phase shifts of all these effects add up, causing the emission along these field lines to spread out in $\phi_{\rm L}$. However, on the trailing edge, these effects nearly cancel causing the photon propagation directions to bunch in $\phi_{\rm L}$, forming caustics which are visible as peaks in the light curves. This is shown in Figure 3.7 for the Vela pulsar where the left side of each curve represents the leading edge (spread in $\phi_{\rm L}$) and the right side the trailing edge (bunched in $\phi_{\rm L}$). The two curves at $\phi_{\rm L} = 0.5$ and $\phi_{\rm L} = 1.0$ refer to emission from opposite PCs.

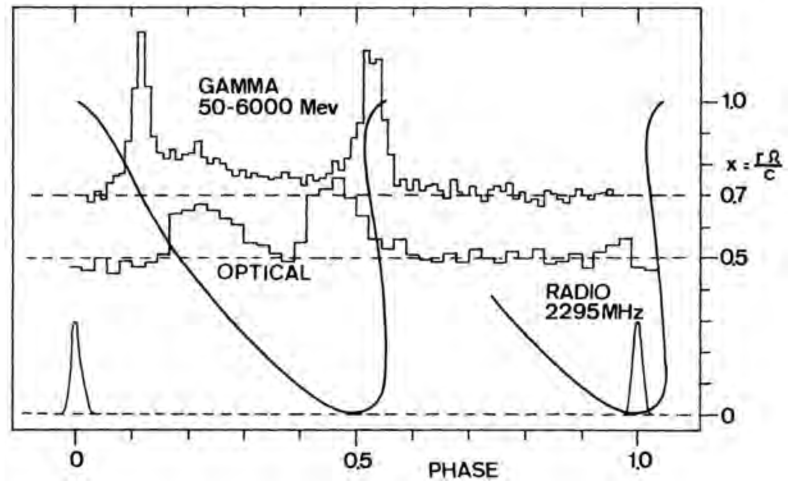

Figure 3.7: Illustration of the emission regions of the Vela pulsar. The curves represents the arrival phases of photons emitted from the NS surface, tangent to the last open field line, up to the light cylinder at different emission radii x. Each curve refers to a different PC, where the left-side branch represents the leading edge and the right-side the trailing edge. From Morini (1983).

3.3.4 Calculating sky maps and light curves

After the footpoints of the field lines have been determined (as described in Section 3.3.1) for each B-field geometry, particles are followed along these lines (Figure 3.5c), and emission from them is collected in bins of pulse phase $\phi_{\rm L}$ and ζ. A sky map is formed when one plots the bin contents (divided by the solid angle subtended by the bin) for a given α, and it is therefore a projection of the radiation beam. To simulate light curves, one chooses a sky map corresponding to a fixed α, then fix ζ and plot the intensity $I(\alpha, \zeta, \phi_{\rm L})/\Delta\Omega$ per solid angle. For a more detailed discussion we refer the reader to Chapter 6.

3.4 Summary

The physical pulsar emission models consider the electrodynamics in the pulsar magnetosphere, which is important for understanding the HE emission. However, there are still a number of uncertainties in the pulsar electrodynamics. We therefore considered geometric models, i.e., the TPC (with the SG its physical representation) and OG models, to constrain the pulsar geometry (e.g., α and ζ), as well as the γ-ray emission region's location and extent.

The magnetospheric structure and special relativistic effects, e.g., aberration, time of flight delays, and B-field sweepback, are crucial for the geometric models. Therefore, we studied the impact of different magnetospherics structures (Section 3.1) on the predicted γ-ray profiles detected by *Fermi*, by performing geometric light curve modelling, e.g., using a geometric pulsar code (Dyks & Harding, 2004; Breed et al., 2014, 2015). This code already includes the static dipole and RVD solutions, the TPC and OG geometries, and the relevant special relativistic effects (see Section 3.3.3). We extended this code by incorporating an additional B-field, i.e., the offset dipole field, as well as its SG $E_{\|}$-field (to modulate the emissivity). We discuss this implementation in the next chapter.

In Chapter 6 we present our sky maps and light curves we constructed for the various B-field and geometric model combinations, as well as for several different pulsar parameters. In our results these special relativistic effects are visible, since they lead to piling up, leading to caustic emission structure as well as some prominent features consistent with the observed characteristics of HE pulsar emission.

Chapter 4

Implementation of an offset dipole B-field and associated E-field

In this study we investigated the effect of different magnetospheric structures on γ-ray pulsar light curves. The γ-ray light curves have, e.g., been modelled in the geometric context of the SG (see Section 2.7.2), i.e., the TPC (see Section 3.2.1), and OG (see Sections 2.7.3 and 3.2.2) pulsar models. The assumption of the B-field structure is very important since this directly influences the resulting light curve shapes. Moreover, the associated E-field may strongly influence the emissivity. It is thus important to take the latter into account when there are expressions available for the accelerating E-field. This Chapter deals with our implementation of an offset dipole B-field (Section 3.1.3) combined with an SG E-field (Breed et al., 2014).

In Section 4.1 we briefly describe the transformation, from the magnetic frame to the rotational frame, of the offset dipole B-field components (more details in Appendix A). In Section 4.2 we describe how we searched for the PC rim associated with this offset dipole field. The magnitude of the offset is determined by the parameter ϵ (Section 3.1.3). At first, the code (see Section 3.3) would only run for small values of ϵ (~ 0.05). In Section 4.2 we describe how we extended the range of ϵ, thereby allowing larger PC offsets. In Section 4.3 we specify expressions for an SG E-field parallel to the local B-field ($E_{\parallel,\mathrm{SG}}$), which are respectively valid at low and high-altitudes. These expressions have to be matched at some intermediate altitude $\eta_{\mathrm{c}}(P, \dot{P}, \alpha, \epsilon, \phi_{\mathrm{PC}}, \xi)$, which is necessary to determine the general $E_{\parallel,\mathrm{SG}}$ in the entire gap (Section 4.4). With the global solution of the E-field in hand, one can next solve the particle transport equation, assuming CR to be the dominant energy loss process, and determine whether particles reach the CRR limit (where the energy gain rate balances the loss rate; Section 4.5). We give a summary in Section 4.6.

4.1 Transformation of the magnetic field from the magnetic frame to the rotational frame

We implemented an offset dipole B-field for the symmetric case (where the PCs of both hemispheres are offset in the same direction with respect to the magnetic ($\boldsymbol{\mu}$) axis; see Section 3.1.3) in our geometric code (Section 3.3). Since the offset dipole field is given in terms of magnetic frame co-ordinates ($\hat{\mathbf{z}}' \parallel \boldsymbol{\mu}$; Harding & Muslimov, 2011b) it was necessary to transform this solution to the (corotating) rotational frame ($\hat{\mathbf{z}} \parallel \boldsymbol{\Omega}$, with $\boldsymbol{\Omega}$ the rotation axis). In order to do so, we first performed transformations between the spherical and Cartesian co-ordinates and bases, and then a rotation of the co-ordinate axes to move from the magnetic frame to the rotational frame. We lastly transformed the Cartesian co-ordinates of the position vector from the magnetic to the rotational frame. For a more detailed discussion, we refer the reader to Appendix A.

Consider a general B-field specified in the magnetic frame (indicated by the primed co-ordinates), in terms of spherical co-ordinates

$$\mathbf{B}'(r',\theta',\phi') = B'_r(r',\theta',\phi')\hat{\mathbf{r}}' + B'_\theta(r',\theta',\phi')\hat{\boldsymbol{\theta}}' + B'_\phi(r',\theta',\phi')\hat{\boldsymbol{\phi}}'. \tag{4.1}$$

This field may then be transformed to a Cartesian basis and co-ordinate system:

$$\mathbf{B}'(x',y',z') = B'_x(x',y',z')\hat{\mathbf{x}}' + B'_y(x',y',z')\hat{\mathbf{y}}' + B'_z(x',y',z')\hat{\mathbf{z}}'. \tag{4.2}$$

This is done using expressions that specify spherical unit vectors and co-ordinates in terms of Cartesian co-ordinates (see e.g., Griffiths, 1995). Next, one may rotate the B-field components (i.e., the Cartesian frame) through an angle $-\alpha$ (the angle between the $\boldsymbol{\Omega}$ and $\boldsymbol{\mu}$ axes), thereby transforming the B-field from the magnetic to the rotational frame (indicated by the unprimed co-ordinates).

$$\mathbf{B}(x',y',z') = B_x(x',y',z')\hat{\mathbf{x}}' + B_y(x',y',z')\hat{\mathbf{y}}' + B_z(x',y',z')\hat{\mathbf{z}}'. \tag{4.3}$$

Lastly, we transform the magnetic co-ordinates to rotational co-ordinates:

$$\mathbf{B}(x,y,z) = B_x(x,y,z)\hat{\mathbf{x}} + B_y(x,y,z)\hat{\mathbf{y}} + B_z(x,y,z)\hat{\mathbf{z}}. \tag{4.4}$$

4.2 Finding the PC rim and extending the range of ϵ

After initial implementation of the offset dipole field in the geometric code, we discovered that we could solve the PC rim (see Section 3.3.1; Dyks & Harding, 2004) in a similar manner as for the RVD B-field, but only for small values of the offset parameter ϵ ($\epsilon \lesssim 0.05 - 0.1$, depending on α). As illustrated in Figure 4.1, the code first selects a magnetic polar angle θ at some fixed magnetic azimuthal angle ϕ_1 and then traces the B-field line up to the light cylinder using a fourth-order integration routine. If the field line closes inside the light cylinder, e.g, the case of $\theta \approx \theta_{\rm out}$, the code chooses a smaller θ. If this new line closes outside of the light cylinder, e.g., the case of $\theta \approx \theta_{\rm in}$, the code chooses a larger θ. This process continues until a field line is found that closes near the light cylinder (within a specified tolerance, i.e., $\theta = \theta_{\rm centre}$ is found; Section 3.3.1). The code then stores that particular B-field footpoint position ($\theta_{\rm centre}$,ϕ_1). The code next chooses a new ϕ_2 and repeats the process until the PC rim has been defined. The magnetic structure at the light cylinder therefore determines the PC shape (Dyks & Harding, 2004).

We improved the range of ϵ by varying the colatitude parameters $\theta_{\rm in}$ and $\theta_{\rm out}$ which delimit a bracket ("solution space") in colatitude thought to contain the footpoint of last open field line (tangent to the light cylinder $R_{\rm LC}$). Figure 4.2 indicates the progressively larger range of ϵ that we were able to use upon decreasing $\theta_{\rm in}$ (for $\theta_{\rm out} = 2.0$, see Figure 4.2a) and increasing $\theta_{\rm out}$ (for $\theta_{\rm in} = 0.3$, see Figure 4.2b), i.e., increasing the colatitude bracket where solutions are searched for. We found a maximum $\epsilon = 0.18$ valid for the full range of α

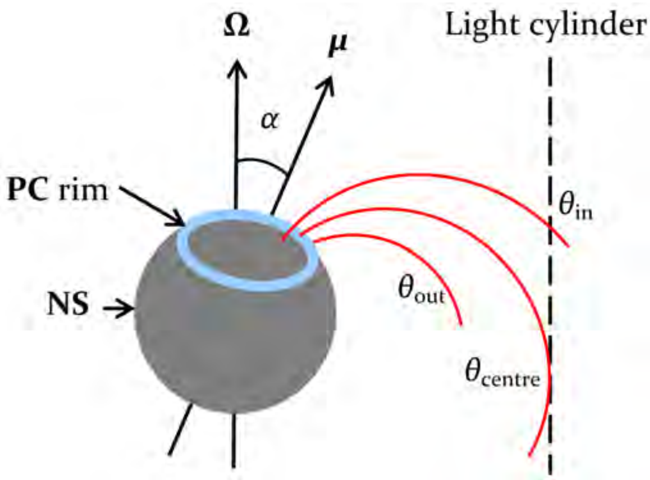

Figure 4.1: A colatitude bracket ($\theta_{\rm in}, \theta_{\rm out}$) delimiting the range in θ where the last open field line (at $\theta_{\rm centre}$) is found.

(see saturation lines in Figure 4.2). Choosing a maximal solution bracket in colatitude would in principle work, but the code would take much longer to find the PC rim compared to when a smaller bracket (that does contain the correct solution) is used. Therefore, we generalised the search for optimal $\theta_{\rm in}$ and found (by trail and error) that the following linear equation $\theta_{\rm in} = [(-31/18)\epsilon + 0.6]\theta_{\rm PC}$ involving parameter ϵ, for a fixed $\theta_{\rm out} = 2.0$, resulted in $\theta_{\rm in}$ that yielded maximum values for ϵ. From this equation follows that an increase in ϵ results in a decrease in $\theta_{\rm in}$. Thus, for each run of the code (see Chapter 6) for a certain set of parameters, the code searches for the correct $\theta_{\rm in}$ value to find the PC rim.

4.3 Incorporating the SG electric field

It is important to take the accelerating E-field into account (in a physical pulsar model) when such expressions are available, since this will modulate the emissivity ϵ_ν in the gap, as opposed to geometric models where we assume constant ϵ_ν per unit length in the corotating frame. For the offset dipole field we only considered the SG model, since there are no E-field expressions available for the OG model for this particular B-field.

For the SG case we implemented the full E-field in the rotational frame, corrected for general relativistic effects (e.g., Muslimov & Harding, 2003, 2004a), up to high altitudes. The SG $E_{\|}$-field solution at low altitudes in the offset dipole magnetosphere is given by (Harding, private communication)

$$\begin{aligned} E_{\|,\rm low} \quad &\approx \quad -3\mathcal{E}_0\nu_{\rm SG}x^a\Big\{\frac{\kappa}{\eta^4}e_{1\rm A}\cos\alpha + \frac{1}{4}\frac{\theta_{\rm PC}^{1+a}}{\eta}[e_{2\rm A}\cos\phi_{\rm PC} \\ &\quad + \frac{1}{4}\epsilon\kappa e_{3\rm A}(2\cos\phi_0' - \cos(2\phi_{\rm PC} - \phi_0'))]\sin\alpha\Big\}(1-\xi_*^2), \end{aligned} \tag{4.5}$$

with $\mathcal{E}_0 = (\Omega R/c)^2(B_r/B)B_0$, B_0 the surface B-field, $\nu_{\rm SG} \equiv (1/4)\Delta\xi_{\rm SG}^2$, $\Delta\xi_{\rm SG}$ the colatitudinal gap width in units of dimensionless colatitude $\xi = \theta/\theta_{\rm PC}$, $\theta_{\rm PC}$ the standard PC angle, $x = r/R_{\rm LC}$ the normalised radial distance in units of $R_{\rm LC} = c/\Omega$, Ω the angular speed, c the speed of light, $a = \epsilon\cos(\phi' - \phi_0')$ the effective

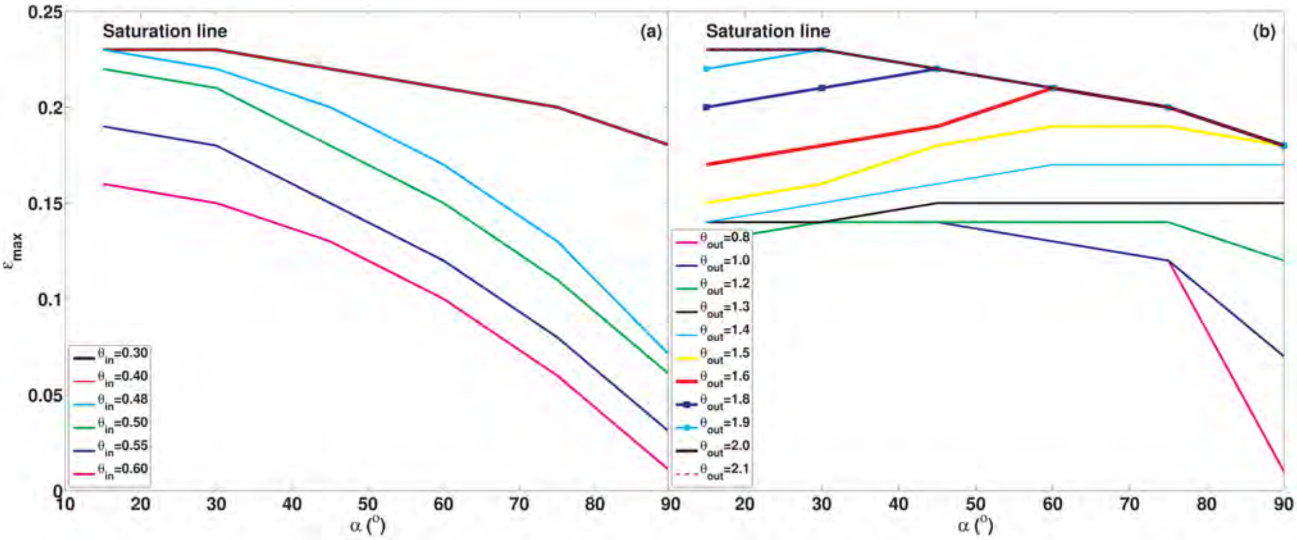

Figure 4.2: Plots illustrating the maximum offset parameter $\epsilon_{\rm max}$ as a function of α for which the PC rim may be found. In (a) and (b) the colours represent different colatitude values ($\theta_{\rm in}$,$\theta_{\rm out}$) in units of PC angle $\theta_{\rm PC} \approx \sqrt{R/R_{\rm LC}}$ (with R the stellar radius). There is a notable decrease in $\epsilon_{\rm max}$ for larger α. The saturation lines represent the maximum offset parameter $\epsilon_{\rm max}$ obtained as a function of α. In (a) a smaller $\theta_{\rm in}$, for a fixed $\theta_{\rm out} = 2.0\theta_{\rm PC}$, results in larger $\epsilon_{\rm max}$ values. In (b) a larger $\theta_{\rm out}$, for a fixed $\theta_{\rm in} = 0.3\theta_{\rm PC}$, also results in larger $\epsilon_{\rm max}$.

offset of the PC in the $x-z$ plane, $\phi' = \arctan(y'/x')$ the magnetic azimuthal angle used when transforming the B-field (Section 4.1), ϕ'_0 the magnetic azimuthal angle defining the plane in which the PC offset occurs (we choose $\phi'_0 = 0$ in what follows), $\kappa \approx 0.15 I_{45}/R_6^3$ a general relativistic compactness parameter characterising the frame-dragging effect near the stellar surface (Muslimov & Harding, 1997), $I_{45} = I/10^{45}$ g cm^2, I the moment of inertia, $R_6 = R/10^6$ cm, $\eta = r/R$ the dimensionless radial co-ordinate in units of stellar radius R, $e_{1\rm A} = 1 + a(\eta^3 - 1)/3$, $e_{2\rm A} = (1+3a)\eta^{(1+a)/2} - 2a$, $\phi_{\rm PC}$ the magnetic azimuthal angle defined for usage with the E-field, being π out of phase with ϕ' (one chooses the negative x-axis towards $\mathbf{\Omega}$ to coincide with $\phi_{\rm PC} = 0$, labelling the "favourably curved" B-field lines), $e_{3\rm A} = (5-3a)/(\eta^{(5-a)/2} + 2a)$, ξ_* the dimensionless colatitude of the gap field lines (defined such that $\xi_* = 0$ corresponds to the field line in the middle of the gap and $\xi_* = 1$ at the boundaries; Muslimov & Harding, 2003). We approximate the high-altitude SG E-field by (Muslimov & Harding, 2004a)

$$E_{\parallel,\rm high} \approx -\frac{3}{8}\left(\frac{\Omega R}{c}\right)^3 \frac{B_0}{f(1)}\nu_{\rm SG}x^a\left\{\left[1+\frac{1}{3}\kappa\left(5-\frac{8}{\eta_{\rm c}^3}\right)+2\frac{\eta}{\eta_{\rm LC}}\right]\cos\alpha + \frac{3}{2}\theta_{\rm PC}H(1)\sin\alpha\cos\phi_{\rm PC}\right\}(1-\xi_*^2), \quad (4.6)$$

with $f(\eta) \sim 1 + 0.75x + 0.6x^2$ a general relativistic correction factor of order 1 for the dipole component of the magnetic flux through the magnetic hemisphere of radius r in a Schwarzchild metric, $x = \epsilon_{\rm g}/\eta$, $\epsilon_{\rm g} = r_{\rm g}/R$, $r_{\rm g}$ the gravitational radius of the NS, $\eta_{\rm c} = r_{\rm c}/R$ the critical scaled radius where the high-altitude and low-altitude E-field solutions are matched, $\eta_{\rm LC} = R_{\rm LC}/R$, and $H(\eta) \sim 1 - 0.25x - 0.16x^2 - 0.5(\kappa/\epsilon_{\rm g}^3)x^3(1 - 0.25x - 0.21x^2)$ is a general relativistic correction factor of order 1. The factors $f(\eta)$ and $H(\eta)$ account for the static part of the curved spacetime metric and have a value of 1 in flat space (Muslimov & Harding, 1997). This high-altitude solution (excluding the factor x^a) is actually valid for the SG model assuming a static (non-offset) dipole field; we therefore scaled the E-field by a factor x^a to generalise this expression for the offset dipole field. The general E-field valid from R to $R_{\rm LC}$ (i.e., over the entire length of the gap) is constructed as follows (see Eq. [59] of Muslimov & Harding, 2004a)

$$E_{\|,\rm SG} \simeq E_{\|,\rm low} \exp\left(\frac{-(\eta - 1)}{(\eta_{\rm c} - 1)}\right) + E_{\|,\rm high}. \tag{4.7}$$

A more detailed discussion of the electrodynamics in the SG geometry may be found in Muslimov & Harding (2003) and Muslimov & Harding (2004a). In the next section, we solve for $\eta_{\rm c}(P, \dot{P}, \alpha, \epsilon, \xi, \phi_{\rm PC})$.

4.4 Determining the matching parameter $\eta_{\rm c}$

As noted in Section 4.3, we used analytic expressions for a low-altitude and high-altitude SG E-field in an offset dipole magnetic geometry. These are matched at a critical scaled radius $\eta_{\rm c} = r_{\rm c}/R$ to obtain a general E-field valid for all altitudes (Eq. [4.7]). At first, we set $\eta_{\rm c} = 1.4$ for simplicity (Breed et al., 2014), however we realized that $\eta_{\rm c}$ may strongly vary for different parameters. Thus, we had to solve $\eta_{\rm c}(P, \dot{P}, \alpha, \epsilon, \xi, \phi_{\rm PC})$ on each field line. In what follows we consider electrons to be the radiating particles, and our discussion will therefore generally deal with the negative of the E-field.

We solved for the matching parameter in the following way. First, we calculated $E_{\|,\rm low}$, which is independent of $\eta_{\rm c}$, along the B-field (since particle orbits approximately coincide with the B-field lines, it is important to consider the behaviour of the E-field as a function of arclength s rather than η). If $-E_{\|,\rm low} < 0$ for all η, it will never intersect with $E_{\|,\rm high}$ and we set $\eta_{\rm c} = 1.1$, thereby basically using $E_{\|,\rm SG} \approx E_{\|,\rm high}$. Second, we stepped through $\eta_{\rm c}$ (in the range $1.1 - 5.1$), calculating $E_{\|,\rm SG}$ and $E_{\|,\rm high}$ as well as their ratio $S_i = S(\eta_i)$ at $i = 1, .., N$ different radii η_i. If $S_i > 1$ we used $1/S_i$. We next calculated a test statistic $T(\eta_{\rm c}) = \sum_i^N (S_i - 1)^2/N$ using only E-field values where $-E_{\|,\rm low} > -E_{\|,\rm high}$ (i.e., we basically fit $E_{\|,\rm SG}$ to $E_{\|,\rm low}$ when $-E_{\|,\rm low} > -E_{\|,\rm high}$). We then minimised T to find the optimal $\eta_{\rm c}$ (similar to what was done in Figure 2 of Venter et al., 2009). In Figure 4.3a, the intersection radius $\eta_{\rm cut} > \eta_{\rm LC}$ (i.e., $E_{\|,\rm low}$ and $E_{\|,\rm high}$ do not intersect within the light cylinder) and therefore we imposed the restriction that the solution of $\eta_{\rm c}$ should lie below 5.1. When $-E_{\|,\rm low}$ did not decrease as rapidly (e.g., as in Figure 4.3b) we found reasonable solutions (Figure 4.3b). We noted that $E_{\|,\rm SG}$ produced a bump when $-E_{\|,\rm low}$ decreased more rapidly. To circumvent this problem we tested whether $-E_{\|,\rm SG} < -E_{\|,\rm high}$ and in this case we used the intersection radius $\eta_{\rm cut}$ of $E_{\|,\rm low}$ and $E_{\|,\rm high}$, rather than $\eta_{\rm c}$, to match our solutions (see Figure 4.3c). We lastly observed that for $\phi_{\rm PC} = \pi$ (on "unfavourably curved" field lines) for larger α the magnitude of $-E_{\|,\rm low}$ field changes sign, resulting in a small $\eta_{\rm c} = \eta_{\rm cut} = 1.7$ value (Figure 4.3d).

In Figure 4.4 we give the reader a broader perspective on our matching solutions. In this figure we present contours for our solution of $\eta_{\rm c}$ on a $(\xi, \phi_{\rm PC})$-grid (the latter in radians). These contours are for the following parameters: $P = 0.0893$ s, $B_0 = 1.05 \times 10^{13}$ G, $I = 0.4MR^2 = 1.14 \times 10^{45}$ g cm^2, $\alpha \in [0°, 90°]$ with 5° resolution, and $\epsilon = 0$. In each case the colour bar represents $\eta_{\rm c} = 1.1 - 5.1$, with 1.0 corresponding to the NS surface and 5.1 to the limit we placed on $\eta_{\rm c}$ when $\eta_{\rm cut}$ becomes too large. For the case of $\alpha = 0°$ nearly all $\eta_{\rm c} \approx 5.1$, except at the SG boundary where $E_{\|,\rm SG} = 0$ and therefore at values of $\xi = [0.95, 1.0]$ we set $\eta_{\rm c} \approx 1.1$. In this case, all the field lines are "favourably curved", and only the first term in the E-field $\propto \cos\alpha$ (Eq. [4.5] and [4.6]) contributes to the radiation. In the $\alpha = 5°$ contour, one can see a small contribution of the second

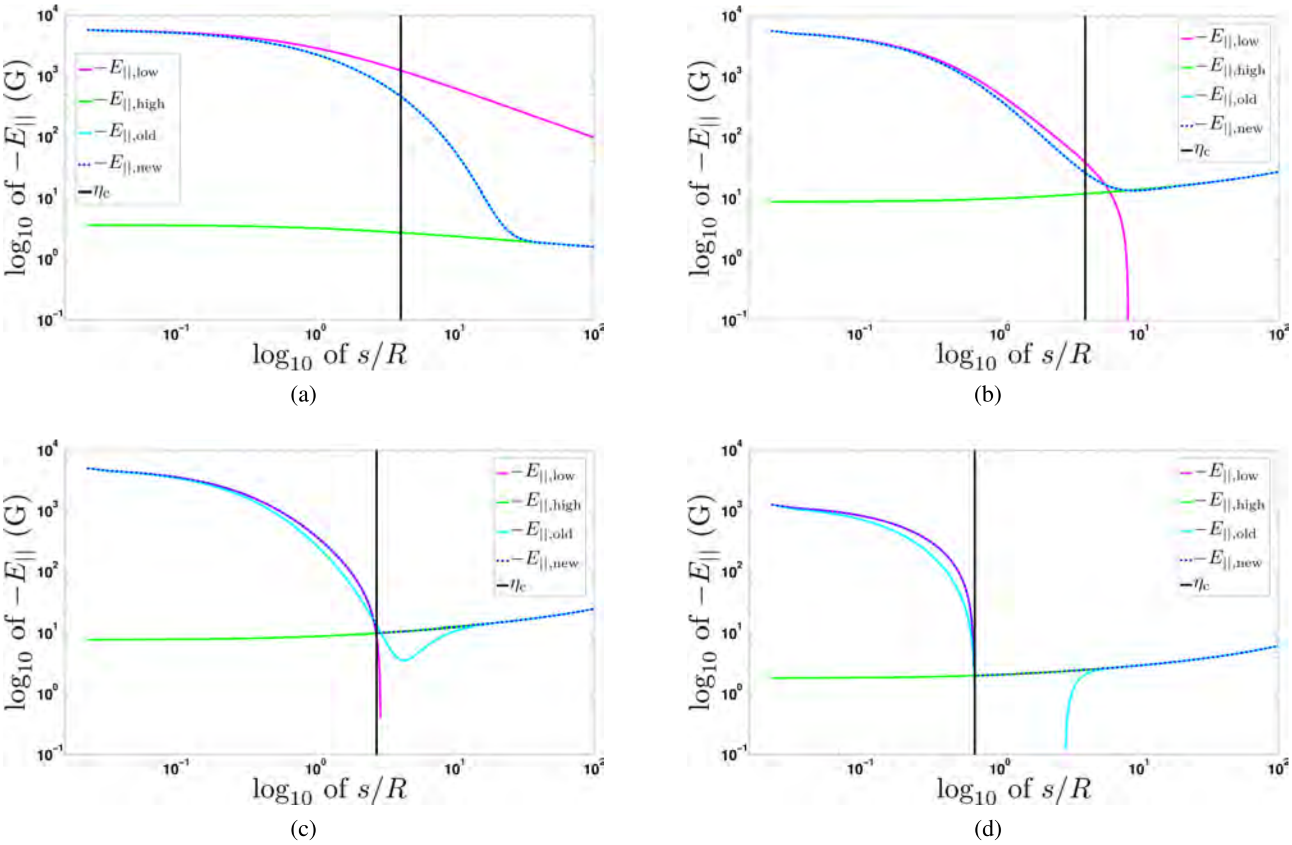

Figure 4.3: Examples of the general SG E-field ($E_{||,\mathrm{new}}$, dashed dark blue line) we obtained by matching the $E_{||,\mathrm{low}}$ (magenta line) and $E_{||,\mathrm{high}}$ (green line). We plotted the various E-fields as functions of the normalised arclength s along the B-field lines, in units of R. We indicated the matching parameter η_c (vertical black line) by using $s_c/R = \eta_c - 1$ (which is valid for low altitudes). These plots were obtained for the following parameters: $P = 0.0893$ s, $B_0 = 1.05 \times 10^{13}$ G, $R = 10^6$ cm, $M = 1.4M_\odot$, $\epsilon = 0.18$, and $\xi = 0.975$ (i.e., $\xi_* = 0$). In (a) we chose $\alpha = 90^\circ$, $\phi_{\mathrm{PC}} = 0$ radians. Here we use $\eta_c = 5.1$ since $\eta_{\mathrm{cut}} > \eta_{\mathrm{LC}}$. In (b) we chose $\alpha = 15^\circ$, $\phi_{\mathrm{PC}} = \pi$. We find a solution of $\eta_c = 5.1$. In (c) we chose $\alpha = 30^\circ$, $\phi_{\mathrm{PC}} = \pi$. If $-E_{||,\mathrm{low}}$ as well as $-E_{||,\mathrm{old}}$ (as defined in Eq. (4.7), light blue) are below $-E_{||,\mathrm{high}}$ beyond some radius η, we use η_{cut} (in this case $\eta_c = \eta_{\mathrm{cut}} = 3.7$) to match $E_{||,\mathrm{low}}$ and $E_{||,\mathrm{high}}$, resulting in the $-E_{||,\mathrm{new}}$ (dashed dark blue). In (d) we chose $\alpha = 75^\circ$, $\phi_{\mathrm{PC}} = \pi$. For large α we observe that $-E_{||,\mathrm{low}}$ changes sign over a small η range. In this case we also use $\eta_c = \eta_{\mathrm{cut}} = 1.7$ to match the solutions.

term $\propto \sin\alpha\cos\phi_{\mathrm{PC}}$. At $\phi_{\mathrm{PC}} \simeq \pi$, this term is negative, decreasing $-E_{||,\mathrm{low}}$ (as η increases) and resulting in smaller η_c with values ~ 3.5. However, at $\phi_{\mathrm{PC}} = 0$ the second term is positive and result in large η_c values of ~ 5.1 As α increases, the second term's contribution becomes larger and thus the solutions for $\eta_c = 5.1$ stay the same for $\phi_{\mathrm{PC}} \simeq 0$ (on "favourably curved" field lines), but become consistently smaller for $\phi_{\mathrm{PC}} \simeq \pi$ ("unfavourably curved" field lines). For the cases of $\alpha \approx 90^\circ$ the second term dominates the first term, and leads to regions where $-E_{||,\mathrm{SG}} < 0$ for all η values due to ρ_{GJ} that becomes positive. We ignored the B-field lines in the geometric code for these cases since we assume that only electrons emit radiation and that the other particles, possibly iron nuclei from the stellar surface, do not emit any radiation. For plotting purposes we set $\eta_c = 11$ (with no significant meaning for the number 11) to represent such ignored field lines, as indicated by the black region on the contours.

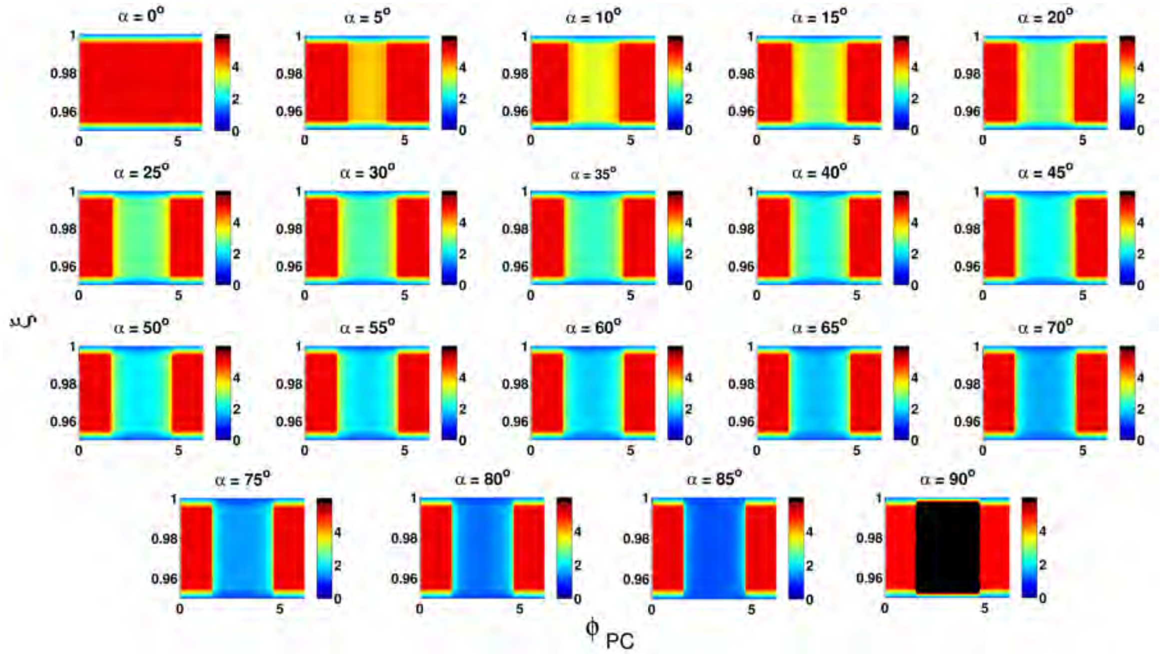

Figure 4.4: Contour plots for our solution of η_c for $P = 0.0893$ s, $B_0 = 1.05\times10^{13}$ G, $I = 0.4MR^2 = 1.14\times10^{45}$ g cm^2, $\alpha \in [0°, 90°]$ with 5° resolution, $\epsilon = 0$, and $\phi'_0 = 0$. In each case ξ and ϕ_{PC} (in radians) represent the scaled colatitudinal and azimuthal magnetic co-ordinates, with the negative x'-axis ($\phi_{PC} = 0$) directed toward the $\mathbf{\Omega}$-axis. The colour bar represents our η_c solutions ranging between $1.1 - 5.1$, with 1.0 corresponding to the NS surface and 5.1 to our limit for η_c when η_{cut} becomes too large. As α increases the second term in E-field expressions start to dominate and the solutions for η_c become larger for $\phi_{PC} = 0$ ("favourably curved" field lines), and smaller for $\phi_{PC} = \pi$ ("unfavourably curved" field lines) until no solutions are found (e.g., the black regions where the $-E_{||,SG}$ becomes negative).

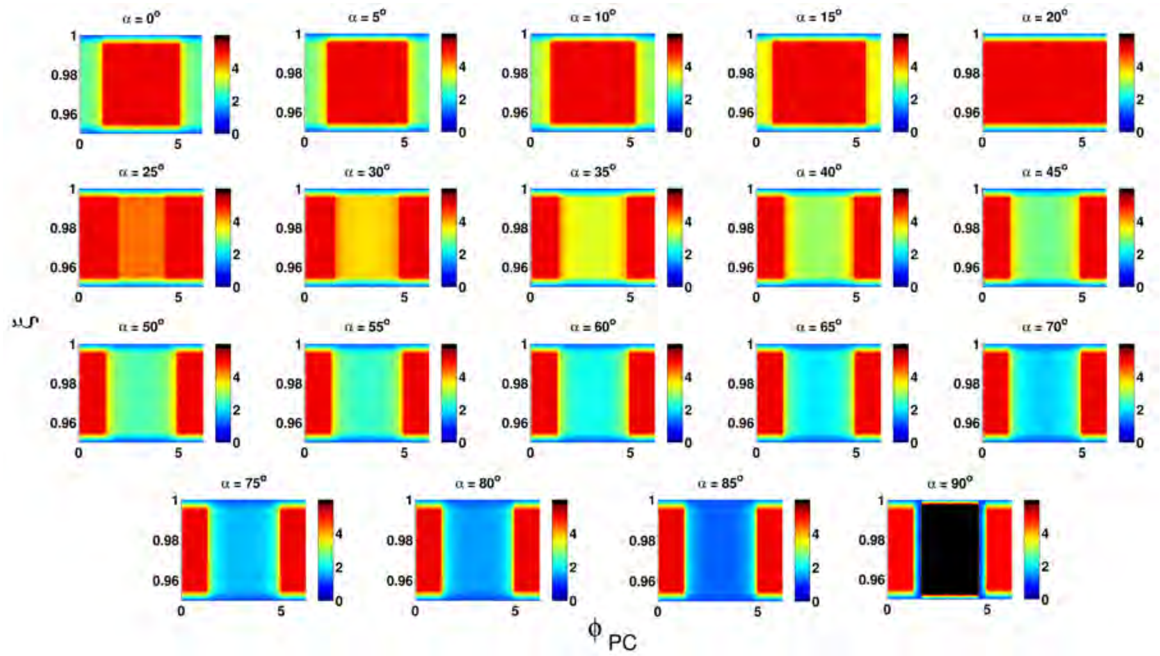

Figure 4.5: Contour plots for our solution of η_c, similar to Figure 4.4 but for $\epsilon = 0.18$.

In Figure 4.5 we present η_c contours for the same parameters as in Figure 4.4, but for an offset $\epsilon = 0.18$. Since the E-field solutions have an $x^a = x^{[\epsilon\cos(\phi'-\phi_0')]} = x^{[-\epsilon\cos\phi_{\rm PC}]}$ factor dependence, a larger offset results in different matching contours than for $\epsilon = 0$. In the case of $\alpha = 0$, the first term $\propto \cos\alpha$ is the only contribution to the E-field, with the factor $x^a e_{1\rm A}$ (with an ϵ dependence) being initially larger at low η for $\phi_{\rm PC} = 0$ than for $\phi_{\rm PC} = \pi$ (x^a dominates), but rapidly decreasing with η ($e_{1\rm A}$ dominates), leading to a lower value of η_c for $\phi_{\rm PC} = 0$. One should therefore note that the magnitude of one instance of the E-field with low η_c may initially be higher than another instance with high η_c, but the first will decrease rapidly with η and eventually become lower than the second. For a slightly larger α the second term in Eq. (4.5) and (4.6), starts to contribute to the radiation. This is due to the $\sin\alpha$ term with an ϵ dependence that delivers an extra contribution which were zero in the case for $\epsilon = 0$. At $\alpha = 20°$ the effects of the first and second terms seem to balance each other and therefore we find the same solution of $\eta_c = 5.1$ everywhere except on the SG model boundary where $\eta_c = 1.1$, just as in the case of $\epsilon = 0$ and $\alpha = 0°$. For values of $\alpha > 20°$ the second term $\sim \cos\phi_{\rm PC}$ starts to dominate and thus we find solutions of $\eta_c \sim 5.1$ for $\phi_{\rm PC} \simeq 0$ and systematically smaller solutions for $\phi_{\rm PC} \simeq \pi$ as α increases and the second term $\propto \sin\alpha$ becomes increasingly important, as in Figure 4.4. At $\alpha = 90°$ we obtain the same solution as in Figure 4.4 where the second term dominates (for this case $-E_{\|,\rm SG} < 0$ for all η, since $\rho_{\rm GJ}$ becomes positive). We note that the η_c-distribution reflects two symmetries (about $\phi_{\rm PC} = \pi$ and $\xi = 0.975$, i.e., $\xi_* = 0$, given our gap boundaries at $\xi \in [0.95, 1.0]$): that of the $\cos\phi_{\rm PC}$ term and that of the $(1-\xi_*^2)$ term in the $E_\|$ solutions.

Once we solved η_c, we could calculate the general E-field in order to solve the particle transport equation to obtain the particle Lorentz factor γ_e, necessary for determining the CR emissivity. Below we also discuss the behaviour of our newly matched E-field as a function of arclength along the B-field lines in more detail.

4.5 Solving the particle transport equation

Using the general E-field we found by matching the low-altitude and high-altitude solutions as explained above, we next solved the particle transport equation (Breed et al., 2014)

$$\dot{\gamma} = \dot{\gamma}_{\rm gain} + \dot{\gamma}_{\rm loss} = \frac{eE_{\|,\rm total}}{mc} - \frac{2e^2\gamma_e^4}{3\rho_{\rm curv}^2 mc} = \frac{1}{mc^2}\left[ceE_{\|,\rm total} - \frac{2ce^2\gamma_e^4}{3\rho_{\rm curv}^2}\right], \tag{4.8}$$

to obtain the particle Lorentz factor $\gamma_e(\eta, \phi, \xi_*)$, taking only CR losses into account. Radiation reaction occurs when the energy gain balances the losses and $\dot{\gamma} = 0$. In Figure 4.6 we plot the $\log_{10}$ of the high-altitude $-E_{\|,\rm high}$ (solid cyan line), low-altitude $-E_{\|,\rm low}$ (solid blue line), general $-E_{\|,\rm SG}$-field before matching ($-E_{\|,\rm old}$, solid green line) and after matching ($-E_{\|,\rm new}$, dashed red line), gain (acceleration) rate $\dot{\gamma}_{\rm gain}$ (solid yellow line), loss rate $\dot{\gamma}_{\rm loss}$ (solid magenta line), and the Lorentz factor γ_e (solid black line) as a function of arclength s/R. For each case we represent $\epsilon = 0$ (thick lines) and $\epsilon = 0.18$ (thin lines) on the same plot. We note that the values for $\phi_{\rm PC}$ appearing on the figure are actually values on the stellar surface; these may change along the B-field lines.

In Figure 4.6, we set $\alpha = 0°$ so that only the first term in Eq. (4.5) and (4.6) contributes. In this case, $-E_{\|,\rm low} \propto x^a[1 + a(\eta^3 - 1)/3]$, where $a = -\epsilon\cos\phi_{\rm PC}$. The sign of x^a stays the same but at small values of η, $x^a \approx 3$ for $\phi_{\rm PC} = 0$ and $x^a \approx 1/3$ for $\phi_{\rm PC} = \pi$. This explains why $-E_{\|,\rm low}$ is higher for $\phi_{\rm PC} = 0$ than for $\phi_{\rm PC} = \pi$ (for $\epsilon \neq 0$) at low η. In the case of $\phi_{\rm PC} = \pi/2$, $a = 0$ and the values of $E_{\|,\rm low}$ are very nearly the same for both

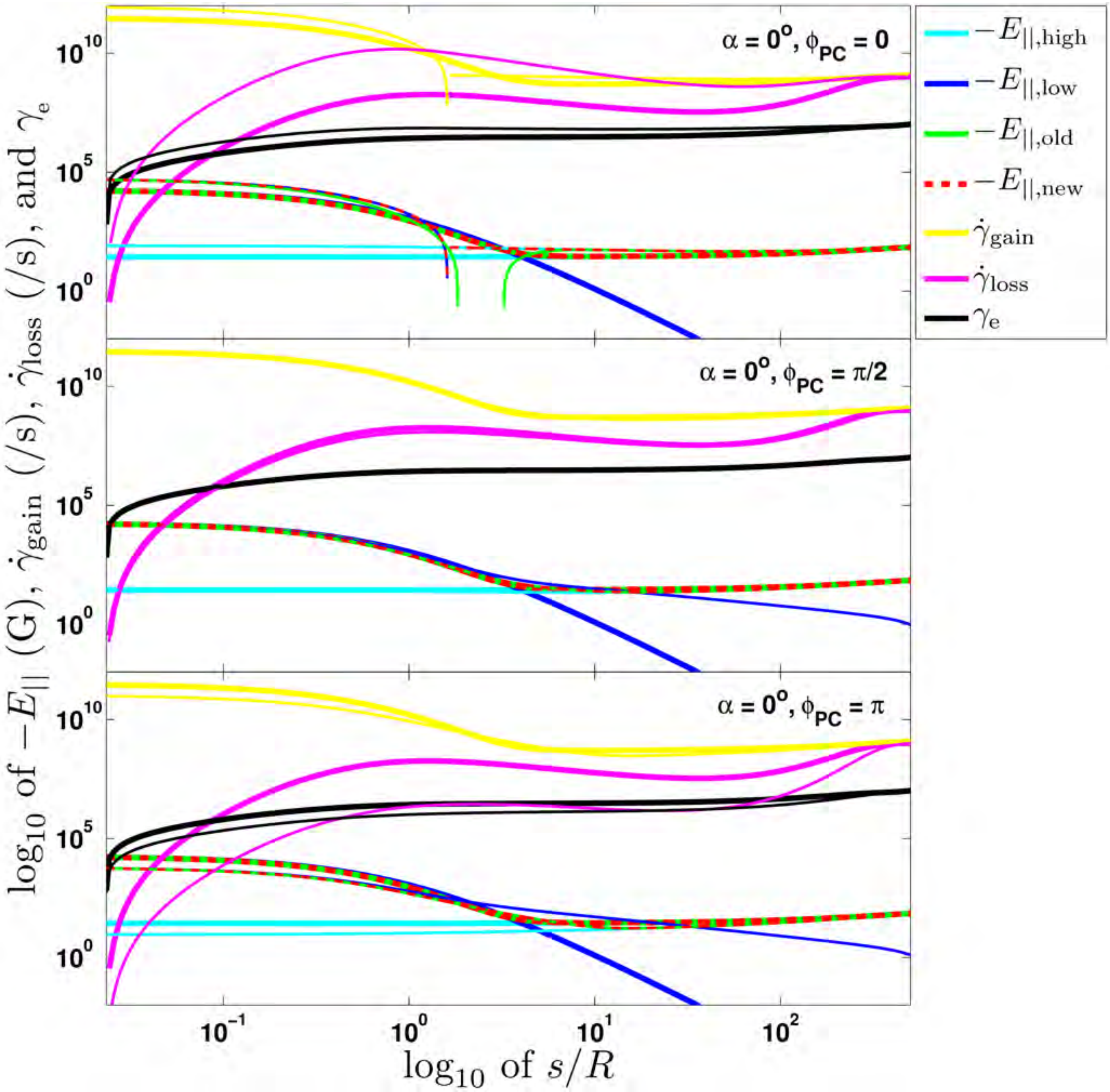

Figure 4.6: Plot of $\log_{10}$ of $-E_{||,\mathrm{high}}$ (solid cyan line), $-E_{||,\mathrm{low}}$ (solid blue line), $-E_{||,\mathrm{SG}}$ before matching ($-E_{||,\mathrm{old}}$, solid green line) and after matching ($-E_{||,\mathrm{new}}$, dashed red line), gain (acceleration) rate $\dot{\gamma}_{\mathrm{gain}}$ (solid yellow line), loss rate $\dot{\gamma}_{\mathrm{loss}}$ (solid magenta line), and the Lorentz factor γ_e (solid black line) as a function of arclength s/R. In each case we used $P = 0.0893$ s, $B_0 = 1.05 \times 10^{13}$ G (corrected for general relativistic effects), $I = 0.4MR^2 = 1.14 \times 10^{45}$ g cm^2, $\alpha = 0°$, and $\xi = 0.975$ (i.e., $\xi_* = 0$). On each panel we represent the curves for $\epsilon = 0$ (thick lines) and $\epsilon = 0.18$ (thin lines). The top panel is for "favourably curved" field lines for $\phi_{\mathrm{PC}} = 0$, the middle panel for $\phi_{\mathrm{PC}} = \pi/2$, and the bottom panel for "unfavourably curved" field lines for $\phi_{\mathrm{PC}} = \pi$. These choices reflect the values of ϕ_{PC} at the stellar surface; they may change as the particle moves along the B-field line, since $B_\phi \neq 0$.

$\epsilon = 0$ and $\epsilon \neq 0$, the only difference stemming from the B-field structure that enters into Eq. (4.5) through $\mathcal{E}_0$. The low-altitude E-field is therefore enhanced in the direction of the "favourably curved" B-field lines. The term $[1 + a(\eta^3 - 1)/3]$ changes sign beyond some η for $\phi_{\rm PC} = 0$, explaining the behaviour of $-E_{||,\rm low}$ beyond $s \approx 2R$. This effect is also noticeable in Figure 4.5 for $\alpha \approx 0°$, where smaller values of the matching altitude $\eta_{\rm c}$ are found for $\phi_{\rm PC} = 0$ or $\phi_{\rm PC} = 2\pi$. This is contrary to the case of $\phi_{\rm PC} = \pi$ where the sign stays the same for all η. Correspondingly, $\eta_{\rm c} \approx 5$ around $\phi_{\rm PC} \neq 0$ in Figure 4.5 for $\alpha \approx 0°$. For $-E_{||,\rm high} \propto x^a[1 + 2\eta/\eta_{\rm LC}]$, we note that for $\phi_{\rm PC} = (0, \pi/2, \pi)$, $x^a = (3 \to 1, 1 \to 1, 1/3 \to 1)$ (for $\epsilon \neq 0$, otherwise $x^a = 1$) while $[1 + 2\eta/\eta_{\rm LC}] = 1 \to 3$, with the number to the left of $\to$ valid for $\eta \ll 1$ and the number to the right of $\to$ valid for $\eta \gg 1$. The combined effect of these two terms is such that $-E_{||,\rm high} = (3 \to 3, 1 \to 3, 1/3 \to 3)$ for $\phi_{\rm PC} = (0, \pi/2, \pi)$ and $\epsilon \neq 0$, and $-E_{||,\rm high} = 1 \to 3$ for $\epsilon = 0$, for all $\phi_{\rm PC}$. Therefore the high-altitude E-field is again enhanced in the direction of the "favourably curved" B-field lines at low values of η, coinciding at high η for the different $\phi_{\rm PC}$. It follows that $\dot{\gamma}_{\rm gain}$, γ_e, and $\dot{\gamma}_{\rm loss}$ are higher for $\phi_{\rm PC} = 0$ and $\epsilon \neq 0$, and lower for $\phi_{\rm PC} = \pi$. We note that $E_{||,\rm high}$ is not so strongly dependent on η as $E_{||,\rm low}$. There is no effect in changing $\phi_{\rm PC}$ in the case of $\alpha = 0°$ and $\epsilon = 0$, since the first term is not dependent on $\phi_{\rm PC}$.

In Figure 4.7, $\alpha = 45°$ so that the second term in $-E_{||,\rm low}$ starts to contribute. At low η the first term still dominates, but the second term starts to dominate beyond $\eta \sim 1.5$. This effect is less prominent for $-E_{||,\rm high}$, given the additional multiplicative factor $\theta_{\rm PC} \ll 1$ in the second term. We therefore note the same behaviour for $-E_{||,\rm low}$ and $-E_{||,\rm high}$ at low η as before: the E-fields are higher for $\phi_{\rm PC} = 0$ than for $\phi_{\rm PC} = \pi$ (for $\epsilon \neq 0$), but they nearly coincide at $\phi_{\rm PC} = \pi/2$ for $\epsilon \neq 0$ and $\epsilon = 0$. At higher η, the first term of $-E_{||,\rm low}$ changes sign abruptly as η increases but this is counteracted by the fact that the second term changes much slower with η. The net effect is that $-E_{||,\rm low}$ does not change sign as η is increased for $\phi_{\rm PC} = 0$. We notice the change in sign of $-E_{||,\rm low}$ for $\phi_{\rm PC} = \pi/2$ and $\epsilon \neq 0$ is due to the non-zero B_ϕ component in this case. When $\phi_{\rm PC} = \pi$ the second term of $-E_{||,\rm low}$ is always negative (since $\cos\phi_{\rm PC} = -1$), forcing this E-field to change sign close to the stellar surface. Although the second term of $-E_{||,\rm high}$ is also negative for all η, its magnitude is too small to counteract the dominant first term such that $-E_{||,\rm high}$ does not change sign with an increase in η.

In Figure 4.8, we note that $-E_{||,\rm high}$ displays the same behaviour at low η as previously: for $\phi_{\rm PC} = 0$, $-E^{\epsilon\neq 0}_{||,\rm high} > -E^{\epsilon=0}_{||,\rm high}$; these are the same for $\phi_{\rm PC} = \pi/2$, and $-E^{\epsilon\neq 0}_{||,\rm high} < -E^{\epsilon=0}_{||,\rm high}$ for $\phi_{\rm PC} = \pi$. For $\phi_{\rm PC} = \pi/2$, the first term of $-E_{||,\rm high}$ dominates the second, and for $\phi_{\rm PC} = \pi$, the second term of $-E_{||,\rm high}$ is always negative, but the positive first term dominates and therefore $-E_{||,\rm high}$ does not change sign as η increases. Similar behaviour is seen for $-E_{||,\rm low}$ (boosted for non-zero ϵ and $\phi_{\rm PC} = 0$). However, for $\phi_{\rm PC} = \pi$, $-E^{\epsilon\neq 0}_{||,\rm low}$ is not smaller than $-E^{\epsilon=0}_{||,\rm low}$ at low η. In this case the second term of $-E_{||,\rm low}$ is always negative, and the sum of the two terms are very close for both $\epsilon \neq 0$ and $\epsilon = 0$ so that $-E^{\epsilon\neq 0}_{||,\rm low} \approx -E^{\epsilon=0}_{||,\rm low}$. Since $\alpha \approx 90°$ the second term of $-E_{||,\rm low} \sim x^a \cos\phi_{\rm PC}$ is comparable to the first at low η, but quickly dominates as η increases (for $\phi_{\rm PC} = 0$). The second term of $-E_{||,\rm low}$ remains positive so that we find $\eta_{\rm c} = 5.1$ in this case (compare Figure 4.4 and 4.5). For $\phi_{\rm PC} = \pi/2$ the first and second terms are positive for all η and comparable in magnitude for $-E_{||,\rm low}$ so that the sign change in the case of $\epsilon \neq 0$ may be ascribed to the structure of the offset dipole B-field ($\phi_{\rm PC}$ increases along the field line so that $\cos\phi_{\rm PC}$ becomes negative). For $\phi_{\rm PC} = \pi$, the second term of $-E_{||,\rm low}$ is negative, forcing this field to change sign almost immediately (it takes slightly longer when $\epsilon \neq 0$). The fact that $-E_{||,\rm high}$ is positive leads to a "recovery" of the total E-field, so that it becomes positive again at larger η.

We note that when an electron encounters a positive E-field ($-E_{||} < 0$ for $\alpha \approx 90°$ and $\phi_{\rm PC} \approx \pi$) at some

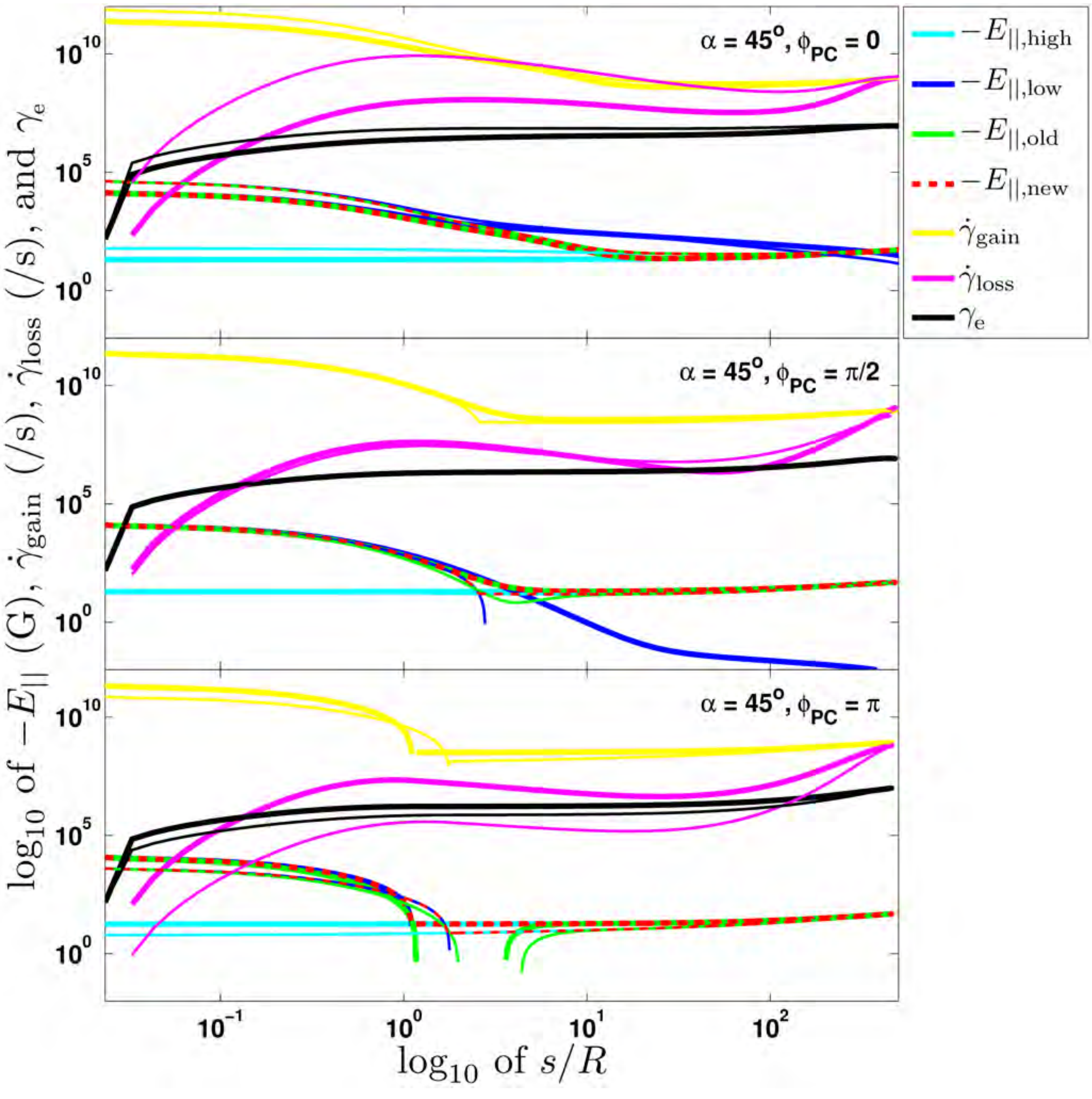

Figure 4.7: Same as Figure 4.6 but for α = 45°.

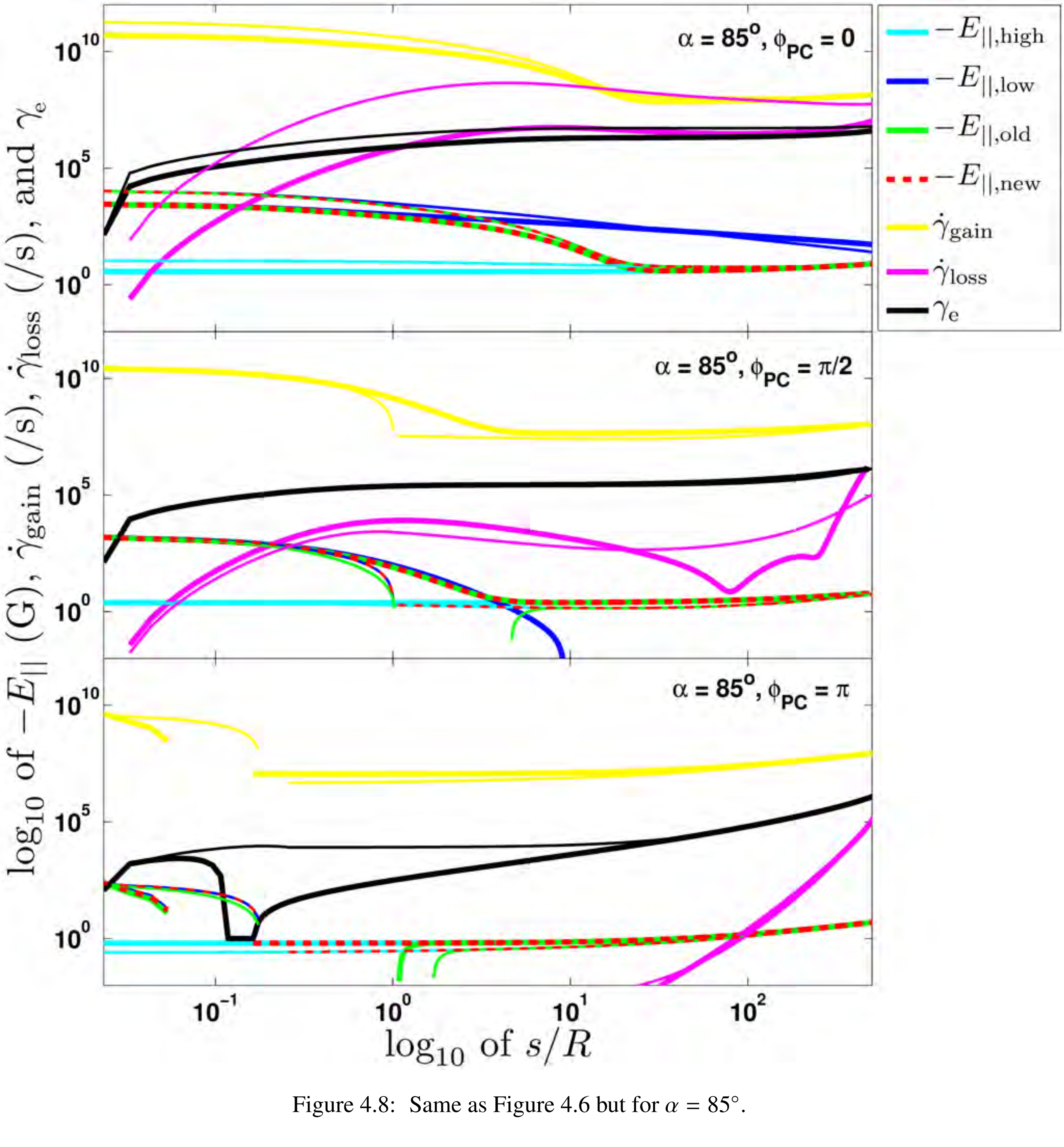

Figure 4.8: Same as Figure 4.6 but for α = 85°.

η, it may stop and turn around, encountering an E-field of opposite sign closer to the star. This should lead to oscillatory motion, violating the steady-state assumption of the model. Such motion should furthermore lead to a build-up of charge, which should screen the local E-field, removing the impediment (positive E-field) to the outflowing electron motion, so that these particles may "coast" along the field line to regions where $-E_{||} > 0$ and further acceleration may take place. We have therefore treated such cases by requiring that the Lorentz factor does not decrease to an unphysical value $\gamma_e < 1$; see the plateau formed by γ_e vs. s/R when $\epsilon = 0$ (thick black line) in the last panel of Figure 4.8.

As mentioned above the sign of $\rho_{\rm GJ}$ changes near $\alpha \approx 90^\circ$ and $\phi_{\rm PC} \approx \pi$, and we ignored such B-field lines when calculating the emission from the pulsar. This is also the reason why our plots of γ_e vs. s/R only go up to $\alpha = 85^\circ$, since we only consider electrons to be emitters of HE γ-rays in our model.

We lastly notice that the CRR limit is in fact reached in some cases (the yellow and magenta lines reach the same value): e.g., beyond $\eta \approx 0.7R_{\rm LC}$ for $\phi_{\rm PC} = 0$ and $\alpha = 0^\circ$, and beyond $\eta \approx R_{\rm LC}$ for $\phi_{\rm PC} = 0$ and $\alpha = 45^\circ$. The notable exception occurs at large α where the first term of the E-field becomes lower and the second term plays a larger role, leading to smaller gain rates and therefore smaller Lorentz factors. We note the importance of actually solving $\eta_{\rm c}$ on each B-field line. Previously when we set $\eta_{\rm c} = 1.4$ for all cases the particles did not attain the CRR limit. Only when we allowed larger values of $\eta_{\rm c}$ was $-E_{||,\rm low}$ boosted and did we find particles reaching the CRR limit in many more cases. The relatively low SG E-field leads to small caustics on the phase plots constructed for photon energies > 100 MeV (see Section 6.1.5). We expect that a higher E-field should lead to extended caustic structures on these phase plots, resulting in qualitatively different light curve shapes.

4.6 Summary

We implemented an offset dipole B-field (Section 3.1.3) characterised by an offset parameter ϵ, in the geometric code we adapted from Dyks & Harding (2004). First we needed to transform this field from the magnetic frame to the rotational frame, before we could solve for the PC rim. The rim was searched for in a similar way to what was done for the static dipole and RVD cases (Section 3.3). We extended the range for ϵ for which the PC rim could be found by increasing the colatitude bracket where solutions of the last open B-field line are searched for. We obtained a maximum offset of $\epsilon = 0.18$ over the whole range of α. Larger ϵ values result in larger PC offsets.

For the offset dipole we included the full SG E-field up to high altitudes since these expressions are available. We assumed CR to be our dominating radiation process. To obtain the E-field over all altitudes we calculated the matching parameter $\eta_{\rm c}(P, \dot{P}, \alpha, \epsilon, \phi_{\rm PC}, \xi)$, the critical radius where the low-altitude and high-altitude E-field solutions are matched. Lastly, we could modulate the emissivity ϵ_ν by solving the particle transport equation (using the general E-field) and found particle Lorentz factors of up to $\sim 10^7$, so that the CRR limit is reached in some cases. Using these Lorentz factors, we could next construct phase plots for photon energies > 100 MeV (Section 6.1.5).

Chapter 5

Chi-squared goodness-of-fit test

Before the implementation of statistical estimators, the quality of light curve fits was determined by searching by eye for certain emission characteristics, including the number of peaks the light curve displays, the phases of the predicted peaks, relative phase lag δ (radio-to-γ phase lag), γ-ray peak separation Δ, etc. (e.g., Venter et al., 2009; Bai & Spitkovsky, 2010; Venter et al., 2012). A statistical estimator is a time-saving fitting technique, and is useful for finding the best-fit model light curve to the data, also when multi-wavelength properties are considered. Another benefit of such a fitting procedure is that when the parameter space is increased, e.g., various gap widths, emission altitudes, etc. are considered, phase space becomes exceedingly large (i.e., prohibitive for by-eye searches) and the statistical technique can be carried out to estimate the best-fit parameters for a given geometry by scanning over the entire parameter space. A statistical test is furthermore unbiased, circumventing arbitrary choices of best fits, and can attach a significance to the best fit of a particular model, providing a mathematical basis for comparison.

The maximum likelihood estimator is a well-known statistical fitting method that can be used to fit simulated light curves to observations for various combinations of geometries and model parameters (e.g., Johnson et al., 2014). The likelihood function was introduced by Fisher (1925) and was used to determine the model parameters based on the dataset, i.e., the set of model parameters which describes the data the most accurately. Neyman & Pearson (1928) initiated a likelihood ratio test that is useful for hypothesis testing in order to eliminate one model in favour of another. A relation between the likelihood function and the chi-square (χ^2) distribution was proved by Wilks (1938), assuming that the data have Gaussian errors

$$\Delta\ln(\mathcal{L}) = -\frac{\Delta\chi^2}{2}, \tag{5.1}$$

with $\mathcal{L}$ the likelihood, and $\Delta\ln(\mathcal{L})$ the likelihood ratio. For a large number of counts we make the assumption that the data is Gaussian distributed and therefore, in what follows, we use a χ^2 test rather than a log-likelihood one.

In this chapter we describe the χ^2 statistical fitting method we used to determine the best-fit parameters for each of our B-field and geometric model combinations in Section 5.1. In Section 5.2 we briefly discuss other fitting methods we have considered, although we eventually decided not to make use of them. The figures in this chapter are used for the purpose of indicating the problems we encountered in each method, and I refer the reader to Chapter 6 for more details on how we applied the χ^2 method to find the best-fit model parameters.

5.1 Chi-squared fitting method

Statistical methods are useful for examining differences in, e.g., emission features between the model and observed light curves. The χ^2-statistic is a goodness of fit measure, therefore we used this technique as a tool to determine how well the model explains what we observe. The general expression for χ^2 is the square of the difference between the observed and expected (model) values, divided by the variance, and is given by:

$$\begin{aligned} \chi^2 &= \sum_{i=1}^{N_{\rm bins}} \frac{(Y_{{\rm d},i} - Y_{{\rm m},i})^2}{\sigma^2_{{\rm m},i}}, \\ &= \sum_{i=1}^{N_{\rm bins}} \frac{(Y_{{\rm d},i} - Y_{{\rm m},i})^2}{\sigma^2_{{\rm d},i}}, \\ &\approx \sum_{i=1}^{N_{\rm bins}} \frac{(Y_{{\rm d},i} - Y_{{\rm m},i})^2}{Y_{{\rm d},i}}, \end{aligned} \tag{5.2}$$

where $Y_{{\rm d},i}(\phi_{{\rm L},i})$ and $Y_{{\rm m},i}(\phi_{{\rm L},i})$ are the number of counts of the observed (relative units) and modelled (relative flux) light curves respectively, and $\sigma_{{\rm m},i}(\phi_{{\rm L},i}) \approx \sqrt{Y_{{\rm m},i}(\phi_{{\rm L},i})}$ the uncertainty (e.g., root-mean-square error or standard deviation, assuming Poisson statistics) of the model light curves in each phase bin $i = 1, ..., N_{\rm bins}$. Since we do not know the uncertainty of the model, we approximate the model error by the data error. Therefore, we use the uncertainty of the observations, assuming $\sigma^2_{{\rm m},i}(\phi_{{\rm L},i}) \approx \sigma^2_{{\rm d},i}(\phi_{{\rm L},i}) = Y_{{\rm d},i}(\phi_{{\rm L},i})$. When searching for the optimal fit, we need to renormalise our model to best approximate the data. This involves a free "amplitude" parameter A (see Eq. [6.1]). Furthermore, we also introduce the free parameter $\Delta\phi_{\rm L}$ which represents an arbitrary phase shift of the model light curve so as to align the model and data peaks. In what follows, we thus minimise the χ^2 over a set of four free parameters (α,ζ,A,$\Delta\phi_{\rm L}$) to find the optimal model.

Using Eq. (5.2) we define the χ^2 of the optimum model, i.e., the one with the comparatively lowest χ^2, as:

$$\chi^2_{\rm opt} \approx \sum_{i=1}^{N_{\rm bins}} \frac{\left(Y_{{\rm d},i} - Y_{{\rm opt},i}\right)^2}{\sigma^2_{{\rm d},i}}, \tag{5.3}$$

with $\chi^2_{\rm opt}$ the optimal χ^2, and $Y_{{\rm opt},i}(\phi_{{\rm L},i})$ the number of counts of the optimal modelled light curve in each phase bin i.

If faint pulsars (with low numbers of counts) are modelled, Poisson statistics will be sufficient to describe the observations, since the emission characteristics are not as well defined as those of bright pulsars such as Vela. We modelled light curves for the bright Vela pulsar, with a large number of observed counts in each phase bin i. Therefore we assumed Gaussian statistics which yields small errors, since the emission characteristics are more significant than those of faint pulsars. However, these small errors on the data yield large values for the reduced $\chi^2_{\rm opt}$, implying a large uncertainty in the statistical fits obtained. The χ^2 method assumes that the optimal model light curve acquired for each model combination describes the observed light curve fairly well, therefore the optimal fit of the model to the data requires a reduced $\chi^2_\nu = \chi^2/N_{\rm dof} = 1$, with $N_{\rm dof}$ the number of degrees of freedom (the difference between the number of bins $N_{\rm bins}$ and number of free parameters). In order to satisfy this requirement for the optimal fit, we therefore needed to rescale (divide) the χ^2 values by $\chi^2_{\rm opt}$ and

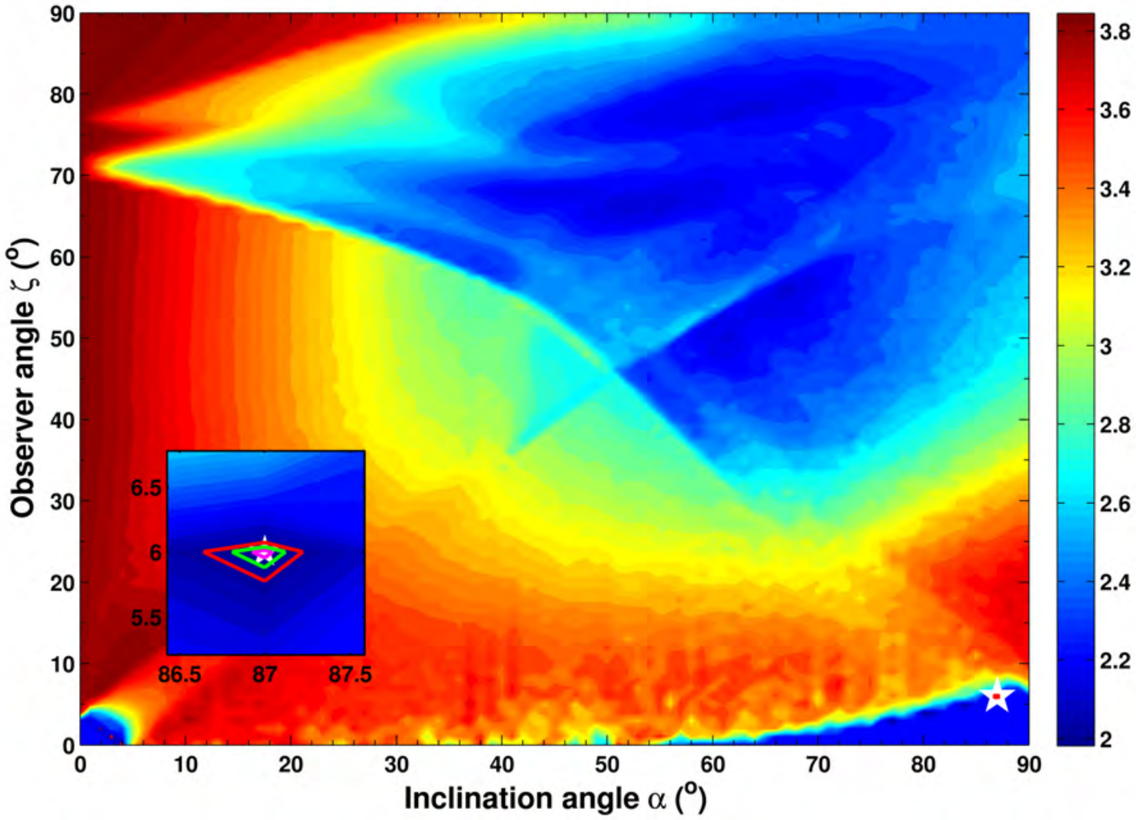

Figure 5.1: Contour plot for the initial best-fit solution we obtained for the RVD field and TPC model on an (α,ζ) grid. The colour bar of the contour plots represent $\log_{10}\xi^2$, with 1.98 corresponding to the best-fit solution, indicated by the white star. The confidence contour for 1σ (magenta line), 2σ (green line), and 3σ (red line) are also shown with an enlargement in the bottom left corner.

multiply by $N_{\rm dof}$. The scaled χ^2 and the reduced scaled χ^2 are presented by ξ^2 and ξ^2_ν (Pierbattista et al., 2014):

$$\xi^2 = N_{\rm dof}\frac{\chi^2}{\chi^2_{\rm opt}}, \tag{5.4}$$

$$\xi^2_\nu = \frac{\chi^2}{\chi^2_{\rm opt}}. \tag{5.5}$$

From Eq. (5.4) and (5.5) the ξ^2 and ξ^2_ν for the optimal model are as follows.

$$\xi^2_{\rm opt} = N_{\rm dof}\frac{\chi^2_{\rm opt}}{\chi^2_{\rm opt}} = N_{\rm dof}, \tag{5.6}$$

$$\xi^2_{{\rm opt},\nu} = \frac{\chi^2_{\rm opt}}{\chi^2_{\rm opt}} = 1. \tag{5.7}$$

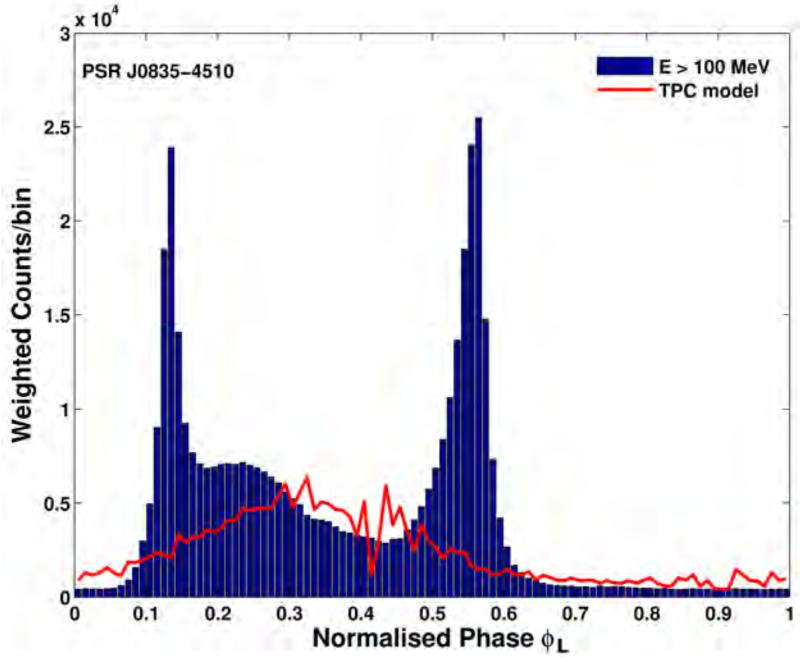

Figure 5.2: Best-fit light curve from the initial best-fit solution we obtained for the RVD field and TPC model.

If one wishes to compare the optimal model to alternative models, e.g., in our case a B-field combined with several geometric models, confidence contours for 68% (1σ), 95.4% (2σ), and 99.73% (3σ) can be constructed by estimating the difference in the $\xi^2_{\rm opt}$ and the ξ^2 of the alternative models:

$$\Delta\xi^2 \quad = \xi^2 - \xi^2_{\rm opt} = N_{\rm dof} \left(\frac{\chi^2}{\chi^2_{\rm opt}} - 1 \right). \tag{5.8}$$

The confidence intervals can be estimated by reading the $\Delta\xi^2$ (i.e., $\Delta\xi^2_{1\sigma,\mu_{\rm dof}}$, $\Delta\xi^2_{2\sigma,\mu_{\rm dof}}$, and $\Delta\xi^2_{3\sigma,\mu_{\rm dof}}$) values from a standard χ^2 table for the specified confidence interval at $\mu_{\rm dof} = 2$ (corresponding to the two-dimensional inclination angle α and observer angle ζ grid). Using these values for $\Delta\xi^2$ and $\xi^2_{\rm opt} = N_{\rm dof}$, we can determine $\xi^2 = \xi^2_{\rm opt} + \Delta\xi^2 = N_{\rm dof} + \Delta\xi^2$ (i.e., $\xi^2_{1\sigma}$, $\xi^2_{2\sigma}$, and $\xi^2_{3\sigma}$) from Eq. (5.8), which is the value at which we plot each confidence contour. To enhance the contrast of the colours on the filled χ^2 contours, we plotted $\log_{10}\xi^2$ on an (α,ζ) grid, with a minimum value of $\log_{10}\xi^2_{\rm opt} = \log_{10}(N_{\rm dof}) = 1.98$ (corresponding to the best-fit solution by construction, i.e., after rescaling, with $N_{\rm dof} = 100 - 4 = 96$ in our study, see Figure 5.1). This best-fit solution is indicated by the white star on the contour with the confidence contour for 1σ (magenta line), 2σ (green line), and 3σ (red line) surrounding it. We show an enlargement in the bottom left corner of these contour plots, since the confidence intervals are very small. Using this enlargement the best-fit parameters as well as upper and lower errors on α and ζ can be estimated. We determined errors on α and ζ for the best-fit solution of each B-field and model combination using the 3σ interval connected contours. We chose errors of 1° for cases when the errors were smaller than one degree (given a model resolution of 1°). The corresponding light curve fit of the model (solid red line) for the best-fit geometry to the Vela data (blue histogram) are also shown (e.g., Figure 5.2). The observed γ-ray light curve represents the weighted counts per bin as function of normalised

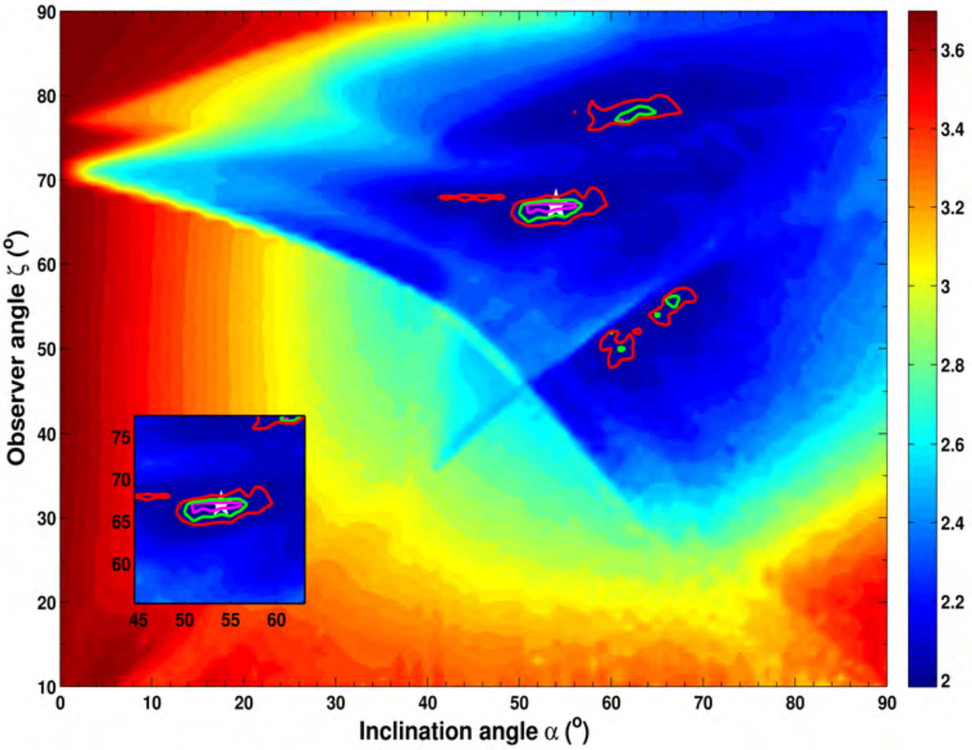

Figure 5.3: Contour for an alternative best-fit solution we obtained for the RVD field and TPC model (by requiring that $\zeta \geq 10°$).

pulse phase $\phi_L = [0, 1]$. We note that the observed light curve of the Vela pulsar shows no off-pulse emission between $\phi_L = 0 - 0.06$ and $\phi_L = 0.7 - 1$ and displays three peaks (Abdo et al., 2013). The first peak is visible at $\phi_L = 0.1 - 0.15$, the second at $\phi_L = 0.48 - 0.61$ and the "bump" is identified as the third peak at $\phi_L = 0.18 - 0.32$. However, for some model combinations we encountered poor qualitative and statistical fits using the χ^2 method. We noticed that for the fits some of the main emission characteristics did not fit well or they were not visible. Thus, the optimal fits to the observations were not significant and it was necessary to search for an alternative fit to explain what we observe. As one example we present the χ^2 contours and light-curve fits for the RVD and TPC model for both the initial, i.e., an optimal best-fit, and alternative, i.e., a second-best solution.

Figure 5.1 shows the initial best-fit solution we obtained: an optimal fit at $\alpha = 87^{+1}_{-1}\,^\circ$, $\zeta = 6^{+1}_{-1}\,^\circ$, normalisation factor $A = 0.6$, phase shift $\Delta\phi_L = 0.65$, and $\chi^2 = 2.3212 \times 10^5$. In Figure 5.3, we searched for an alternative best fit by limiting ζ to the range from 10° to 90° with a 1° resolution and found a second set of optimal values at $(\alpha, \zeta, A, \Delta\phi_L) = (54^{+5}_{-5}\,^\circ, 64^{+5}_{-3}\,^\circ, 0.5, 0.05)$, $\chi^2 = 3.278 \times 10^5$. We accepted the alternative best fit as our optimal best fit as presented in Chapter 6 in Table 6.1.

In Figure 5.2 and 5.4 we present our best-fit light curves for the "initial" and "alternative" solutions respectively. The alternative optimal fit was qualitatively a better fit than the first solution. We noticed that the unscaled χ^2 value is larger for the second fit, but qualitatively the initial solution does not fit the peaks of the observed light curve very well. The second fit finds the three peaks of the observed light curve, although they are very low or too broad. We explored alternative fitting procedures in the next section to examine the effect

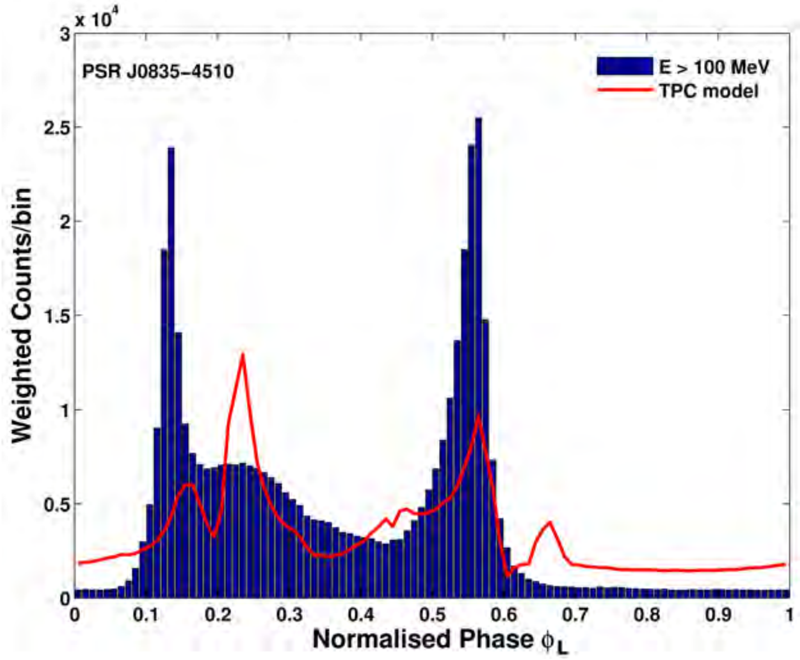

Figure 5.4: Best-fit light curve for an alternative best-fit solution we obtained for the RVD field and TPC model.

of the choice of fitting procedure has on the best-fit γ-ray light curve.

5.2 Alternative fitting techniques

We tested several other statistical fitting methods, including a χ^2 method where we only used the emission in the on-peak phase range, a weighted χ^2 where we weighted the χ^2 values by the observed bin intensity to emphasise the peaks, and an average ratio test. Each of these methods reveal some good light curve fits for certain combinations of B-field and model geometries. However, when it comes to the explanation of the confidence contours we obtained for our best fits for each different fitting method, it becomes a bit challenging since one can not apply the standard interpretation (as for the usual χ^2) using 1σ, 2σ, and 3σ contours. In this section I will explain the alternative fitting procedures we considered and the problems we encountered with each of them.

5.2.1 χ^2 for the on-peak region only

The observations of the Vela pulsar display on-peak emission, including the "bridge", between rotation phases $\phi_{\rm L} = 0.08 - 0.65$. For phases outside this range, the level of off-peak emission is very low. We chose to fit the model to the observations for the on-peak region only. We determined the value of the scaled χ^2 for the on-peak region of the model, $\xi^2_{\rm op}$ using Eq. (5.4). The equation is as follows:

$$\xi^2_{\rm op} = N_{\rm dof}\frac{\chi^2_{\rm op}}{\chi^2_{\rm op,opt}}; \quad \phi_{{\rm L},i} \in [0.08, 0.65]. \tag{5.9}$$

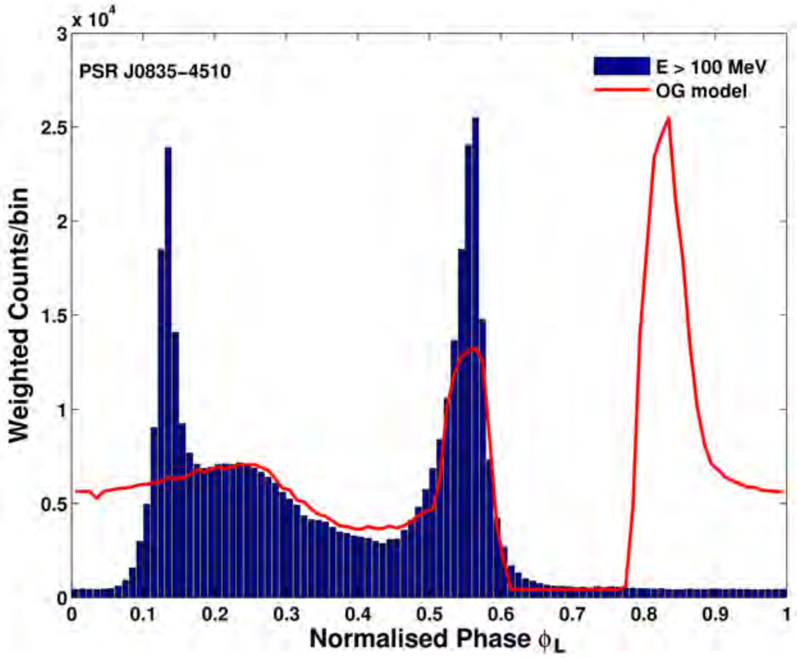

Figure 5.5: Best-fit light curve for the static dipole field and OG model.

From the above equation it follows that for the optimal fit the scaled χ^2 for the on-peak region is

$$\xi^2_{\rm op,opt} = N_{\rm dof}\frac{\chi^2_{\rm op,opt}}{\chi^2_{\rm op,opt}} = N_{\rm dof}; \quad \phi_{{\rm L},i} \in [0.08, 0.65]. \tag{5.10}$$

We encountered problems with the χ^2 method when we considered the on-peak region only during the fitting process. The model fits the "bridge" emission and the second peak, but formation of extra peaks is visible in the off-peak region, implying that the technique is blind to bad fits in the off-peak region. There are several such cases, but we show one example of a light curve fit which is for the static dipole field and OG model in Figure 5.5. It is therefore best to fit both the on-peak and off-peak emission regions of the observed light curves. Therefore we eliminated this fitting technique as our preferred method to find our optimal fit.

5.2.2 Weighted χ^2

We explored another fitting method where we weighted the χ^2-statistic with the intensity of the Vela light curve, i.e., we used Eq. (5.2) and multiplied it by $Y_{{\rm d},i}$ to emphasize the peaks more:

$$\begin{aligned}\chi^2_{\rm w} &\equiv \sum_{i=1}^{N_{\rm bins}} \frac{(Y_{{\rm d},i} - Y_{{\rm m},i})^2}{Y_{{\rm d},i}} Y_{{\rm d},i}, \\ &= \sum_{i=1}^{N_{\rm bins}} (Y_{{\rm d},i} - Y_{{\rm m},i})^2 , \end{aligned} \tag{5.11}$$

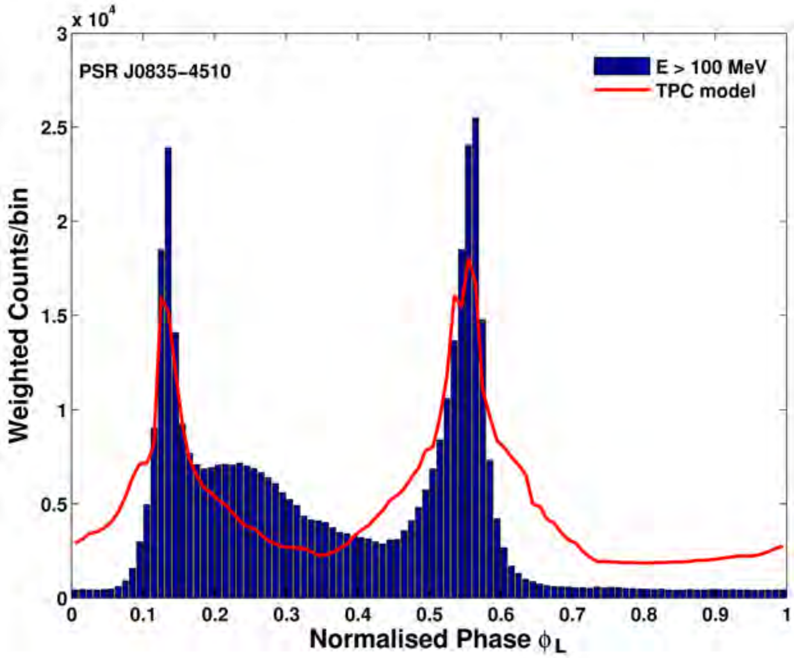

Figure 5.6: Best-fit light curve for the RVD and TPC model for a weighted χ^2 method.

with the weighted χ^2, $\chi^2_{\rm w}$ approximately some average error squared times the usual χ^2:

$$\chi^2 = \sum_{i=1}^{N_{\rm bins}} \frac{(Y_{{\rm d},i} - Y_{{\rm m},i})^2}{\sigma^2_{{\rm d},i}} = \frac{1}{\overline{\sigma}^2} \sum_{i=1}^{N_{\rm bins}} (Y_{{\rm d},i} - Y_{{\rm m},i})^2 = \frac{1}{\overline{\sigma}^2}\chi^2_{\rm w}. \tag{5.12}$$

If $\overline{\sigma}$ is a constant over α, ζ, A, and $\Delta\phi_{\rm L}$ we would be able to show

$$\begin{aligned} \xi^2_{\rm w} &= \left(\frac{\chi^2_{\rm w}}{\chi^2_{\rm w,opt}}\right) N_{\rm dof}, \\ &= \left(\frac{\overline{\sigma}^2\chi^2}{\overline{\sigma}^2\chi^2_{\rm opt}}\right) N_{\rm dof}, \\ &= \left(\frac{\chi^2}{\chi^2_{\rm opt}}\right) N_{\rm dof} = \xi^2. \end{aligned} \tag{5.13}$$

However, we find that this is generally not true. This is because for both χ^2 and $\chi^2_{\rm w}$ different optimal A and $\Delta\phi_{\rm L}$ values are obtained at fixed α and ζ. One can therefore not assume $\chi^2_{\rm w} \sim \overline{\sigma}^2\chi^2$, since $\overline{\sigma}^2$ would actually be a function of α and ζ. Thus, $\chi^2_{\rm w}$ is not χ^2-distributed.

For most of our B-field and model geometry combinations this weighting method fits the model and observed light curves very well. We obtained problems with this weighted method when we needed to interpret the contour plots, since $\chi^2_{\rm w}$ is not distributed like the usual χ^2. The contour plots for the former could therefore not be interpreted (in terms of assigning errors to best-fit parameters) in the same manner as those of χ^2, prompting us to discard this method. Figure 5.6 represents the best-fit light curve for the optimal solution of the RVD field and TPC model using $\chi^2_{\rm w}$. This fit yielded two peaks and more off-peak emission than the observed

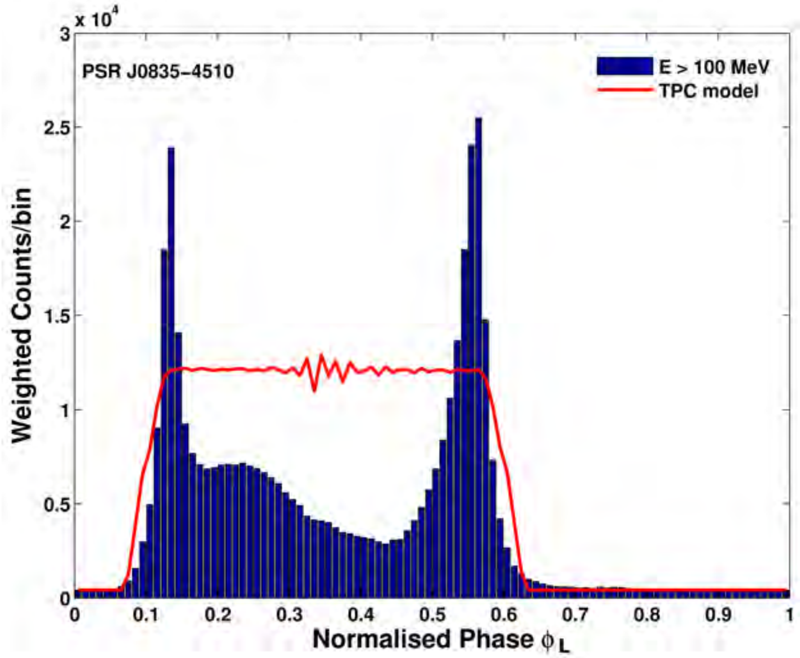

Figure 5.7: Best-fit light curve for the RVD and TPC model for the ratio test using a ratio factor $X = 2$.

light curve.

5.2.3 Average ratio test

We lastly applied a method in which we determined the ratio of model to data counts for each bin:

$$r_i = \frac{Y_{\mathrm{m},i}}{Y_{\mathrm{d},i}}. \tag{5.14}$$

We tested whether these ratios were "too large", i.e., when $r_i > X > 1$ for a chosen factor X, we penalised this ratio by using $r'_i = r_i$. Alternatively, we tested if the ratios were "too small", i.e., if $r_i < 1$ and $1/r_i > X$, we use $r'_i = 1/r_i$. We lastly added all these ratios r'_i (which are less than unity if the model is within a factor X of the data, or else larger than X) and divided by the number of bins to obtain an "average bin ratio" R':

$$R' = \frac{1}{N_{\mathrm{bins}}} \sum_{i=1}^{N_{\mathrm{bins}}} r'_i. \tag{5.15}$$

We lastly minimised R' to obtain our best-fit light curves in this case.

We illustrated a few examples of best-fit light curves obtained using this fitting method, for values $X = 2$ and $X = 3$ respectively to see the effect it would have on the best-fit light curves. In Figure 5.7 (for $X = 2$) and 5.8 (for $X = 3$) we present the optimal solution for the TPC model using the RVD field. We noticed that the best fits display a "block-shape" profile rather than the peaks of the observations (since this profile corresponded to the minimum average ratio R'). Therefore, we regarded the optimal solution of the RVD field and TPC model as a poor fit when using this method. In Figure 5.9 (for $X = 2$) and 5.10 (for $X = 3$) we present the TPC model

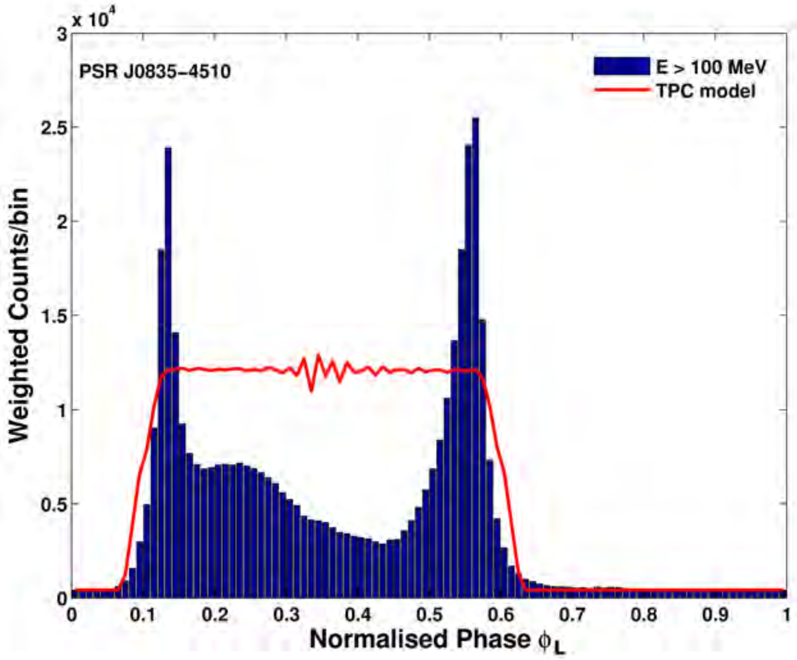

Figure 5.8: Best-fit light curve for the RVD and TPC model for the ratio test using a ratio factor $X = 3$.

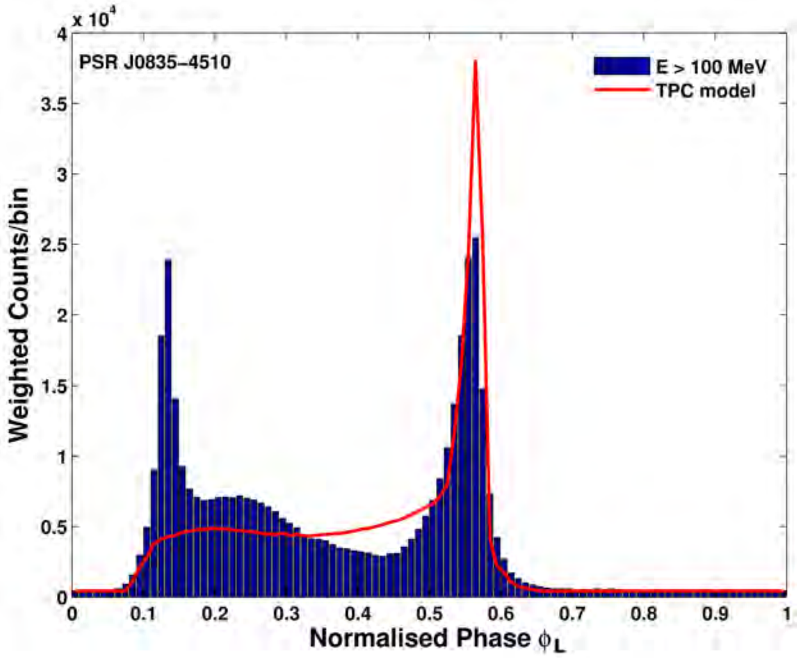

Figure 5.9: Best-fit light curve for the offset dipole field and TPC model for the ratio test using a ratio factor $X = 2$, considering constant ϵ_ν and $\epsilon = 0.03$.

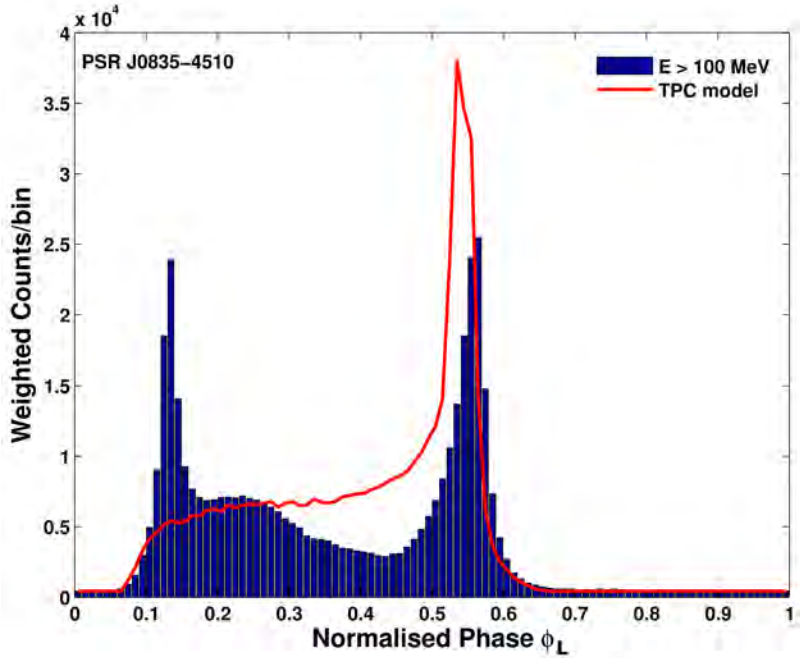

Figure 5.10: Best-fit light curve for the offset dipole field and TPC model for the ratio test using a ratio factor $X = 3$, considering constant ϵ_ν and $\epsilon = 0.03$.

using the offset dipole field, with an offset $\epsilon = 0.03$ and assuming constant emissivity ϵ_ν. We found that for a larger X, this test is less stringent in its requirements, thus, we may need to restrict ζ or experiment with smaller X when using this test. We also noticed that for the offset dipole field the model light curve displays only a single peak coinciding with the second peak of the observed light curve. Given this difficulties, we chose the standard χ^2 test as our preferred goodness-of-fit test.

5.3 Summary

We applied a standard χ^2 statistical fitting technique to assist us in finding the pulsar geometry which describes the observed γ-ray light curve of the Vela pulsar best. We determined the optimal χ^2 value for each B-field and geometric model combination over a parameter space of free model parameters spanning α, ζ, A, and $\Delta\phi_{\rm L}$. For the bright Vela pulsar we found large values of χ^2 and therefore we needed to scale the optimal χ^2 value so that the reduced χ^2 value would be $\chi^2_\nu = 1$. We constructed contour plots and best-fit light curves to demonstrate our optimal fit, surrounded by 1σ, 2σ, and 3σ confidence contours to indicate how well the model statistically fits the observations.

We presented examples of statistical fits we considered when using the χ^2 method. We obtained poor statistical or qualitative fits for some geometric combinations, thus an alternative optimal solution had to be selected to acquire a "better" qualitative fit of the model to the data. We studied alternative fitting methods including a χ^2 method for the on-peak region only, a weighted χ^2 technique, and an average ratio test. These other fitting techniques found good fits for some B-field and geometric model combinations, however, difficulties arose with the interpretation of the (α,ζ) contour plots, since the methods varied from the usual χ^2 statistical estimator.

We therefore preferred the χ^2 statistical method above the other fitting methods, since we assigned standard significances to the optimal fits with this method and could straightforwardly interpret the contour plots.

Chapter 6

Results

Several approaches have been followed to model the emission from γ-ray pulsars in order to understand its origin, location, and distribution. These approaches include (phase-resolved and average) spectral and light curve modelling using full *radiation* models (or physical models), e.g., Harding et al. (2008), Hirotani (2011), and Wang et al. (2011). In these models primary electrons are accelerated by an E-field parallel to the local B-field, i.e., $E_{||}$ which determines the emissivity ϵ_ν (per unit length) as well as whether the CRR limit, where the energy gain rate equals the energy loss rate, is reached by these particles. When the emitted photon energy and the local B-field are high enough magnetic pair production will occur, leading to a cascade of secondary electron-positron pairs. Photon-photon pair production may also occur in some cases. These processes (and other) included in physical models are not well understood or constrained.

A more simplistic approach is light curve modelling using *geometric* models as performed by, e.g., Watters et al. (2009); Venter et al. (2009); Bai & Spitkovsky (2010); Johnson et al. (2014). The emissivity ϵ_ν of HE photons within the gap region of a geometric model is usually assumed to be uniform in the corotating frame and the γ-rays are expected to be emitted tangentially to the local B-field in this frame (Dyks & Harding, 2004). All the physical and geometric pulsar models have been discussed in more detail in Section 2.7 and 3.2.

The light curves of HE γ-ray pulsars detected by the $Fermi$ LAT show great variety in profile shape and peak position relative to their radio profiles. This variety hints at distinct underlying magnetospheric and/or emission geometries for the individual pulsars, therefore geometric light curve modelling may provide constraints on the magnetospheric and emission characteristics.

In this chapter, we use the geometric modelling code described in Section 3.3, in which different B-field solutions and geometric gap models have been implemented to simulate γ-ray light curves for the bright Vela pulsar (PSR J0835−4510). The B-field structures which were studied includes the static dipole (Griffiths, 1995), the RVD (Deutsch, 1955), and the offset dipole (Harding & Muslimov, 2011b; see Section 3.1). We implemented the symmetric case of the latter as described in Chapter 4. We used these B-fields in conjunction with the TPC and OG geometries, assuming uniform ϵ_ν. We also considered an SG model (with an E-field producing a variable ϵ_ν) for the offset dipole field but not an OG model, since we do not have an OG E-field expression available for this particular B-field. In Section 6.1 we present phase plots and light curves for the various combinations. We applied a chi-squared (χ^2) statistical method (Section 6.2), as discussed in Chapter 5, to find the best-fit solution (Section 6.3) of the simulated γ-ray light curves to the observed Vela profile (Abdo et al., 2013). We lastly compared the best fits from the various B-field and gap model combinations statistically

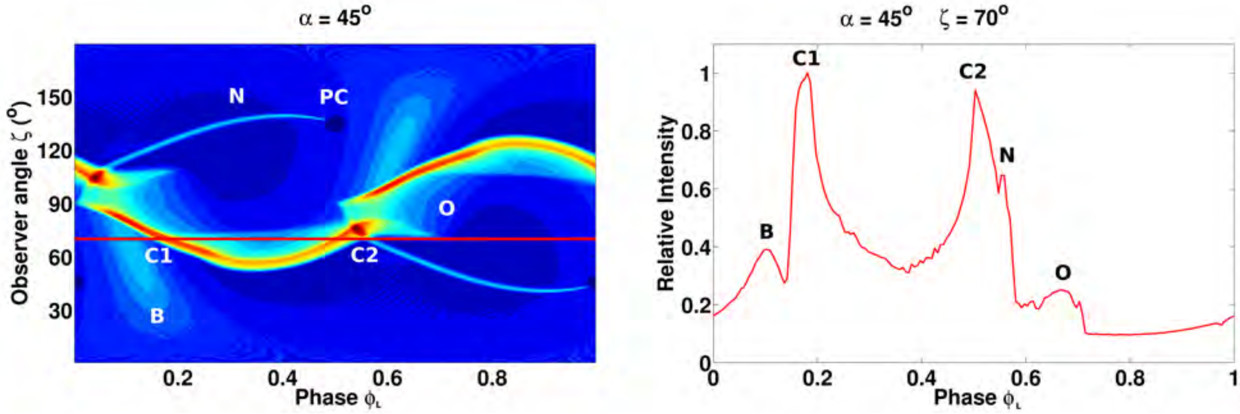

Figure 6.1: Phase plot (left) and light curve (right) from the TPC model using an RVD B-field. The phase plot illustrates the emission per solid angle versus ζ and $\phi_{\rm L}$ for $\alpha = 45^\circ$. For the same α-value the corresponding light curve is denoted by the solid red line for $\zeta = 70^\circ$. The symbols on both the phase plot and light curve denote features and are explained in the text (see Dyks et al. 2004a; Seyffert et al. 2015).

(Section 6.4) and summarise our results in Section 6.5.

6.1 Phase plots and light curves

We simulated light curves assuming an NS with mass $M = 1.4M_\odot$, radius $R = 10^6$ cm (where the mass and radius influence $E_\parallel$) and a pulse period $P = 89$ ms. We considered different geometric models (TPC / OG), and B-field solutions (static dipole, RVD, and offset dipole), choosing constant or variable ϵ_ν (in the latter case, we used $E_\parallel$-field expressions in an SG geometry applicable to the offset dipole field). We performed these simulations using a geometric modelling code which has the following free parameters: inclination angle α, observer angle ζ, offset parameter ϵ (in case of the offset dipole field). We fixed the scaled co-latitude of the innermost ring of the gap $r_{\rm ovc}^{\rm min}$, polar cap rim $r_{\rm ovc}^{\rm max}$, and gap width $w = r_{\rm ovc}^{\rm max} - r_{\rm ovc}^{\rm min}$ as follows: $[r_{\rm ovc}^{\rm min}, r_{\rm ovc}^{\rm max}] = [0.95, 1.00]$, i.e., a gap width $w = 0.05$. We assumed that for the TPC model the emission starts at the NS surface (minimum emission radius $R_{\rm min} = R = 0.0024R_{\rm LC}$) and for the OG model at the NCS, being emitted tangentially to the B-field lines and extending up to a maximum emission radius $R_{\rm max} = 1.2R_{\rm LC}$, with a maximum cylindrical distance of $\rho_{\rm max} = 0.95R_{\rm LC}$ (measured from the rotation axis; see Section 3.3.2). We chose $\alpha \in [0^\circ, 90^\circ]$ with a 1° resolution, since the simulations show symmetry in both the northern and southern hemispheres of the pulsar. This implies that the emission signature for α is the same as to that of $\pi - \alpha$, except that the phase is shifted by half a rotation, i.e., a pulse phase $\phi_{\rm L} = 0.5$. This symmetry in α is also visible in ζ (e.g., Figure 6.1). For the offset dipole we chose for the TPC (assuming uniform ϵ_ν) and SG (assuming variable ϵ_ν) models a range of $\epsilon \in [0.00, 0.18]$ with a resolution of 0.03. The emission intensity per solid angle $I(\phi_{\rm L}, \zeta)/\Delta\Omega$ was stored in bins of $\phi_{\rm L}$ and ζ (called phase plots) for a constant α. We used ranges of $\phi_{\rm L} \in [-180^\circ, 180^\circ]$ and $\zeta \in [0.5^\circ, 179.5^\circ]$, both with a resolution of 2°. A cut at constant ζ through each phase plot results in a light curve, which is the relative intensity as function of normalised $\phi_{\rm L} = [0, 1]$. An example of a phase plot and light curve for the RVD field and TPC model are shown in Figure 6.1 for $\alpha = 45^\circ$ and $\zeta = 70^\circ$. Unique emission characteristics are visible in light curves depending on the choice of α, ζ, B-field structure, and emission geometry (Dyks et al., 2004a). On the phase plot (left), dark circles appear at $(\phi_{\rm L}, \zeta) = (0, 45^\circ)$, and onward at $(\phi_{\rm L}, \zeta) = (0.5, 135^\circ)$, which is known to be the non-emitting PCs, with bright blue lines (marked with N) following from the notch of each PC. A notch is a deformation of the PC in the RVD B-field, stemming from the B-field structure at the light cylinder, at a radius $R_{\rm LC}$ (for more details see Section 3.1 and 3.3). The feature marked N on the light curve (right) is generated when the observer's line of sight crosses the emission due to these bunching field lines. Another feature is formed when B-field lines extending from opposite poles overlap, as indicated by O. Bright red and yellow features are visible which are defined as caustics (labelled C1 and C2) on the trailing side of the PC, described in Section 3.3.3. The feature B follows from the bunching of emission on trailing B-field lines due to rotation of the pulsar and caustic effects, only visible for the TPC case.

Which of these features are visible on a light curve greatly depends on the choice of ζ. If $\zeta < \alpha$, only a few or no features will appear on the light curves. However, if $\zeta \gtrsim \alpha$ more features will become visible as shown in our example where the light curve reveals five peaks associated with certain features at the same $\phi_{\rm L}$ compared to that of the phase plot. These include the precursor "bump" B at $\phi_{\rm L} = 0.1$, a cut through the caustic at two positions C1 (at $\phi_{\rm L} = 0.16$) and C2 (at $\phi_{\rm L} = 0.5$), a hint of feature N ($\phi_{\rm L} \sim 0.5$), and the last peak is due to the tangential cut through feature O. Near $\phi_{\rm L} = 0.7$ and onwards the emission decreases significantly, and this is termed the off-peak region. The peaks C1 and C2 on the light curve are connected by "bridge emission". If we compare the phase plots and light curves for the RVD field for both the TPC (Figure 6.1 and 6.4) and OG (Figure 6.5) geometries, we observe that in the OG model not all of phase space is filled (due to emission that occurs only above the NCS and therefore visible from only one magnetic pole). Features only become visible at larger values for α and ζ in this case. There are also fewer features and less off-peak emission visible in the OG case.

In the sections that follow, we will present various phase plots and their light curves for different geometric parameters and combinations of emission geometries and B-fields. In Appendix B we present light curve atlases for different α and ζ values, and discuss features for combinations of gap geometries and B-fields in more detail, also considering different values for ϵ and the presence of the SG $E_{\|}$. These atlases are simply a collection of light curves in (α,ζ)-space, with both α and ζ ranging from $10° - 90°$ with increments of $10°$. By studying these atlases one can get an idea of how the features depend on the geometric parameters, as well as the effect of the B-field and E-field on the light curves. Below we discuss the phase plots and light curves for each model combination.

6.1.1 Phase plots and light curves for a static dipole field and TPC geometry

In Figure 6.2 we present the phase plots and their corresponding light curves we obtained for the TPC model, using a static dipole B-field. We considered a range of $\alpha \in [0°, 90°]$ and $\zeta \in [15°, 90°]$, for a $15°$ resolution. Each phase plot (left) is for a different α value, and the corresponding light curves (right) are for different ζ slices through the particular phase plot. On each phase plot there appear dark circles, the PCs, at phases $\phi_{\rm L} = [0.0, 0.5]$. The PCs are followed by sharp, bright regions near it, called the main caustics. The caustic structure is qualitatively different for distinct values of α, leading to differences in the resulting light curves. The caustics seem wider (fill more of phase space) and more pronounced for larger α values accompanied by a change in the position of the PCs to values closer to $\zeta = [\alpha, 180° - \alpha]$. For large α the caustics extend over a larger range in ζ, with the emission forming a "closed loop" at $\alpha = 90°$.

The TPC model is visible at nearly all angle combinations and thus fills nearly all of phase space. This is

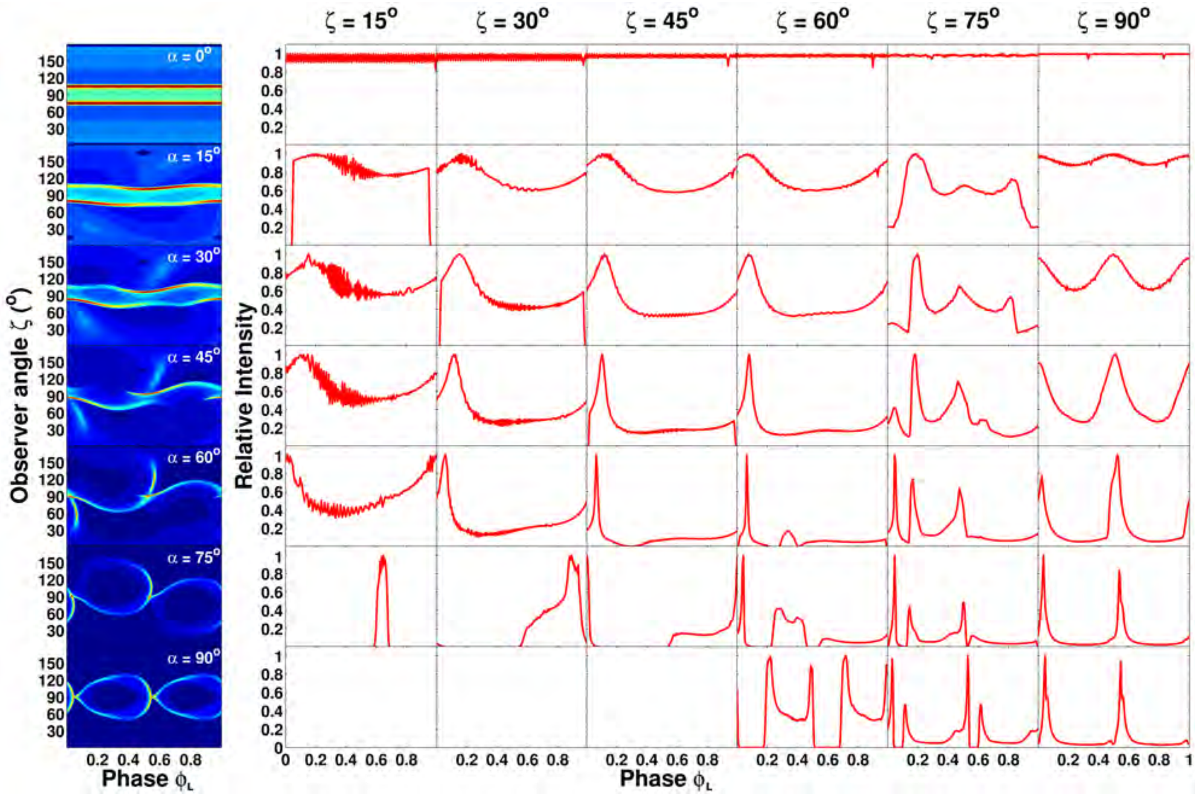

Figure 6.2: Phase plots (first column) and light curves (second column and onwards) for the TPC model using a static dipole B-field. Each phase plot is for a different α value ranging from 0° to 90° with a 15° resolution, and their corresponding light curves are denoted by the solid red lines for different ζ values, ranging from 15° to 90°, with a 15° resolution.

due to the fact that some emission occurs below the null charge surface for the TPC model, in contrast to the OG model. Although, in the case for $\alpha = 90°$ and ζ below 45° no light curves are visible, i.e., no emission is observed due to the "closed loop" structure of the caustics, which is characteristic of the static dipole case. The TPC model light curves exhibit the features as discussed in Section 6.1, depending on the angle combination. At $\alpha = 0°$ and small ζ values, mostly background noise is observed and as α increases, the caustic emission becomes visible. As α and ζ increase, more features are visible, and the light curves also exhibit relatively more off-pulse emission than in the OG case. In the TPC model, emission is visible from both poles forming double peaks in some cases, whereas in the OG model emission is visible from a single pole. One does obtain double peaks in the OG case, however, when the line of sight crosses the caustic at two different phases.

6.1.2 Phase plots and light curves for a static dipole field and OG geometry

In Figure 6.3 we show the phase plots and their corresponding light curves for an OG model, using a static dipole B-field. On each phase plot the caustics are less pronounced compared to Figure 6.2 for the TPC case, due to fact that the emission does not occur below the null charge surface for the OG model. Therefore the OG models are not observable at all angle combinations and thus do not fill all of phase space.

The OG model light curves exhibit relatively less off-pulse emission, as well as fewer features (as discussed in Section 6.1) than the TPC case. Unlike the TPC model, where emission is visible from both poles, the light

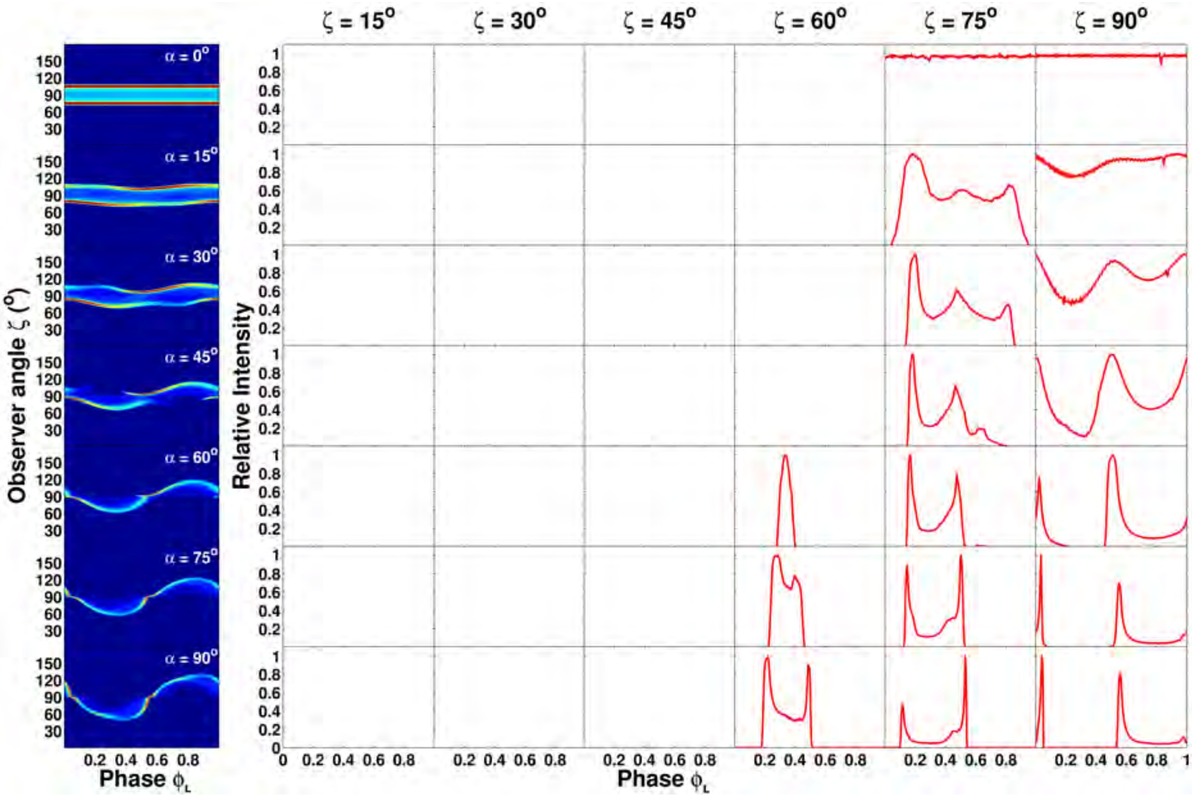

Figure 6.3: The same as in Figure 6.2, but for the OG model using a static dipole B-field.

curves in the OG models are due to emission from one pole only. This can be seen if we compare the TPC and OG light curves for, e.g., the angle combination $\alpha = 90°$ and $\zeta = 60°$. This also may be noticed on the phase plot where only half of the "closed loop", which is formed in the TPC case, is visible in the OG case. This effect is also seen at other angle variations for larger α and ζ values.

6.1.3 Phase plots and light curves for an RVD field and TPC geometry

In Figure 6.4 we present the phase plots and their corresponding light curves for an RVD B-field and TPC model. On each phase plot the PCs are visible at $\phi_L = [0.0, 0.5]$. The caustic structure is qualitatively different compared to Figure 6.2 for the static dipole case and TPC model, leading to variations in the light curves. As α increases the caustics extend over a larger range in ζ, and are associated with the repositioning of the PCs up to $\zeta = 90°$. A thin line of emission due to the 'notch' (formed by distortions in the RVD B-field) is also visible in the latter case. At $\alpha = 90°$ an "open" vertical curved pattern is visible, which is different compared to the "closed loop" in Figure 6.2.

As mentioned in Section 6.1.1 the TPC model light curves exhibit relatively more off-pulse emission than the OG case, with emission visible from both poles as seen for large α and ζ. If we compare Figure 6.2 and 6.4, which are for two different B-fields for the TPC model, we notice that the B-field structure has a great influence on the resulting phase plots and light curves. As α and ζ increase, more features (as discussed in Section 6.1) are visible in the RVD case as opposed to the static dipole (Figure 6.2). At $\alpha = 0°$ and small ζ values, mostly background noise is observed. As ζ increases the caustic emission becomes visible.

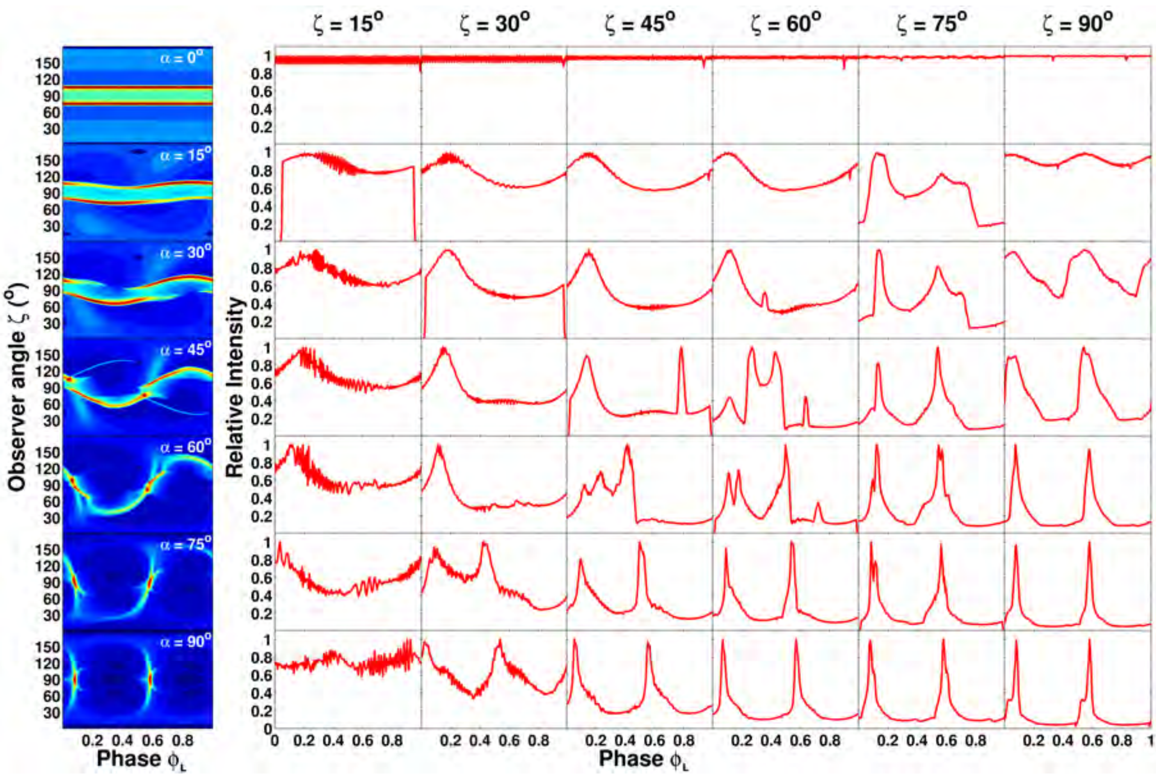

Figure 6.4: The same as in Figure 6.2, but for the TPC model using an RVD *B*-field.

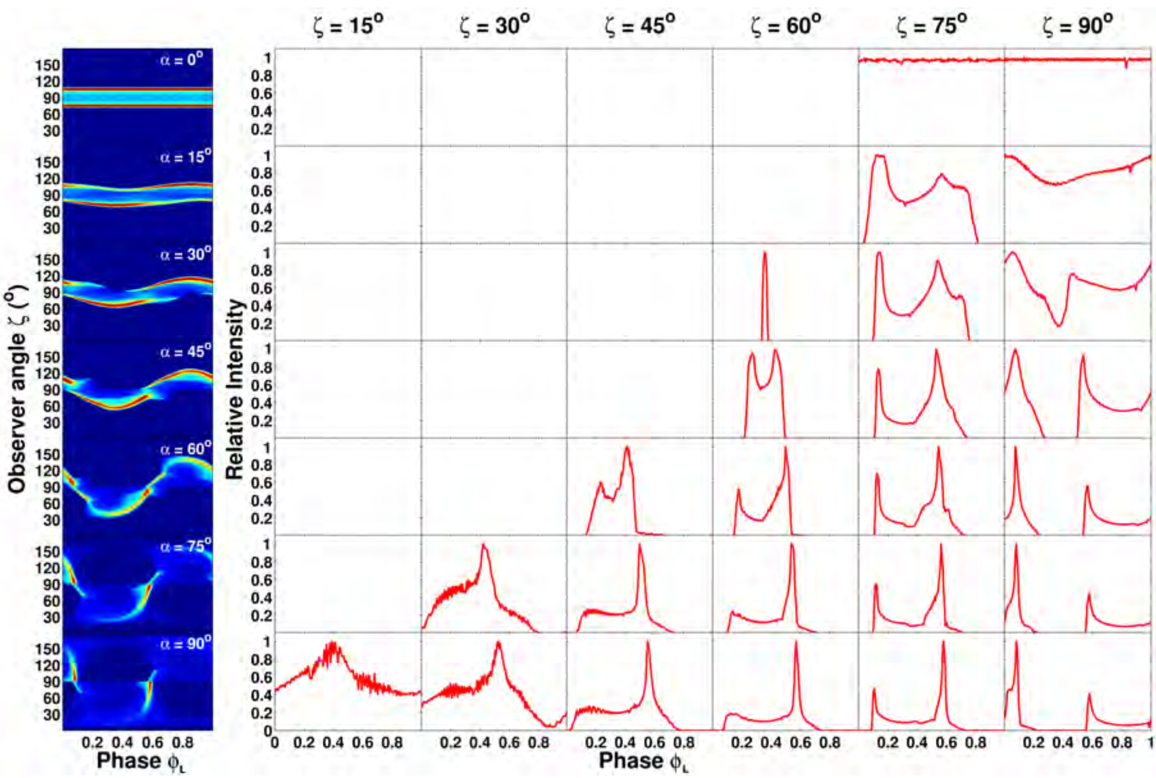

Figure 6.5: The same as in Figure 6.2, but for the OG model using an RVD *B*-field.

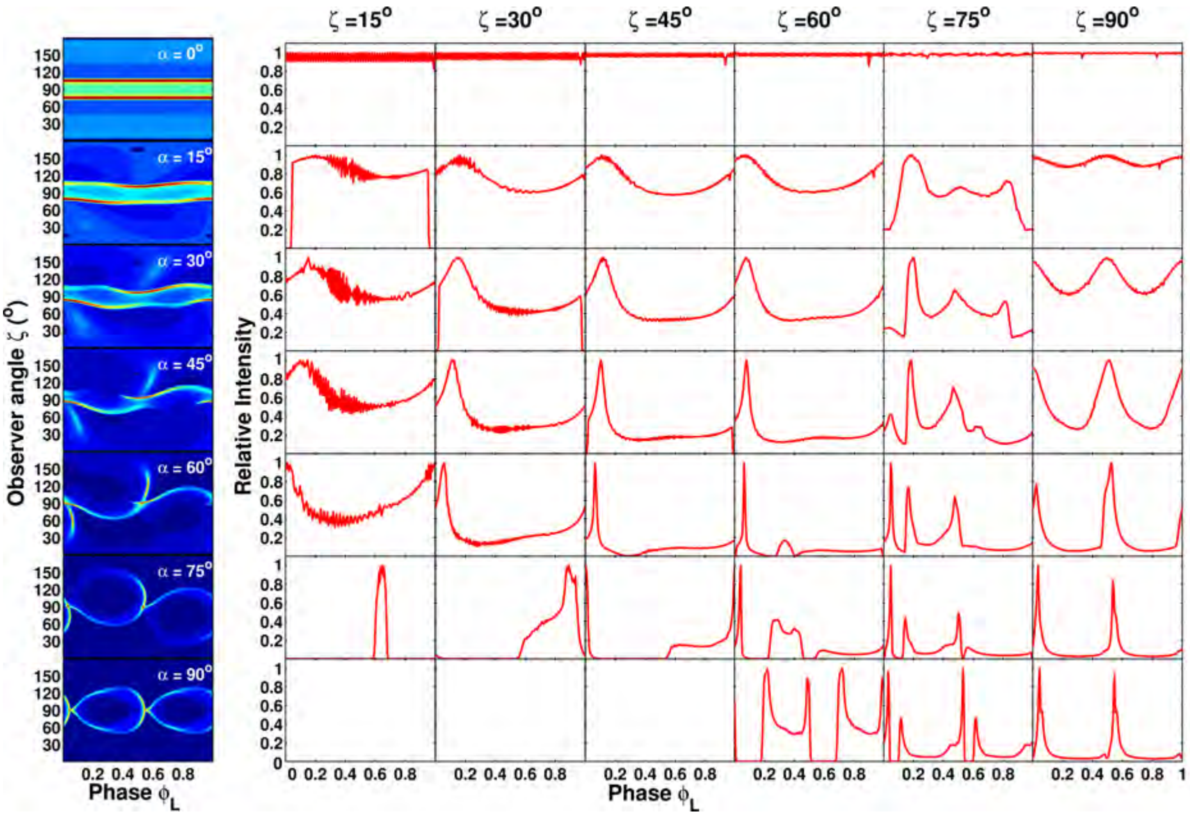

Figure 6.6: The same as in Figure 6.2, but for the TPC model using an offset dipole field, for a fixed value of $\epsilon = 0.00$, for constant ϵ_ν.

6.1.4 Phase plots and light curves for an RVD field and OG geometry

In Figure 6.5 we present phase plots and their corresponding light curves for the RVD B-field and OG model. As mentioned in the Section 6.1.2 the caustics occupy a smaller region of phase space compared to Figure 6.4 for the TPC case. The emission occurs above the null charge surface in the OG model, and is thus not visible at all angle combinations. The OG model light curves also exhibit relatively fewer features and less off-peak emission (as discussed in Section 6.1). Again, one can see for the OG case the emission is visible from a single pole, e.g., $\alpha = 90°$ and $\zeta = 60°$ where half of the light curve is visible compared to the TPC case (Figure 6.4). This effect is visible at other angle variations for larger α and ζ values as well. At larger α and ζ values more phase space is filled for the RVD than for the static dipole field.

6.1.5 Phase plots and light curves for TPC and SG geometries in an offset dipole field

In Figure 6.6 and Figure 6.7 we present the phase plots and their corresponding light curves we obtained for the offset dipole B-field we have implemented (see Chapter 4 and Appendix A). For Figure 6.6 we chose an offset parameter $\epsilon = 0.00$ and assumed that the emission is uniform in the corotating frame for the TPC geometry. If we compare Figure 6.6 with Figure 6.2 we notice that the phase plots and light curves are identical at all angle combinations. Thus, for the constant ϵ_ν case with $\epsilon = 0.00$, the offset dipole solution reduces to the case of the static dipole solution, both for a TPC geometry (see Section 6.1.1). This important test case implies that we successfully transformed our offset dipole B-field, as discussed in Appendix A.

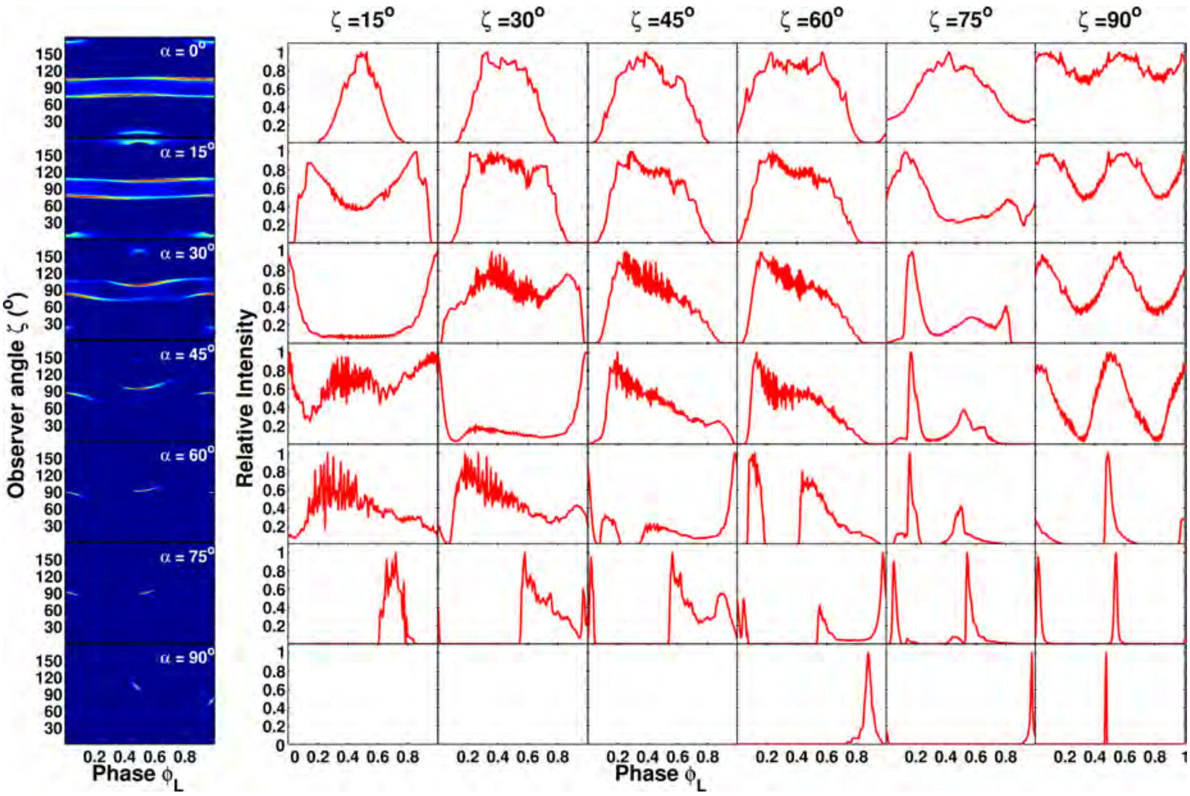

Figure 6.7: The same as in Figure 6.2, but for the SG model using an offset dipole field, for a fixed value of $\epsilon = 0.18$, for variable ϵ_ν.

For Figure 6.7 we chose $\epsilon = 0.18$, assuming variable emissivity, i.e., due to using an SG E-field solution (with curvature radiation the dominating process for emitting γ-rays; see Sections 2.7.2 and 4.3). The non-emitting PCs are invisible, but we see the sharp, bright regions (emission caustics) where radiation is bunched due to relativistic effects. The caustic structure and resulting light curves are qualitatively different for various α compared to the constant ϵ_ν case. The caustics appear smaller and less pronounced for larger α values, and extend over a smaller range in ζ.

If we compare Figure 6.7 with Figure 6.6, we notice that when we take $E_{\|}$ into account the phase plots and light curves change considerably. At $\alpha = 90°$ a small "wing-like" pattern is visible in the phase plot, which is different compared to the "closed loop" emission patterns in Figure 6.2. Therefore we see that both the B-field and E-field have an impact on the predicted light curves. This small "wing-like" caustic pattern is due to the fact that we only included photons in the phase plot with energies > 100 MeV. The photon energy is related to the question whether particles reach the CRR limit (Section 4.3). We find that the CRR limit is in fact reached (where the energy gain rate equals the loss rate) for certain parameter combinations of (α, ϵ and $\phi_{\rm PC}$; see Figure 4.6, 4.7 and 4.8), albeit only at large values of η. Notably, this is not the case at large α where the first term of each E-field expression (see Eq. [4.5] and [4.6]) becomes lower and the second term plays a larger role, leading to smaller gain rates and therefore smaller Lorentz factors. Given the relatively low E-field there are only a few photons with energies exceeding 100 MeV.

The SG model is visible at nearly all angle combinations and thus fills nearly all of phase space. At some angle combinations no emission is visible, whereas at other combinations the emission becomes visible, with

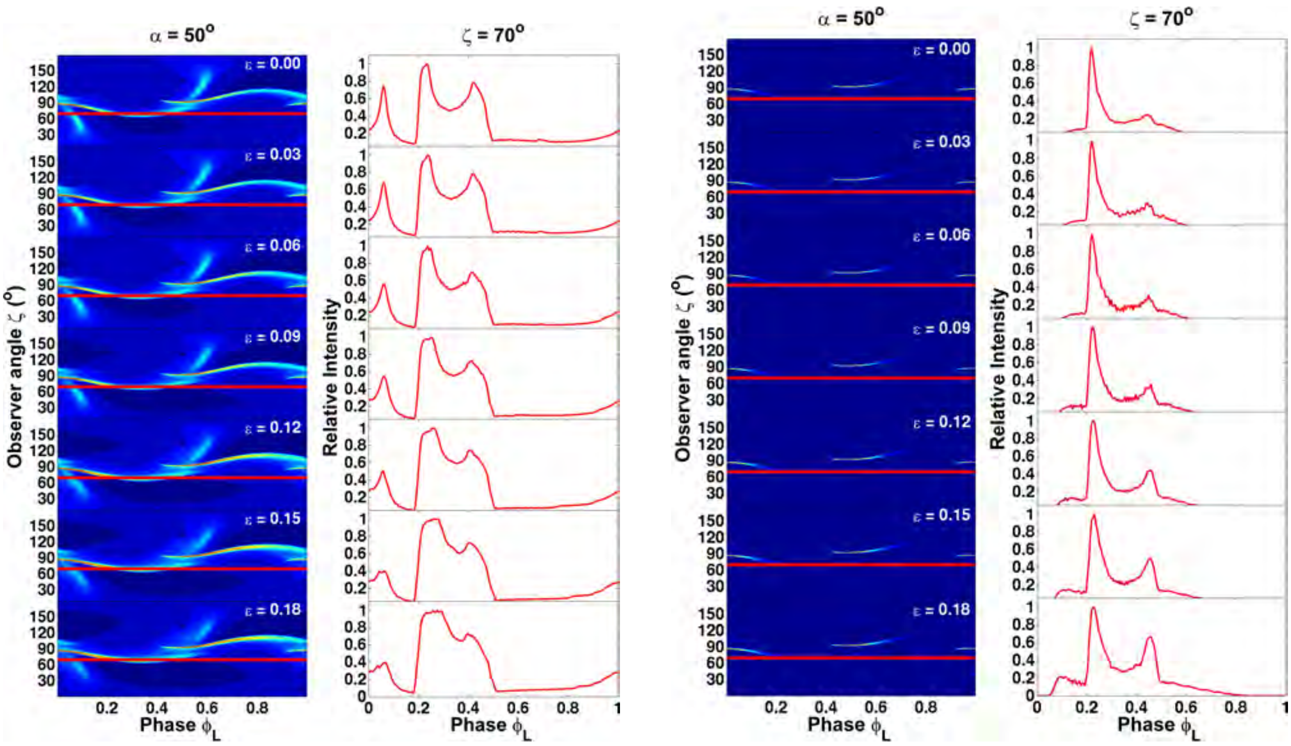

(a) (b)

Figure 6.8: Phase plots and light curves for a TPC (SG for variable ϵ_ν) model using an offset dipole field, for (a) constant and (b) variable ϵ_ν, for $\alpha = 50°$, $\zeta = 70°$, and different ϵ values.

the light curves generally displaying only one broad peak with less off-peak emission compared to Figure 6.6. As α and ζ increase, more peaks become visible, with emission still visible from both poles as seen for larger α and ζ values, e.g., $\alpha = 75°$ and $\zeta = 75°$.

The offset of the PCs for an offset dipole field is described by two parameters, i.e., the magnetic azimuthal angle ϕ'_0 (which determines the direction of the PC offset), as well as the offset ϵ. We next show the effect that different values of ϵ has on phase plots and light curves for both the constant and variable ϵ_ν cases. Figure 6.8 consists of two subfigures which represent phase plots for $\alpha = 50°$, and their corresponding light curves at $\zeta = 70°$ on the particular phase plot, using an offset dipole field with ϵ ranging from 0 to 0.18 with increments of 0.03. Each phase plot is for a different ϵ value, increasing from top to bottom as indicated in the top right corner. Figure 6.8a indicates the TPC model assuming constant ϵ_ν, and Figure 6.8b the SG model with variable ϵ_ν. On each phase plot in Figure 6.8a there appear dark circles (the non-emitting PCs) followed by sharp, bright caustics. The caustic structure is slightly different for different values of ϵ. As ϵ increases, the caustic structure becomes slightly broader and more pronounced in panel (a). When we compare the phase plots of Figure 6.8a and Figure 6.8b, we notice that the non-emitting PCs are now invisible, the caustics are dimmer and smaller in the latter case due to the low SG E-field, and the resulting phase plots and light curves are qualitatively different.

The TPC model light curves in the Figure 6.8a exhibit the features as discussed in Section 6.1, depending on the combination of ζ and ϵ. As ϵ increases, some of the peaks become flatter and less pronounced. When we compare Figure 6.8a to Figure 6.8b we notice that the light curves display less off-peak emission in the latter

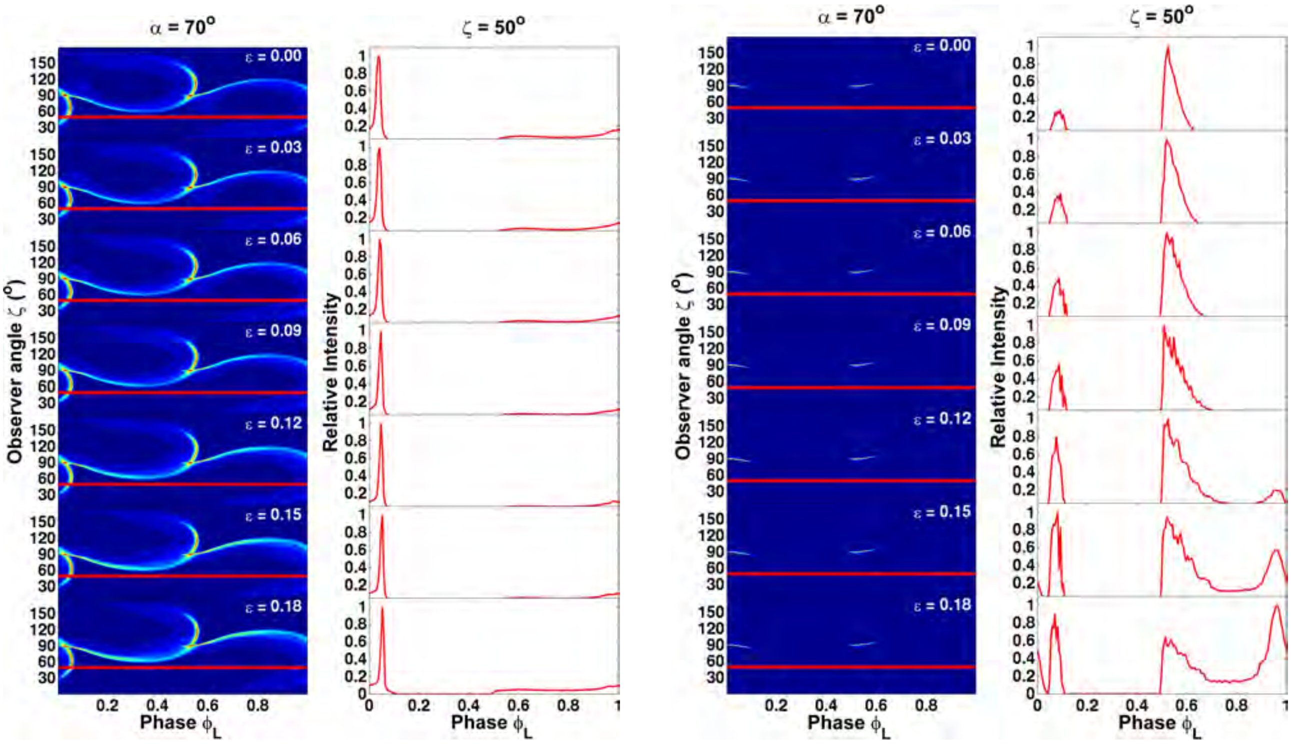

(a) (b)

Figure 6.9: Phase plots and light curves for a TPC (SG for variable ϵ_ν) model using an offset dipole field, for (a) constant and (b) variable ϵ_ν, for $\alpha = 70°$, $\zeta = 50°$, and different ϵ values.

case. In Figure 6.8b we observe a "bump" which follows a sharp peak with less off-peak emission (at $\epsilon = 0$). As ϵ increases the "bump" becomes sharper and a "wing" of off-peak emission develops.

We next present phase plots and light curves in Figure 6.9 for the same geometries and ϵ values as in Figure 6.8, except that we chose $\alpha = 70°$, and $\zeta = 50°$ in order to point out the change in the phase plot and light curve shape, as well as the caustic structure. Figure 6.9a presents the TPC model assuming constant ϵ_ν and Figure 6.9b the SG model assuming variable ϵ_ν. On each phase plot in Figure 6.9a the dark circles represent the non-emitting PCs followed by the caustics. The caustic structure is slightly different for different values of ϵ. When we compare the phase plots of Figure 6.9a and Figure 6.9b, we notice dimmer and smaller caustics in the latter case due to the low SG E-field. Therefore the resulting phase plots and light curves are qualitatively different when including $E_{\parallel}$.

For $\epsilon = 0$ and ϵ_ν constant the light curve has a single peak and as ϵ increases the peak becomes slightly narrower. When we compare Figure 6.9a and Figure 6.9b, we notice that the light curves in Figure 6.9b are due to background noise. The phase plots and light curves are very different between Figure 6.8 and 6.9. In the former case for relatively small α and large ζ, more emission features are visible. As α becomes larger and ζ smaller, therefore the caustics appear sharper and fewer features are observable. This comparison between Figure 6.8 and 6.9 underscores the dependency of the light curves on the B-field, model geometry, and geometric parameters. In Appendix B we constructed light curve atlases for various combinations of B-field structure, gap geometry, and geometric pulsar parameters.

6.2 Constructing $\chi^2(\alpha, \zeta)$ contours and finding best-fit light curves

We tested several fitting methods which we could apply to our γ-ray light curve fitting in order to select the most suitable one. We decided to use the standard χ^2 method from Chapter 5 to determine the best fit of our simulated light curves to the *Fermi* data for Vela, with energies $E > 100$ MeV. For each combination of B-field and geometric model, we calculated χ^2 for each set of free geometric model parameters α, ζ, amplitude A (a normalisation factor), and phase shift $\Delta\phi_{\rm L}$, and selected the optimal χ^2 ($\chi^2_{\rm opt}$) which corresponds to our best-fit parameters.

Since we used geometric models, with an uncertainty in the absolute *intensity*, we assumed that the *shape* of the light curve was correct. The data possess a background which is also uncertain. Furthermore, *Fermi* has a certain response function that influences the intrinsic shape of the light curve, which is the sum of many pulsar rotations. Given all these uncertainties, we decided to incorporate a free amplitude parameter A, to allow more freedom in terms of finding the best fit of the model light curves to the data.

We next chose the phase shift $\Delta\phi_{\rm L}$ as a free parameter due to the uncertainty in the definition of $\phi_{\rm L} = 0$. Radio observers have used different definitions for $\phi_{\rm L} = 0$, e.g., the maximum radio intensity, or the position of the maximal Fourier power. In the rotating vector model (RVM), $\phi_{\rm L} = 0$ corresponds to the phase at which the observer crosses the "fiducial" plane (a reference plane containing the rotation $\boldsymbol{\Omega}$ and magnetic $\boldsymbol{\mu}$ axes). At this crossing point, the polarization angle displays a maximum sweep. However, we know the B-field is not necessarily a pure dipole, thus the radio beam is not necessarily circular, nor symmetric. There are also special relativistic effects such as aberration and retardation that complicate the matter even further. In our model, $\phi_{\rm L} = 0$ is defined as the phase where the observer line of sight crosses the $\boldsymbol{\mu}$ axis. Aberration causes the radio pulse to occur at $\phi_{\rm L} \sim -r/R_{\rm LC}$ (with r the radial emission height), since the pulse is emitted at a non-zero altitude. We don't want to make any changes to the data, but given the uncertainties in the definition of $\phi_{\rm L} = 0$, we introduce the free parameter $\Delta\phi_{\rm L}$ (see, e.g., Johnson et al., 2014 who also used A and $\Delta\phi_{\rm L}$). An important note we want to make is that we have not changed the relative position (the radio-to-γ phase lag δ), since this is a crucial model prediction. The radio and γ-ray emission regions are tied to the same underlying B-field structure, and δ therefore reflects important physical conditions (or model assumptions) such as a difference in emission heights of the radio and γ-ray beams.

Before we determine the best-fit parameters for each of our B-field and gap model combinations, it was necessary to prepare the simulated (model) light curve, so that it could be compared directly to the data. This was done as follows. We normalised the model light curve $Y'_{\rm m}(\phi_{{\rm L},i})$ to range from 0 to the maximum number of observed counts k_2 by using the following expression:

$$Y'_{\rm m}(\phi_{{\rm L},i}) = \frac{Y_{\rm m}(\phi_{{\rm L},i})}{(k_1 + \epsilon_0)} A(k_2 - {\rm BG}) + {\rm BG} \approx \frac{Y_{\rm m}(\phi_{{\rm L},i})}{k_1} k_2, \tag{6.1}$$

with i the bin number, $k_1 = \max(Y_{\rm m}(\phi_{{\rm L};i}))$ the maximum number of counts of the model light curve $Y_{\rm m}(\phi_{{\rm L},i})$, $k_2 = \max(Y_{\rm d}(\phi_{{\rm L},i}))$ the maximum number of counts of the observed light curve $Y_{\rm d}(\phi_{{\rm L},i})$, ϵ_0 a small value added to ensure that we do not divide by zero, A the normalisation factor, and BG the background level of $Y_{\rm d}(\phi_{{\rm L},i})$.

We treated the data as being cyclic so we needed to ensure that the model light curve was cyclic as well. We made the model light curve cyclic by duplicating the light curve to simulate various rotations, e.g., for phases -2.0 to -1.0, -1.0 to 0.0, 0.0 to 1.0, 1.0 to 2.0, etc. This helped with the smoothing (discussed below) at the end points, e.g., at $\phi_{\rm L} = 1.0$ the program would take into account the points at $\phi_{\rm L} = 0.0$ to interpolate model intensities at $\phi_{\rm L} = 1.0$. There were therefore no edge effects (no change in the light curves at the boundaries), since there were always neighbouring data points. Since the model light curves were simulated with 180 phase bins, whereas the observed light curves had 100 bins (with fixed bin width), the model light curve had to be re-binned in order to have the same amount of bins in $\phi_{\rm L}$ as the data. We used a Gaussian Kernel Density Estimator function to smooth the model light curve, i.e., equalize the number of model light curve and data bins (Parzen, 1962).

After preparation of the model light curve, we searched for the best-fit solution for each of our B-field and gap combinations over a parameter space of $\alpha \in [0°, 90°]$, $\zeta \in [0°, 90°]$ (both with 1° resolution), $0.5 < A < 1.5$ with 0.1 resolution, and $0 < \Delta\phi_{\rm L} < 1$ with 0.05 resolution. For a chosen B-field and model geometry we iterated over each set of parameters and searched for a local minimum χ^2 value at a particular α and ζ. Once we have iterated over the entire parameter space (α,ζ,A,$\Delta\phi_{\rm L}$), we obtained a global minimum value for χ^2 (also called $\chi^2_{\rm opt}$). We refer the reader to Section 5.1 for the equations used to calculate χ^2 and $\chi^2_{\rm opt}$. For the reasons discussed in Section 5.1, we needed to scale the χ^2 and $\chi^2_{\rm opt}$ using $N_{\rm dof}$ (with $N_{\rm dof}$ the number of degrees of freedom, which is the difference between the number of bins, $N_{\rm bins}$, and number of free parameters) in order to satisfy the requirement of a reduced $\chi^2_\nu = 1$. We used $N_{\rm dof} = 96$, with $N_{\rm bins} = 100$ and for 4 free parameters. We represented the scaled χ^2 by the symbol ξ^2 and the reduced scaled χ^2 by ξ^2_ν. The best-fit solution was denoted by $\xi^2_{\rm opt} = N_{\rm dof}$ and its reduced χ^2 by $\xi^2_{{\rm opt},\nu} = 1$ (Pierbattista et al., 2014; see Section 5.1 for more details and equations).

We lastly determined the 68% (1σ), 95.4% (2σ), and 99.73% (3σ) confidence contours surrounding the best-fit solution in (α,ζ) space as described in Section 5.1. We used the χ^2 probability density function for $\mu_{\rm dof} = 2$, given the two dimensions α and ζ of the χ^2 contour plots. Therefore, we obtained $\Delta\xi^2_{1\sigma,\mu_{\rm dof}} = 2.30$, $\Delta\xi^2_{2\sigma,\mu_{\rm dof}} = 6.17$, and $\Delta\xi^2_{3\sigma,\mu_{\rm dof}} = 11.8$ (for the table see Press et al., 1992). The best-fit solution is positioned at $\xi^2_{\rm opt} = 96$ and enclosed by the confidence contours with values of $\xi^2_{1\sigma,N_{\rm dof}} = 96 + 2.30$, $\xi^2_{2\sigma,N_{\rm dof}} = 96 + 6.17$, and $\xi^2_{3\sigma,N_{\rm dof}} = 96 + 11.8$ (see Eq. [5.8]).

6.3 Results: $\chi^2(\alpha, \zeta)$ contours and best-fit light curves

In this section we present our best-fit solutions of the simulated light curves to the Vela data. In what follows, to enhance contrast, we plotted $\log_{10}\xi^2$ (with ξ^2 the scaled χ^2) on an (α,ζ) grid ranging over $\alpha \in [0°, 90°]$ and $\zeta \in [0°, 90°]$ (1° resolution), with the colour bar representing $\log_{10}\xi^2$, with a minimum of $\log_{10}\xi^2_{\rm opt} = \log_{10}N_{\rm dof} = 1.98$ (corresponding to the best-fit solution by construction). This best-fit solution is indicated by the white star on the contour surrounded by the confidence contours for 1σ (magenta line), 2σ (green line), and 3σ (red line). We show an enlargement in the bottom left corner of these contours, since the confidence intervals are typically very small. Using this enlargement, the upper and lower errors on the optimal fit could be determined. We determined errors on α and ζ for the optimal solution of each B-field and gap model combination using the 3σ connected contours. We considered a bounding box delimited by a minimum and maximum value in both α and ζ which surrounds the 3σ contour. The lower errors are measured from the position in α and ζ of the optimal solution to the minimum boundary, and similar for the upper errors concerning the maximum boundary. We illustrated this in Figure 6.10 with the white lines indicating the bounding box

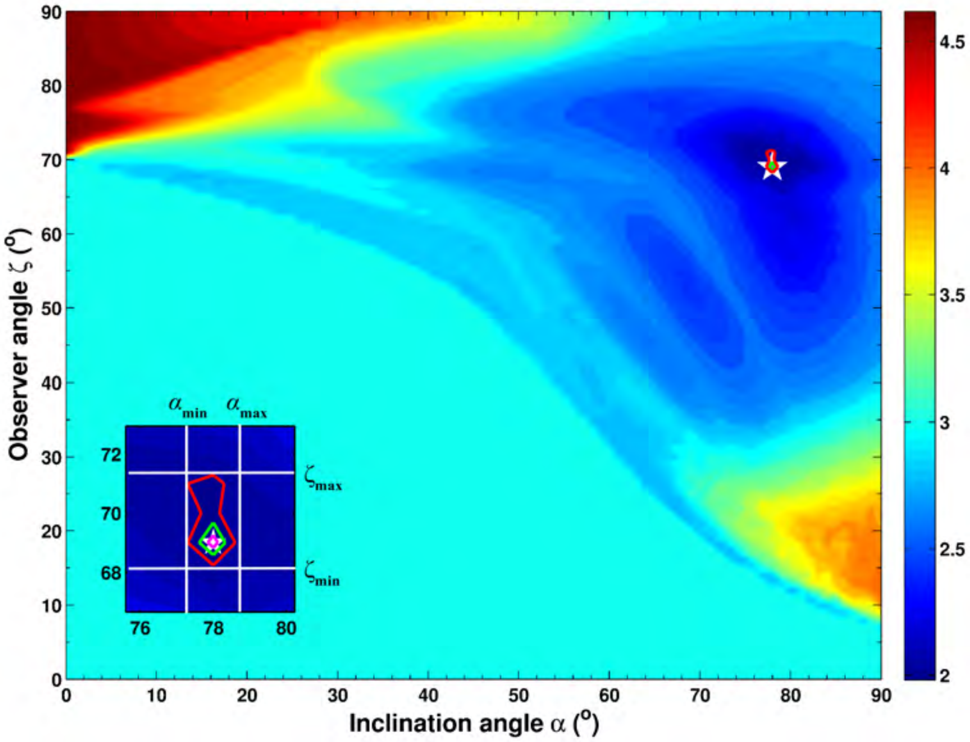

Figure 6.10: Contour plot for the RVD B-field and OG model on an (α,ζ) grid. The colour bar represents $\log_{10}\xi^2$, with 1.98 corresponding to the best-fit solution, indicated by the white star. The confidence contours for 1σ (magenta line), 2σ (green line), and 3σ (red line) are also shown with an enlargement in the bottom left corner. The white lines on the enlargement indicate the bounding box with $[\alpha_{\rm min}, \alpha_{\rm max}]$ and $[\zeta_{\rm min}, \zeta_{\rm max}]$ the lower and upper errors on α and ζ, respectively, as measured from the position of the optimal solution.

$[\alpha_{\rm min}, \alpha_{\rm max}]$ and $[\zeta_{\rm min}, \zeta_{\rm max}]$. We chose errors of 1° for cases when the errors were smaller than one (given our chosen resolution of 1°). The corresponding light curve fit of the model (solid red line) for the best-fit geometry to the Vela data (blue histogram) is also shown (Figure 6.11). The observed light curve represents weighted counts per bin as function of normalised $\phi_{\rm L} = [0, 1]$. We note that the observed light curve of the Vela pulsar shows no off-pulse emission between $\phi_{\rm L} = 0.0 - 0.06$ and $\phi_{\rm L} = 0.7 - 1.0$, and also displays three peaks (Abdo et al., 2013). The first peak (P1) is visible at $\phi_{\rm L} = 0.1 - 0.15$, the second (P2) at $\phi_{\rm L} = 0.48 - 0.61$, and the "bump" (P3) at $\phi_{\rm L} = 0.18 - 0.32$ is identified as the third peak, which is part of the "bridge" emission (emission between P1 and P2).

In Figure 6.10 we present our scaled χ^2 contour, $\log_{10}\xi^2$ for our overall best statistical fit, for an OG model using an RVD field. We found a best-fit at $\alpha = 78^{+1^\circ}_{-1}$, $\zeta = 69^{+2^\circ}_{-1}$, $A = 1.3$, and $\Delta\phi_{\rm L} = 0$. The curved region ranging from $\zeta = 70°$ downward to $\zeta = 10°$, over the entire range of α, is caused by the caustic structure as seen on the phase plots (i.e., there is no emission visible for low values of α and ζ – the turquoise bottom-left region). In Figure 6.11 our best-fit light curve for an RVD field and OG model is shown. The model light curve yields a qualitatively good fit to the Vela data. The model exhibits distinct qualitative features including the three peaks at the same phases, with the same width, as seen in the Vela data. The peaks are approximately the same height as those of the data, and the model also displays a low level of off-peak emission. P1 and P3 of the model are slightly lower than those of the data, and P2 of the model slightly higher. The OG model fits the

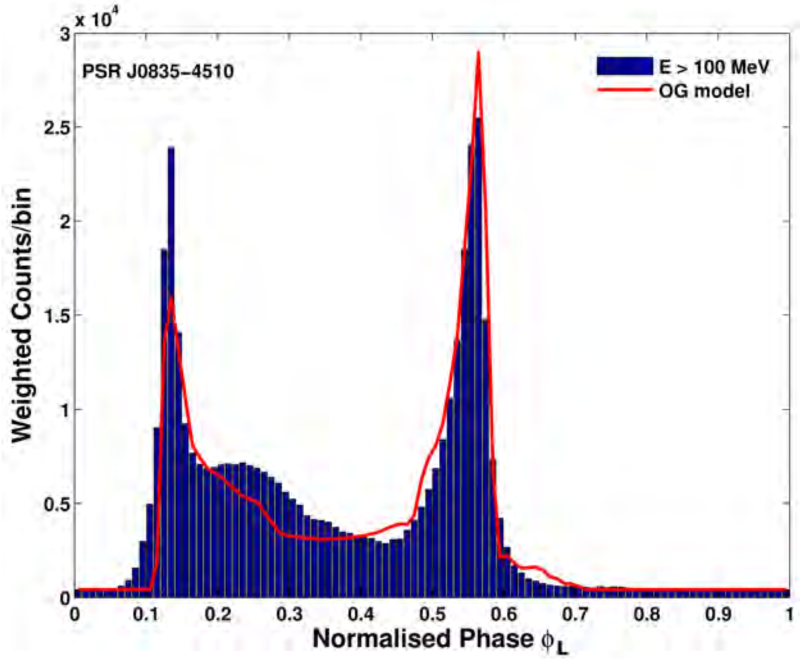

Figure 6.11: Corresponding best-fit light curve for the RVD and OG model. The blue histogram denotes the observed Vela profile (for energies $E > 100$ MeV, Abdo et al., 2013) and the red line the geometric model light curve.

data qualitatively better than the TPC model since the OG model displays less off-pulse emission, as seen in the phase plots and light curves in Sections 6.1.3 and 6.1.4.

In Figure 6.12 we present our significance contour $\log_{10}\xi^2$ and in Figure 6.13 the corresponding best-fit light curve for a TPC model assuming an offset dipole field, with $\epsilon = 0.00$ and a constant ϵ_ν. This best-fit solution corresponds to the best fit found for the static dipole field and TPC case (see Table 6.1). For the offset dipole field and TPC model ($\epsilon = 0$), we find an optimal solution at $\alpha = 73^{+3^\circ}_{-2}$, $\zeta = 45^{+4^\circ}_{-4}$, $A = 1.3$, and $\Delta\phi_{\rm L} = 0.55$. Disconnected confidence intervals are visible in this case, with the 3σ errors (using connected confidence contours) on α and ζ yielding larger values than in Figure 6.10. At most angle combinations the fit is quite poor, however at large α, over all ζ, the fit becomes statistically better. The curved region ranging from $\zeta = 0^\circ$ upward to $\zeta = 56^\circ$, over all α, is due to the caustic structure, and is significantly different compared to the RVD field and OG model case. The best-fit model light curve yields a reasonable fit to the Vela data, since the model exhibits one peak coinciding with P2 in the data. The model also displays a low level of off-peak emission similar to the data and the "bridge" emission is very low. However, the observed P1 and P3 are not reproduced by the model. If we compare Figure 6.11 to Figure 6.13, we notice that the light curves are different, underscoring the importance of the magnetic structure and geometric model.

In Figure 6.14 we present our significance contour $\log_{10}\xi^2$ and in Figure 6.15 the corresponding best-fit light curve for an SG model using an offset dipole field, with $\epsilon = 0.18$ and a variable ϵ_ν. For this combination, we find a best-fit solution at $\alpha = 75^{+2^\circ}_{-1}$, $\zeta = 40^{+6^\circ}_{-4}$, $A = 0.5$, and $\Delta\phi_{\rm L} = 0.55$. At most angle combinations the fit is qualitatively better than for the TPC case (Figure 6.12), however at $\alpha > 70^\circ$, over all ζ, the fit becomes statistically even better. The curved region ranging from $\zeta = 0^\circ$ upward to $\zeta = 56^\circ$, over $\alpha = 60^\circ - 90^\circ$, is due to the caustic structure, and is significantly different compared to the previous two cases. The model light curve

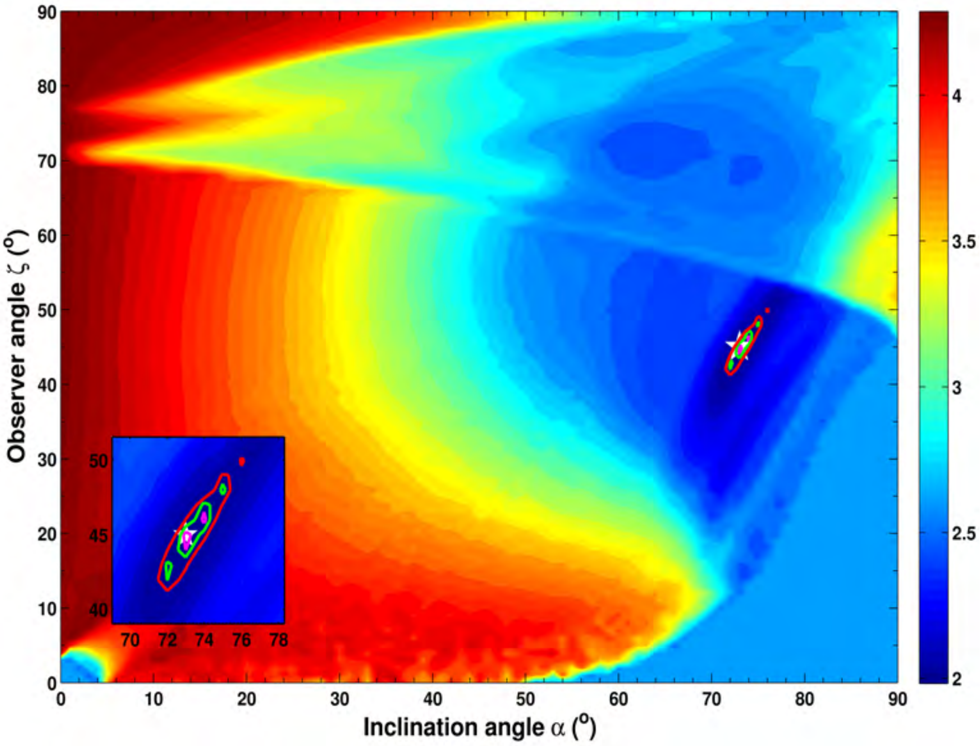

Figure 6.12: The same as Figure 6.10 but for the offset dipole B-field and TPC model for constant ϵ_ν and ϵ = 0.00. This contour is equivalent to the optimal fit for the static dipole and TPC model.

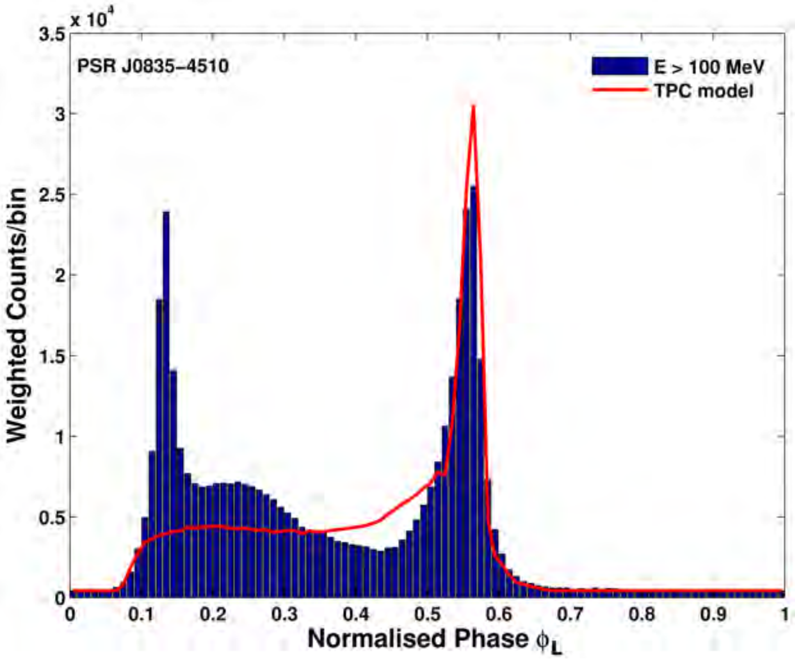

Figure 6.13: The same as Figure 6.11 but for the offset dipole B-field and TPC model for constant ϵ_ν and ϵ = 0.00. This best-fit light curve is equivalent to the optimal fit for the static dipole and TPC model.

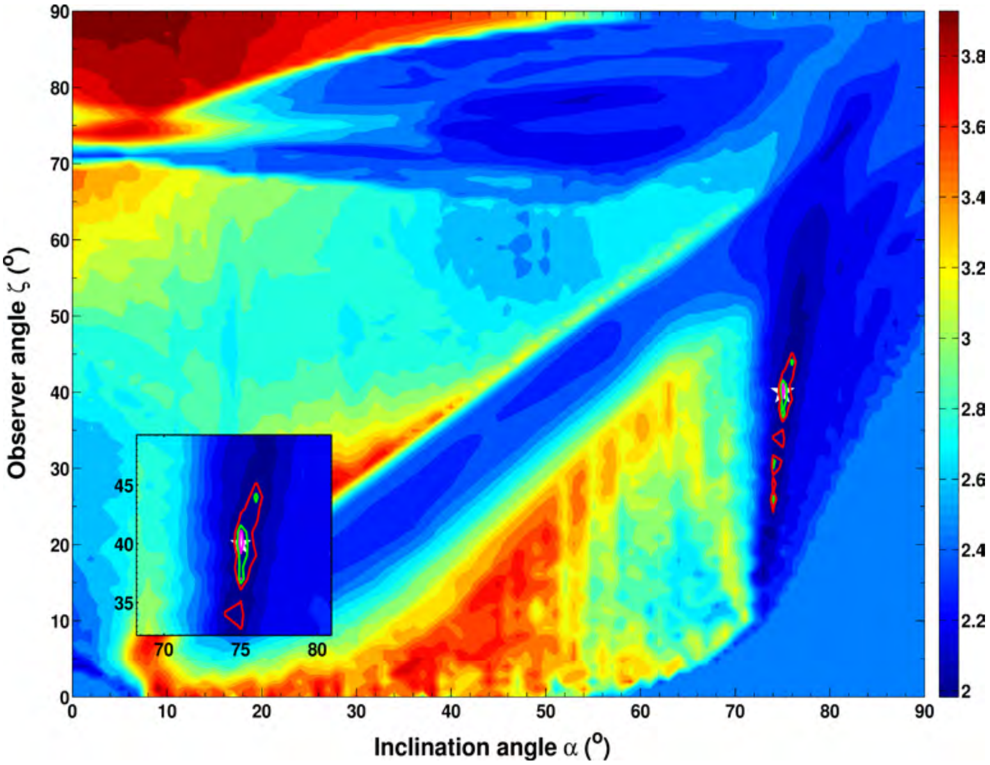

Figure 6.14: The same as Figure 6.10 but for the offset dipole and SG model for variable ϵ_ν and $\epsilon = 0.18$.

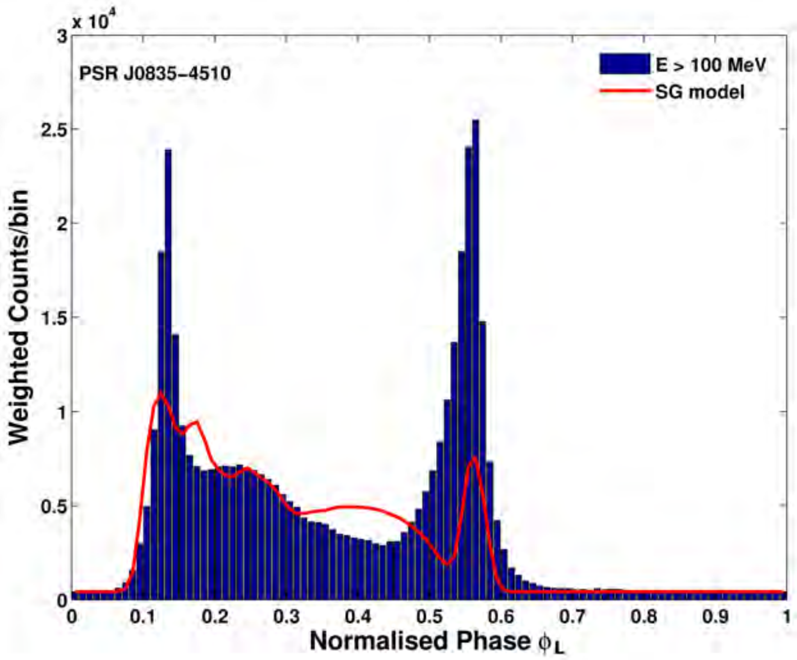

Figure 6.15: The same as Figure 6.11 but for the offset dipole B-field and SG model for variable ϵ_ν and $\epsilon = 0.18$.

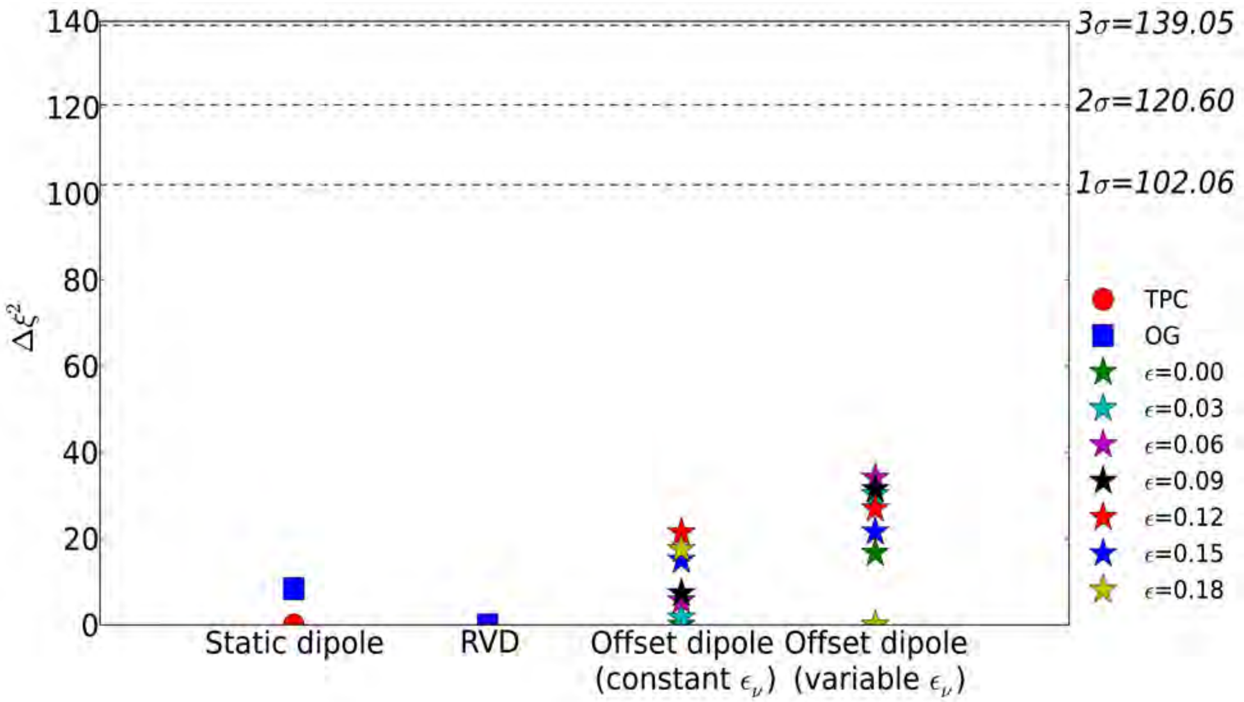

Figure 6.16: Comparison of the relative goodness of the fit solutions, obtained for each B-field for the different geometric models for the Vela pulsar. The difference between the optimum and alternative model is expressed as $\Delta\xi^2$, with the horizontal dashed lines indicating the confidence levels. Circles and squares refer to the TPC and OG models for both the static dipole and RVD. The stars refer to the different ϵ values for the offset dipole and TPC model, for both the constant and variable ϵ_ν cases.

yields a reasonable fit to the Vela data, but the peaks are low (constrained by the low level of off-peak emission, i.e., the χ^2 prefers a small value for A) and very broad compared to the data. The peaks of the model light curve do not line up with respect to the observed peaks and it displays a low level of off-peak emission. If we compare Figure 6.11 and Figure 6.13 with Figure 6.15, we notice that the light curve is qualitatively different.

6.4 Comparison of different models

We next follow the same approach as Pierbattista et al. (2014), who compared the relative goodness of the fit solutions in order to test which alternative models could also give good fits besides the optimal model, and which models to reject. Pierbattista et al. (2014) performed a χ^2 test to determine the best-fit solutions for several LAT-observed radio-quiet and radio-loud young pulsars, using geometric radio and γ-ray models. For each B-field, we determine the difference between the optimal model, $\xi^2_{\rm opt}$ (the overall best fit) and the other models (ξ^2) using Eq. (5.8), and substitute $N_{\rm dof} = 96$ as well as the unscaled values of χ^2, as summarised in Table 6.1. These symbols have the same definition as in Chapter 5 and the sections above.

In Figure 6.16 we illustrate the different B-field structures along the x-axis, and $\Delta\xi^2$ on the y-axis. We represent the TPC geometry with a red circle, the OG with a blue square, and for the offset dipole field we represent the various ϵ values, for both constant and variable ϵ_ν, by different coloured stars. The horizontal lines on the figure indicate our confidence levels for $N_{\rm dof} = 96$, using Eq. (5.8) and a χ^2 distribution table to obtain the levels corresponding to $N_{\rm dof} = 96$. We calculate the $\Delta\xi^2$ values using an online χ^2 statistic calculator[1], using p-values of $p_{1\sigma} = 1 - 0.682$, $p_{2\sigma} = 1 - 0.954$, and $p_{3\sigma} = 1 - 0.9973$, and obtained the critical values of $\Delta\xi^2 = 102.06$ (1σ), 120.60 (2σ), and 139.05 (3σ) respectively. These confidence levels are used as indicators of when to reject or accept an alternative fit solution compared to the optimum fit solution.

For the static dipole field the TPC model gives the optimum fit and the OG model is within 1σ, implying that the OG geometry may provide an acceptable alternative fit to the data. For the RVD field the TPC model is significantly rejected beyond the 3σ level (not shown on plot), and the OG model is preferred. We show two cases for the offset dipole field, including the TPC model assuming constant ϵ_ν, and SG model assuming variable ϵ_ν. The optimal fits for the offset dipole field and TPC model reveal that a smaller offset is preferred for constant ϵ_ν, while a larger offset is preferred for variable ϵ_ν (but not significantly), with all alternative fits falling within 1σ.

The best-fit parameters for each B-field and geometric model combination are summarised in Table 6.1. The table includes the different model combinations, the optimal unscaled χ^2 value for each combination, the best-fit free parameters with 3σ-errors on α and ζ, the comparison between models using the difference between the respective optimal values of ξ^2, represented by $\Delta\xi^2$ (with $\Delta\xi^2 = 0$ representing the best-fit solution for each B-field; Pierbattista et al., 2014), and several multi-wavelength reference fits (all for the Vela pulsar).

Several multi-wavelength studies have been performed for Vela, using the radio, X-ray, and γ-ray data, in order to find constraints on α and ζ. We only fitted the γ-ray light curve, because we do not want to bias our results with a simplistic radio model. However, Johnston et al. (2005) determined the radio polarisation position angle from polarisation data by applying an RVM fit to the data. They established that the RVM fit is robust for Vela, and obtained best-fit values of $\alpha = 53^\circ$ and $\zeta = 59.5^\circ$, with an impact angle of $\beta = \zeta - \alpha = 6.5^\circ$. The Vela pulsar is situated inside the pulsar wind nebula (PWN) Vela X. Ng & Romani (2008) applied a torus-fitting technique (Ng & Romani, 2004) to fit the *Chandra* PWN data in order to constrain the PWN geometry, in which the torus is assumed to be perpendicular to the $\mathbf{\Omega}$-axis and therefore constrains ζ. They used a χ^2 estimator and derived a value of $\zeta = 63.6^{+0.07^\circ}_{-0.05}$. More similar to what we have done is the geometric light curve modelling performed by Watters et al. (2009) and DeCesar (2013). Watters et al. (2009) modelled light curves using the PC, TPC, and OG geometries in conjunction with an RVD field, thereby constraining the geometrical parameters α and ζ. They found a good fit for their TPC model at $\alpha = 62^\circ - 68^\circ$ and $\zeta = 64^\circ$, and for the OG geometry at $\alpha = 75^\circ$ and $\zeta = 64^\circ$. If we compare our best-fit values for the RVD field, for both the TPC and OG models, with those found by Watters et al. (2009), we conclude that our best-fit values are close to these results. DeCesar (2013) followed a similar approach to ours, but for the RVD and FF B-fields combined with emission geometries such as the SG (symmetric and asymmetric cases) and OG. They have different free model parameters including α, ζ, w (gap width), and $R_{\rm max}$ (maximum emission radius), and determined errors on their best fits using the 3σ confidence interval. They found best-fit solutions for the RVD and OG model at $\alpha = 88^{+2^\circ}_{-3}$ and $\zeta = 66.5^\circ$, which is within 10° or less compared to our best-fit solution. For the RVD B-field and symmetric SG they obtained $\alpha = 44^{+4^\circ}_{-1}$ and $\zeta = 54.5^{+1.0^\circ}_{-5.0}$. Their overall best fit was for the FF B-field and OG geometry, with $\alpha = 80^{+1^\circ}_{-1}$ and $\zeta = 52.5^{+1^\circ}_{-1}$. Pierbattista et al. (2014) found a best-fit solution for Vela using the RVD field and OG model combination, at $\alpha = 71^{+2^\circ}_{-2}$ and $\zeta = 83^{+2^\circ}_{-2}$, with ζ exceeding the best-fit solution we found by nearly 15°. They fitted both the γ-rays and radio, which may explain this discrepancy.

[1]http://easycalculation.com/statistics/critical-value-for-chi-square.php, using $1 - p$

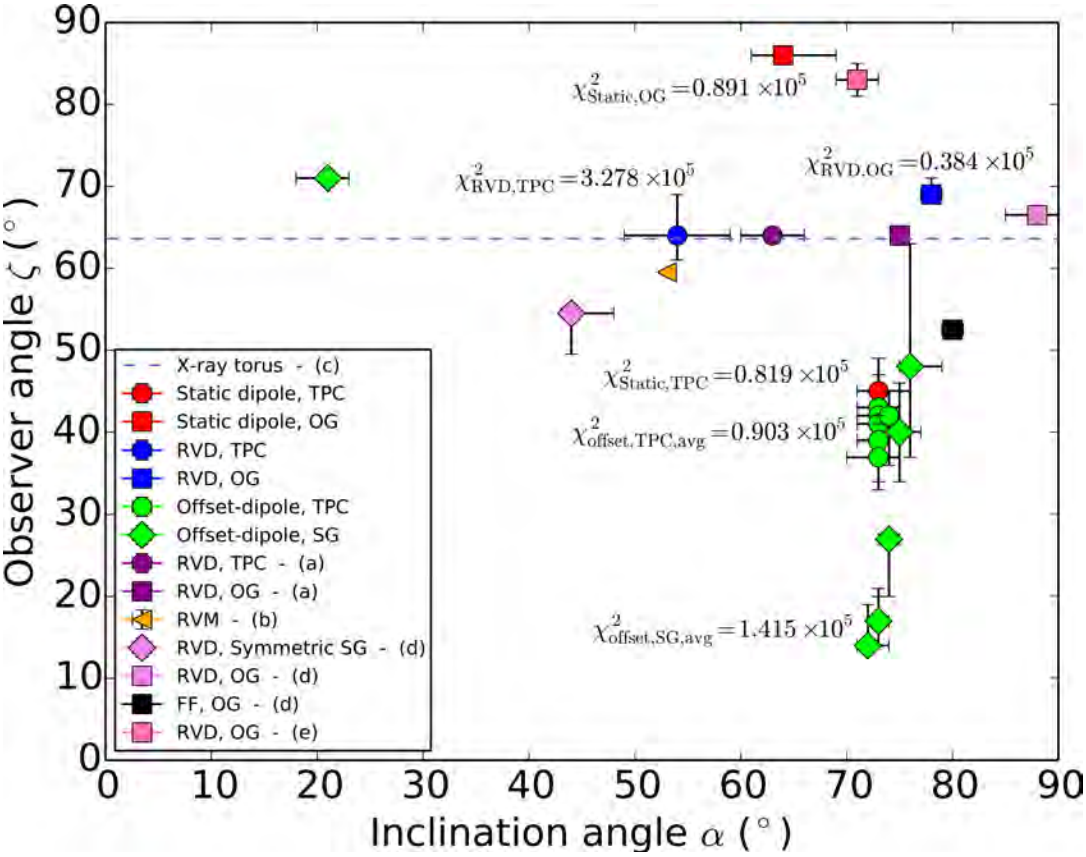

Figure 6.17: Comparison between the best-fit α and ζ, with errors, obtained from this and other studies. Each marker represents a different case as summarised in Table 6.1, with the unscaled χ^2 value of our fits indicated. For the offset dipole, for both the TPC and SG models we indicate the average χ^2 value over the range of ϵ.

We graphically summarise the best-fit α and ζ, with errors, from this and other works in Figure 6.17. We notice that the best fits generally prefer a large α or ζ or both. A significant fraction of fits furthermore lie near the $\alpha - \zeta$ diagonal, i.e., the prefer a small impact angle, probably due to radio visibility constraints. For an isotropic distribution of pulsar viewing angles, one expects ζ values to be distributed as $\sin(\zeta)$ between $\zeta = [0^\circ, 90^\circ]$, i.e., large ζ values are much more likely than small ζ values, which seems to correspond to the large best-fit ζ values we obtain. There seems to be a reasonable correspondence between our results obtained for geometric models and those of other authors, but less so for the offset dipole B-field, and in particular for the SG E-field case. Although our best fits for the offset dipole B-field are clustered, it seems that increasing ϵ leads to a marginal decrease in ζ for the TPC model. It is lastly encouraging that many of the best-fit solution do lie near the ζ inferred from the PWN torus fitting (Ng & Romani, 2008), notably for the RVD B-field.

6.5 Summary

We made use of geometric light curve modelling in order to constrain the emission geometry of the Vela pulsar. We implemented various B-field structures into a geometric modelling code and simulated light curves for combinations of these B-fields with different geometric gap models and geometric parameters. We constructed various phase plots and light curve atlases. The observed light curves reveal certain emission characteristics,

Table 6.1: Best-fit parameters for each *B*-field and geometric model combination.

Combinations		Our model parameters						Other multi-wavelength fits		
Model	ϵ	χ^2 ($\times 10^5$)	α (°)	ζ (°)	A	$\Delta\phi_{\rm L}$	$\Delta\xi^2$	α (°)	ζ (°)	References
Static dipole B-field										
TPC	–	0.819	73^{+3}_{-2}	45^{+4}_{-4}	1.3	0.55	0.00			
OG	–	0.891	64^{+5}_{-3}	86^{+1}_{-1}	1.3	0.05	8.44			
RVD B-field										
TPC	–	3.278	54^{+5}_{-5}	67^{+5}_{-3}	0.5	0.05	723.50			
OG	–	0.384	78^{+1}_{-1}	69^{+2}_{-1}	1.3	0.00	0.00			
Offset dipole B-field for constant ϵ_v										
TPC	0.00	0.819	73^{+3}_{-2}	45^{+4}_{-4}	1.3	0.55	0.00			
	0.03	0.834	73^{+2}_{-2}	43^{+4}_{-5}	1.3	0.55	1.76			
	0.06	0.867	73^{+2}_{-2}	42^{+5}_{-5}	1.3	0.55	5.63			
	0.09	0.882	73^{+1}_{-2}	41^{+3}_{-5}	1.3	0.55	7.39			
	0.12	1.000	74^{+1}_{-3}	42^{+3}_{-6}	1.4	0.55	21.22			
	0.15	0.948	73^{+1}_{-2}	39^{+3}_{-5}	1.4	0.55	15.12			
	0.18	0.969	73^{+2}_{-3}	37^{+4}_{-4}	1.3	0.55	17.58			
Offset dipole for variable ϵ_v										
SG	0.00	1.587	21^{+3}_{-3}	71^{+1}_{-1}	0.5	0.85	17.03			
	0.03	1.627	73^{+1}_{-1}	17^{+4}_{-3}	0.7	0.55	30.19			
	0.06	1.525	72^{+2}_{-1}	14^{+5}_{-1}	0.5	0.60	34.07			
	0.09	1.452	73^{+1}_{-1}	17^{+3}_{-1}	0.6	0.55	31.74			
	0.12	1.437	74^{+1}_{-1}	27^{+1}_{-7}	0.8	0.55	27.10			
	0.15	1.156	76^{+3}_{-1}	48^{+15}_{-11}	0.7	0.55	21.68			
	0.18	1.119	75^{+2}_{-1}	40^{+6}_{-4}	0.5	0.55	0.00			
RVD & TPC								62 – 68	64	a
RVD & OG								75	64	a
RVM								53	59.5	b
X-ray torus									$63.6^{+0.07}_{-0.05}$	c
RVD & Symmetric SG								44^{+4}_{-1}	$54.5^{+1.0}_{-5.0}$	d
RVD & OG								88^{+2}_{-3}	66.5^{+1}_{-1}	d
FF & OG								80^{+1}_{-1}	52.5^{+1}_{-1}	d
RVD & OG								71^{+2}_{-2}	83^{+2}_{-2}	e

References:
[a]Watters et al. (2009)
[b]Johnston et al. (2005)
[c] Ng & Romani (2008)
[d]DeCesar (2013)
[e] Pierbattista et al. (2014)

Notes - The table summarises the best-fit parameters α (°), ζ (°), A, and $\Delta\phi_{\rm L}$, for each model combination, with the error bars denoting the 3σ connected confidence intervals. We chose a minimum error of 1° if the confidence contour yielded smaller errors. We included the unscaled χ^2 to indicate which geometry yields the optimal fit to the Vela data (i.e., the OG model and RVD *B*-field).

thus we fitted our model light curves to the observed light curve to determine which geometry and *B*-field combination describes the observations the best. We performed a χ^2-fitting procedure to find the optimal fit of the model to the data. We illustrated the fits as $\chi^2(\alpha, \zeta)$ contours and best-fit light curves (including the model and the observed light curve).

We compared the optimal model to the alternative models for each *B*-field, by calculating the difference between the respective scaled χ^2 values using Eq. (5.8). All the combinations of *B*-field and model geometries delivered good fits within 2σ, except the RVD and TPC model case (see Table 6.1). The OG model fits the data qualitatively better than the TPC or SG model, since the Vela pulsar displays less off-peak emission. We only fitted the γ-ray light curve for Vela, although multi-wavelength studies performed by other pulsar researchers have found constraints on geometric parameters α and ζ which are close to the values we found in our studies. Therefore the choice of pulsar geometry and geometric parameters is essential to predict the observations.

Chapter 7

Summary

Pulsars are compact NSs that rotate at tremendous rates and contain strong electric, magnetic, and gravitational fields (e.g., Abdo et al., 2010b). These extreme conditions make pulsars valuable laboratories for studying a wide range of topics. Pulsars emit pulsed emission across the entire electromagnetic spectrum, including radio, optical, X-rays, and γ-rays, in addition to injecting HE particles (cosmic-ray leptons) into the ambient environment. In this project we focused on γ-ray pulsars, specifically the Vela pulsar (a bright pulsar in the GeV band) which serves as a calibration source for the *Fermi* Large Area Telescope and has been detected at a very high significance.

The field of γ-ray pulsars has been revolutionised by the launch of *Fermi*, increasing the population from 7 to 161[1]. The light curves of these γ-ray pulsars exhibit a variety of profile shapes, and also different relative phase lags with respect to their radio pulses. Detailed geometric modelling (e.g., Dyks et al., 2004a; Venter et al., 2009; Watters et al., 2009; Johnson et al., 2014; Pierbattista et al., 2014) of the radio and γ-ray light curves provided constraints on the *B*-field structure, pulsar geometry (inclination angle α and the observer angle ζ), as well as the γ-ray emission region's location and extent.

The aim of this study was to investigate the impact of different magnetospheric structures on the predicted γ-ray pulsar light curve characteristics. We had access to a geometric modelling code which already included the static (non-rotating) dipole and the rotating RVD solutions (Dyks & Harding, 2004; Deutsch, 1955). We extended this code by implementing an additional *B*-field, i.e., the symmetric offset dipole field (Harding & Muslimov, 2011a,b), with an offset of the magnetic PCs (from the $\boldsymbol{\mu}$ axis) characterised by parameters ϵ (with $\epsilon = 0$ corresponding to the static dipole case) and magnetic azimuthal angle ϕ_0' (specifying the meridional plane in which the PCs are offset). We determined the PC rim in a similar manner as for the static dipole and RVD cases. We next extended the range of ϵ yielding numeric solutions for the PC rim.

It is important to take the accelerating *E*-field into account (in a physical model) when such an expression is available, since this will modulate the γ-ray emissivity ϵ_ν in the acceleration region, as opposed to geometric models where we assume constant ϵ_ν per unit length in the corotating frame. For the offset dipole we included the full accelerating (parallel to the local *B*-field) SG *E*-field (corrected for general relativistic effects) up to high altitudes. If one considers an HE emission model, assuming that curvature radiation from primary particles is the dominant radiation process, it is useful to test whether the primary particles reach the CRR limit (when the energy gain balances the losses, and the time-derivative of the Lorentz factor $\dot{\gamma} = 0$). The general *E*-field

[1] https://confluence.slac.stanford.edu/display/GLAMCOG/Public+List+of+LAT-Detected+Gamma-Ray+Pulsars

enables us to solve the transport equation in order to test whether this limit is reached.

We performed geometric light curve modelling assuming standard pulsar emission geometries, i.e., the TPC (of which the SG is its physical representation; Dyks & Rudak, 2003), and OG (Romani, 1996) models. The B-field structure is, however, essential for predicting the light curves seen by the observer, since photons are expected to be emitted tangentially to the local B-field lines in the corotating pulsar frame (Daugherty & Harding, 1982). Even a small difference in the magnetospheric structure will therefore have an impact on the light curve predictions. We utilized the static dipole, RVD, and offset dipole solutions, in conjunction with the TPC and OG geometries. The offset dipole solution is a heuristic model (a perturbation of a static dipole B-field) that mimics deviations from the static dipole at low altitudes (near the NS surface) analytically such as occur in complex solutions, e.g., dissipative (Kalapotharakos et al., 2012; Li et al., 2012; Li, 2014; Tchekhovskoy et al., 2013) and force-free (Contopoulos et al., 1999) fields. These complex B-fields have only numerical solutions, and are limited by the resolution of the assumed spatial grid. Since these fields display some degree of offset in their PCs, the offset dipole case provides an easier analytical description of this effect.

For the offset dipole field we only considered the TPC (assuming uniform ϵ_ν) and SG (modulating the ϵ_ν using the E-field) models, since we do not have E-field expressions available for the OG model for this B-field. The implementation of the offset dipole field involved a transformation of the B-field components from the magnetic to the rotational frame, as well as Cartesian to spherical co-ordinates (Appendix A). As mentioned above, we extended the range of ϵ in order to determine the PC rim, since the code could not find any solutions given the predefined solution space involving the colatitude of the last open field line footpoints. We matched low-altitude and high-altitude solutions of the SG $E_{\|}$ by determining the matching parameter $\eta_{\rm c}(P, \dot{P}, \alpha, \epsilon, \xi, \phi_{\rm PC})$ (with ξ the dimensionless colatitude, and $\phi_{\rm PC}$ the magnetic azimuthal angle) on each field line. We therefore needed to solve for $\eta_{\rm c}$ in multivariate space. Once we calculated the general E-field we could solve the particle transport equation. This yielded the particle Lorentz factor $\gamma_e(\eta)$ (as a function of normalised radial distance η in units of $R_{\rm LC}$), necessary for determining the curvature radiation emissivity and to test whether the CRR limit is attained.

We constructed sky maps (the intensity per solid angle as a function of α, ζ and phase $\phi_{\rm L}$) and light curves (the flux as a function of time or $\phi_{\rm L}$) for the various B-field and geometric model combinations, as well as for several different pulsar parameters (α, ζ and ϵ). We wanted to compare our model light curves to the superior-quality γ-ray light curve of the Vela pulsar as measured by *Fermi* in the GeV energy range (> 100 MeV). To do this, we applied a chi-squared (χ^2) method. The χ^2 method searches the multivariate solution space for optimal model parameters, facilitating the statistical selection of the best-fit solution for the Vela pulsar light curve for each of the different models. We also studied alternative fitting methods but preferred the χ^2 statistical method, since we could determine errors on the best-fit parameters in the usual way in this case (by constructing 1σ, 2σ, and 3σ confidence contours). This was also useful for comparing the best fits for each model combination.

We compared these sky maps and light curves to study the effect of different B-field structures and geometric models on the predicted pulsar light curves. It was evident from our phase plots and light curves that the magnetospheric structure and emission geometry determine the pulsar visibility and also the γ-ray pulse shape. We noticed that for the TPC geometry, prominent light curve features (i.e., double-peak profiles, wings, bridge emission, a level of non-vanishing off-peak emission, and radio pulse leading the γ-ray pulse) are visible. Also, more of phase space (α, ζ) is filled with emission visible from both poles. The OG model also exhibits some of these features (i.e., double-peak profiles, bridge emission, and radio pulse leading the γ-ray pulse), however it displays nearly no off-peak emission, with the emission being visible from a single magnetic pole only. See Appendix B for a more detailed discussion.

There is a small but noticeable effect for the symmetric offset dipole field in the phase plots and light curves. When we increased ϵ, we observed that the PC was indeed offset, compared to the case of the static dipole when assuming a constant emissivity, although the offset was not significant. When we assumed $\epsilon = 0$ and a constant ϵ_ν, we obtained the same phase plots and light curves as those for the static dipole solution, validating our implementation of the offset dipole field (Appendix A). However, when we included an SG E-field, thereby modulating ϵ_ν, the resulting phase plots and light curves became qualitatively different compared to the geometric case. When we modulated ϵ_ν, we found that the CRR limit is reached for many parameter combinations of (α, ϵ and $\phi_{\rm PC}$; see Figure 4.6, 4.7 and 4.8), albeit only at large η. A notable exception occurs at large α where the first term of each E-field expression (e.g., Eq. [4.5] and [4.6]) becomes lower and the second term plays a larger role, leading to smaller gain rates and therefore smaller Lorentz factors. This is important to know when interpreting the observed pulsar spectral cutoffs (e.g., Abdo et al., 2010c).

We fitted our model light curves to the observed Vela light curve for each B-field and geometric model combination and found an optimal fit in each case using our χ^2 fitting method. For each optimal fit we derived 3σ errors on α and ζ (see Table 6.1). We furthermore found that the RVD field in combination with an OG model fitted the observed light curve the best for $(\alpha, \zeta, A, \Delta\phi_{\rm L}) = (78^{+1}_{-1}{}^\circ, 69^{+2}_{-1}{}^\circ, 1.3, 0.00)$ with the unscaled $\chi^2 = 3.84 \times 10^4$. We also statistically compared the best fits of the different model combinations.

7.1 Conclusions

From our results we conclude that the magnetospheric structure and emission geometry have an important effect on the predicted γ-ray pulsar light curves. However, the presence of an E-field may have an even greater effect than small changes in the B-field and geometric models. The E-field is crucial for solving the transport equation and determining whether particles reach the CRR limit.

We compared the optimal light curve model to alternative models for each B-field geometry by calculating the difference between the respective scaled χ^2 values using Eq. (5.8). As seen in Figure 6.16 we noted that for the RVD field an OG model is significantly preferred over the TPC model. Since the Vela light curve possesses characteristically low off-peak emission, the OG geometry fits the Vela data better than the TPC model. However, for the other field and model combinations there are no significant preferred model since all the alternative models may provide an acceptable alternative fit to the data, within 1σ. The offset dipole field for constant ϵ_ν favours smaller values of ϵ, and for variable ϵ_ν larger ϵ values, but not significantly so ($< 1\sigma$).

7.2 Future prospects

The tools we have developed during the course of this study encourage us to envision some new projects. We want to continue to extend the range of ϵ for which our code finds the PC rim, since more complex offset field solutions, e.g., the dissipative and force-free field structures may be associated with larger PC offsets. Larger offsets will also enable us to find a significantly preferred best fit for the offset dipole field (see Figure 6.16).

Since we now have the analytical means for transforming between a magnetic and rotational frame, we can continue to produce light curves using improved geometric models and new B-fields specified in the magnetic frame. We can extend this project even further by including new E-field solutions. Such E-field expressions would require the solution of the transport equation to test if the particles reach the CRR limit.

A possible improvement to the analysis that may help with the χ^2 fitting method would be to use weighted counts for the light curve. From these weights we can estimate the background level, thereby estimating where to put the baseline in our model light curves. Also, we can consider our model light curves as normalised probability density functions along with the weighted counts to determine the log-likelihood for each (α,ζ) pair. However, to obtain the maximum advantage from these improvements, we will need more refined models.

One could furthermore redo light curve fitting, using more data, in order to search for best-fit profiles, thereby ensuring more constraining power on the pulsar geometry on α and ζ. However, there is also potential for multi-wavelength studies, such as light curve modelling in the other energy bands, e.g., radio and γ-rays. The light curves obtained for both the radio and γ-rays are fitted, considering the radio-peak multiplicity, radio to γ-ray phase lag, and the γ-ray profile shape. Inclusion of radio light curves will restrict optimal solutions to small values of $\beta \equiv \zeta - \alpha$ (impact angle between $\boldsymbol{\mu}$ and ζ, see Seyffert et al., 2010, 2012; Pierbattista et al., 2014).

Another potential project is to model energy-dependent light curves, such as those available for Vela using *Fermi* data (e.g., Abdo et al., 2009). There is an energy evolution visible in the light curve features. As the energy increases, the third peak shifts in phase. Also, peak one and two become narrower, and there is a decrease in the ratio of the intensity of peak one and peak two. One can lastly apply the above mentioned projects for several other bright pulsars and not only for the Vela pulsar.

Appendix A

Transformations

A.1 General passive rotation of rectangular axes

Consider two sets of rectangular axes, (x, y, z) and (x', y', z'), the latter representing the rotated system. These two sets are illustrated in Figure A.1. To find a relation between the components of the position vector $\mathbf{r}$ in each of the two co-ordinate systems, we make use of Cartesian tensors to perform a passive rotation, meaning that the axes can undergo multiple rotations, with the position vector $\mathbf{r}$ and origin held fixed (Boas, 2006). This relation can be found in the following way. Let $\hat{\mathbf{x}}$, $\hat{\mathbf{y}}$, and $\hat{\mathbf{z}}$ be the unit basis vectors along the (x, y, z) axes and $\hat{\mathbf{x}}'$, $\hat{\mathbf{y}}'$ and $\hat{\mathbf{z}}'$ along the (x', y', z') axes. Consider a position vector $\mathbf{r}$ which can be written in terms of either set of co-ordinates and its associated unit basis vectors:

$$\mathbf{r} = x\hat{\mathbf{x}} + y\hat{\mathbf{y}} + z\hat{\mathbf{z}} = x'\hat{\mathbf{x}}' + y'\hat{\mathbf{y}}' + z'\hat{\mathbf{z}}'. \tag{A.1}$$

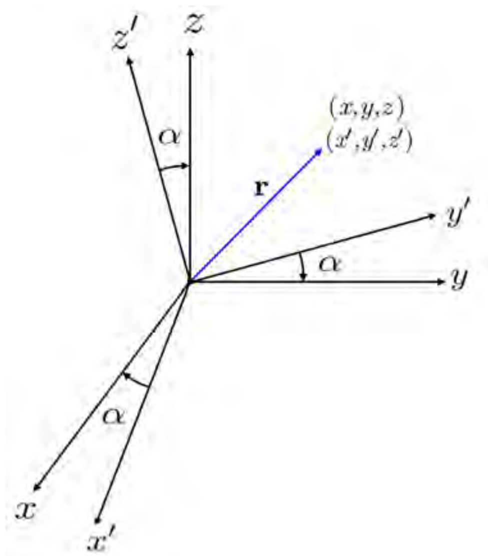

Figure A.1: Illustration of two sets of rectangular axes (x, y, z) and (x', y', z'), rotated with respect to each other by an angle α. The blue line represents a position vector $\mathbf{r}$.

Table A.1: A table summarising the cosines of the angles between various unit basis vectors, used to calculate rotations between (x,y,z) and (x', y', z') axes.

	x	y	z
x'	l_1	m_1	n_1
y'	l_2	m_2	n_2
z'	l_3	m_3	n_3

Taking the scalar product of Eq. (A.1) with $\hat{\mathbf{x}}'$, $\hat{\mathbf{y}}'$ and $\hat{\mathbf{z}}'$ respectively, we obtain the (x', y', z') co-ordinates in terms of the (x, y, z) co-ordinates, using the relations $\hat{\mathbf{x}}'\cdot\hat{\mathbf{x}}' = \hat{\mathbf{y}}'\cdot\hat{\mathbf{y}}' = \hat{\mathbf{z}}'\cdot\hat{\mathbf{z}}' = 1$, $\hat{\mathbf{x}}'\cdot\hat{\mathbf{y}}' = \hat{\mathbf{x}}'\cdot\hat{\mathbf{z}}' = \hat{\mathbf{y}}'\cdot\hat{\mathbf{x}}' = \hat{\mathbf{y}}'\cdot\hat{\mathbf{z}}' = \hat{\mathbf{z}}'\cdot\hat{\mathbf{x}}' = \hat{\mathbf{z}}'\cdot\hat{\mathbf{y}}' = 0$, and $\hat{\mathbf{x}}\cdot\hat{\mathbf{x}}' = \cos\theta_{l_1} = l_1$, $\hat{\mathbf{y}}\cdot\hat{\mathbf{x}}' = \cos\theta_{m_1} = m_1$, $\hat{\mathbf{z}}\cdot\hat{\mathbf{x}}' = \cos\theta_{n_1} = n_1$, etc. (see Table A.1):

$$\begin{aligned} x' &= l_1 x + m_1 y + n_1 z, \\ y' &= l_2 x + m_2 y + n_2 z, \\ z' &= l_3 x + m_3 y + n_3 z. \end{aligned} \tag{A.2}$$

In the same manner, taking the scalar product of Eq. (A.1) with $\hat{\mathbf{x}}$, $\hat{\mathbf{y}}$ and $\hat{\mathbf{z}}$ respectively, we obtain the (x, y, z) co-ordinates in terms of the (x', y', z') co-ordinates, using the relations $\hat{\mathbf{x}}\cdot\hat{\mathbf{x}} = \hat{\mathbf{y}}\cdot\hat{\mathbf{y}} = \hat{\mathbf{z}}\cdot\hat{\mathbf{z}} = 1$, $\hat{\mathbf{x}}\cdot\hat{\mathbf{y}} = \hat{\mathbf{x}}\cdot\hat{\mathbf{z}} = \hat{\mathbf{y}}\cdot\hat{\mathbf{x}} = \hat{\mathbf{y}}\cdot\hat{\mathbf{z}} = \hat{\mathbf{z}}\cdot\hat{\mathbf{x}} = \hat{\mathbf{z}}\cdot\hat{\mathbf{y}} = 0$, and $\hat{\mathbf{x}}'\cdot\hat{\mathbf{x}} = \cos\theta_{l_1} = l_1$, $\hat{\mathbf{y}}'\cdot\hat{\mathbf{x}} = \cos\theta_{l_2} = l_2$, $\hat{\mathbf{z}}'\cdot\hat{\mathbf{x}} = \cos\theta_{l_3} = l_3$, etc. (see Table A.1):

$$\begin{aligned} x &= l_1 x' + l_2 y' + l_3 z', \\ y &= m_1 x' + m_2 y' + m_3 z', \\ z &= n_1 x' + n_2 y' + n_3 z'. \end{aligned} \tag{A.3}$$

Eq. (A.2) and (A.3) are referred to as transformation equations and can be written concisely in matrix notation:

$$\begin{bmatrix} x' \\ y' \\ z' \end{bmatrix} = \begin{bmatrix} l_1 & m_1 & n_1 \\ l_2 & m_2 & n_2 \\ l_3 & m_3 & n_3 \end{bmatrix} \begin{bmatrix} x \\ y \\ z \end{bmatrix} \tag{A.4}$$

(or $\mathbf{r}' = A\mathbf{r}$) and

$$\begin{bmatrix} x \\ y \\ z \end{bmatrix} = \begin{bmatrix} l_1 & l_2 & l_3 \\ m_1 & m_2 & m_3 \\ n_1 & n_2 & n_3 \end{bmatrix} \begin{bmatrix} x' \\ y' \\ z' \end{bmatrix} \tag{A.5}$$

(or $\mathbf{r} = A^{\mathrm{T}}\mathbf{r}'$) with A^{T} the transpose of A.

A.2 Rotation of rectangular axes about the y-axis

As an application of Section A.1, we consider passive rotation of the rectangular axes about the y-axis, with $\mathbf{y}||\mathbf{y}'$, as illustrated in Figure A.2. Assume that the two sets of rectangular axes are rotated by an angle α with

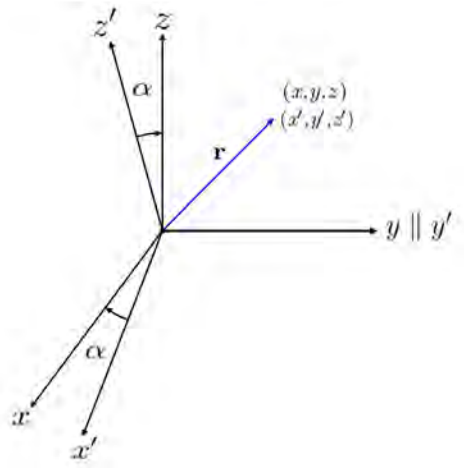

Figure A.2: Illustration of two sets of rectangular axes (x, y, z) and (x', y', z'), rotated with respect to each other about the y-axis by an angle α. The blue line represents the position vector $\mathbf{r}$.

respect to each other. Using Eq. (A.2), together with Table A.1, the following equations are obtained:

$$\begin{aligned} x' &= (\cos\alpha)x + (\cos 90^\circ)y + (\cos(90^\circ+\alpha))z, \\ y' &= (\cos 90^\circ)x + (\cos 0^\circ)y + (\cos 90^\circ)z, \\ z' &= (\cos(90^\circ-\alpha))x + (\cos 90^\circ)y + (\cos\alpha)z. \end{aligned} \tag{A.6}$$

This gives the co-ordinates of the rotated (primed) co-ordinate system in terms of the fixed (unprimed) co-ordinate system. This can be written in matrix form as follows:

$$\begin{bmatrix} x' \\ y' \\ z' \end{bmatrix} = \begin{bmatrix} \cos\alpha & \cos 90^\circ & \cos(90^\circ+\alpha) \\ \cos 90^\circ & \cos 0^\circ & \cos 90^\circ \\ \cos(90^\circ-\alpha) & \cos 90^\circ & \cos\alpha \end{bmatrix} \begin{bmatrix} x \\ y \\ z \end{bmatrix}. \tag{A.7}$$

This is equal to

$$\begin{bmatrix} x' \\ y' \\ z' \end{bmatrix} = \begin{bmatrix} \cos\alpha & 0 & -\sin\alpha \\ 0 & 1 & 0 \\ \sin\alpha & 0 & \cos\alpha \end{bmatrix} \begin{bmatrix} x \\ y \\ z \end{bmatrix}. \tag{A.8}$$

The (x, y, z) in terms of the (x', y', z') can be obtained in the same manner, using Eq. (A.3):

$$\begin{aligned} x &= (\cos\alpha)x' + (\cos 90^\circ)y' + (\cos(90^\circ-\alpha))z', \\ y &= (\cos 90^\circ)x' + (\cos 0^\circ)y' + (\cos 90^\circ)z', \\ z &= (\cos(90^\circ+\alpha))x' + (\cos 90^\circ)y' + (\cos\alpha)z'. \end{aligned} \tag{A.9}$$

which equals

$$\begin{bmatrix} x \\ y \\ z \end{bmatrix} = \begin{bmatrix} \cos\alpha & 0 & \sin\alpha \\ 0 & 1 & 0 \\ -\sin\alpha & 0 & \cos\alpha \end{bmatrix} \begin{bmatrix} x' \\ y' \\ z' \end{bmatrix}. \tag{A.10}$$

where the matrix in Eq. (A.10) represents the transpose of that in Eq. (A.8). One may also obtain Eq. (A.10) from Eq. (A.8) by making the substitution $\alpha \to -\alpha$.

A.3 Transformation of magnetic field components from the magnetic to the rotational frame

In our study we implemented an additional B-field structure, i.e., the symmetric offset dipole (see Section 3.1.3 and Chapter 4). Since the B-field, Eq. (3.14), is specified in the magnetic frame we needed to do a rotation of the co-ordinate axes to transform from the magnetic to the rotational frame. We derive the transformation for a general B-field below.

Consider the following magnetic field (given in terms of spherical co-ordinates) in the magnetic frame ($\hat{\mathbf{z}}' \parallel \boldsymbol{\mu}$) (with $\boldsymbol{\mu}$ the magnetic axis):

$$\mathbf{B}'(r',\theta',\phi') = B'_r(r',\theta',\phi')\hat{\mathbf{r}}' + B'_\theta(r',\theta',\phi')\hat{\boldsymbol{\theta}}' + B'_\phi(r',\theta',\phi')\hat{\boldsymbol{\phi}}'. \tag{A.11}$$

The spherical unit vectors may be expressed in terms of the Cartesian unit vectors (Griffiths, 1995):

$$\begin{aligned}
\hat{\mathbf{r}}' &= (\sin\theta'\cos\phi')\hat{\mathbf{x}}' + (\sin\theta'\sin\phi')\hat{\mathbf{y}}' + (\cos\theta')\hat{\mathbf{z}}', \\
\hat{\boldsymbol{\theta}}' &= (\cos\theta'\cos\phi')\hat{\mathbf{x}}' + (\cos\theta'\sin\phi')\hat{\mathbf{y}}' - (\sin\theta')\hat{\mathbf{z}}', \\
\hat{\boldsymbol{\phi}}' &= -(\sin\phi')\hat{\mathbf{x}}' + (\cos\phi')\hat{\mathbf{y}}'.
\end{aligned} \tag{A.12}$$

To transform the B-vector components, from a spherical base unit vector set to a Cartesian one, substitute Eq. (A.12) into Eq. (A.11):

$$\begin{aligned}
\mathbf{B}'(r',\theta',\phi') &= B'_r\{\sin\theta'\cos\phi'\hat{\mathbf{x}}' + \sin\theta'\sin\phi'\hat{\mathbf{y}}' + \cos\theta'\hat{\mathbf{z}}'\} \\
&+ B'_\theta\{\cos\theta'\cos\phi'\hat{\mathbf{x}}' + \cos\theta'\sin\phi'\hat{\mathbf{y}}' - \sin\theta'\hat{\mathbf{z}}'\} \\
&+ B'_\phi\{-\sin\phi'\hat{\mathbf{x}}' + \cos\phi'\hat{\mathbf{y}}'\}.
\end{aligned} \tag{A.13}$$

Rearrange Eq. (A.13) according to unit basis vectors and compare with:

$$\mathbf{B}'(r',\theta',\phi') = B'_x(r',\theta',\phi')\hat{\mathbf{x}}' + B'_y(r',\theta',\phi')\hat{\mathbf{y}}' + B'_z(r',\theta',\phi')\hat{\mathbf{z}}' . \tag{A.14}$$

This yields:

$$\begin{aligned}
B'_x(r',\theta',\phi') &= B'_r\sin\theta'\cos\phi' + B'_\theta\cos\theta'\cos\phi' - B'_\phi\sin\phi', \\
B'_y(r',\theta',\phi') &= B'_r\sin\theta'\sin\phi' + B'_\theta\cos\theta'\sin\phi' + B'_\phi\cos\phi', \\
B'_z(r',\theta',\phi') &= B'_r\cos\theta' - B'_\theta\sin\theta'.
\end{aligned} \tag{A.15}$$

To transform the spherical co-ordinates in Eq. (A.15), to Cartesian co-ordinates in the magnetic frame, use (Griffiths, 1995)

$$\begin{aligned}
x' &= r'\sin\theta'\cos\phi', \\
y' &= r'\sin\theta'\sin\phi', \\
z' &= r'\cos\theta'.
\end{aligned} \tag{A.16}$$

We then have

$$\mathbf{B}'(x', y', z') \;=\; B'_x(x', y', z')\hat{\mathbf{x}}' \;+\; B'_y(x', y', z')\hat{\mathbf{y}}' \;+\; B'_z(x', y', z')\hat{\mathbf{z}}' \;. \tag{A.17}$$

The magnetic field components in Eq. (A.19) will transform in a way similar to the position vector components under rotation of axes, as given in Eq. (A.10). We can therefore use a rotation to transform from the magnetic frame ($\hat{\mathbf{z}}' \parallel \boldsymbol{\mu}$) to the spin-axis-aligned frame ($\hat{\mathbf{z}} \parallel \boldsymbol{\Omega}$). Assume a rotation angle $+\alpha$ between the rotational and magnetic frame (see Eq. [A.10]), letting $\mathbf{y} \parallel \mathbf{y}'$ as in Section A.2:

$$\begin{bmatrix} B_x \\ B_y \\ B_z \end{bmatrix} = \begin{bmatrix} \cos\alpha & 0 & \sin\alpha \\ 0 & 1 & 0 \\ -\sin\alpha & 0 & \cos\alpha \end{bmatrix} \begin{bmatrix} B'_x \\ B'_y \\ B'_z \end{bmatrix}. \tag{A.18}$$

This gives

$$\mathbf{B}(x', y', z') \;=\; B_x(x', y', z')\hat{\mathbf{x}}' \;+\; B_y(x', y', z')\hat{\mathbf{y}}' \;+\; B_z(x', y', z')\hat{\mathbf{z}}' \;. \tag{A.19}$$

Lastly, we rotate the Cartesian co-ordinates (x', y', z') through an angle $-\alpha$. This gives

$$\begin{bmatrix} x' \\ y' \\ z' \end{bmatrix} = \begin{bmatrix} \cos\alpha & 0 & -\sin\alpha \\ 0 & 1 & 0 \\ \sin\alpha & 0 & \cos\alpha \end{bmatrix} \begin{bmatrix} x \\ y \\ z \end{bmatrix}. \tag{A.20}$$

Substitute Eq. (A.18) and (A.20) into (A.19) to obtain

$$\mathbf{B}(x, y, z) \;=\; B_x(x, y, z)\hat{\mathbf{x}} \;+\; B_y(x, y, z)\hat{\mathbf{y}} \;+\; B_z(x, y, z)\hat{\mathbf{z}} \;. \tag{A.21}$$

Appendix B

Light curve atlases

In this Appendix we illustrate our light curve atlases, i.e., a collection of light curves in (α,ζ)-space, which we constructed for various inclination angles α and cuts at constant observer angles ζ, as well as different combinations of pulsar geometries and B-fields. In each atlas α (along y-axis) and ζ (along x-axis) range from 10° to 90° with a 10° resolution, and increase from top left to bottom right (the combination of angles is indicated in top right corner of each panel). The pulse shape maxima are normalised to unity (y dimension), with $\phi_{\rm L} \in [0, 1]$ (x dimension) in each case. The combinations of pulsar B-fields and geometries include the static dipole and RVD fields both for the TPC and OG models, as well as the offset dipole for the TPC (assuming uniform emissivity ϵ_ν) and SG (variable ϵ_ν) models. For the offset dipole case we used an offset parameter $\epsilon \in [0, 0.18]$ with increments of 0.03. The study of light curve atlases may provide insight into the dependence of the emission features (discussed in Section 6.1) on the geometric parameters and pulsar geometry (as mentioned in Chapter 1). Thus, the effect of the pulsar geometry and B-field structure on the predicted light curves is visible in these atlases. Below, we briefly discuss each atlas.

Figure B.1: The combination of a static dipole field and TPC geometry. As α and ζ increase the peaks of the light curves become narrower, some features (as discussed in Section 6.1) become more pronounced or more features arise. Broad, single peaks are visible for low α and ζ, and double peaks are visible for large α and ζ. Significant changes in the light curves are visible for $\zeta > 70°$. In this geometry, emission is visible from both magnetic poles and nearly fill all of phase space. This case also displays more off-peak emission relative to the OG model.

Figure B.2: The combination of a static dipole field and OG geometry. Significant changes in the light curves are visible for $\zeta > 70°$. As in Figure B.1 the peaks of the light curves become narrower, some features become more pronounced, or more features arise for larger α and ζ. For this case emission is visible from a single pole and < 50% of phase space is filled. The light curves also display less off-peak emission compared to Figure B.1.

Figure B.3: The combination of an RVD field and TPC geometry. As the angle combinations of α and ζ increase gradually, the light curve shape changes significantly. More features (see Section 6.1) arise than in Figure B.1, and the same narrowing in the light curve peaks become visible. The light curves for various α and $\zeta = [50°, 60°, 70°, \text{etc.}]$ varies significantly compared to the other angle combinations. For this case emission is visible from both poles, all of phase space is filled, and more off-peak emission is noticeable compared to Figure B.1, especially at lower (α, ζ).

Figure B.4: The combination of an RVD field and OG geometry. Significant changes in the light curves are observed for $\zeta > 70°$. As in Figure B.3, the peaks of the light curves become narrower, some features become more pronounced, or more features arise. If we compare Figure B.2 and B.4 we notice that more of phase space is filled, and the profiles seem broader.

Figure B.5: The combination of an offset dipole field and TPC geometry with $\epsilon = 0.00$ and a constant emissivity ϵ_ν. This case represents the same light curves as in Figure B.1 for the static dipole field and TPC model. This is an important validation of our B-field transformation (Appendix A).

Figure B.6: The same combination as in Figure B.5 with $\epsilon = 0.03$. The light curves have a similar shape as those in Figure B.5, although over the whole range of α and ζ the peaks become slightly smoother, e.g., $\alpha = 80°$, and $\zeta = 40°$ and $50°$ (depending on the model resolution). As for Figures B.1 and B.3 the emission is visible from both poles, nearly fills all of phase space, and also displays more off-peak emission than OG model.

Figure B.7: The same combination as in Figure B.5 with $\epsilon = 0.06$. The light curves have a similar shape, however the peaks become slightly "block shaped", e.g., $\alpha = 10°$, and $\zeta = 90°$. Some features become less pronounced, e.g., $\alpha = 90°$ and $\zeta = 50°$ or disappear, e.g., $\alpha = 40°$ and $\zeta = 70°$. At some angle combinations new features appear, e.g., $\alpha = 90°$ and $\zeta = 60°$.

Figures B.8, B.9, B.10, and B.11: The light curves have the same general shape as in B.5. The change is gradual for small increments of ϵ.

Figure B.12: The combination of an offset dipole field and SG, with $\epsilon = 0.00$ and a variable emissivity ϵ_ν. This case looks very different from Figure B.5, which is for a constant ϵ_ν. Single broad peaks are mostly observed, as well as low levels of off-peak emission, and less features are visible. At certain angle combinations of α and ζ more features appear, e.g., $\alpha = 40°$ and $\zeta = 70°$. For this case emission is visible from both poles, however with the SG $E_{\|}$-field causing a variable ϵ_ν, the emission is qualitatively different compared to the uniform ϵ_ν case. In Figure B.12 there is less phase space filled compared to Figure B.5 due to the low SG $E_{\|}$-field (and the fact that we only included emission with energy > 100 MeV in our phase plots).

Figure B.13: The same combination as in Figure B.12 with $\epsilon = 0.03$. For an increase in ϵ the light curves have the same general shape as Figure B.12, although, some of the peaks becomes slightly sharper, e.g., $\alpha = 70°$, and $\zeta = 70°$, and some features become less or more pronounced, e.g., the two peaks for $\alpha = 60°$ and $\zeta = 70°$.

Figures B.14, B.15, B.16, B.17, and B.18: The same combination as in Figure B.12, for an increase in ϵ. The light curves have the same general shape as Figure B.12. However, at different angle combinations some features are more pronounced, new ones arise, or features disappear. We notice that for an increase in ϵ more of phase space becomes filled and the relative peak heights and shapes change.

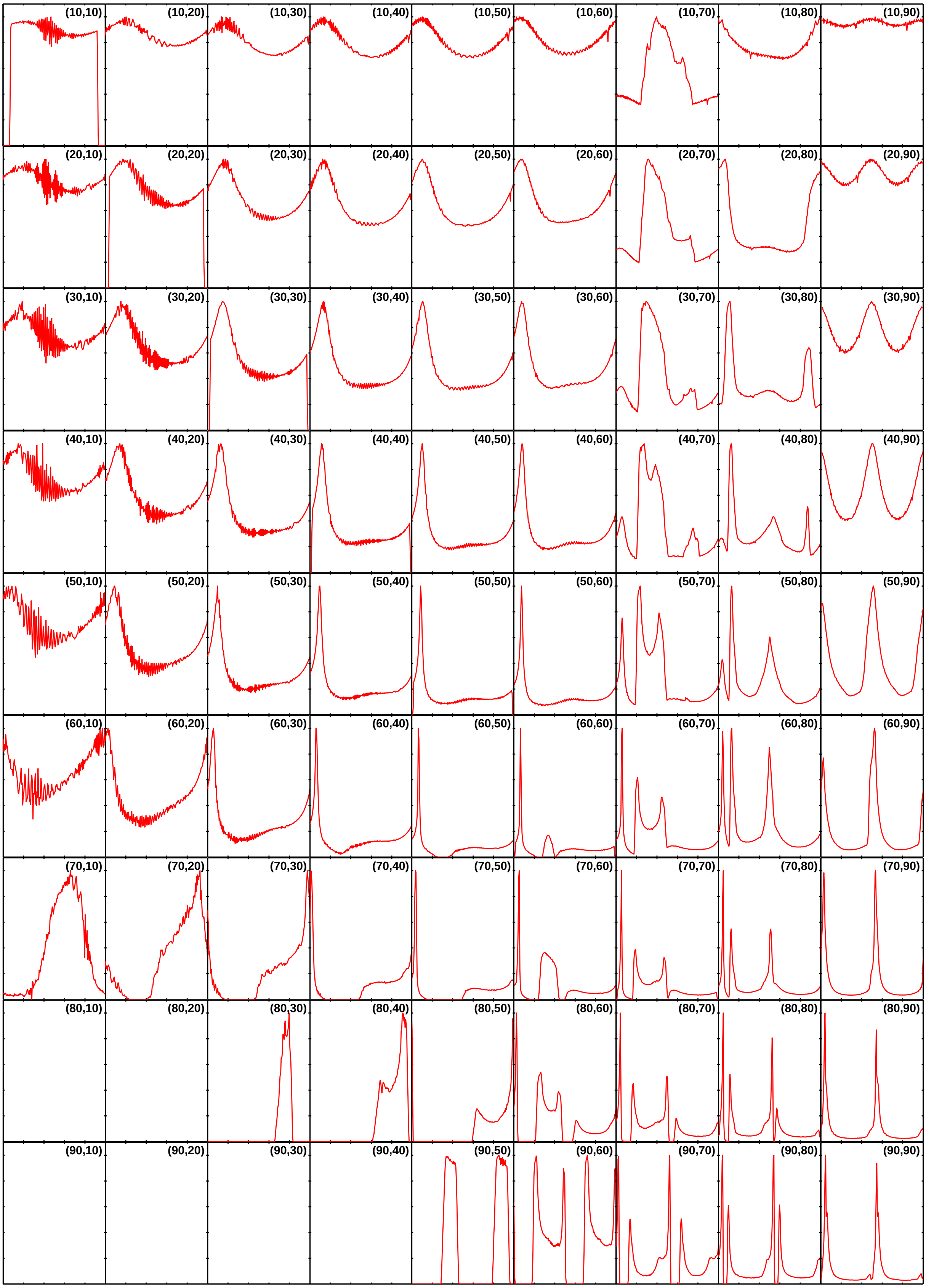

Figure B.1: A light curve atlas for the static-dipole B-field and TPC model. The inclination angle α varies along the y-axis, and the observer angle ζ along the x-axis. Both α and ζ increase from top left to bottom right, ranging from 10° to 90° with a 10° resolution. The pulse shape maxima are normalised to unity, and the phase range goes from 0 to 1 in each case.

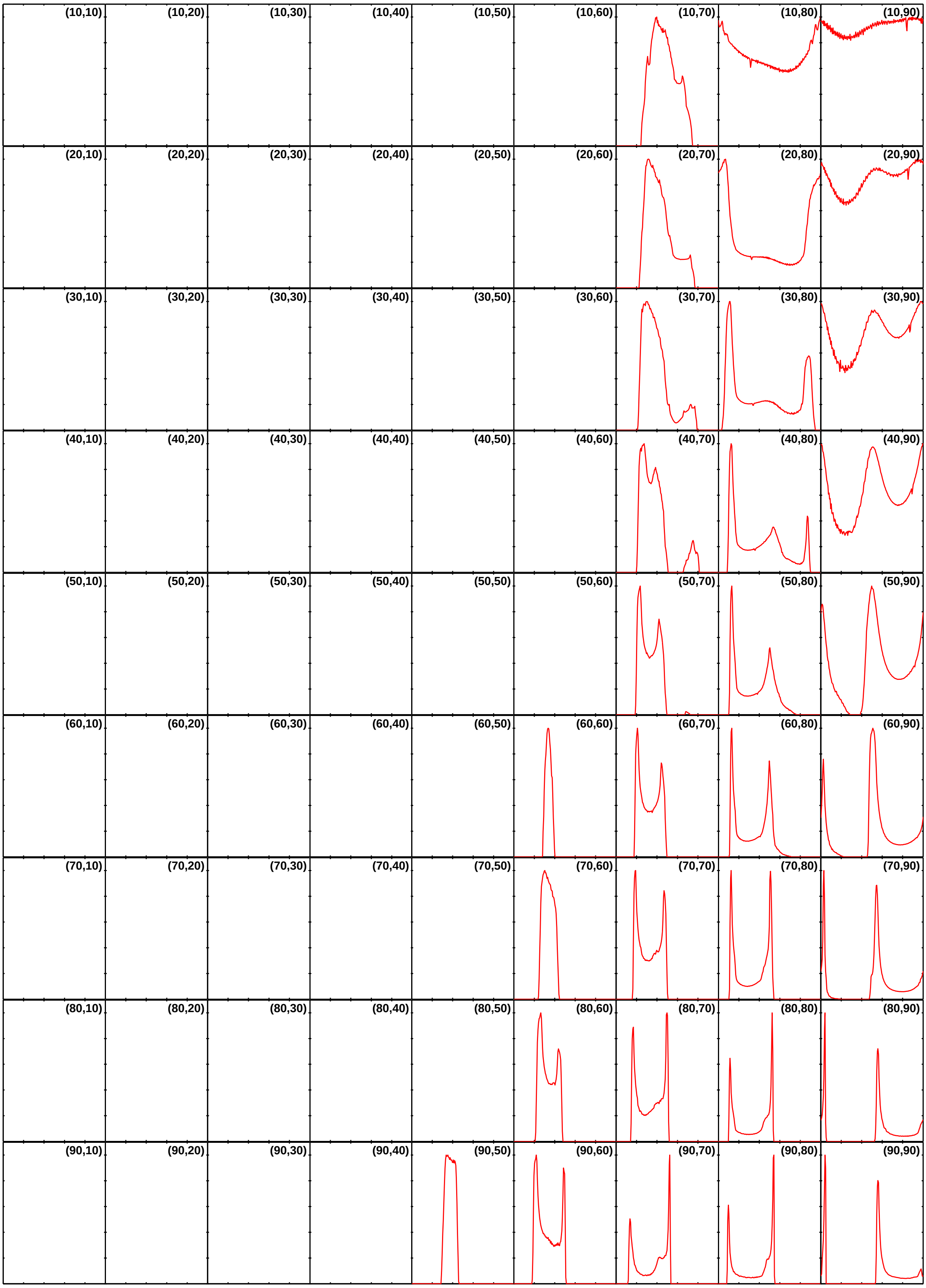

Figure B.2: Same as Figure B.1 but for the static dipole *B*-field and OG model.

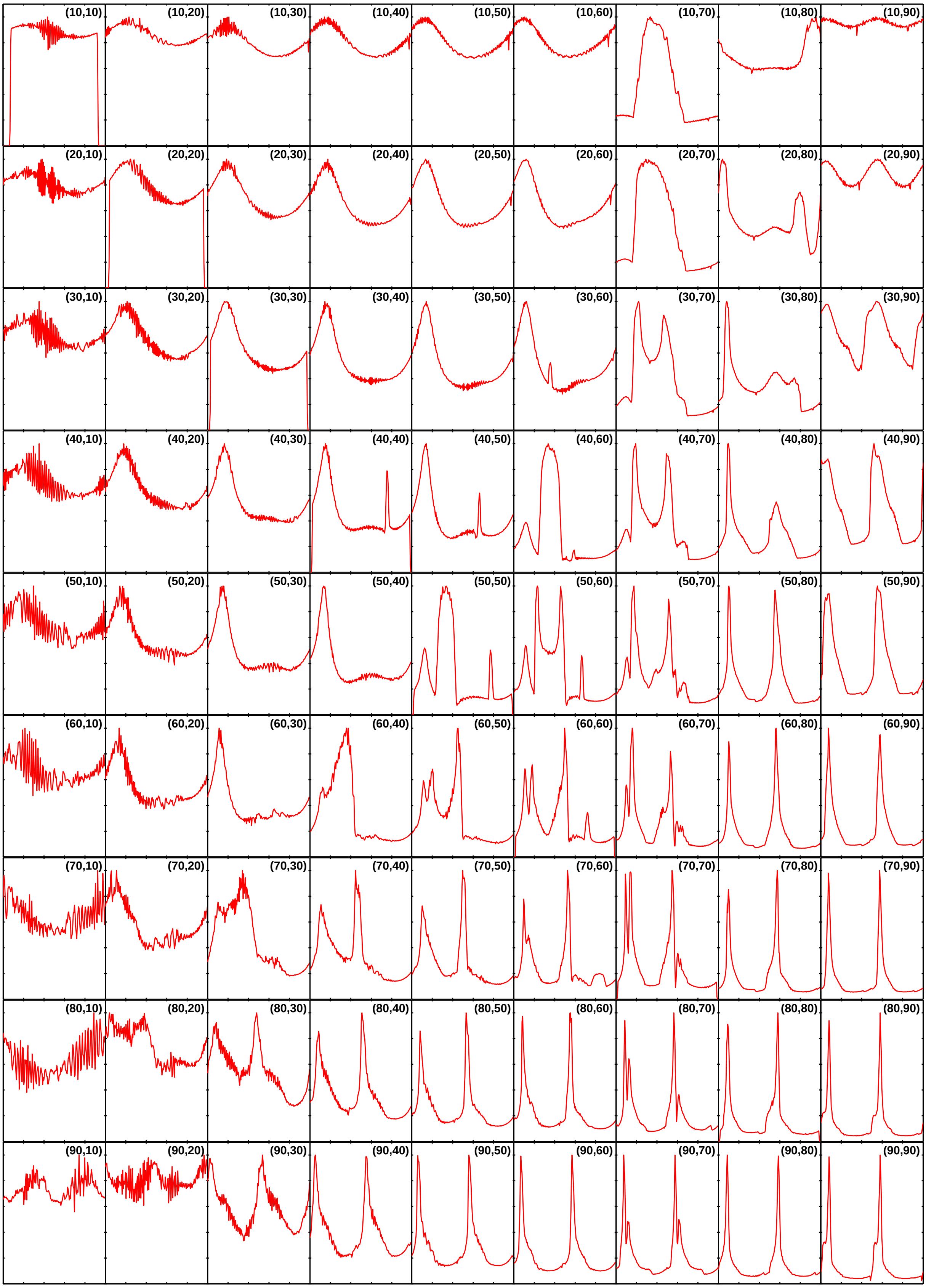

Figure B.3: Same as Figure B.1 but for the RVD B-field and TPC model.

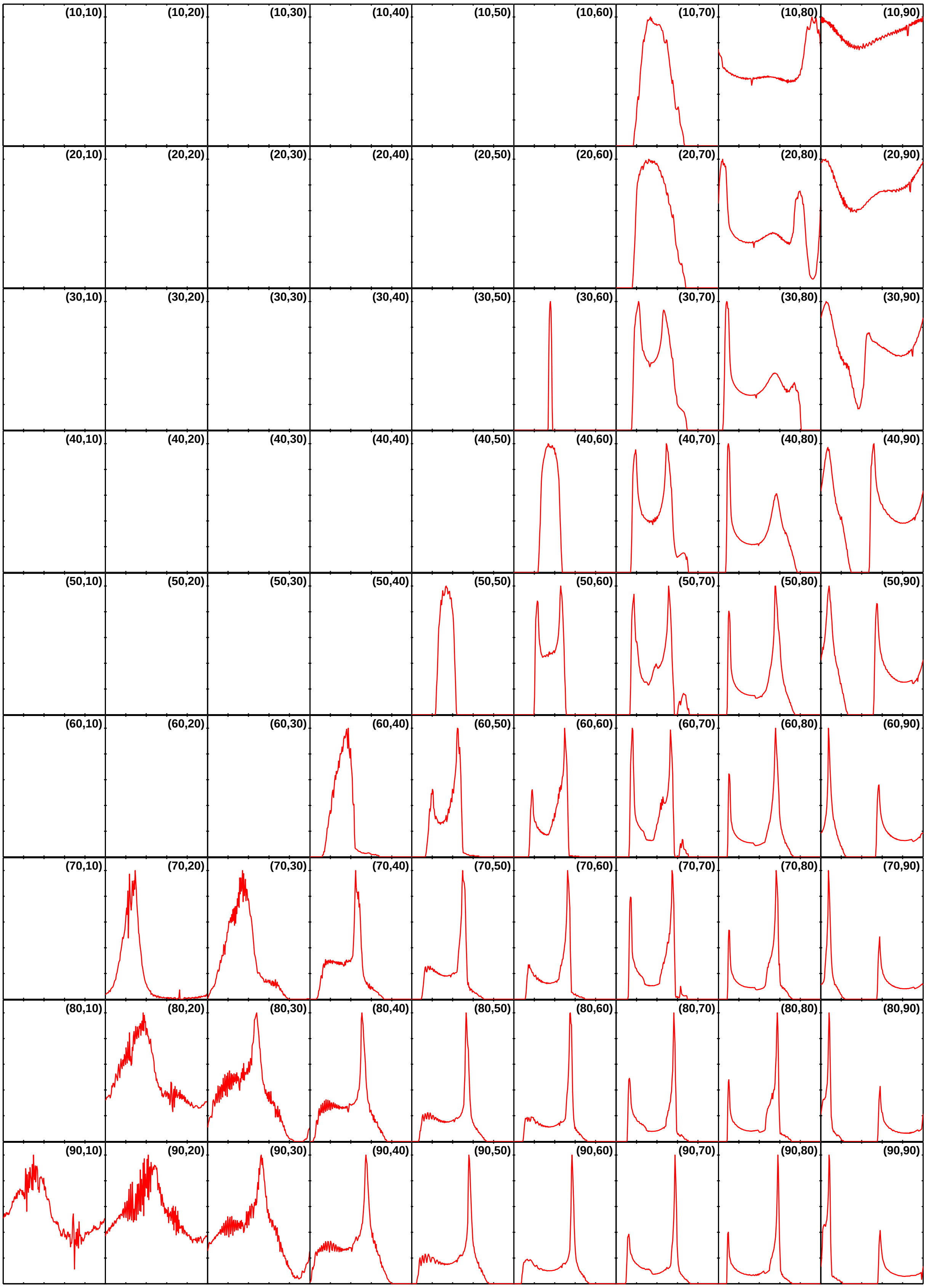

Figure B.4: Same as Figure B.1 but for the RVD *B*-field and OG model.

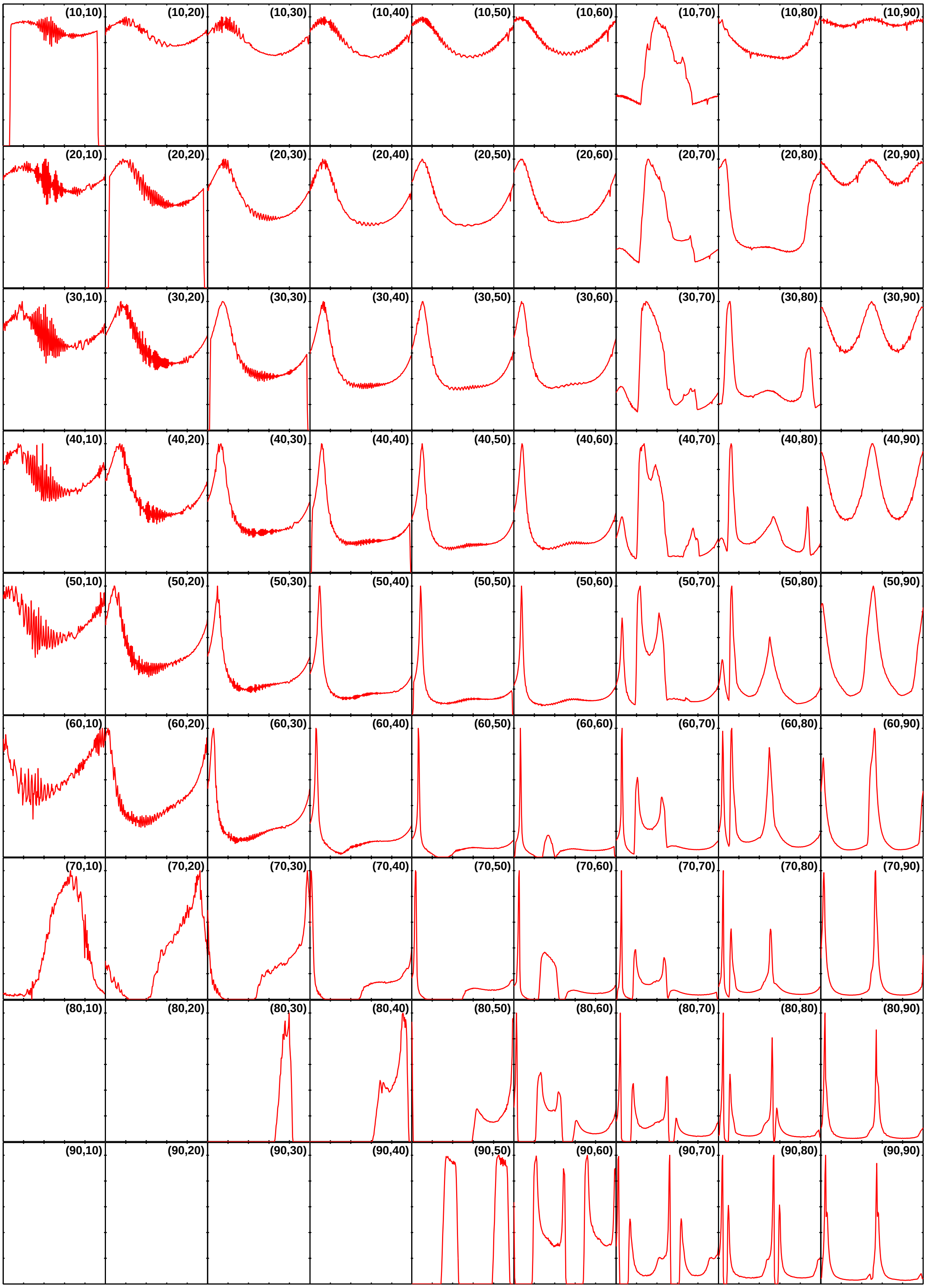

Figure B.5: Same as Figure B.1 but for the offset dipole B-field and the TPC model, with $\epsilon = 0.00$ and a constant ϵ_ν. This is the same as the case of a static dipole and TPC model.

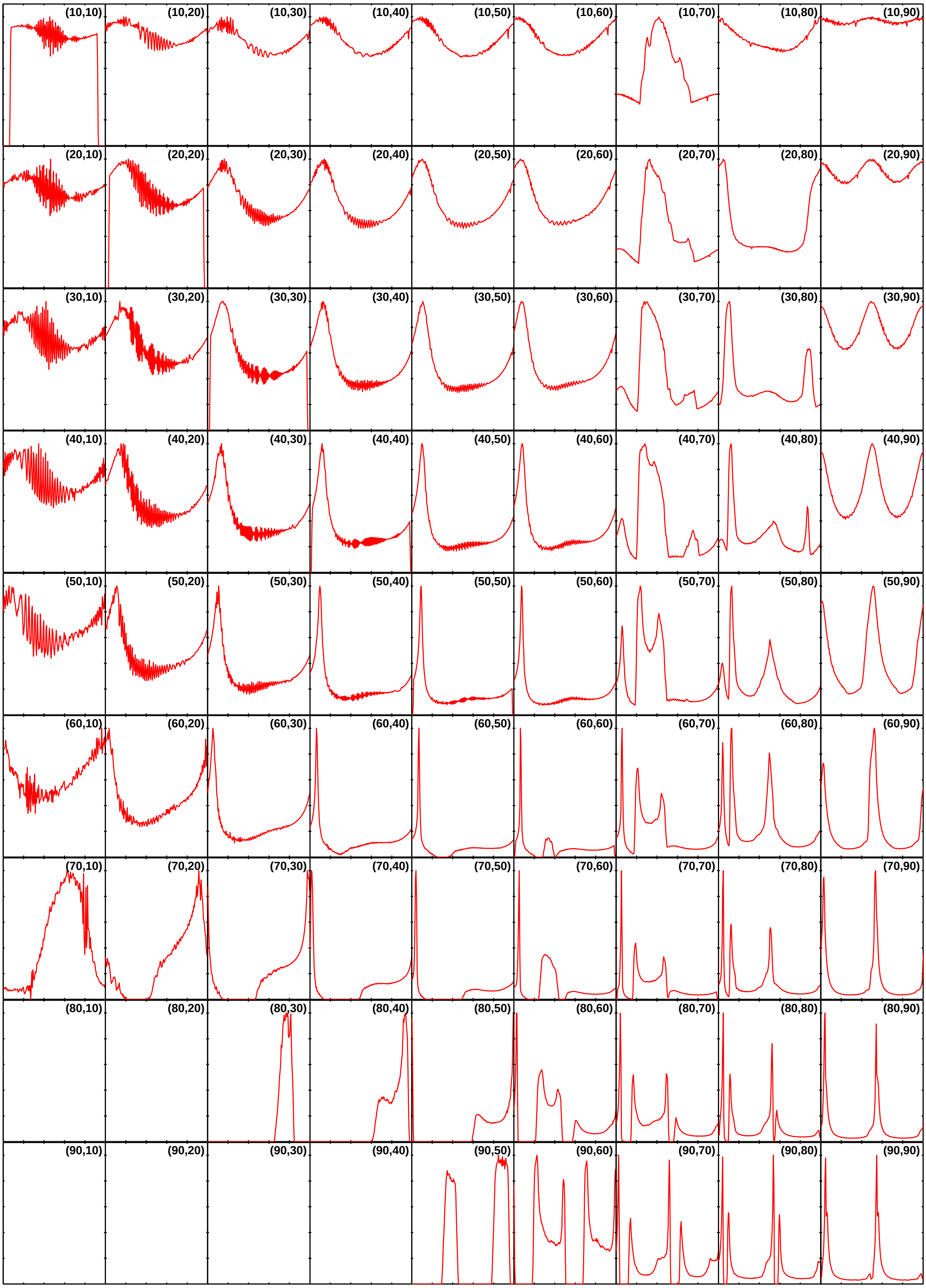

Figure B.6: Same as Figure B.1 but for the offset dipole B-field and the TPC model, with $\epsilon = 0.03$ and a constant ϵ_ν.

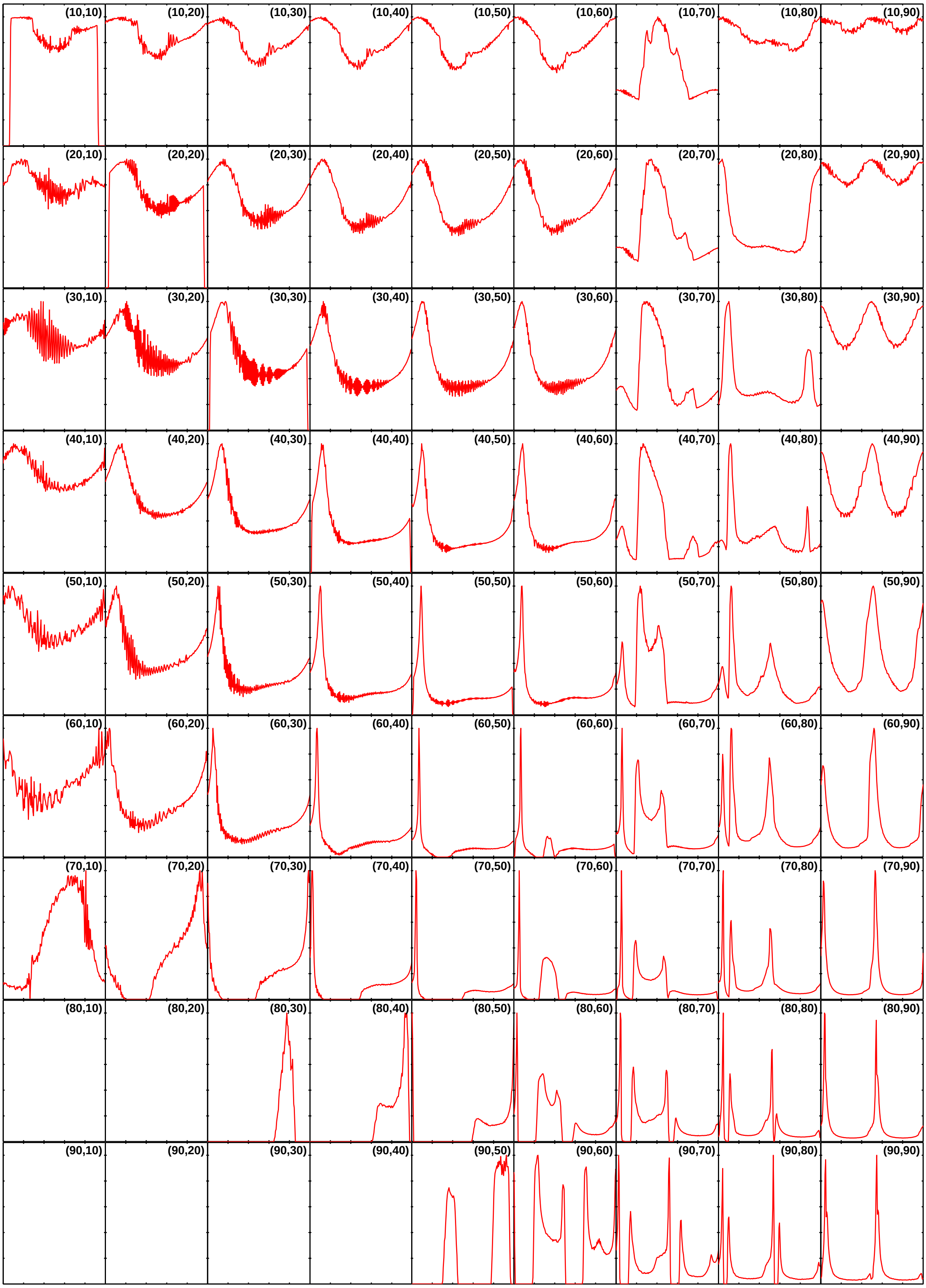

Figure B.7: Same as Figure B.1 but for the offset dipole B-field and the TPC model, with $\epsilon = 0.06$ and a constant ϵ_ν.

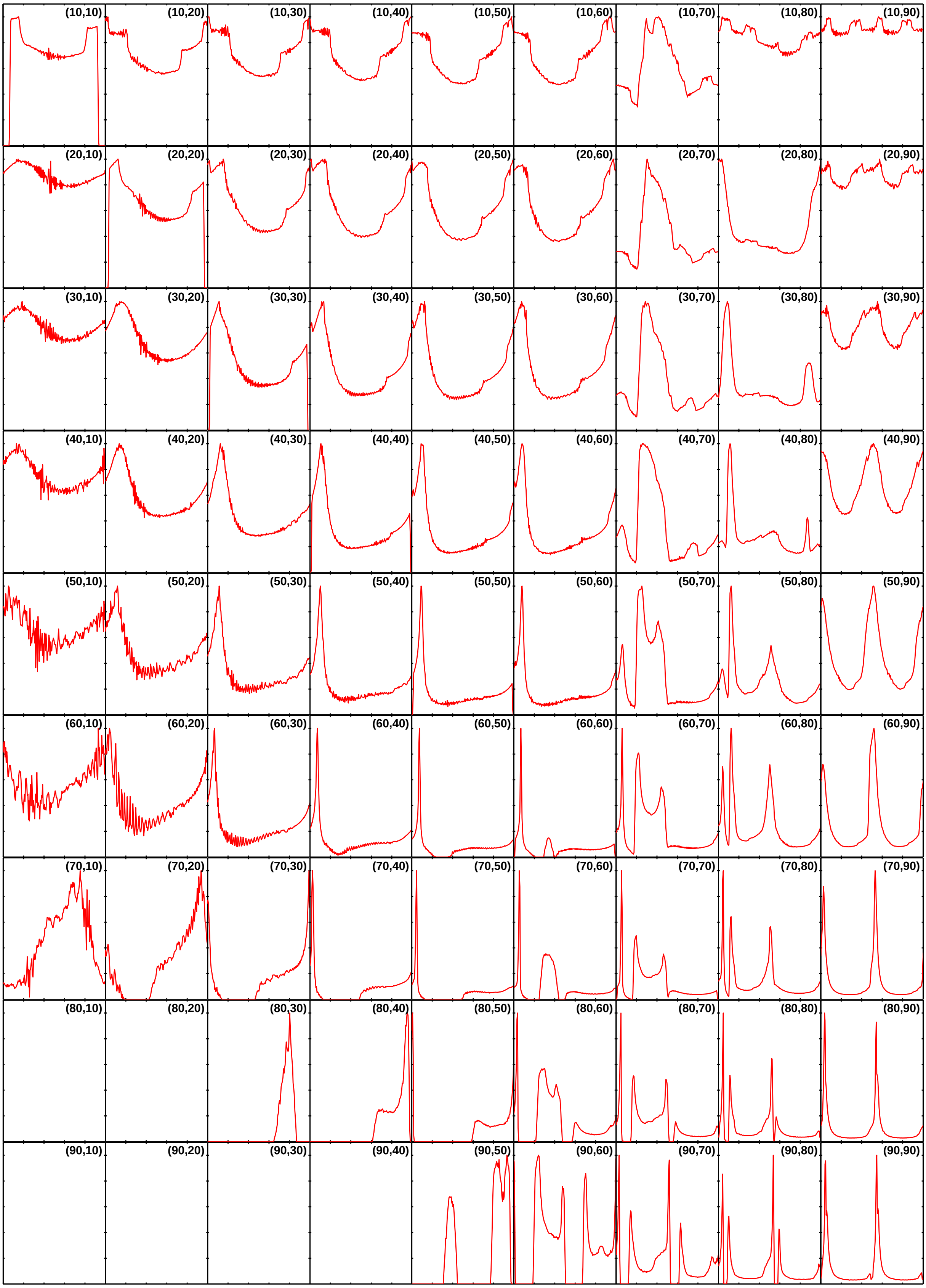

Figure B.8: Same as Figure B.1 but for the offset dipole B-field and the TPC model, with $\epsilon = 0.09$ and a constant ϵ_ν.

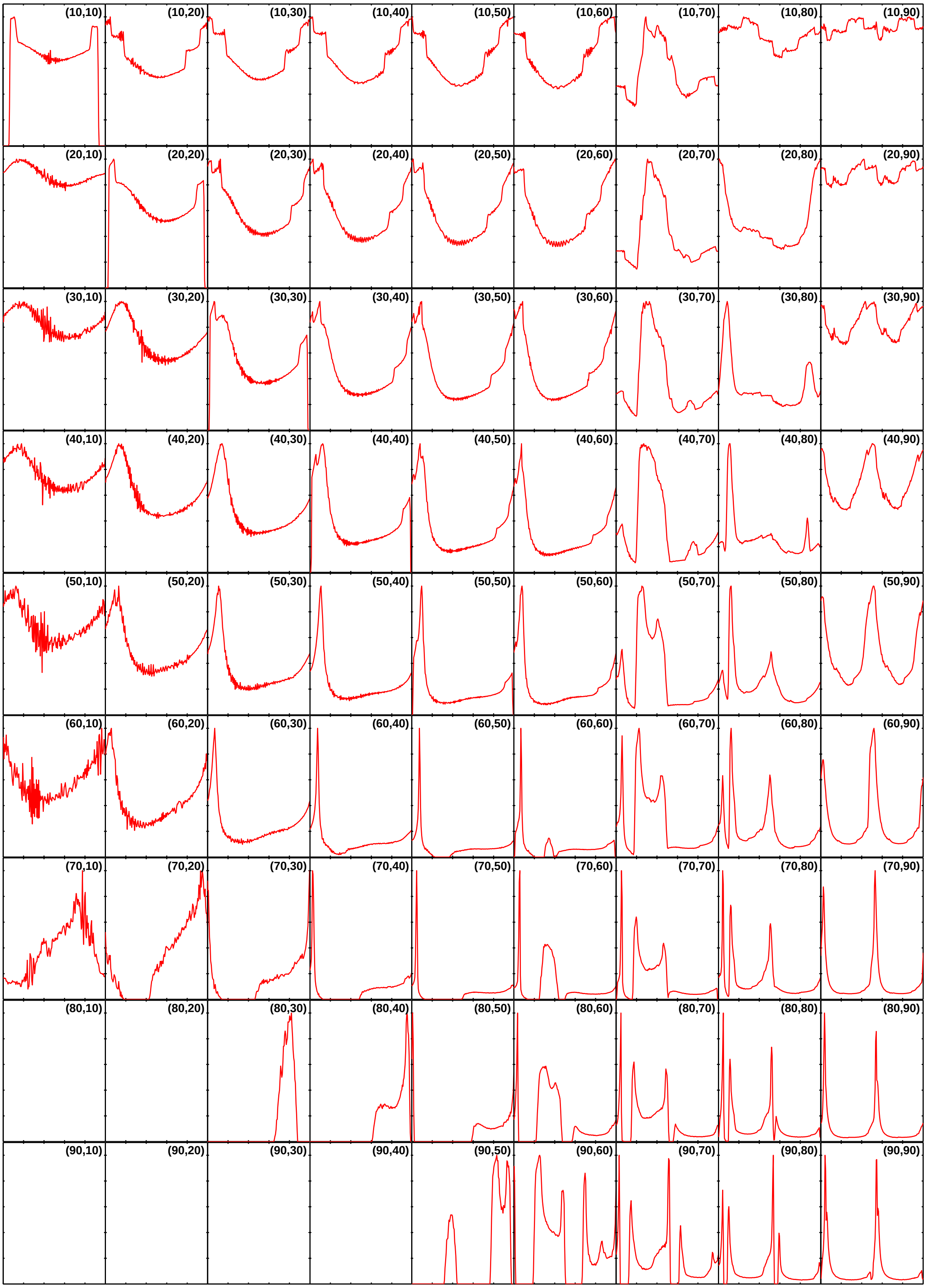

Figure B.9: Same as Figure B.1 but for the offset dipole B-field and the TPC model, with $\epsilon = 0.12$ and a constant ϵ_ν.

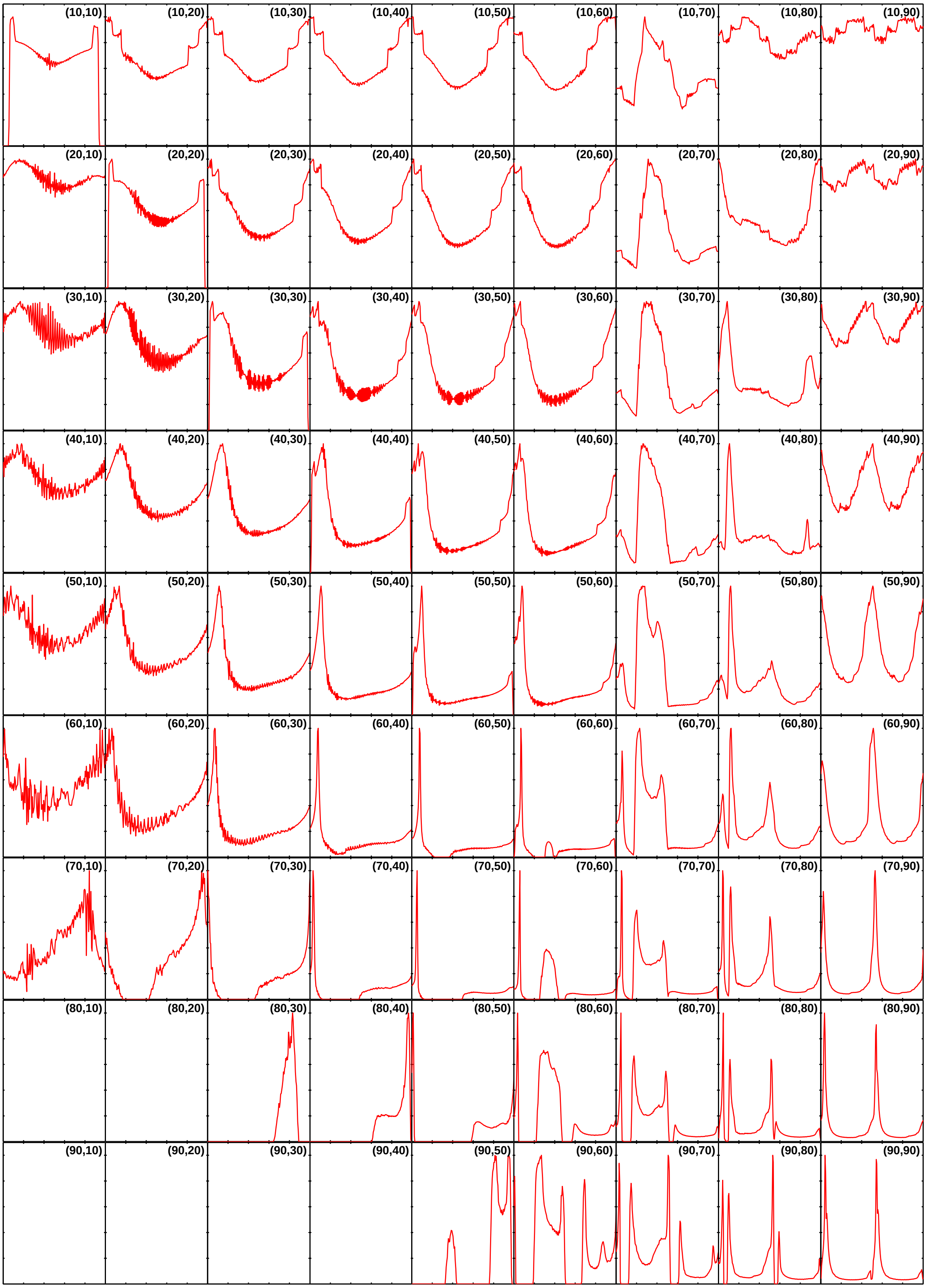

Figure B.10: Same as Figure B.1 but for the offset dipole B-field and the TPC model, with $\epsilon = 0.15$ and a constant ϵ_ν.

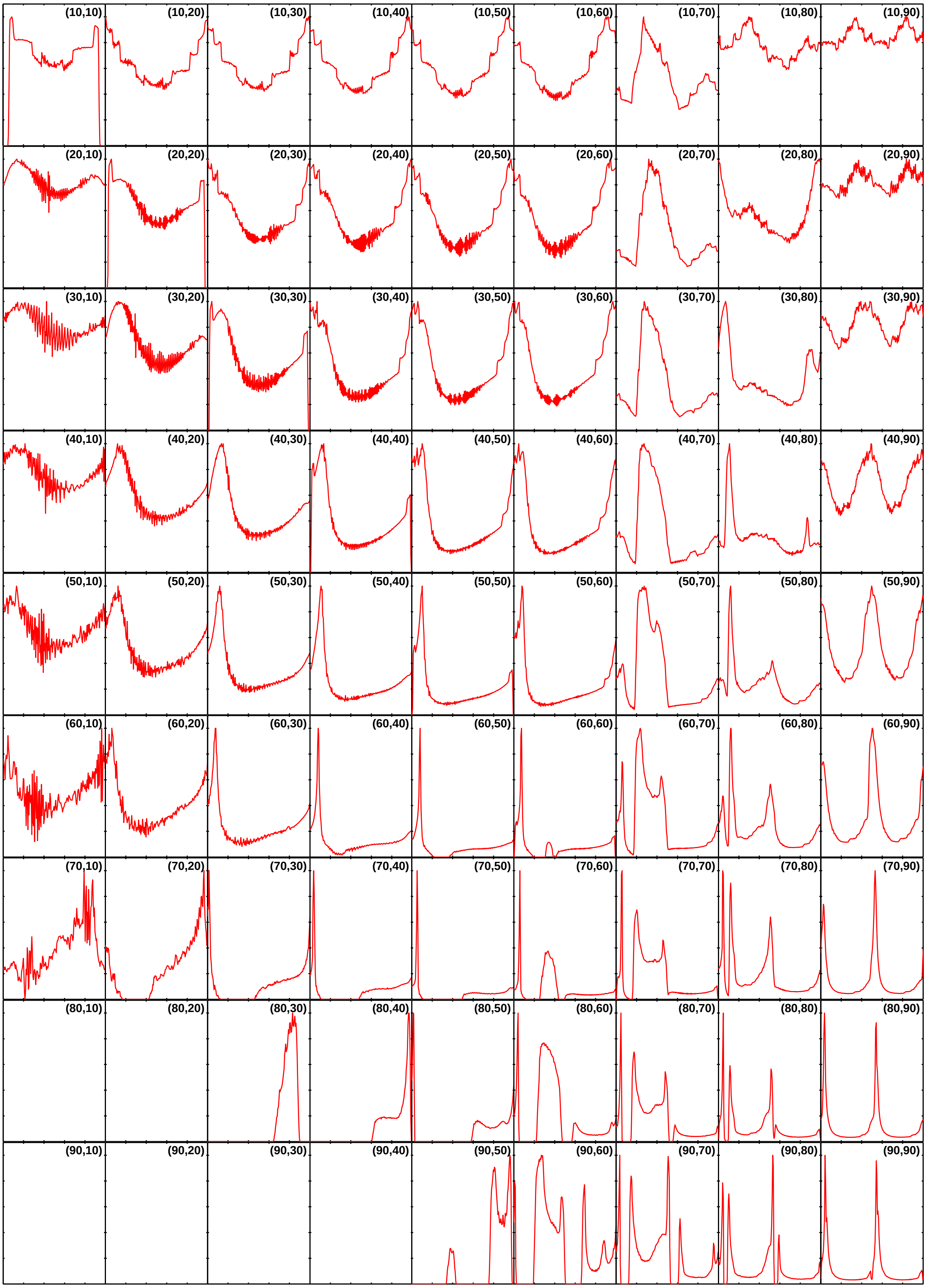

Figure B.11: Same as Figure B.1 but for the offset dipole B-field and the TPC model, with $\epsilon = 0.18$ and a constant ϵ_ν.

Figure B.12: Same as Figure B.1 but for the offset dipole B-field and the SG model, with $\epsilon = 0.00$ and a variable ϵ_ν.

Figure B.13: Same as Figure B.1 but for the offset dipole B-field and the SG model, with $\epsilon = 0.03$ and a variable ϵ_ν.

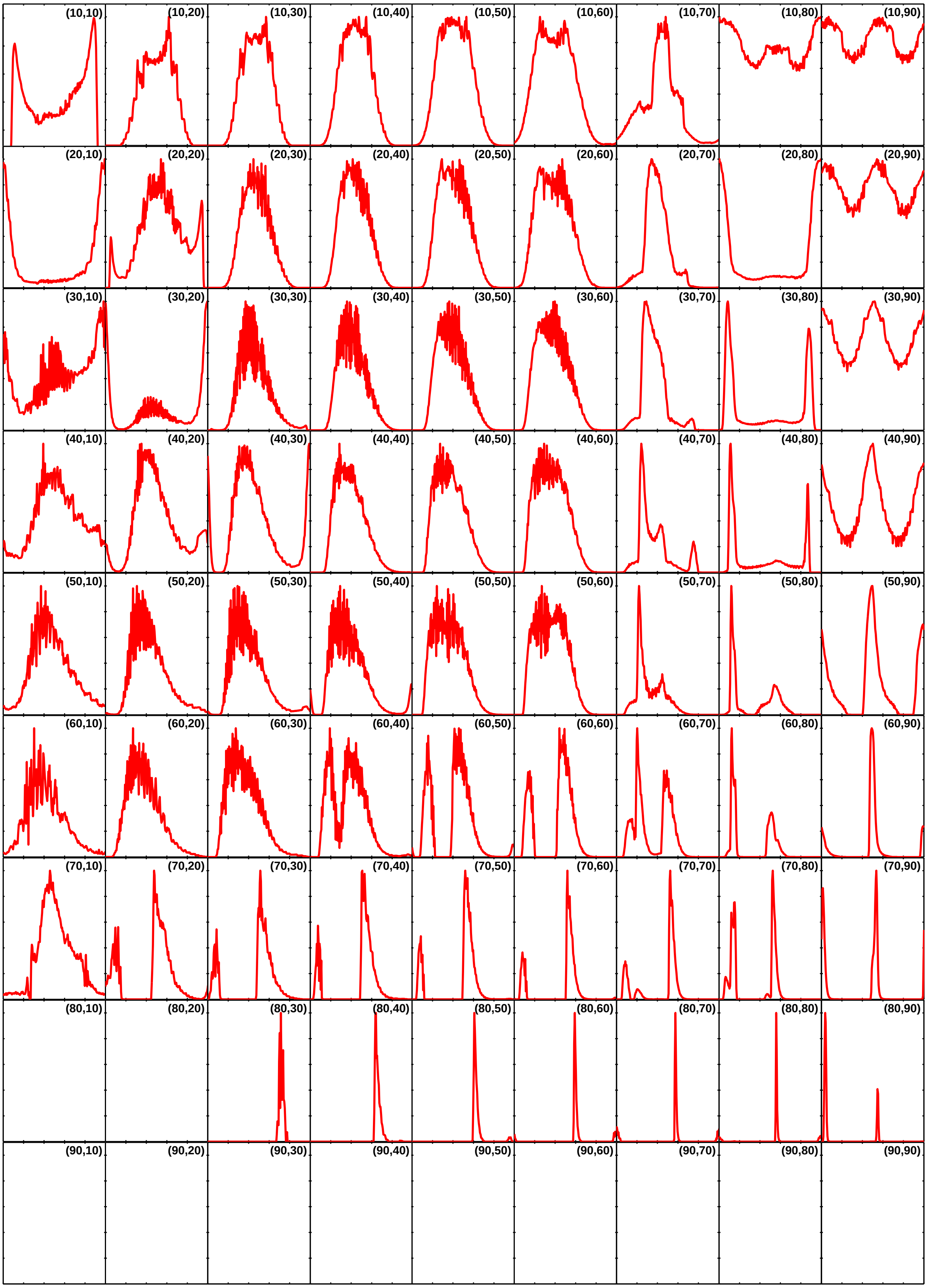

Figure B.14: Same as Figure B.1 but for the offset dipole B-field and the SG model, with $\epsilon = 0.06$ and a variable ϵ_ν.

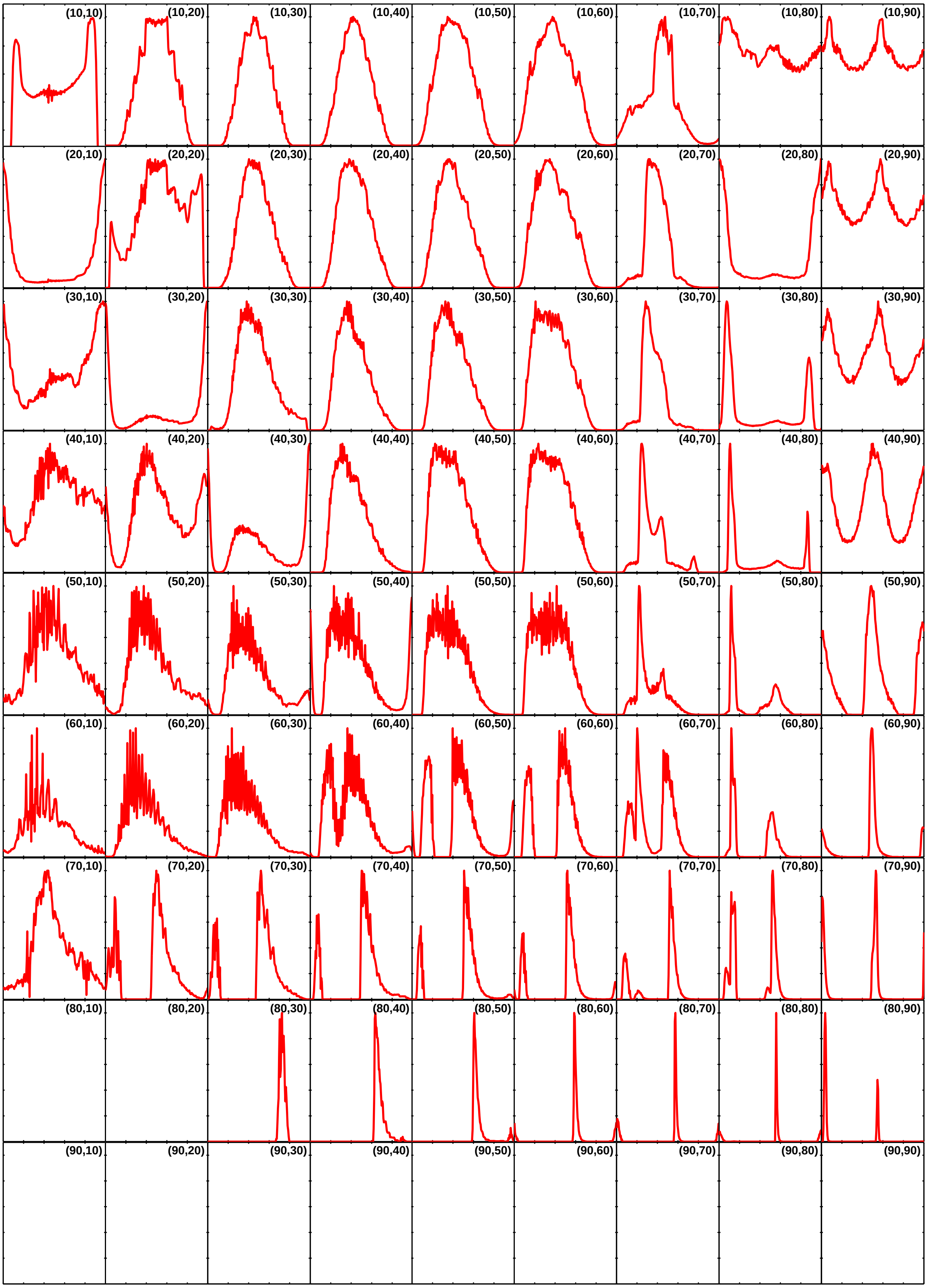

Figure B.15: Same as Figure B.1 but for the offset dipole B-field and the SG model, with $\epsilon = 0.09$ and a variable ϵ_ν.

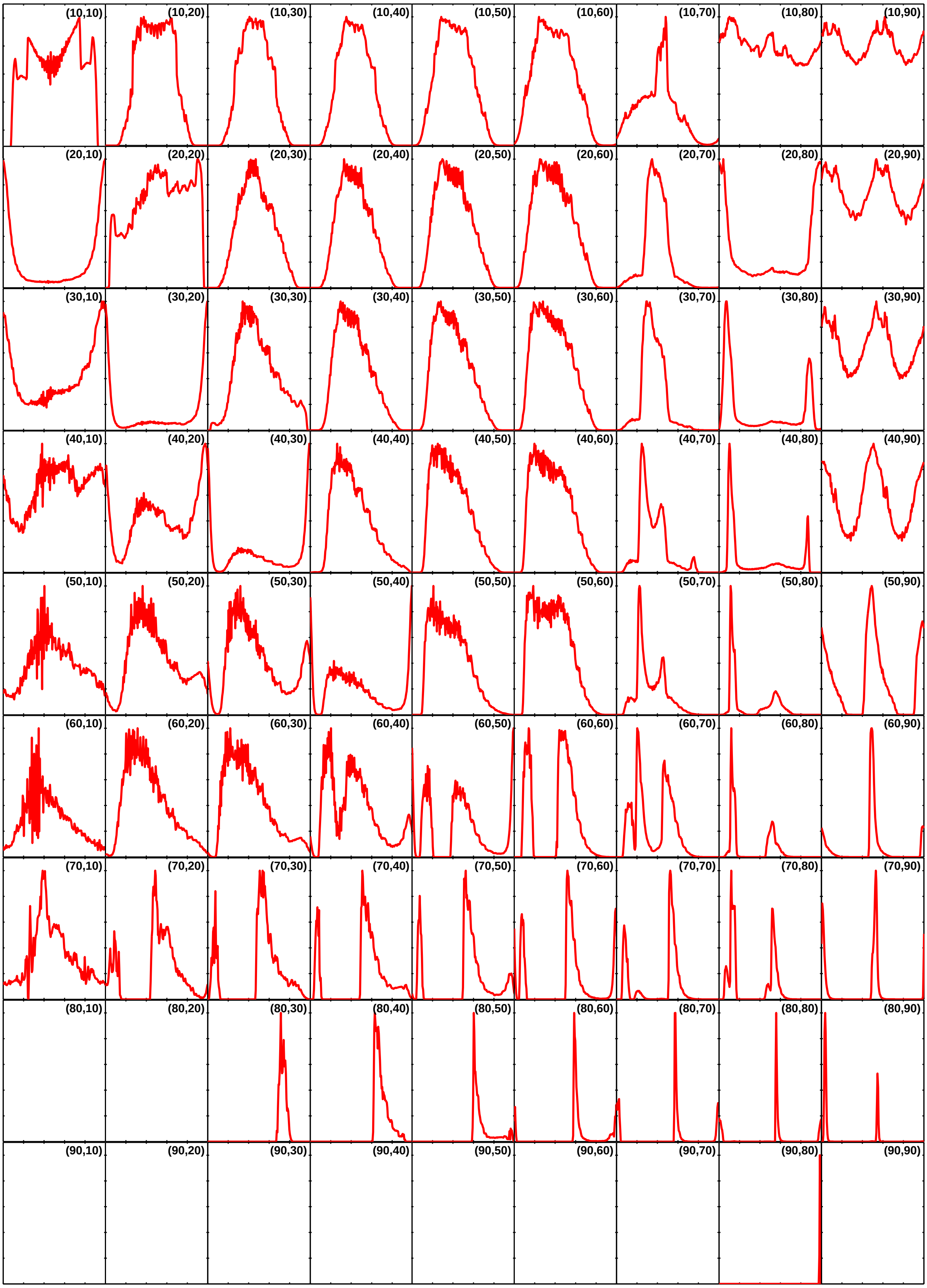

Figure B.16: Same as Figure B.1 but for the offset dipole B-field and the SG model, with $\epsilon = 0.12$ and a variable ϵ_ν.

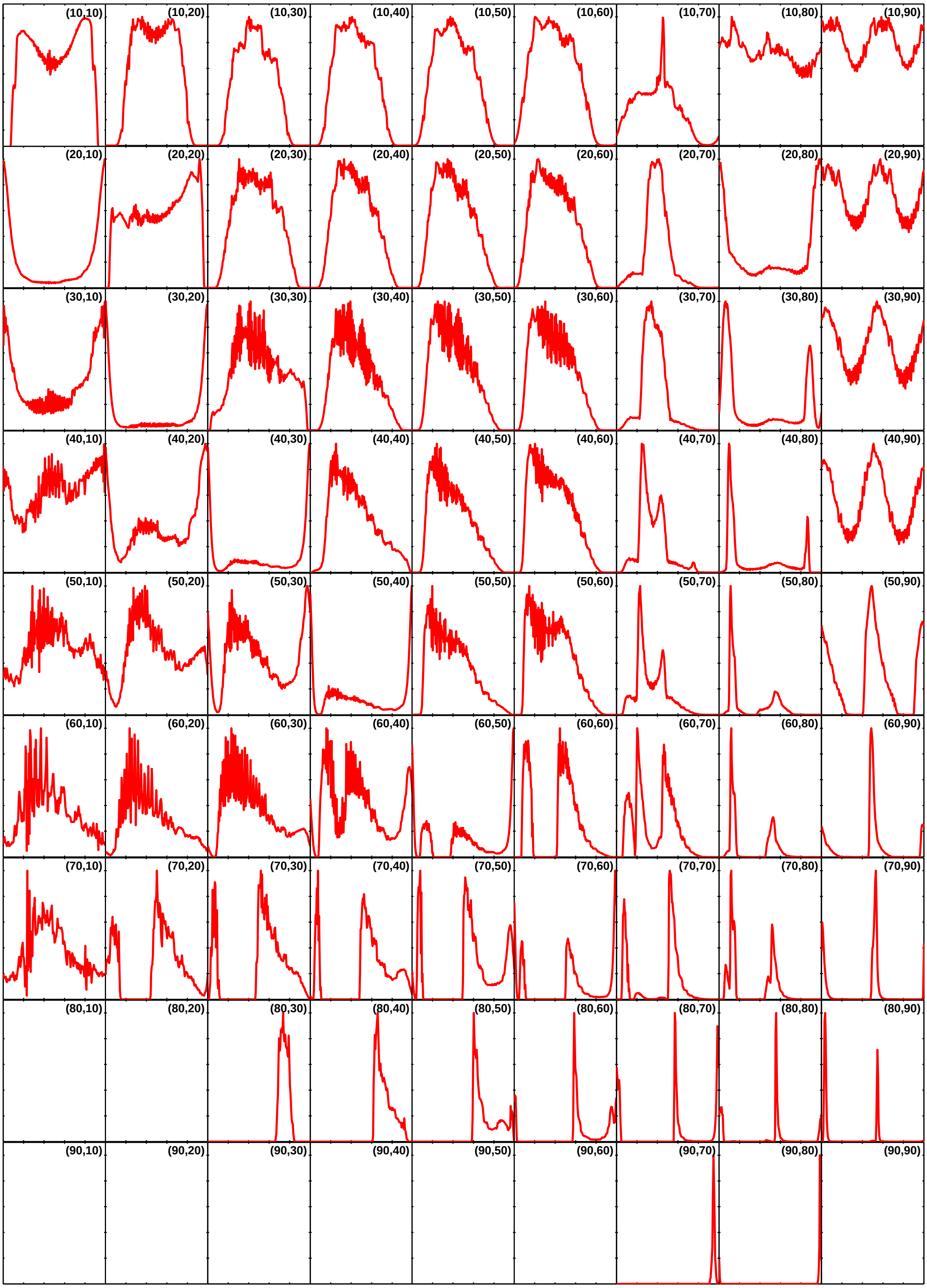

Figure B.17: Same as Figure B.1 but for the offset dipole B-field and the SG model, with ϵ = 0.15 and a variable ϵ_ν.

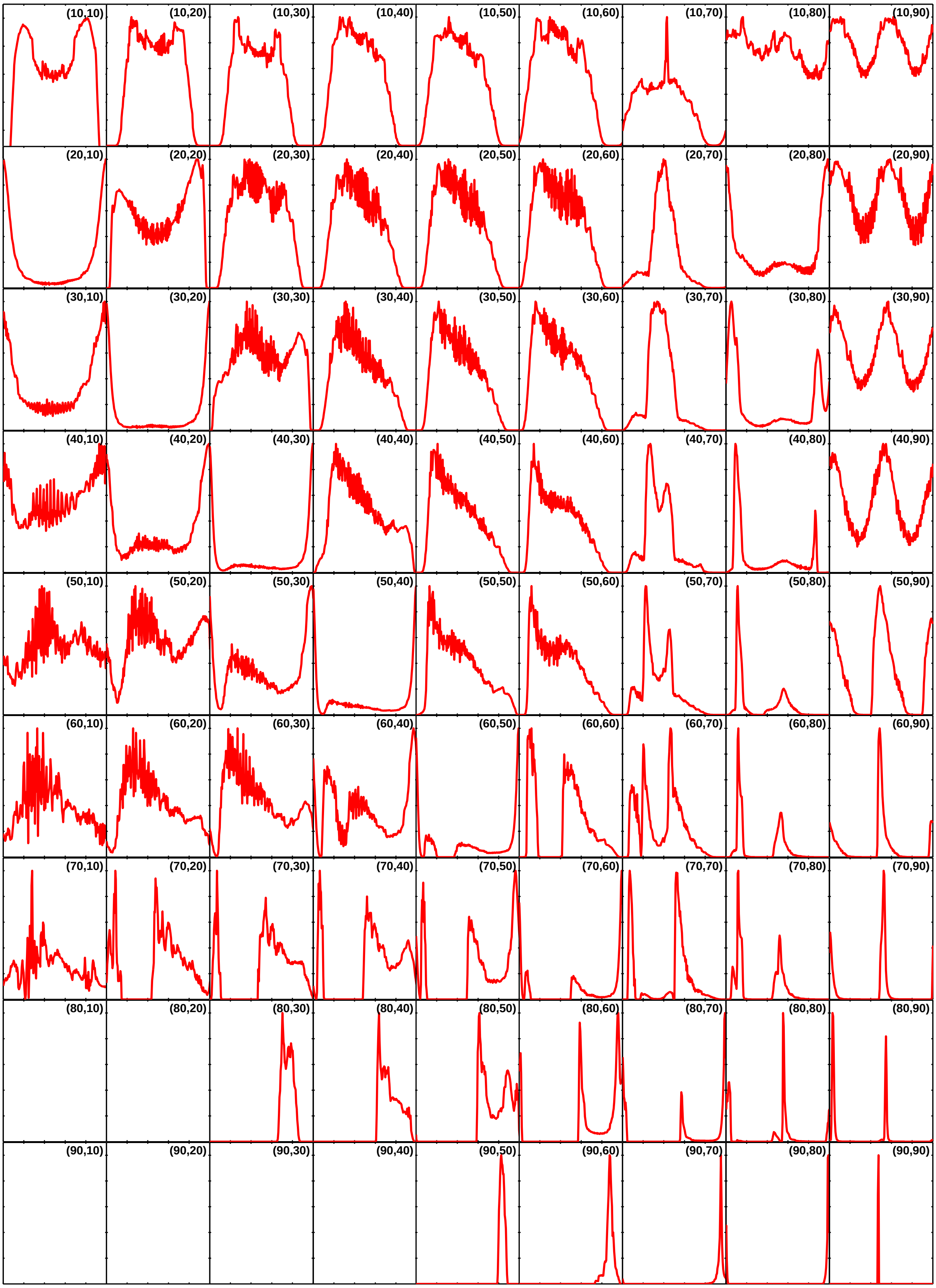

Figure B.18: Same as Figure B.1 but for the offset dipole *B*-field and the SG model, with $\epsilon = 0.18$ and a variable ϵ_ν.

Bibliography

Abdo, A. A., Ackermann, M., Ajello, M., et al. 2010a, ApJ, 708, 1254

—. 2010b, ApJS, 187, 460

—. 2010c, ApJ, 713, 154

Abdo, A. A., Ackermann, M., Atwood, W. B., et al. 2009, ApJ, 696, 1084

Abdo, A. A., Ajello, M., Allafort, A., et al. 2013, ApJS, 208, 17

Aharonian, F. A., Bogovalov, S. V., & Khangulyan, D. 2012, Nature, 482, 507

Aleksić, J., Alvarez, E. A., Antonelli, L. A., et al. 2011, ApJ, 742, 43

—. 2012, A&A, 540, A69

Aleksić, J., Ansoldi, S., Antonelli, L. A., et al. 2014, ArXiv Astrophysics e-prints (astro-ph/1406.6892)

Aliu, E., Anderhub, H., Antonelli, L. A., et al. 2008, Science, 322, 1221

Aliu, E., Arlen, T., Aune, T., et al. 2011, Science, 334, 69

Alpar, M. A., Cheng, A. F., Ruderman, M. A., & Shaham, J. 1982, Nature, 300, 728

Antoniadis, J., et al. 2013, 340, 448

Arendt, Jr., P. N., & Eilek, J. A. 1998, ArXiv Astrophysics e-prints (astro-ph/9801257)

Arons, J. 1983, ApJ, 266, 215

Arons, J., & Scharlemann, E. T. 1979, ApJ, 231, 854

Atwood, W. B., Abdo, A. A., Ackermann, M., et al. 2009, ApJ, 697, 1071

Baade, W., & Zwicky, F. 1934a, Proc. Nat. Acad. Sci. 20, 259

—. 1934b, Proc. Nat. Acad. Sci. 20, 254

Backer, D. C., Kulkarni, S. R., Heiles, C., et al. 1982, Nature, 300, 615

Bai, X.-N., & Spitkovsky, A. 2010, ApJ, 715, 1282

Becker, W., & Pavlov, G. 2002, The Century of Space Science, ed. J. A. Bleeker et al. (Dordrecht: Kluwer, astro-ph/0208356)

Blumenthal, G. R., & Gould, R. J. 1970, Rev. Mod. Phys., 42, 237

Boas, M. L. 2006, Mathematical methods in the physical sciences (3rd ed.; New York: John Wiley and Sons, Inc.)

Bogdanov, S., & Grindlay, J. E. 2009, ApJ, 703, 1557

Bogdanov, S., Rybicki, G. B., & Grindlay, J. E. 2007, ApJ, 670, 668

Bowers, R. L., & Deeming, T. 1984, Astrophysics I - Stars (Boston: Jones & Bartlett Publishers, Inc.)

Bowyer, S., Byram, E. T., Chubb, T. A., & Friedman, H. 1964, Nature, 201, 1307

Bradt, H., Rappaport, S., & Mayer, W. 1969, Nature, 222, 728

Breed, M., Venter, C., Harding, A. K., & Johnson, T. J. 2014, ArXiv Astrophysics e-prints (astro-ph/1411.1835)

—. 2015, ArXiv Astrophysics e-prints (astro-ph/1501.05117)

Burns, M. L., & Harding, A. K. 1984, ApJ, 285, 747

Chadwick, J. 1932, Nature, 129, 312

Chaisson, E. J., & McMillan, S. 2002, Astronomy Today (4th ed.; New Jersy: Prentice Hall)

Chandrasekhar, S. 1931, ApJ, 74, 81

Chen, K., & Ruderman, M. 1993, ApJ, 402, 264

Cheng, K. S. 2011, in High-Energy Emission from Pulsars and their Systems: Proc. of the First Session of the Sant Cugat Forum on Astrophysics, ed. D. F. Torres & N. Rea (Springer: Springer-Verlag Berlin Heidelberg)

Cheng, K. S., Ho, C., & Ruderman, M. 1986a, ApJ, 300, 500

—. 1986b, ApJ, 300, 522

Cheng, K. S., Ruderman, M., & Zhang, L. 2000, ApJ, 537, 964

Chiu, H.-Y., & Salpeter, E. E. 1964, Phys. Rev. Lett., 12, 413

Cocke, W. J., Disney, M. J., & Taylor, D. J. 1969, Nature, 221, 525

Contopoulos, I., Kazanas, D., & Fendt, C. 1999, ApJ, 511, 351

Daugherty, J. K., & Harding, A. K. 1982, ApJ, 252, 337

—. 1983, ApJ, 273, 761

—. 1994, ApJ, 429, 325

De Jager, O. C., Harding, A. K., Sreekumar, P., & Strickman, M. 1996, A&A Suppl., 120, C441

DeCesar, M. E. 2013, PhD thesis, Univ. of Maryland, College Park

Deutsch, A. J. 1955, Ann. d'Astrophys., 18, 1

Dodson, R., Legge, D., Reynolds, J. E., & McCulloch, P. M. 2003, ApJ, 596, 1137

Du, Y. J., Qiao, G. J., Han, J. L., et al. 2010, MNRAS, 406, 2671

Duncan, R. C., & Thompson, C. 1992, ApJL, 392, L9

Dyks, J., & Harding, A. K. 2004, ApJ, 614, 869

Dyks, J., Harding, A. K., & Rudak, B. 2004a, ApJ, 606, 1125

Dyks, J., & Rudak, B. 2003, ApJ, 598, 1201

Dyks, J., Rudak, B., & Harding, A. K. 2004b, ApJ, 607, 939

Erber, T. 1966, Rev. Mod. Phys., 38, 626

Fichtel, C. E., Hartman, R. C., Kniffen, D. A., et al. 1975, ApJ, 198, 163

Fierro, J. M., Michelson, P. F., Nolan, P. L., & Thompson, D. J. 1998, ApJ, 494, 734

Fisher, R. A. 1925, Statistical methods for research workers (Edinburgh: Oliver and Boyd)

Fritz, G., Henry, R. C., Meekins, J. F., et al. 1969, Science, 164, 709

Giacconi, R., Gursky, H., Paolini, F. R., & Rossi, B. B. 1962, Phys. Rev. Lett., 9, 439

Gold, T. 1968, Nature, 218, 731

—. 1969, Nature, 221, 25

Goldreich, P., & Julian, W. H. 1969, ApJ, 157, 869

Grenier, I. A., Hermsen, W., & Clear, J. 1988, A&A, 204, 117

Griffiths, D. J. 1995, Introduction to Electrodynamics (3rd ed.; San Francisco: Pearson Benjamin Cummings)

Haensel, P., Potekhin, A. Y., & Yakovlev, D. G. 2007, in Astrophysics and Space Science Library, ed. P. Haensel, A. Y. Potekhin, & D. G. Yakovlev, Vol. 326 (New York: Springer)

Halpern, J. P., & Holt, S. S. 1992, Nature, 357, 222

Harding, A. K. 2005a, in AIP Conf. Ser., Vol. 801, Astrophysical Sources of High Energy Particles and Radiation, ed. T. Bulik, B. Rudak, & G. Madejski, 241

Harding, A. K. 2005b, in 22nd Texas Symposium on Relativistic Astrophysics, ed. P. Chen, E. Bloom, G. Madejski, & V. Patrosian, 149

Harding, A. K. 2007a, ArXiv Astrophysics e-prints (astro-ph/0710.3517)

Harding, A. K. 2007b, in AIP Conf. Ser., Vol. 921, The First GLAST Symposium, ed. S. Ritz, P. Michelson, & C. A. Meegan, 49

Harding, A. K., & Grenier, I. A. 2011, in High-Energy Emission from Pulsars and their Systems: Proc. of the First Session of the Sant Cugat Forum on Astrophysics, ed. D. F. Torres & N. Rea (Springer: Springer-Verlag Berlin Heidelberg)

Harding, A. K., & Lai, D. 2006, Rep. Prog. Phys., 69, 2631

Harding, A. K., & Muslimov, A. G. 1998, ApJ, 508, 328

Harding, A. K., & Muslimov, A. G. 2003, in Pulsars, AXPs and SGRs Observed with BeppoSAX and Other Observatories, ed. G. Cusumano, E. Massaro, & T. Mineo, 121

—. 2011a, ApJL, 726, L10

—. 2011b, ApJ, 743, 181

Harding, A. K., & Preece, R. 1987, ApJ, 319, 939

Harding, A. K., Stern, J. V., Dyks, J., & Frackowiak, M. 2008, ApJ, 680, 1378

Harding, A. K., Usov, V. V., & Muslimov, A. G. 2005, ApJ, 622, 531

Hewish, A. 1975, Rev. Mod. Phys., 47, 567

Hewish, A., Bell, S. J., Pilkington, J. D. H., et al. 1968, Nature, 217, 709

Hillier, R. R., Jackson, W. R., Murray, A., et al. 1970, ApJL, 162, L177

Hirotani, K. 2006, ApJ, 652, 1475

—. 2008a, ArXiv Astrophysics e-prints (astro-ph/0809.1283)

—. 2008b, ApJL, 688, L25

—. 2011, ApJL, 733, L49

Hoyle, F., Narlikar, J. V., & Wheeler, J. A. 1964, Nature, 203, 914

Jackson, J. D. 1999, Classical Electrodynamics ($3^{\rm rd}$ ed.; New York: John Wiley and Sons, Inc.)

Johnson, T. J., Venter, C., Harding, A. K., et al. 2014, ApJS, 213, 6

Johnston, S., Hobbs, G., Vigeland, S., et al. 2005, MNRAS, 364, 1397

Kalapotharakos, C., Kazanas, D., Harding, A., & Contopoulos, I. 2012, ApJ, 749, 2

Kanbach, G. 2001, in The Universe in Gamma Rays, ed. V. Schönfelder, 127–158

Kanbach, G., Arzoumanian, Z., Bertsch, D. L., et al. 1994, A&A, 289, 855

Keane, E. F., Kramer, M., Lyne, A. G., et al. 2011, MNRAS, 415, 3065

Kniffen, D. A., Hartman, R. C., Thompson, D. J., et al. 1974, Nature, 251, 397

Lamb, F. K., Boutloukos, S., Van Wassenhove, S., et al. 2009, ApJ, 706, 417

Landau, L. D. 1932, Phys. Z. Sowjetunion, 1, 285

Large, M. I., Vaughan, A. E., & Mills, B. Y. 1968, Nature, 220, 340

Li, J., Spitkovsky, A., & Tchekhovskoy, A. 2012, ApJ, 746, 60

Li, J. G. 2014, PhD thesis, Princeton Univ.

Lichnerowicz, A. 1967, Relativistic Hydrodynamics and Magnetohydrodynamics (New York: Benjamin)

Lorimer, D. R., & Kramer, M. 2004, Handbook of Pulsar Astronomy (Cambridge: Cambridge Univ. Press)

Lyne, A. G., & Graham-Smith, F. 1990, Pulsar astronomy (Cambridge, England and New York: Cambridge Univ. Press (Cambridge Astroph. Ser., No. 16))

Lyutikov, M., Otte, N., & McCann, A. 2012, ApJ, 754, 33

Manchester, R. N., Hobbs, G. B., Teoh, A., & Hobbs, M. 2005, Astron. J., 129, 1993

Manchester, R. N., & Taylor, J. H. 1977, Pulsars (San Francisco: W. H. Freeman)

Mattox, J. R., Bertsch, D. L., Fichtel, C. E., et al. 1992, ApJL, 401, L23

McLaughlin, M. A., Lyne, A. G., Lorimer, D. R., et al. 2006, Nature, 439, 817

Medin, Z., & Lai, D. 2007, MNRAS, 382, 1833

Mereghetti, S. 2008, Astron. Astrophys. Rev. 15, 225

Mészáros, P. 1992, High-energy radiation from magnetized neutron stars. (Chicago: The Univ. of Chicago Press)

Minkowski, R. 1942, ApJ, 96, 199

Mochol, I., & Pétri, J. 2015, MNRAS, 449, L51

Morini, M. 1983, MNRAS, 202, 495

Morrison, P. 1958, Il Nuovo Cimento, 7, 858

Morrison, P., Olbert, S., & Rossi, B. 1954, Phys. Rev., 94, 440

Muslimov, A., & Harding, A. K. 1997, ApJ, 485, 735

Muslimov, A. G., & Harding, A. K. 2003, ApJ, 588, 430

—. 2004a, ApJ, 606, 1143

—. 2004b, ApJ, 617, 471

Muslimov, A. G., & Tsygan, A. I. 1992, MNRAS, 255, 61

Neyman, J., & Pearson, E. S. 1928, On the Use and Interpretation of Certain Test Criteria for Purposes of Statistical Inference: Part I (Biometrika Trust)

Ng, C., & Romani, R. W. 2008, ApJ, 673, 411

Ng, C. Y., & Romani, R. W. 2004, ApJ, 601, 479

Oppenheimer, J. R., & Volkoff, G. M. 1939, Phys. Rev., 55, 374

Ostriker, J. P., & Gunn, J. E. 1969, ApJ, 157, 1395

Pacini, F. 1967, Nature, 216, 567

Padmanabhan, T. 2000, Theoretical Astrophysics - Volume 1, Astrophysical Processes (Cambridge: Cambridge Univ. Press)

—. 2001, Theoretical Astrophysics - Volume 2, Stars and Stellar Systems (Cambridge: Cambridge Univ. Press)

Palen, S. E. 2002, Shaum's Outline of Theory and Problems of Astronomy (New York: McGRAW-HILL)

Parzen, E. 1962, Ann. Math. Stat., 33, 1065

Pellizzoni, A., Pilia, M., Possenti, A., et al. 2009, ApJ, 691, 1618

Pierbattista, M., Harding, A. K., Grenier, I. A., et al. 2014, ArXiv Astrophysics eprints (astroph/1403.3849)

Press, W. H., Teukolsky, S. A., & Flannery, B. P. 1992, Numerical Recipes in C: The Art of Scientific Computing (2^{nd} ed.; Cambridge: Press Syndicate of the Univ. of Cambridge)

Ramana Murthy, P. V., & Wolfendale, A. W. 1986, Gamma-ray astronomy (Cambridge: Cambridge Univ. Press)

Rea, N., & Esposito, P. 2011, in High-Energy Emission from Pulsars and their Systems: Proc. of the First Session of the Sant Cugat Forum on Astrophysics, ed. D. F. Torres & N. Rea (Springer: Springer-Verlag Berlin Heidelberg)

Romani, R. W. 1996, ApJ, 470, 469

Romani, R. W., & Watters, K. P. 2010, ApJ, 714, 810

Rudak, B., Dyks, J., & Bulik, T. 2002, in Neutron Stars, Pulsars, and Supernova Remnants, ed. W. Becker, H. Lesch, & J. Trümper, 142

Ruderman, M. A., & Sutherland, P. G. 1975, ApJ, 196, 51

Rybicki, G. B., & Lightman, A. P. 1979, Radiative processes in astrophysics (New York: John Wiley and Sons, Inc.)

Schönfelder, V. 2001, in The Universe in Gamma Rays, ed. V. Shönvelder, A&A Library, 1

Seyffert, A., Venter, C., De Jager, O. C., & Harding, A. K. 2010, in 25th Texas Symposium on Relativistic Astrophysics, 130

Seyffert, A. S., Venter, C., Johnson, T. J., & Harding, A. K. 2012, ArXiv Astrophysics e-prints (astro-ph/1201.4272)

—. 2015, ArXiv Astrophysics e-prints (astro-ph/1501.06768)

Sokolov, A. A., & Ternov, I. M. 1968, Synchrotron radiation (1^{st} ed.; Oxford, NY: Pergamon Press)

Spitkovsky, A. 2006, ApJL, 648, L51

Staelin, D. H., & Reifenstein, III, E. C. 1968, Science, 162, 1481

Story, S. A., Gonthier, P. L., & Harding, A. K. 2007, ApJ, 671, 713

Sturrock, P. A. 1971, ApJ, 164, 529

Svensson, R. 1982, ApJ, 258, 335

Takata, J., Shibata, S., & Hirotani, K. 2004, MNRAS, 354, 1120

Tananbaum, H., Gursky, H., Kellogg, E. M., et al. 1972, ApJL, 174, L143

Tayler, R. J. 1994, The Stars, Their Structure and Evolution (Cambridge: Cambridge University Press)

Tchekhovskoy, A., Spitkovsky, A., & Li, J. G. 2013, MNRAS, 435, L1

Thompson, D. J., Fichtel, C. E., Kniffen, D. A., & Ogelman, H. B. 1975, ApJL, 200, L79

Timokhin, A. N. 2006, MNRAS, 368, 1055

—. 2010, MNRAS, 408, 2092

Timokhin, A. N., & Arons, J. 2013, MNRAS, 429, 20

Truemper, J., Pietsch, W., Reppin, C., et al. 1978, ApJL, 219, L105

Usov, V. V., & Melrose, D. B. 1995, Austr. J. Phys., 48, 571

Venter, C., & De Jager, O. C. 2010, ApJ, 725, 1903

Venter, C., Harding, A. K., & Guillemot, L. 2009, ApJ, 707, 800

Venter, C., Johnson, T. J., & Harding, A. K. 2012, ApJ, 744, 34

Wang, Y., Takata, J., & Cheng, K. S. 2010, ApJ, 720, 178

—. 2011, MNRAS, 414, 2664

Watters, K. P., Romani, R. W., Weltevrede, P., & Johnston, S. 2009, ApJ, 695, 1289

Wheeler, J. A. 1966, Ann. Rev. Astron. Astrophys., 4, 393

Wilks, S. S. 1938, Ann. Math. Stat., 9, 60

Will, C. M. 1994, Phys. Usp., 37, 697

Yadigaroglu, I. A. G. 1997, PhD thesis, Stanford University

Zavlin, V. E., Pavlov, G. G., Sanwal, D., et al. 2002, ApJ, 569, 894